AD-A043 398 STANFORD RESEARCH INST MENLO PARK CALIF F/G 8/7
LABORATORY INVESTIGATION OF ROCK CAVITY REINFORCEMENT.(U)
APR 76 T C KENNEDY, H E LINDBERG DNA001-75-C-0101
UNCLASSIFIED DNA-4023F NL

1 OF 3
AD
A043 398

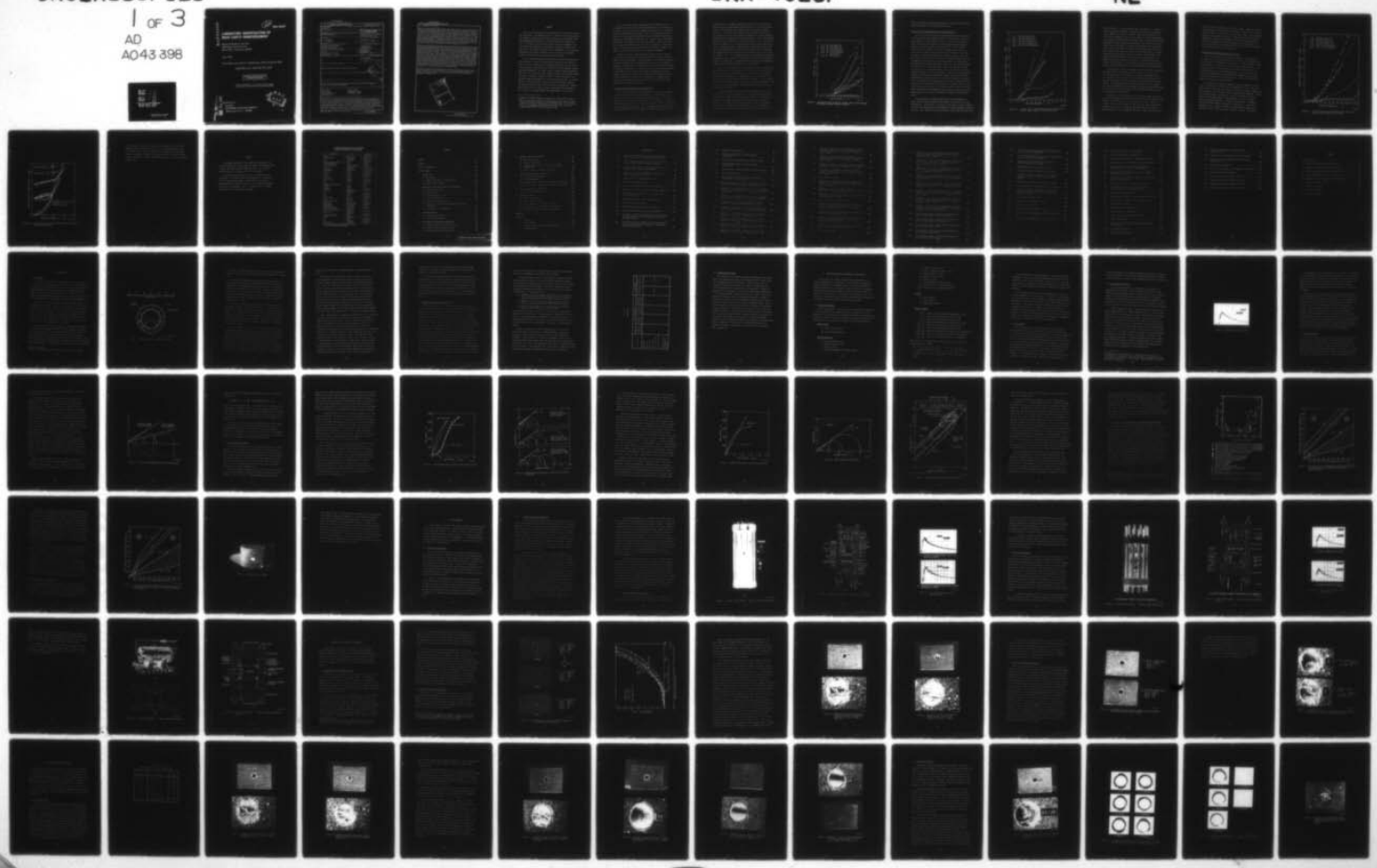

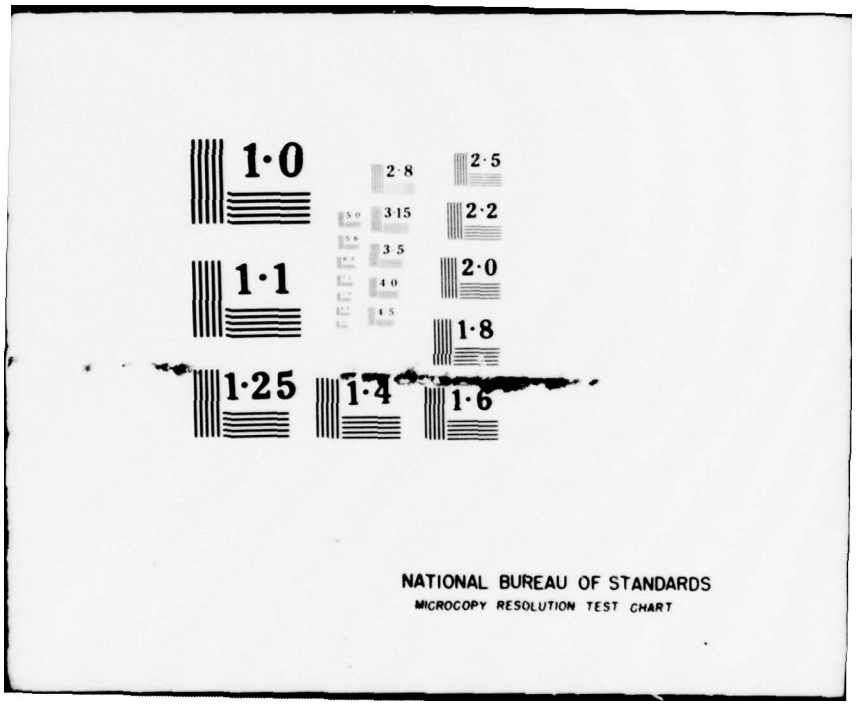
1·0
1·1
1·25
1·4
1·6
1·8
2·0
2·2
2·5
2·8
3·15
3·5
4·0
4·5
5·0
NATIONAL BUREAU OF STANDARDS
MICROCOPY RESOLUTION TEST CHART

DNA 4023F

LABORATORY INVESTIGATION OF ROCK CAVITY REINFORCEMENT

Stanford Research Institute
333 Ravenswood Avenue
Menlo Park, California 94025

April 1976

Final Report for Period 17 September 1974—16 March 1976

CONTRACT No. DNA 001-75-C-0101

APPROVED FOR PUBLIC RELEASE;
DISTRIBUTION UNLIMITED.

THIS WORK SPONSORED BY THE DEFENSE NUCLEAR AGENCY
UNDER RDT&E RMSS CODE B344075462 J34CAXSX31106 H2590D.

Prepared for
Director
DEFENSE NUCLEAR AGENCY
Washington, D. C. 20305

UNCLASSIFIED

SECURITY CLASSIFICATION OF THIS PAGE *(When Data Entered)*

REPORT DOCUMENTATION PAGE

READ INSTRUCTIONS BEFORE COMPLETING FORM

1. REPORT NUMBER: DNA 4023F	2. GOVT ACCESSION NO.
3. RECIPIENT'S CATALOG NUMBER	
4. TITLE *(and Subtitle)*: LABORATORY INVESTIGATION OF ROCK CAVITY REINFORCEMENT	5. TYPE OF REPORT & PERIOD COVERED: Final Report for Period 17 Sep 74—16 Mar 76
	6. PERFORMING ORG. REPORT NUMBER: SRI Project PYU-3743
7. AUTHOR(s): T. C. Kennedy, H. E. Lindberg	8. CONTRACT OR GRANT NUMBER(s): DNA 001-75-C-0101
9. PERFORMING ORGANIZATION NAME AND ADDRESS: Stanford Research Institute, 333 Ravenswood Avenue, Menlo Park, California 94025	10. PROGRAM ELEMENT, PROJECT, TASK AREA & WORK UNIT NUMBERS: NWET Subtask J34CAXSX311-06
11. CONTROLLING OFFICE NAME AND ADDRESS: Director, Defense Nuclear Agency, Washington, D.C. 20305	12. REPORT DATE: April 1976
	13. NUMBER OF PAGES: 224
14. MONITORING AGENCY NAME & ADDRESS *(if different from Controlling Office)*	15. SECURITY CLASS *(of this report)*: UNCLASSIFIED
	15a. DECLASSIFICATION DOWNGRADING SCHEDULE

16. DISTRIBUTION STATEMENT *(of this Report)*

Approved for public release; distribution unlimited.

17. DISTRIBUTION STATEMENT *(of the abstract entered in Block 20, if different from Report)*

18. SUPPLEMENTARY NOTES

This work sponsored by the Defense Nuclear Agency under RDT&E RMSS Code B344075462 J34CAXSX31106 H2590D.

19. KEY WORDS *(Continue on reverse side if necessary and identify by block number)*

Deep Basing
Scale Models
Structural Response
Rock Response
Lined Tunnels
Backpacked Tunnels
Laboratory Testing

20. ABSTRACT *(Continue on reverse side if necessary and identify by block number)*

The response of monocoque direct-contact and backpacked liners as hardened buried structures was studied through experiments on scale models (5/8-inch-diameter tunnel), guided by analyses of structure and rock response assuming a Mohr-Coulomb rock strength characterization. Two loading machines were modified to extend their capabilities and improve their performance. The modifications to the machines produced improvements in tunnel access, in sealing between vertical and lateral pressure chambers, in dynamic pressure pulses, and in general test procedures.

DD FORM 1 JAN 73 1473 EDITION OF 1 NOV 65 IS OBSOLETE

UNCLASSIFIED

SECURITY CLASSIFICATION OF THIS PAGE *(When Data Entered)*

20. ABSTRACT (Continued)

After the testing machine modifications and calibration tests, we performed static and dynamic structure experiments, mostly with a rock simulant having an unconfined compressive strength of about 4300 psi and a friction angle of 33 degrees. Structures consisted of direct-contact steel liners of three different radius-to-thickness ratios (a/h = 50, 25, 12.5) and backpacked steel liners with a/h = 25 and a/h = 12.5 steel liners and with a backpacking having a radius-to-thickness ratio of R/H = 4.5. After discussing the efficacy of laboratory experiments as a reasonable representation of actual field conditions, we performed a series of isotropic (equal stress in all three directions) and uniaxial-strain loading tests on models in water-saturated rock, followed by uniaxial-strain loading tests on similar models in dry rock.

In the isotropic loading experiments, the load-deformation relationship for the direct-contact liners agreed with pretest theoretical curves from the elastic-plastic analysis and showed substantial increase in strength with increasing liner thickness. At the higher loads, the a/h = 50 and 25 liners buckled and the deformations became larger than predicted from the theory. The a/h = 12.5 liners did not buckle, even at tunnel closures of five percent. With backpacking, the load was increased until the backpacking was severely crushed; the steel liners sustained negligible deformation. Similar behavior was found in uniaxial-strain loading experiments, but 30 to 50 percent less load was required to cause five percent tunnel closure than under isotropic loading. In the uniaxial-strain loading experiments in dry rock, the response was similar to that in saturated rock but with slightly smaller deformations. In cyclic loading experiments (both isotropic and uniaxial-strain) on a direct-contact liner in dry rock, the final deformation of the tunnel was not seriously affected by repeated unloading and reloading (i.e., the tunnel closure system shakes down).

A structures experiment was performed as add-on to the Dining Car Event at NTS. Twelve structures, a factor in ten larger in size than the laboratory models, were fielded. These structures have been recovered, and the results of the test are presented in POR No. 6887.

SUMMARY

The goal of this project is the development of efficient structures for deep basing. Our approach has been to continue the investigation of the response of deep based structures through static and dynamic scale model experiments started under a previous contract and reported in [1].* The model tests are used to relate structural response to the surrounding rock properties, thus making it possible to design structures that are optimally matched to their environments. The scale-model experiments were guided by analyses of structure and rock response assuming a Mohr-Coulomb rock strength characterization.

The two loading machines developed during the previous program [1] were modified to extend their capabilities and improve their performance. One is a hydraulic static loading machine that can test 4-inch (10.2 cm)-diameter rock models with 5/8-inch (1.59 cm)-diameter tunnels, under both isotropic** and a wide range of triaxial loading conditions. The other is an explosive dynamic loading machine to test similar models, also under isotropic or triaxial loading. The modifications to the machines produced improvements in the four following areas: (1) tunnel access, (2) sealing between vertical and lateral pressure chambers, (3) dynamic pressure pulses, and (4) general test procedures. Approximately sixty static and thirty dynamic experiments were performed in the course of the testing machine development phase of the project.

---

*Numbers in brackets designate references at the end of the report.

**The term isotropic loading is used throughout this report to denote loading with equal stresses in all three directions. In the static case it is synonomous with hydrostatic loading, but there is no standard equivalent term for the dynamic case.

After the testing machine modifications and calibration tests, we performed twenty static and three dynamic experiments on rock specimens to explore the basic response of monocoque direct-contact and backpacked liners as hardened buried structures. Most of the experiments were conducted with a rock simulant (6B rock) having an unconfined compressive strength of about 4300 psi (29.6 MPa) and a friction angle of 33 degrees (0.576 rad). In addition to the laboratory tests, a structures experiment add-on to the Dining Car event at NTS was performed. Twelve structures, a factor of ten larger in size than the laboratory models, were fielded. The results of this test are reported in POR 6887.

Before we began the laboratory study of direct-contact and backpacked liners, we performed a series of preliminary tests to check the validity of the experiments. These preliminary tests addressed questions concerning boundary effects, reproducibility, the effect of porewater pressure, and the effect of the absence of a liner. After these studies of laboratory experiments as a representation of actual field conditions, we performed the twenty-three test matrix of experiments on direct-contact and backpacked liners. The remainder of this summary presents a brief description of the results of isotropic and uniaxial-strain loading tests on models in water-saturated rock, and uniaxial-strain loading tests on models in dry rock.

Isotropic Loading Experiments in Saturated Rock

Six static isotropic loading experiments were performed on models in water-saturated rock, with water permitted to drain from the rock during the test so that no porewater pressure developed. The direct-contact liners were made from mild steel [yield strength $\sigma_y \approx 40{,}000$ psi (275 MPa)] with three different radius-to-thickness ratios: $a/h = 50$, 25, 12.5 (see Figure 1-1, page 26). The two backpacked models consisted of steel liners (with $a/h = 25$ and 12.5) surrounded by polyurethane foam

backpacking (with a radius-to-thickness ratio R/H = 4.5), which has a crush strength of about 550 psi (3.79 MPa) up to a strain of 40 percent. Plots of tunnel closure versus pressure for these tests are shown in Figure S-1. We see that the results of the two repeat tests on the a/h = 50 direct contact liners (upper two curves) are in close agreement, demonstrating the reproducibility of the experiment. Both liners buckled during the test, as did the a/h = 25 direct contact liner. The deformation of the thicker (a/h = 25) direct contact liner is less than that in the a/h = 50 liner because it applies greater confining pressure to the rock and also buckles less severely than the thinner liner. Similarly, the deformation of the a/h = 12.5 liner is smaller still, since it does not buckle at all. In the backpacked liners, the backpacking was severely crushed during the test but the steel liners were relatively undeformed because the backpacking had absorbed most of the rock cavity deformation without applying excessive pressure to the steel liners.

Figure S-1 also shows theoretical predictions from an elastic-plastic analysis assuming the Mohr-Coulomb yield criterion and associated flow rule. For the a/h = 25 liner and the a/h = 12.5 liner, the agreement between theory and experiment is surprisingly good. For the a/h = 50 liner, the theory underestimates the amount of closure. This is attributed to liner buckling, which caused the internal pressure applied to the cavity wall to be significantly less than the simple hoop yield value used in the calculations.

A dynamic isotropic loading test was performed on the a/h = 50 direct contact liner in saturated rock. In the dynamic test, water was not permitted to drain from the rock during the test so that porewater pressure did develop. The result is also plotted (star symbol) in Figure S-1. Although this liner buckled like its static counterpart, we see that the deformation in the dynamic case is about 40 percent less than in the static case. This difference can be attributed in

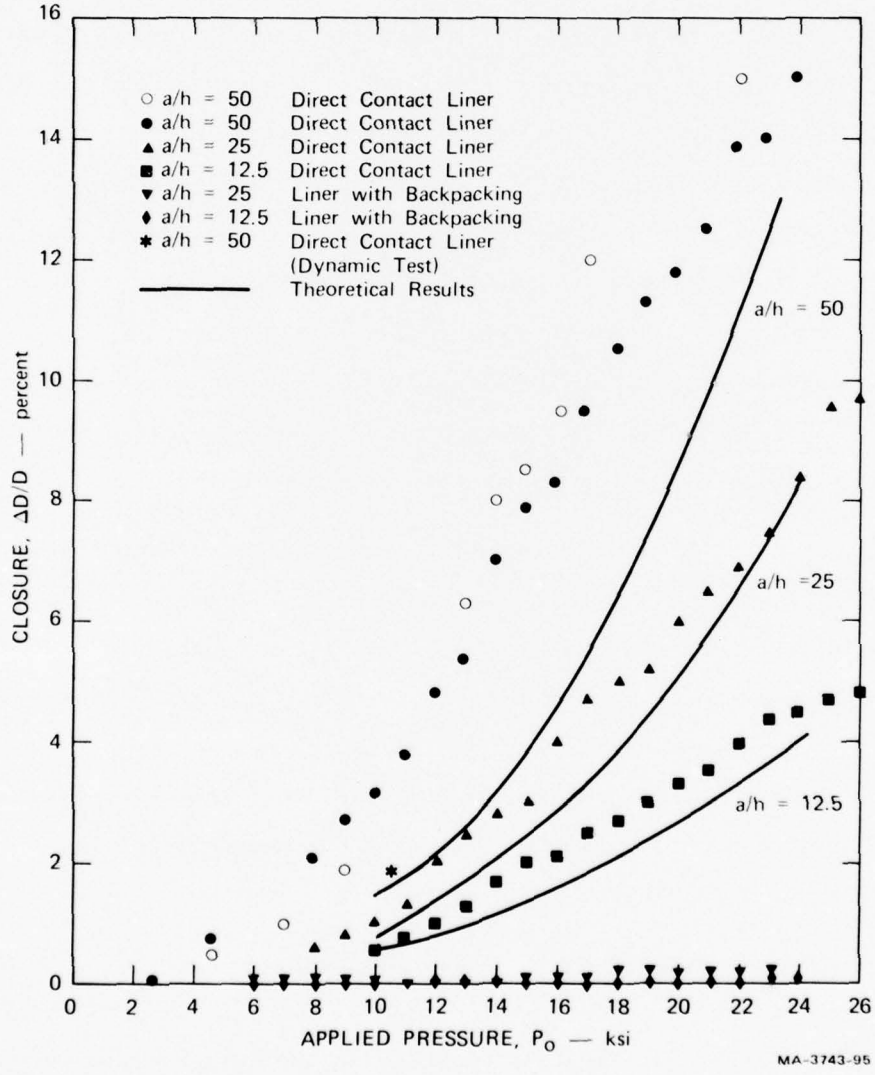

FIGURE S-1 EXPERIMENTAL AND THEORETICAL CLOSURE VERSUS APPLIED PRESSURE FOR STATIC, ISOTROPIC LOADING OF 6B ROCK

part to the presence of porewater pressure in the dynamic loading test, which carries part of the load (see Section 2.4).

Uniaxial Strain Loading Experiments on Saturated Rock

Five static uniaxial-strain loading experiments were performed on the direct-contact and backpacked liners in saturated rock, again with water permitted to drain during the test as in the static isotropic tests. Figure S-2 shows plots of vertical tunnel closure $\Delta D_V/D$ as a function of vertical pressure P_V from these tests. For the direct-contact liners, we observe, as for the isotropic tests, that for a given load the tunnel closure decreases as the thickness of the liner increases. However, the difference in closure from one liner to the next is not nearly as great as it was for isotropic loading (Figure S-1). The apparent reason is that for isotropic loading, the liner resists deformation through hoop compression, which is the most efficient means of resistance for a thin-walled shell. Thus, for isotropic loading, the liner carries a significant part of the total load; i.e., the surrounding rock does not carry all the load. However, for uniaxial-strain loading, the liner resists deformation through a combination of hoop compression and bending, which is a less efficient means of resistance. Thus, for uniaxial-strain loading, the liner carries a smaller part of the load, with the major part being carried by the rock. Since the rock carries most of the load, the type of liner used has little effect, and hence, the reduction in deformation from one liner to the next is small, considering that the liner wall thickness is doubled and then doubled again.

Liner deformation is reduced substantially when backpacking is added. However, under uniaxial-strain loading, the liners now have deformations of a few percent, in contrast to less than one percent throughout the entire loading range under axisymmetric loading (compare Figures S-1 and S-2). The S shape of the load-deformation curves under uniaxial strain

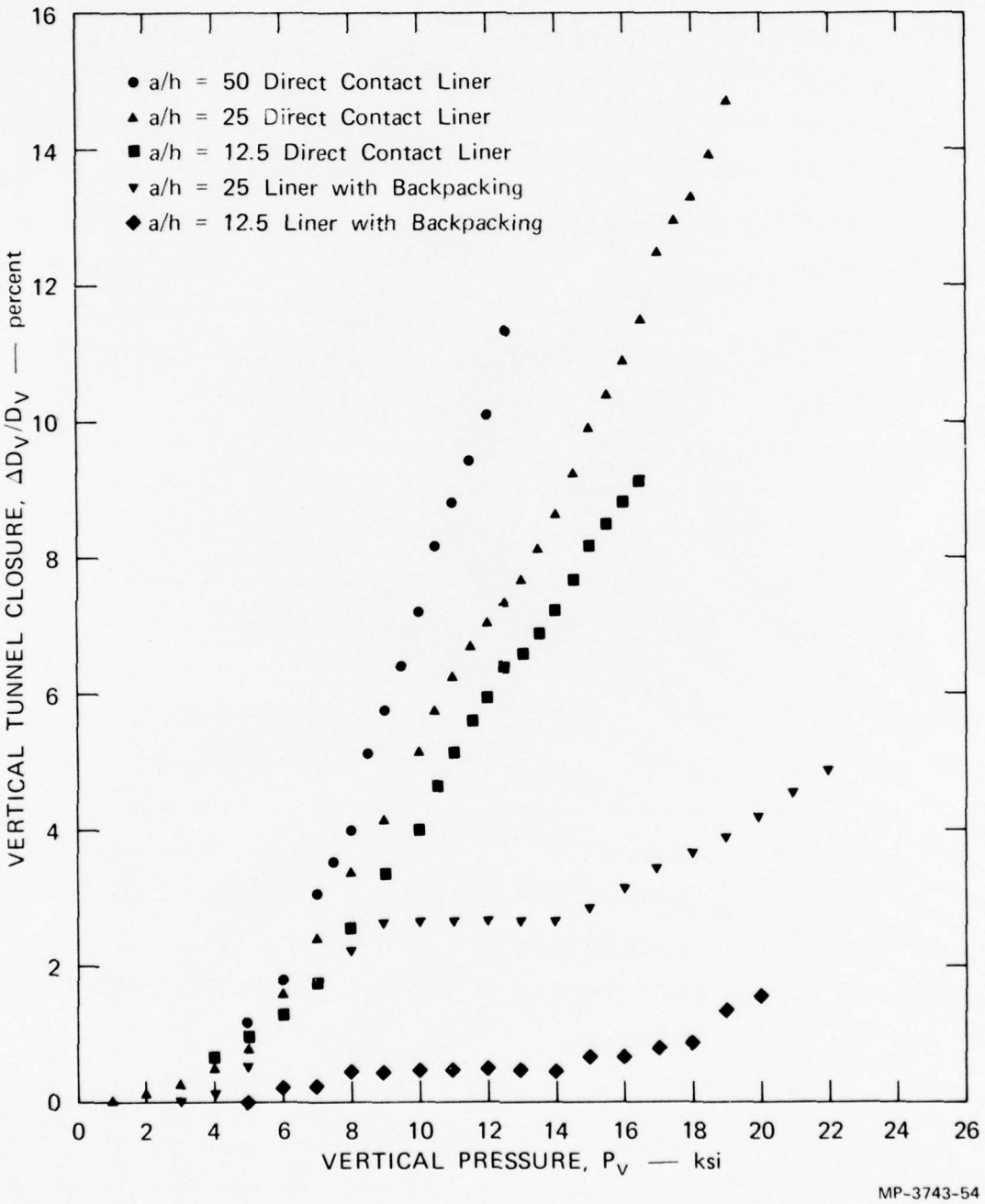

FIGURE S-2 VERTICAL TUNNEL CLOSURE VERSUS VERTICAL PRESSURE FOR UNIAXIAL STRAIN LOADING OF SATURATED 6B ROCK

loading (Figure S-2; the deformation rises, then remains at a plateau, and then rises again) is probably a reflection of the shape of the stress-strain curve of the foam as it crushes. During early deformation the finite initial modulus of the foam gives rise to a radial stress difference around the circumference of the steel liner as the rock cavity closes asymmetrically under uniaxial-strain loading. This causes the liner to deform into an oval shape. At larger cavity closures, this stress difference can no longer increase because the foam begins to crush at constant stress at the crown and invert, where the rock closure is largest. Thus, during this period the curve has a plateau, where the steel liner deformation remains constant as the external loading increases, even though the rock cavity continues to close. At still larger external loading and rock closure, the foam begins to lock up so that the stress again rises and the steel liner once again deforms with increasing load.

This sequence of events is consistent with the plateaus in Figure S-2 extending over the same loading range for both the a/h = 12.5 and a/h = 25 liners, but with the plateau at a larger deformation for the a/h = 25 liner. Being thinner, the a/h = 25 liner must oval more than the a/h = 12.5 liner to resist the stress difference around its circumference. We would expect these plateaus of deformation to be reduced for a foam with more nearly rigid-perfectly plastic stress-strain behavior (as in cellular concrete), rather than elastic-plastic behavior (as in the polyurethane foam used here).

Comparison of the uniaxial-strain and isotropic loading results for saturated rock shows that deformation for a given structure under isotropic loading is considerably lower. For example, for the a/h = 50 direct contact liner, the load required to cause 5 percent tunnel closure under isotropic loading is P_V = 12,000 psi (82.7 MPa) while under uniaxial strain loading, it is P_V = 8,500 psi (58.6 MPa). Thus, for the a/h = 50

liner, the load-carrying capacity between isotropic loading and uniaxial-strain loading is reduced by about 30 percent. This reduction in load-carrying capacity is even larger for the thicker liners. This is another aspect of the increased efficiency of liners under isotropic loading as compared with uniaxial-strain loading. Thus, as the hoop strength of the liner becomes more significant compared with the strength of the rock (a/h decreases), the difference in critical loads between isotropic and uniaxial-strain loading becomes larger.

Uniaxial-Strain Loading Experiments on Dry Rock

Five static uniaxial-strain loading experiments were performed on the direct-contact and backpacked liners in dry rock for comparison with the saturated rock experiments described above. Figure S-3 plots vertical tunnel closure as a function of vertical pressure from these tests. The general behavior of the structures in dry rock is similar to that in saturated rock, and the same conclusions hold. We note, however, that the dry rock results show reduced deformation compared to the saturated rock. This is because the dry rock maintains a larger friction angle at high load than does the saturated rock.

In addition to the monotonic loading tests just discussed, a static, cyclic, uniaxial-strain loading test was performed on an a/h = 12.5 steel-lined tunnel in dry rock. The results of this test are shown in Figure S-4, where vertical tunnel closure is plotted against vertical pressure. During the initial loading to a pressure P_V = 9.5 ksi (65.5 MPa), the tunnel closure reached 2.25 percent. Upon unloading to 1.1 ksi (7.58 MPa), the tunnel expanded slightly to a closure of 1.95 percent. Reloading to 9.5 ksi (65.5 MPa) brought the closure to 2.35 percent, a very slight additional strain. Similar behavior was observed during unloading and reloading in the vicinity of 4 percent closure, as shown. Also shown

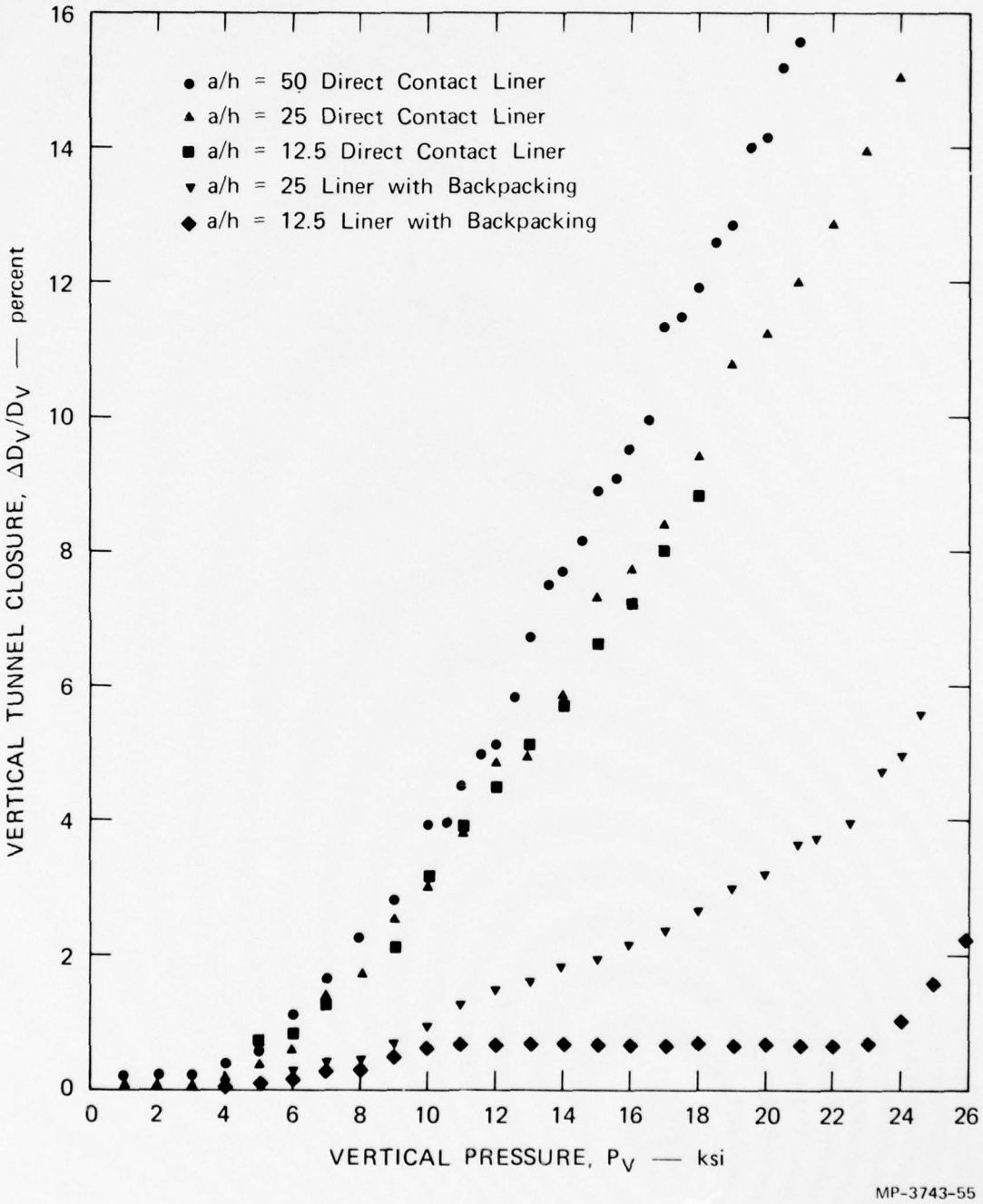

FIGURE S-3 VERTICAL TUNNEL CLOSURE VERSUS VERTICAL PRESSURE FOR UNIAXIAL STRAIN LOADING OF DRY 6B ROCK

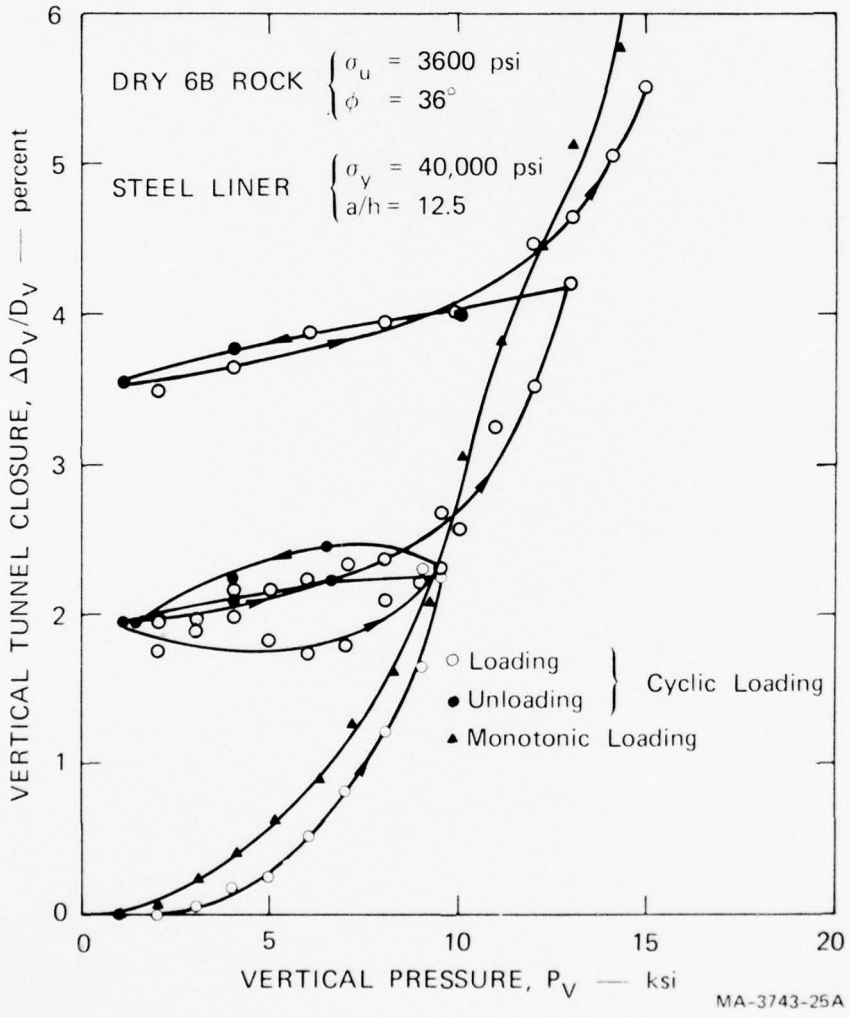

FIGURE S-4 COMPARISON OF CYCLIC AND MONOTONIC LOADING TEST RESULTS— UNIAXIAL STRAIN LOADING

are the monotonic loading test results. The loading part of the cyclic loading results is very close to that of the monotonic loading results. We conclude that the final deformation of the tunnel was not seriously affected by repeated unloading and reloading and that the tunnel closure system "shakes down." Similar behavior was observed in a cyclic, isotropic loading test.

PREFACE

The program described in this report was performed for the Defense Nuclear Agency (DNA) during the period from September 1974 to March 1976 under Contract DNA001-75-C-0101. The technical monitors were Dr. K. Goering and Lt. Col. D. Burgess.

The project was supervised by Drs. A. L. Florence and G. R. Abrahamson. The authors gratefully acknowledge the contribution of J. V. Zaccor who performed the major part of the machine development work. Thanks are also due to G. Matack who performed several of the experiments, and to J. Busma, L. Dary, H. Hannah, and D. Walter for their technical support.

Conversion factors for U.S. customary to metric (SI) units of measurement.

To Convert From	To	Multiply By
angstrom	meters (m)	1.000 000 X E -10
atmosphere (normal)	kilo pascal (kPa)	1.013 25 X E +2
bar	kilo pascal (kPa)	1.000 000 X E +2
barn	meter^2 (m^2)	1.000 000 X E -28
British thermal unit (thermochemical)	joule (J)	1.054 350 X E +3
calorie (thermochemical)	joule (J)	4.184 000
cal (thermochemical)/cm^2	mega joule/m^2 (MJ/m^2)	4.184 000 X E -2
curie	*giga becquerel (GBq)	3.700 000 X E +1
degree (angle)	radian (rad)	1.745 329 X E -2
degree Fahrenheit	degree kelvin (K)	$t_K = (t°f + 459.67)/1.8$
electron volt	joule (J)	1.602 19 X E -19
erg	joule (J)	1.000 000 X E -7
erg/second	watt (W)	1.000 000 X E -7
foot	meter (m)	3.048 000 X E -1
foot-pound-force	joule (J)	1.355 818
gallon (U.S. liquid)	meter^3 (m^3)	3.785 412 X E -3
inch	meter (m)	2.540 000 X E -2
jerk	joule (J)	1.000 000 X E +9
joule/kilogram (J/kg) (radiation dose absorbed)	Gray (Gy)	1.000 000
kilotons	terajoules	4.183
kip (1000 lbf)	newton (N)	4.448 222 X E +3
kip/inch^2 (ksi)	kilo pascal (kPa)	6.894 757 X E +3
ktap	newton-second/m^2 ($N-s/m^2$)	1.000 000 X E +2
micron	meter (m)	1 000 000 X E -6
mil	meter (m)	2.540 000 X E -5
mile (international)	meter (m)	1.609 344 X E +3
ounce	kilogram (kg)	2.834 952 X E -2
pound-force (lbs avoirdupois)	newton (N)	4.448 222
pound-force inch	newton-meter (N·m)	1.129 848 X E -1
pound-force/inch	newton/meter (N/m)	1.751 268 X E +2
pound-force/foot^2	kilo pascal (kPa)	4.788 026 X E -2
pound-force/inch^2 (psi)	kilo pascal (kPa)	6.894 757
pound-mass (lbm avoirdupois)	kilogram (kg)	4.535 924 X E -1
pound-mass-foot^2 (moment of inertia)	kilogram-meter^2 ($kg·m^2$)	4.214 011 X E -2
pound-mass/foot^3	kilogram/meter^3 (kg/m^3)	1.601 846 X E +1
rad (radiation dose absorbed)	**Gray (Gy)	1.000 000 X E -2
roentgen	coulomb/kilogram (C/kg)	2.579 760 X E -4
shake	second (s)	1.000 000 X E -8
slug	kilogram (kg)	1.459 390 X E +1
torr (mm Hg, 0° C)	kilo pascal (kPa)	1.333 22 X E -1

*The becquerel (Bq) is the SI unit of radioactivity; 1 Bq = 1 event/s.
**The Gray (Gy) is the SI unit of absorbed radiation.

CONTENTS

ILLUSTRATIONS

TABLES

1. INTRODUCTION

1.1 Background

The goal of this work is the development of efficient structures for deep basing. Our approach has been to continue the investigation of the response of deep based structures through static and dynamic scale model experiments, which was started under a previous contract and reported in [1].* The model tests are used to relate structural response to the surrounding rock properties, thus contributing to the design of structures that are optimally matched to their environments.

Deep based structures are needed to protect command, control, and communication centers from nuclear attack. Because of the high cost of building these structures, efficiency is important, the most efficient structure being one that provides the required volume and hardness at least cost. The best structure for deep basing will depend on the required volume, type of contents, local geology, and hardness level. Hence, the best type of structure for one range of conditions may not be the best type for another range of conditions.

Typical deep based structures consist of cylindrical or spherical cavities in rock, hardened with liners of steel and concrete. These structures also may have a crushable backpacking material between the liner and the cavity wall, as indicated in Figure 1-1. Reasonable design pressures for a structure of this type are on the order of 1 kbar [2]. Since a shell structure designed to support the full 1-kbar pressure would be impractical, it is apparent that the native rock must carry most

---

*Numbers in brackets designate references at the end of the report.

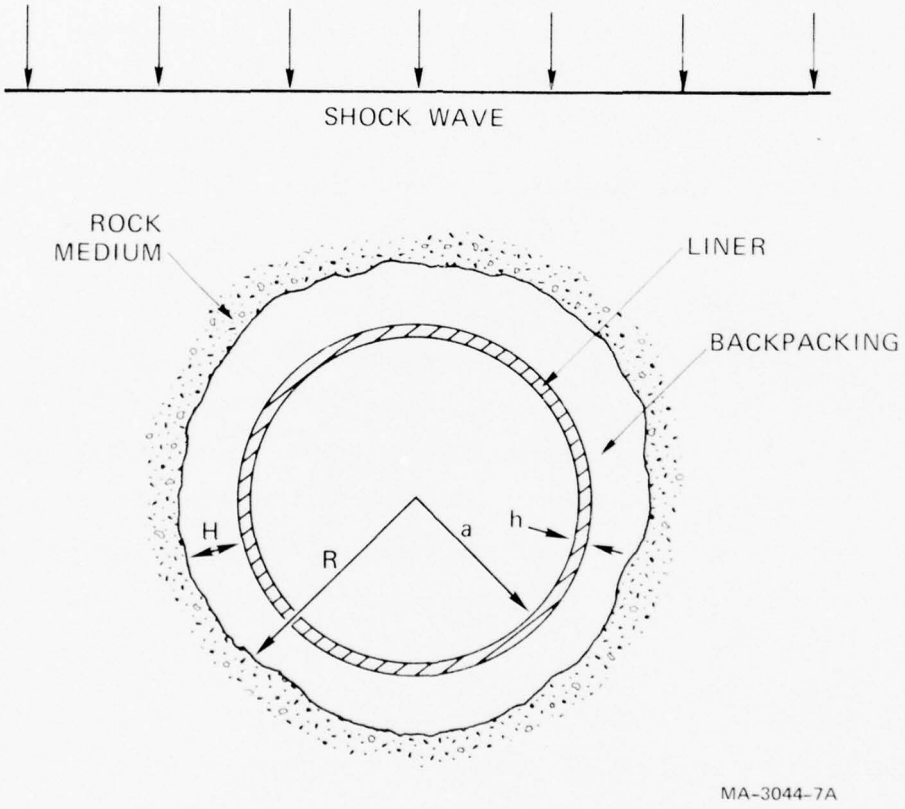

FIGURE 1-1 SHOCK LOADING OF A DEEP-BASED STRUCTURE

of the load. Therefore, the most efficient structures for deep basing will be those that best enhance the load-carrying capacity of the native rock.

Several design concepts for deep basing were investigated in HARD HAT and PILE DRIVER, and additional designs will be tested in the MIGHTY EPIC and DIABLO HAWK underground tests. These tests provide much useful information of a general nature. However, more detailed observations over a wider range of geologic conditions and loads are required to determine quantitative limits on the applicability of the various design concepts. Only from such observations are new design concepts likely to arise.

The ability to apply loads on a laboratory scale is the key to developing efficient structures for deep basing. In the laboratory, detailed observations can be made economically for various deep basing concepts over a wide range of geologic and loading conditions. From such observations will come an understanding of response mechanisms that may lead to new concepts for deep basing. The laboratory method can then be reapplied for rapid and economical evaluation of new concepts as they are developed.

Previous experiments on scale models of deep based structures have been devoted almost exclusively to static testing. Daniel, Rowlands, and Singh [3] performed static experiments on unlined and lined tunnel models in limestone and marble. Heuer and Hendron [4] tested unlined openings using a weak rock-matching grout as their rock material. Hendron, Engeling, and Aiyer [5] extended this work to include experiments on lined tunnels in both jointed and intact rock, as did Hendron and Engeling [6]. In all these experiments, damage levels were kept fairly low (i.e., tunnel closure of only a few percent), and many of

these tests were plagued by specimen cracking not associated with the cavity.

The response of deep based structures was studied at SRI [1] through experiments on scale models, guided by analyses of structure and rock response assuming a Mohr-Coulomb rock strength characterization. Most of the experiments were dynamic, with the loading pulse scaled to simulate a long duration ground shock from a nuclear burst. Two new loading machines were designed, fabricated, and developed into working laboratory tools. One is a hydraulic static loading machine that can test 4-inch (10.2 cm)-diameter rock models with or without 5/8-inch (1.59 cm)-diameter tunnels, under both axisymmetric and a wide range of triaxial loading conditions. The other is an explosive dynamic loading machine to test similar models of the same size under dynamic triaxial loadings that closely simulate nuclear loading environments with various flow conditions (*e.g., uniaxial or diverging flows*).

After testing machine development and calibration tests, we performed 16 dynamic experiments on rock specimens to explore basic response of simple unlined and lined tunnels. All the experiments were conducted with a rock simulant having an unconfined compressive strength of 8500 psi (158.6 MPa), a friction angle of 30 degrees (0.523 rad), vertical loading pressures ranging from 8500 psi (158.6 MPa) to 20,000 psi (138 MPa), and horizontal pressures in most experiments adjusted to give a uniaxial-strain loading condition. Eight of the experiments were performed on unlined tunnel models in intact rock. The mode of failure in these specimens was the formation of shear cracks, which originated at the springlines of the tunnel and then spiraled to become vertical cracks extending far into the rock medium. Damage levels ranged from negligible to severe. Four of these eight experiments were repeated on tunnels with steel liners in direct contact with the tunnel cavity.

In each case, the effect of the liner was to cause a considerable reduction in the amount of closure sustained by the tunnel and less extensive fracturing of the rock.

The final four experiments were performed on unlined tunnels in jointed media with two tunnel diameter-to-joint-spacing ratios, D/S = 5 and 10. The joints were introduced in the models as parallel planes oriented parallel to the axis of the tunnel and perpendicular to the vertical direction of primary loading. The jointed models were more highly damaged than their intact counterparts at the same loadings. Also, the models with D/S = 10 sustained more damage than those with D/S = 5.

1.2 Approach and Scope of Investigation

In this investigation, the response of deep based structures to nuclear ground shock loading was studied by continuing the scale model experiments just described. Our initial approach was to develop for each geologic condition of interest an understanding of the damage mechanism and controlling parameters for two present design concepts: tunnels with direct contact liners and tunnels with backpacked liners. Six different structures were tested. The first structure was an unlined tunnel. This is the simplest tunnel and serves as a baseline for comparison with more sophisticated tunnel structures. The next three tunnels had direct-contact steel liners of different radius-to-thickness ratios [a/h = 12.5, 25, 50 (see Figure 1-1)]. With these liners of different thicknesses, we evaluated the effect of internal pressure on tunnel response [the internal pressure between liner and tunnel is at the yield pressure of the liner throughout much of the response of interest, and can be estimated as $p_i = \sigma_y h/a$, where σ_y is about 40,000 psi (276 MPa)]. These models also showed the influence of a/h on monocoque tunnel buckling. Finally, two structures with backpacking (R/H = 4.5)

as well as tunnel liners (a/h = 12.5 and 25) were tested to investigate the effect of backpacking in preventing tunnel closure.

The structures were tested in a rock simulant representing medium strength rock under both dry and water-saturated conditions and under static and dynamic conditions so that any dynamic effects on the response of the structures could be studied. Two types of loading were used: isotropic (axisymmetric with respect to the tunnel axis) and uniaxial-strain loading. The isotropic loading

(1) Simulates the type of loading experienced by the structures in the Dining Car experiment described later (the Dining Car loading is bounded between isotropic and uniaxial strain)

(2) Provides a means of correlating experimental results with current design procedures which assume isotropic loading

(3) Provides a comparison with the uniaxial-strain experiments to ascertain the importan e of load asymmetry.

The test matrix is shown in Table 1.1. Since most of the experiments reported in [1] were dynamic, this work concentrates primarily on static testing. These experiments were supported by a theoretical effort in which currently available elastic and elastic-plastic theories were used to design structures, plan experiments, and interpret the experimental results.

During the course of the work, additional funds were granted to broaden the scope of the project to include performing a structures experiment as an add-on to the Dining Car event at NTS (reported in POR 6887). Twelve structures, a factor of ten larger in size than the laboratory models, were fielded along with their small-scale counterparts which serve as a tie-in to the laboratory tests and also to demonstrate the effect of scaling. The laboratory tests will be used to support this experiment and other planned underground tests of large-scale structures.

Table 1-1

TEST MATRIX

Structure	Saturated Rock				Dry Rock	
	Static Isotropic, Undrained	Static Isotropic, Drained	Static Uniaxial, Drained	Dynamic Isotropic, Undrained	Static Isotropic	Static Uniaxial
Unlined		x		x		x
a/h = 50	x	x	x	x		x
a/h = 25	x	x	x			x
a/h = 12.5	x	x	x		cycled	x + cycled
a/h = 25 + BP		x	x			x
a/h = 12.5 + BP		x	x			x
Aluminum (a/h = 6.8) in Husky Ace RMG				x		

1.3 Organization of Report

The remainder of this report describes the planning of the experiments, the experimental results, and an interpretation of these results with accompanying theoretical analyses. Chapter 2 deals with the theoretical considerations used in the design of the specimens and testing machines and in the planning of the experiments. Chapter 3 presents a brief description of the current operation and capabilities of the testing machines. Chapter 4 presents the results of a series of experiments used to validate the experimental procedure. Chapter 5 describes the results of static and dynamic isotropic loading tests on tunnels with direct contact liners and with backpacked liners. These are scale models of the structures tested in the Dining Car experiment. Chapter 6 presents the results of static uniaxial-strain loading tests on similar structures. The uniaxial-strain loading results are compared with the isotropic loading results. Chapter 7 presents a discussion of the planning and fielding of the Dining Car structures experiment. Chapter 8 gives the theoretical analyses and comparison with experimental results. Appendices A through D give detailed discussions of the theoretical analyses, rock modeling, test machines, and experimental data, respectively.

2. THEORETICAL BASIS FOR LABORATORY INVESTIGATION

In this chapter we discuss the theoretical background for the design and planning of the experiments. This includes a dimensional analysis, discussions of boundary effects, wave propagation effects, porewater pressure, the rock simulant, and the effect of the relationship between rock and liner properties, and a description of the test specimen. The first three of these topics were addressed in [1]. For continuity, the results reported in [1] are repeated here in abbreviated form along with the new results from the present program.

2.1 Dimensional Analysis

Since the usefulness of this investigation depends on the similitude of the scale models, the variables that have a dominant effect on the response of our structures must be appropriately scaled. The dimensional analysis is similar to that in [1] but with several differences that are discussed later. The following variables are considered significant:

Applied Loads

P_V = peak vertical pressure

P_H = peak horizontal pressure

Material Properties

E = Young's modulus of rock

ν = Poisson's ratio of rock

ρ = density of rock

σ_u = unconfined compressive strength of rock

σ_t = tensile strength of rock

ϕ = angle of internal friction of rock

E_L = Young's modulus of liner

ν_L = Poisson's ratio of liner

ρ_L = density of liner

σ_y = yield strength of liner material

σ_{bp} = crush strength of backpacking material

ϵ_{bp} = locking strain of backpacking material

Geometry

D = tunnel diameter

h = liner thickness

H = backpacking thickness

Systems Response

u_r, u_θ = radial and circumferential displacement of rock

ϵ_r, ϵ_θ = radial and circumferential strain of rock

σ_r, σ_θ = radial and circumferential stress of rock

u_{rL}, $u_{\theta L}$ = radial and circumferential displacement of liner

ϵ_{rL}, $\epsilon_{\theta L}$ = radial and circumferential strain of liner

σ_{rL}, $\sigma_{\theta L}$ = radial and circumferential stress of liner

u_{rbp}, $u_{\theta bp}$ = radial and circumferential displacement of backpacking

ϵ_{rbp}, $\epsilon_{\theta bp}$ = radial and circumferential strain of backpacking

σ_{rbp}, $\sigma_{\theta bp}$ = radial and circumferential stress of backpacking

This selection of 35 significant variables leads to the following set of 32 dimensionless groups:

P_V/σ_u, P_H/σ_u, σ_t/σ_u, E/σ_u, E_L/σ_u, ν, ν_L, σ_y/σ_u, ρ_L/ρ, σ_{bp}/σ_u
ϕ, ϵ_{bp}, D/h, D/H, u_r/D, u_θ/D, ϵ_r, ϵ_θ, σ_r/σ_u, σ_θ/σ_u, u_{rL}/D, $u_{\theta L}/D$,
ϵ_{rL}, $\epsilon_{\theta L}$, σ_{rL}/σ_u, $\sigma_{\theta L}/\sigma_u$, u_{rbp}/D, $u_{\theta bp}/D$, ϵ_{rbp}, $\epsilon_{\theta bp}$, σ_{rbp}/σ_u,
$\sigma_{\theta bp}/\sigma_u$

In our experiments, the tunnel diameter D is 5/8 inch (1.59 cm). Consequently, for a 10-foot (3.05 m)-diameter prototype tunnel, this represents a scale factor of about 200. Thus, h, H, u_r, u_θ, u_{rL}, $u_{\theta L}$, u_{rbp}, and $u_{\theta bp}$ must also be scaled by this same factor for similarity. The rest of these variables in our model are identical to those in the prototype.

The rise time and duration of the loading pulse are not scaled in these experiments as they were in [1]. A longer rise time and duration were used in the current experiments to minimize undesirable wave propagation effects in the loading (this is discussed in more detail in Section 2.3). This change in the pulse shape is not expected to have any significant effect on the response of the structure since the response is essentially quasi-static in nature, as will be discussed in Section 2.3. Other variables not scaled are grain size, pore size, and strain rate. Although these variables are not believed to be dominant, more research is needed to ascertain their importance.

2.2 Stress Field

In our experiments we seek to reproduce the stress field that exists around a cavity in an infinite body. Since our specimen must have finite dimensions, the question arises as to how close the boundaries can be to the cavity without significantly altering the stress field. In [1] it was shown that elastic perturbations in the stress field caused by the hole extend only to about 4 radii into the medium. Consequently, our specimens were originally designed so that the boundaries were more than 4 radii away from the cavity. After plastic flow takes place, the elastic calculations are no longer valid. To determine whether the boundaries of the specimen were sufficiently far removed from the cavity to simulate the infinite body case, under plastic flow conditions, a

series of experiments was performed on samples with different hole sizes. It was again found that the 4-radii criterion was sufficient for damage levels of interest. Details of these experiments are given in Section 4.1.

2.3 Wave Propagation Effects

For our dynamic experiments a possibility of undesirable wave propagation effects exists. Since our specimens are finite and our pulse durations long compared with the transit time of a wave across our sample, the waves resulting from the applied loads will reverberate through the specimen several times instead of passing through the structure only once as in the actual case in the field. Therefore, the question of overstress at the cavity wall due to wave effects must be resolved.

A typical experimental pulse is shown in Figure 2-1 (ramp rise to a broad maximum followed by a roughly exponential decay). The rise time is about 1 ms and the total duration is 10 ms. This rise time and duration are longer than those required on a 1/200 scale of a surface nuclear burst.* The justification for the use of a pulse with a rise time and duration that are longer than the scaled pulse is based on calculations given in [1]. There, a pressure-impulse plot for tunnel closure showed that the response of the tunnel in the range of interest is quasi-static in nature) i.e., the amount of closure is sensitive to the peak pressure of the pulse but not to the duration of the pulse. Consequently, our model experiments should be a reasonable representation of the response of deep based structures even though the loading pulses are not closely scaled. The use of a long rise time and duration also eliminates the two undesirable wave propagation effects described next.

---

*Extrapolation of underground data to a 100 MT burst and ranges of a few thousand feet gives rise times and duration of the order of 30 msec and 300 msec, respectively, in full scale. These translate to 0.15 and 1.5 msec in 1/200 scale.

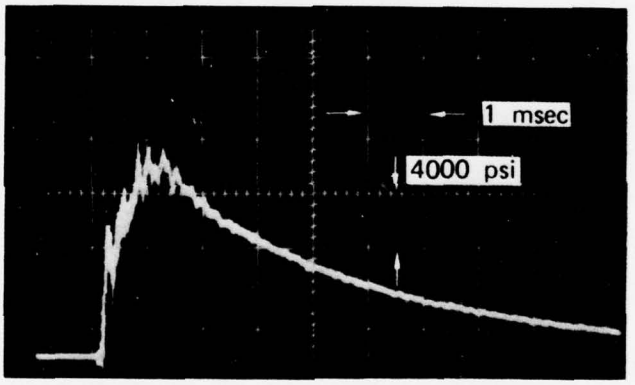

MP-3743-74

FIGURE 2-1 TIME HISTORY OF APPLIED LOAD

As discussed in [1], the diffraction of a plane wave by a cylindrical cavity results in an overstress at the cavity wall. For a step wave with zero rise time, the increase in stress over the static value is about 15 percent. For a wave with a long rise time, as occurs in the actual case in the field, this overstress is less than 15 percent. Thus, wave diffraction effects are not significant in the field nor in our models.

The long rise time also alleviates the problem of overstressing from reflection of the waves at the boundaries of the specimen. This overstress depends on the impedance mismatch between the rock specimen material and the testing machine material that holds the specimen. For a rise time of 1 ms, this overstress is negligible in our rock. Finally, the long rise time and duration reduce the problem of overstressing due to wave reflections in the fluid that surrounds the specimen. This is discussed in detail in Appendix C. The important effects simulated in these dynamic tests that are not simulated in static tests are the dynamic material properties of the rock, including porewater pressure. Porewater pressure often cannot be properly simulated in static tests with tunnels because unrealistic porewater migration causes the tunnels to bulge (see Figure 4-4 and discussion).

2.4 Porewater Pressure

All rocks contain voids that are usually filled with water at the depths of interest for deep basing. The material may be viewed as being composed of a solid rock skeleton traversed by a network of capillaries filled with water. When the rock is loaded, part of the load is carried by the rock skeleton and part by the water. The distribution of the load between the rock skeleton and the water depends on the structure of the skeleton and the relative compressibilities of

the rock grains and the water. The porewater pressure is that part of the load carried by the water.

In performing an analysis of the response of a material with porewater pressure present, the concept of "effective stress" is commonly used. The effective stress is the total stress minus the porewater pressure. The porewater pressure is subtracted from the total stress because it is assumed to have no influence on deformation or failure. A typical Mohr failure envelope for water-saturated rock is shown in Figure 2.2. The dashed circles represent triaxial states of stress, including porewater pressure, at loading conditions under which rock specimens fail (e.g., the dashed circle on the right gives stress states for loading by a vertical pressure σ_2 and confining pressure σ_1). From these data, the total-stress Mohr envelope, indicated by the dashed line, is constructed. If the Mohr circles are replotted with the porewater pressure subtracted (e.g., the solid circles represent a vertical pressure $\sigma_2' = \sigma_2 - p$ and a confining pressure $\sigma_1' = \sigma_1 - p$, where p is the pore pressure), we obtain the effective-stress Mohr failure envelope indicated by the solid line. The assumption of the effective-stress concept is that the effective-stress Mohr envelope is the same as that obtained if the specimens were allowed to drain water during the triaxial tests. The effect of the porewater pressure is to shift the circles to the right and cause a lowering of the Mohr failure envelope.

Porewater pressure will have an effect on the response of our structures. If we consider the elastic response of a body with a cylindrical cavity subjected to a free field pressure P_o, an internal cavity pressure P_i, and a pore pressure p, we find from straightforward

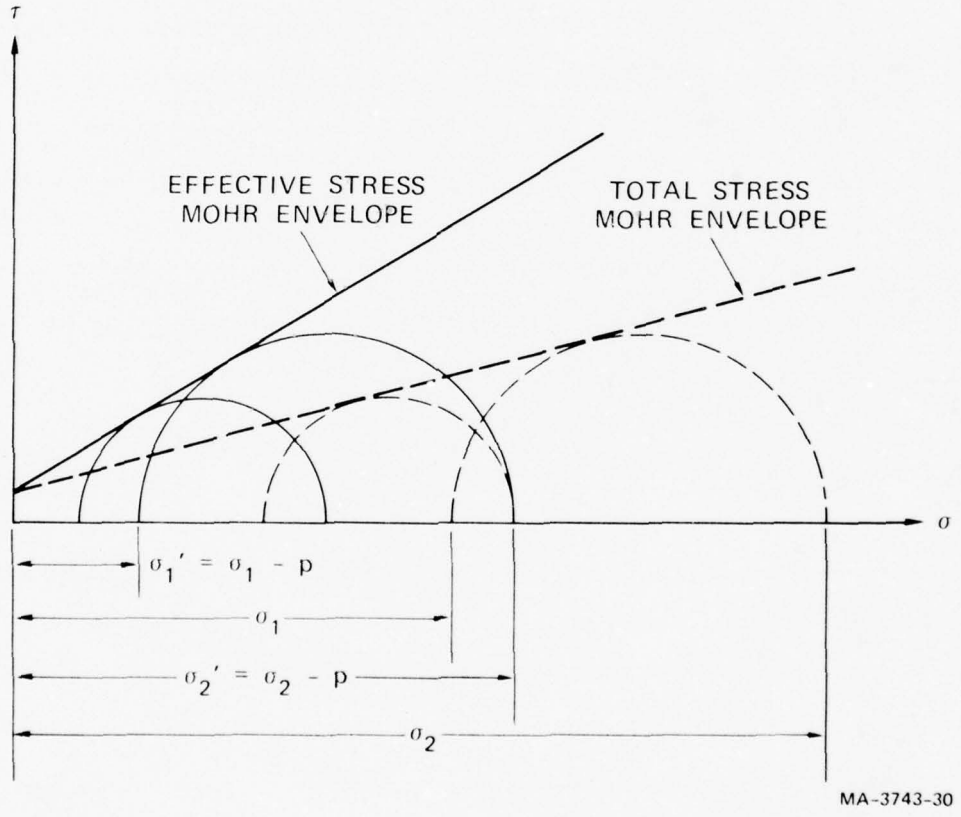

FIGURE 2-2 EFFECT OF PORE PRESSURE ON MOHR FAILURE ENVELOPE

elastic analysis (see Timoshenko and Goodier [7]) that the radial displacement u is

$$u = \frac{(1 + \upsilon)}{E} (P_o - P_i) \frac{a^2}{r} + \frac{(1 + \upsilon)(1 - 2\upsilon)}{E} (P_o - p) r$$

where E is Young's modulus, and υ is Poisson's ratio. We see that as p increases, u decreases. Thus, the effect of porewater pressure is to make the material appear stiffer, since the deformation for a given free field pressure is smaller with porewater pressure than without. This effect can only be examined in a dynamic test as will be discussed in Section 4.2.

The effect of porewater pressure on asymmetrically loaded tunnels is more complicated. If the free field load is asymmetric, then the load applied to the liner by the rock skeleton will be asymmetric. However, the load applied to the liner by the water will be axisymmetric. Therefore, the response of the liner will depend strongly on the distribution of load between the rock skeleton and the water.

2.5 Selection of Rock Simulant

In testing a laboratory model of an underground structure, careful modeling of the surrounding rock is important. The rock can be very difficult to model because faults and joints should be scaled. Moreover, water content is important and overburden pressure may be significant at the depths of interest. Reliable values of these parameters are difficult to obtain, especially for a large volume of rock at great depth. Even if rock can be adequately modeled, the wide range of possible conditions will require simplification.

Rather than attempt to model details of rock structure and texture, we used a grout especially designed to simulate the general characteristics of a rock of interest. Waterways Experiment Station (WES)

provided us with grout specimens (called 6B rock simulant) with strength, modulus, and friction angle representative of medium strength (or jointed high strength) rock. Tunnel experiments were performed on the rock in both the dry and fully water-saturated conditions. The 6 designates that the rock was made from commercial grade sand but with large grains removed by a number 6 sieve. The B designates that it is the second formulation studied by WES. We also used the 6A simulant, which is stronger.

Material property tests were performed on samples of the rock by both WES and SRI. Stress-strain curves for the saturated rock are shown in Figure 2.3. The curve on the left is taken from data provided by WES. The dashed line represents a secant or average elastic modulus. The curve on the right is from tests done at SRI. The curve is offset from the WES data because of the large amount of fictitious strain required to seat the specimen. The unconfined strength and average modulus from the curves are in good agreement. Both curves indicate an unconfined strength of 4000-4500 psi (27.6-31.0 MPa) and an average elastic modulus slightly over 2×10^6 psi (13.8 GPa).

Mohr failure envelopes for the saturated rock at various test ages are shown in Figure 2-4. The rock was kept moist during aging. As the test age increases, the moisture content and degree of saturation increase. This causes the amount of porewater pressure that develops during the test to increase since the specimens are undrained during the test. In the bottom diagram, the specimen is fully saturated and the Mohr circles are shifted a considerable distance to the right because of the porewater pressure. It appears that the angle of internal friction for the effective Mohr failure envelope would be between 30 and 40 degrees (0.523 and 0.698 rad) for low stress levels. For high stress levels [normal stress above 10 ksi (69.9 MPa)] the friction angle is considerably less.

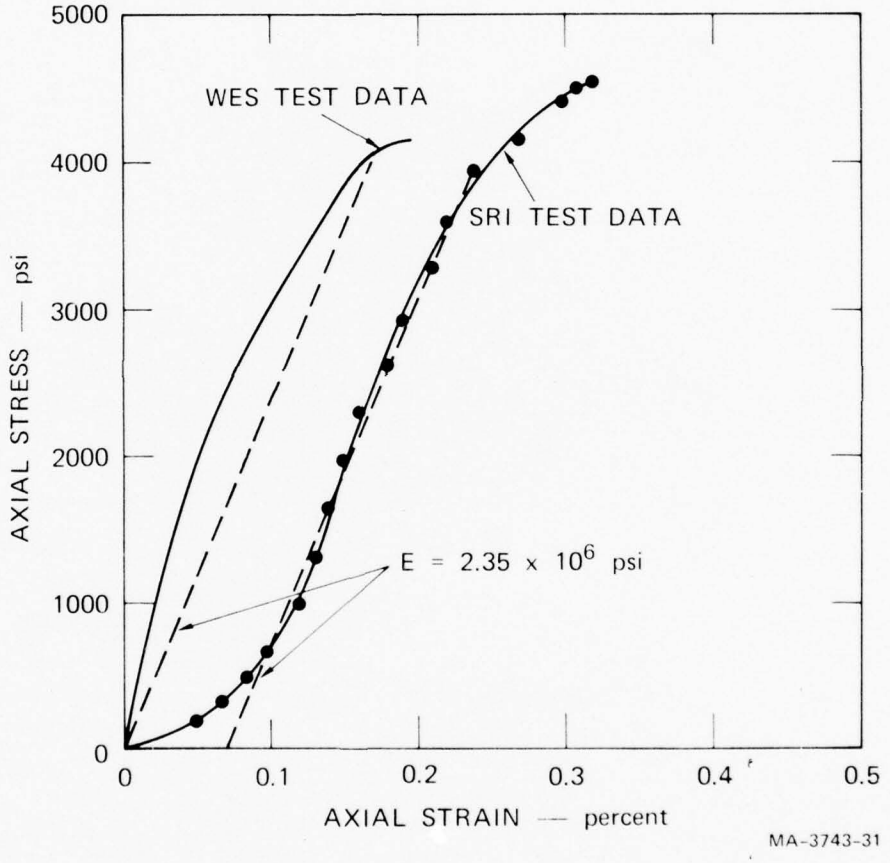

FIGURE 2-3 STRESS-STRAIN CURVES FOR MOISTURIZED 6B ROCK SIMULANT

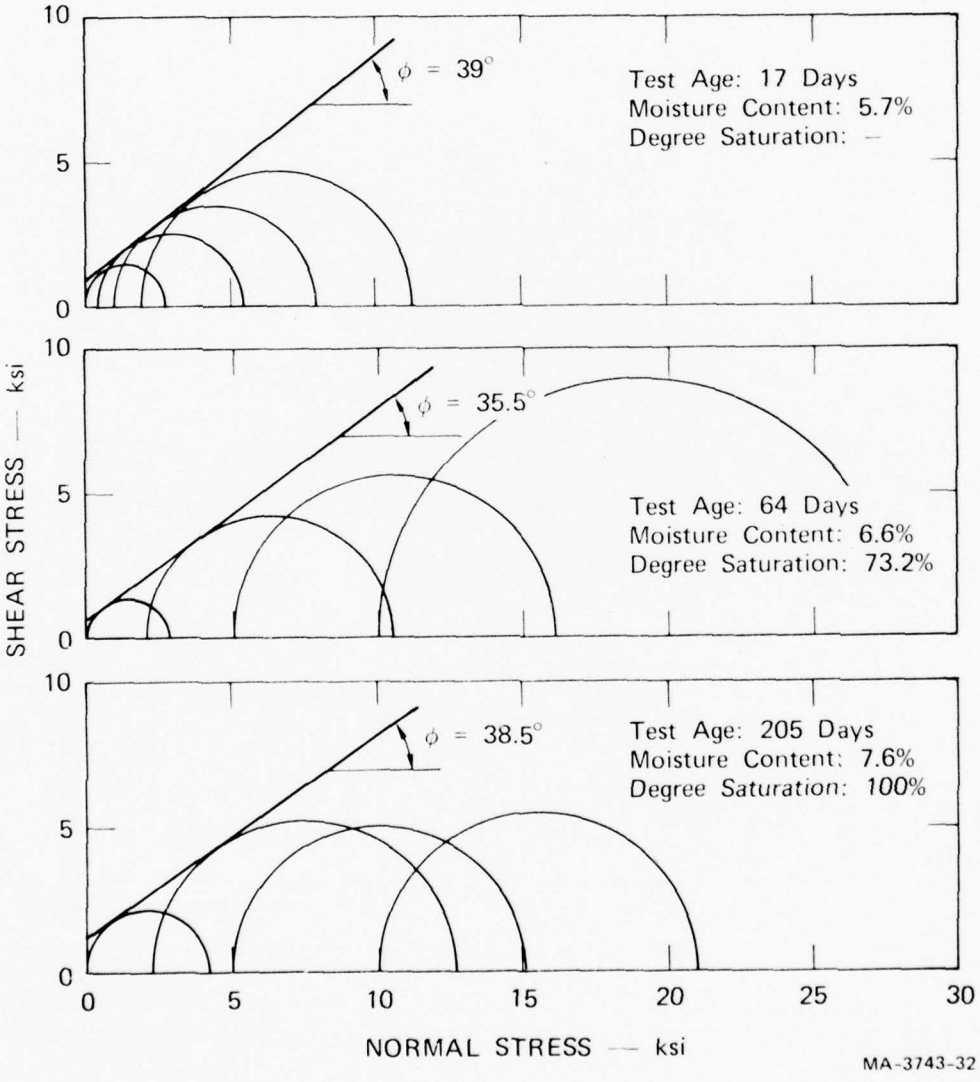

FIGURE 2-4 MOHR DIAGRAMS FOR 6B ROCK AT DIFFERENT TEST AGES (R. L. STOWE, WES)

Figure 2-5 shows a stress-strain curve for dry (~20% saturation) rock. The elastic modulus and unconfined compressive strength are slightly lower than the values for the saturated rock. This is probably due to differences in curing between the saturated rock and dry rock. Figure 2-6 shows a Mohr failure envelope for dry 6B rock. Since no porewater pressure is present, the friction angle is high, ϕ = 36 degrees, for normal stresses up to 2 kbar.

The model rock properties for the laboratory tests have been selected to be representative of either medium strength rock in the intact condition or high strength rock in the jointed condition. The relationships between the model rock properties and in situ rock properties are conveniently displayed in a modulus/strength plot as used by Deere in Chapter 1 of Ref. [8], Figure 2-7. In this plot, intact rocks are characterized by two basic quantities obtained from unconfined compression tests: Young's modulus E and unconfined compressive strength σ_u. Rocks are then classified into five strength categories as shown at the top of the graph, from A [very high strength, σ_u > 32 ksi (220 MPa)] to E [very low strength, σ_u < 4 ksi (27.6 MPa)]. They are also classified into three modulus categories, conveniently specified by a modulus ratio $M = E/\sigma_u$. Constant values of modulus ratio lie on diagonals, as shown by the lines M = 200 and 500. These values separate the three modulus categories of high (M > 500), medium (200 < M < 500), and low (M < 200).

Categories into which common rocks fall are shown on the plot. These include granite, flow (basalt, andesite, dacite, rhyolite) and sedimentary (limestone and dolomite; sandstone) rocks. The granites all fall into the single category of hard rock with medium modulus ratio. Limestone and dolomite range from medium to high strength with medium to high modulus ratio. The flow rocks range widely in strength, from low to very high, but all have medium modulus ratio. Sandstone ranges

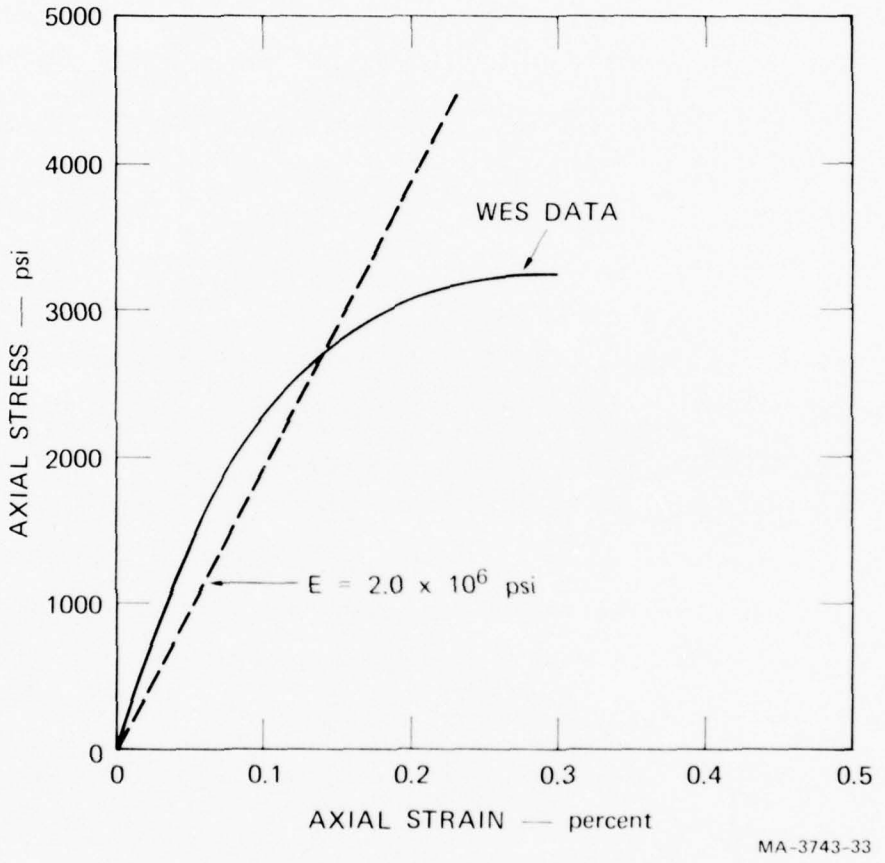

FIGURE 2-5 STRESS-STRAIN CURVES FOR DRY 6B ROCK SIMULANT

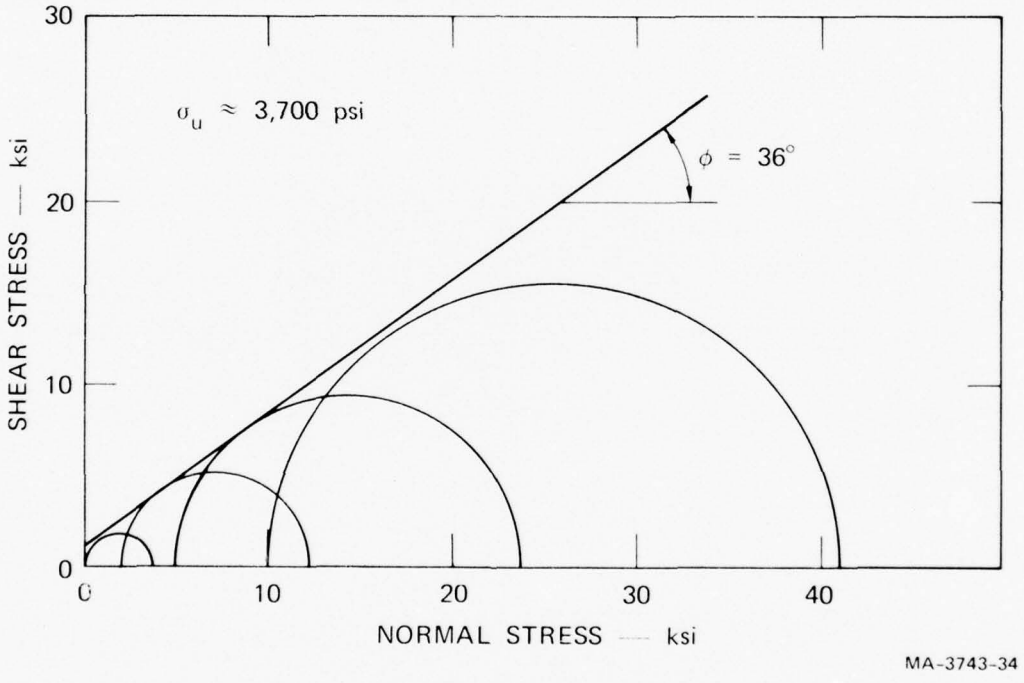

FIGURE 2-6 MOHR DIAGRAM FOR DRY 6B ROCK

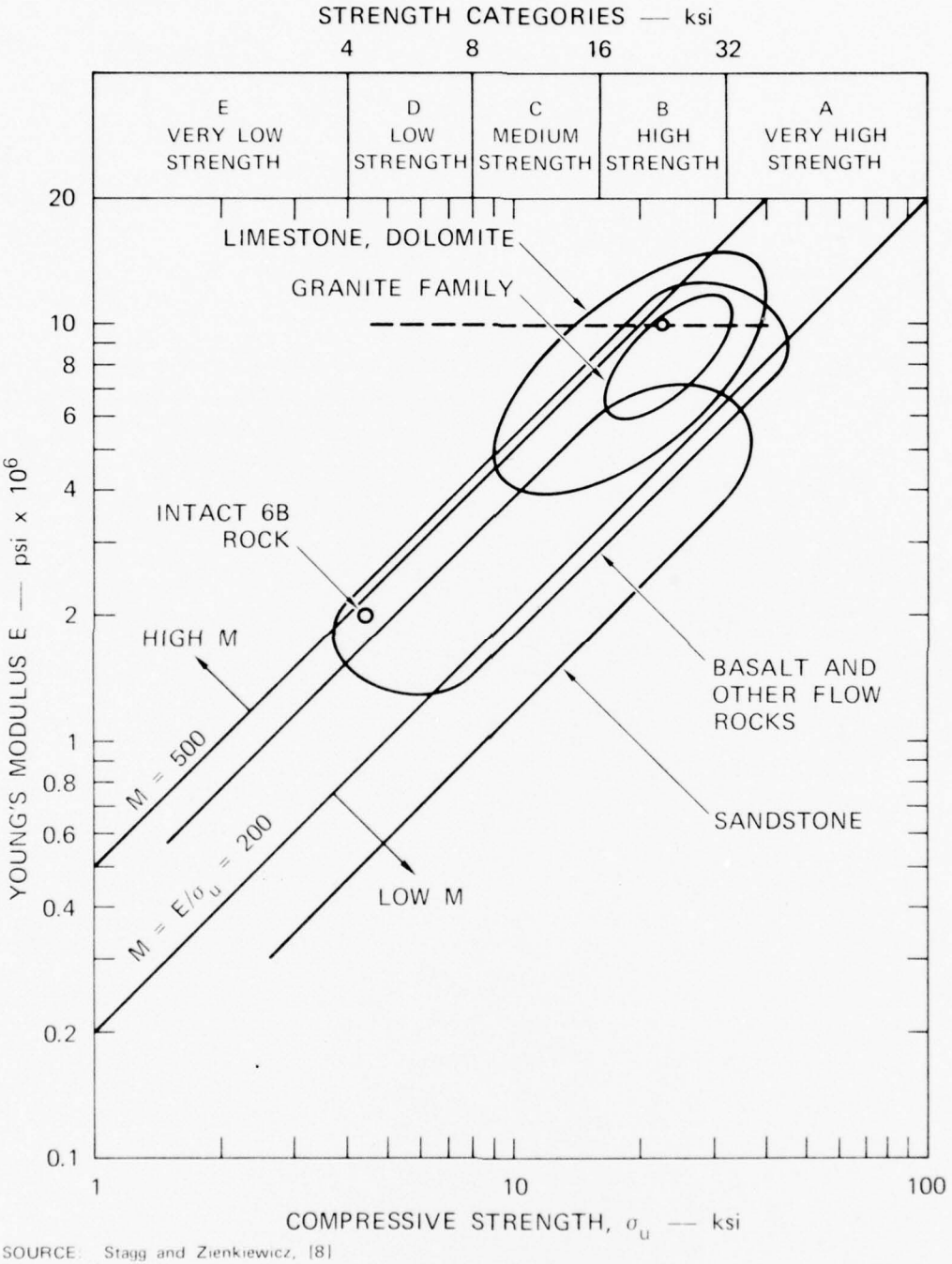

SOURCE: Stagg and Zienkiewicz, [8]

MA-3743-67

FIGURE 2-7 ENGINEERING CLASSIFICATION FOR INTACT ROCKS

most widely of all, from virtually no strength to high strength, with medium or low modulus ratio.

The intact 6B model rock properties are indicated in Figure 2-7 by the point at E = 2 x 10^6 psi (13.8 GPa) and σ_u = 4300 psi (29.6 MPA). This point lies near the low strength extreme of the intact flow rock properties. Interpreted as a model of in-situ jointed rock, however, it models rocks near the high strength extremes. This follows from field observations that the effective modulus of jointed rock is about 1/5 that of intact rock. Thus the jointed rock that the 6B rock models lies some place along the horizontal dotted line drawn at a factor of 5 increase in modulus above the 6B rock point. We know that the strength of the jointed rock will also be less than that of the intact rock, but no quantitative data are available. If we assume that the strength ratio of jointed and intact rock is also about 1/5, then the jointed rock that the intact 6B rock models is represented by the point plotted at the intersection of the dotted line and a 45 degree (0.785 rad) line through the intact properties point. This intersection point [σ_u = 21,500 psi (148 MPa). E = 10 x 10^6 psi (68.9 GPa)] falls in the high strength region where properties of all the rock types overlap. Hence it is representative of properties likely to be found at a wide range of potential sites.

The relationship between the moduli of intact rock and in situ jointed rock was determined from in situ plate jack (about 1-m dia.) and pressure chamber (about 1.7-m dia.) deformation tests [8]. These tests give an effective modulus for rock masses measuring several tens of feet in size. This modulus is related to the intact rock modulus by taking NX core samples from drill holes to a depth of 20 ft (6.1 m) and performing unconfined compression tests on intact specimens. The corings were also used to measure joint spacing, expressed in terms of

"rock quality designation" (RQD).* Data taken from many tests at many sites throughout the world are summarized in Figure 2-8 in a plot of E_r/E_{lab} versus RQD. The important observation is that the median E_r/E_{lab} from all the data is about 1/5. Two -thirds of the data points fall in the range $1/10 < E_r/E_{lab} < 1/3$. Rock quality is in the range $0.4 < RQD < 0.9$ for virtually all of the data. (The Onodera Dam and the heavily jointed quartsite from the Kariba Dam are the only exceptions.) Corresponding average joint spacings range from about 3.5 inches (8.9 cm) to 20 inches (50.8 cm).

2.6 Effect of the Relationship Between Rock and Liner Properties

Our liners in rock simulant are models of tunnels in a rock mass. When the rock is loaded, either the liner or the rock will flow plastically first, depending on the relationship between rock and liner properties. Since the final response of the structure depends on the history of the loading, it is important that the sequence of failures in our models be as close as possible to that in the prototype. Results of an analysis (based on results in [11]) to examine the incipient yield sequence are summarized in Figure 2-9 as a plot of rock-modulus-to-liner-modulus ratio E_R/E_L versus rock-strength-to-liner-strength ratio σ_{uR}/σ_{yL} for liners with various radius-to-thickness ratios. Each curve represents points at which plastic flow occurs in the rock and in the liner simultaneously (an internal friction angle of 30 degrees was assumed for the rock). For points below the curve, the liner always yields first) for points above the curve, the rock yields first.

---

*RQD = $\sum$ length of core pieces 4 inches (10.2 cm) or longer/total length of core run. Average joint spacing S correlates with RQD approximately as S = 2 inches/(1 - RQD).

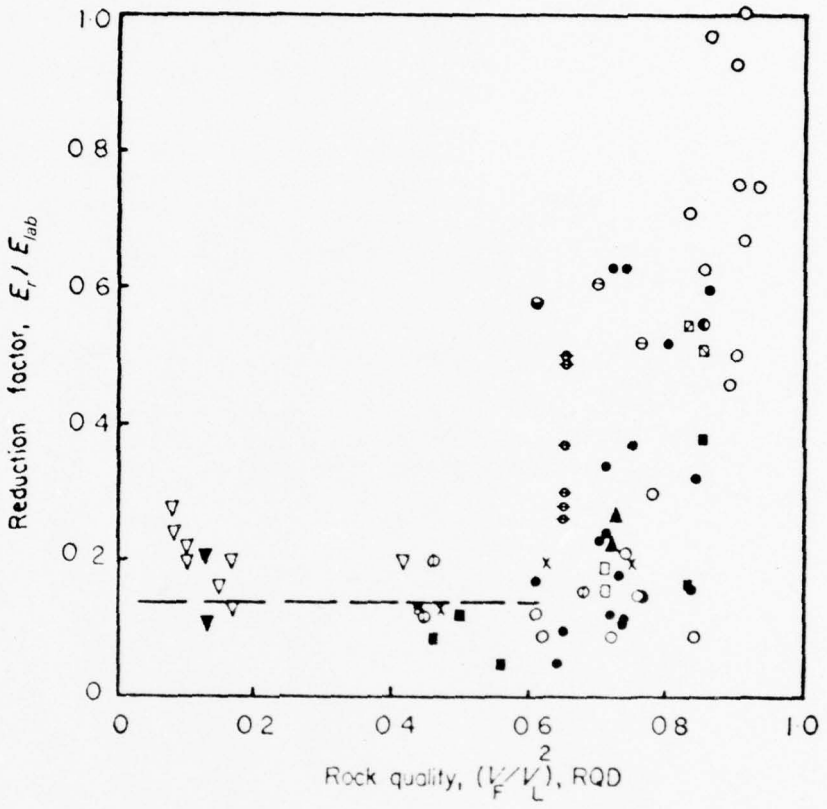

- Dworshak Dam, pressure chamber test (F), buried gauges[17]
- Dworshak Dam, pressure chamber test (F), surface gauges[17]
- Dworshak Dam, pressure chamber test (E), buried gauges[17]
- Dworshak Dam, pressure chamber test (E), surface gauges[17]
- Dworshak Dam, jacking tests, surface gauges[17]
- Dworshak Dam, jacking tests, buried gauges[17]
- Latiyan Dam, Iran[19]
- Kariba Dam, slightly weathered gneiss[19]
- Kariba Dam, heavily jointed quartzite[19]
- Nevada test site, dacite porphyry[20]
- Morrow Point Dam[21,22]
- Ananaigawa Dam[23]
- Agri River, Italy[24]
- Koshibu Dam, jacking tests
- Koshibu Dam, pressure chamber tests
- El Noville, Mexico[25]
- Onodera[26]
- Vajont Dam, Italy, upper slope, pressure chamber test[27,28]

SOURCE: Stagg and Zienkiewicz [8]

MA-3743-68

FIGURE 2-8 VARIATION OF REDUCTION FACTOR WITH ROCK QUALITY

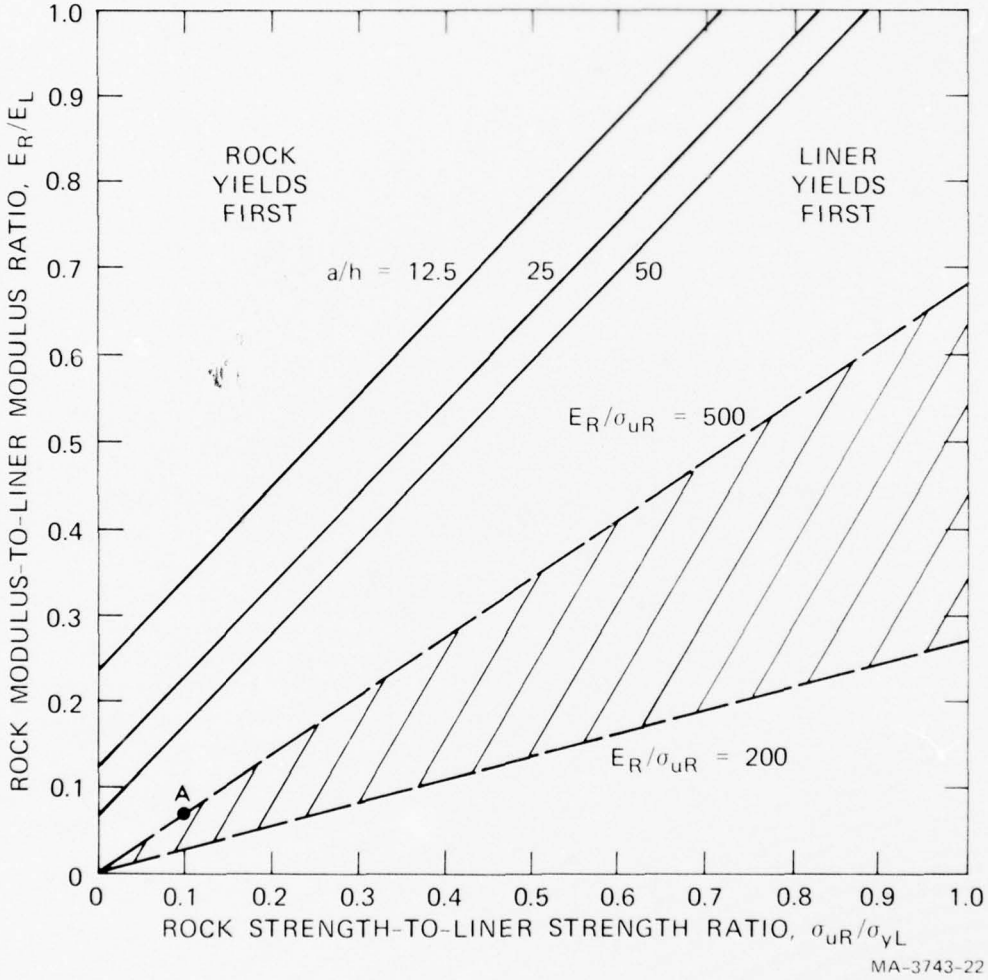

FIGURE 2-9 THE EFFECT OF THE RELATIONSHIP BETWEEN ROCK PROPERTIES AND LINER PROPERTIES ON THE SEQUENCE OF FAILURE FOR ISOTROPIC LOADING

Also shown on the graph is a region occupied by real rocks with mild steel liners. The region is bounded by two values of the ratios of rock-modulus-to-rock-strength E_R/σ_{uR}. This ratio for most rocks falls between $E_R/\sigma_{uR} = 200$ and $E_R/\sigma_{uR} = 500$ (see Figure 2-7). Points closest to the origin are representative of weak or highly jointed rock, and points far from the origin are representative of strong rock relatively free from joints. For our 6B rock simulant, with mild steel liners, we have $E_R/E_L \approx 0.066$ and $\sigma_{uR}/\sigma_{yL} \simeq 0.1$. On the graph this is represented by point A, which falls on the upper boundary for real rock that is either weak or highly jointed. The important observation is that both for our rock simulant and for real rock, the liner always yields first under axisymmetric loading.

Results of similar calculations for uniaxial-strain loading are shown in Figure 2-10. These curves are more complicated than for the axisymmetric loading case. On the straight, upper-right portion of the curves, yielding takes place in both the liner and the rock at the springlines ($\theta = \pm 90^o$ from the uniaxial strain direction). On the curving, lower-left portion of the curves, the liner yields at the springline, but the rock yields at a point between the springline and the crown or the invert. For our 6B rock simulant and most real rocks, the liner yields first for $a/h = 25$ and 50, but for our 6B rock simulant and weak rock, the rock yields first for $a/h = 12.5$. We must be aware of this in interpreting our uniaxial-strain experiments.

2.7 Description of Test Specimen

Test specimens were designed according to the requirements described in the preceding sections. A photograph of one of the unlined tunnel models is shown in Figure 2-11. The specimen is cylindrical with a diameter of 4 inches (10.2 cm) and a height of 3 to 6 inches (7.6 to 15.2 cm). These specimens were cored from the center portion of a

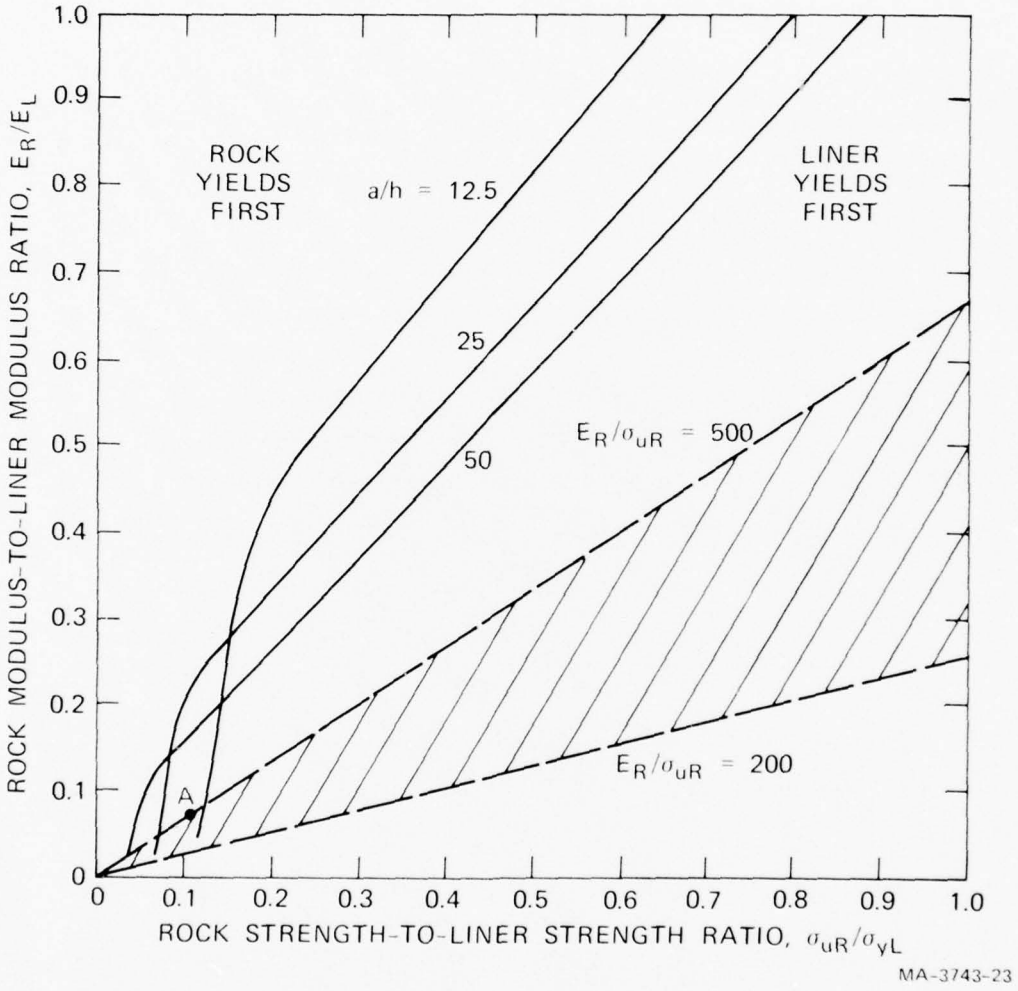

FIGURE 2-10 THE EFFECT OF THE RELATIONSHIP BETWEEN ROCK PROPERTIES AND LINER PROPERTIES ON THE SEQUENCE OF FAILURE FOR UNIAXIAL STRAIN LOADING

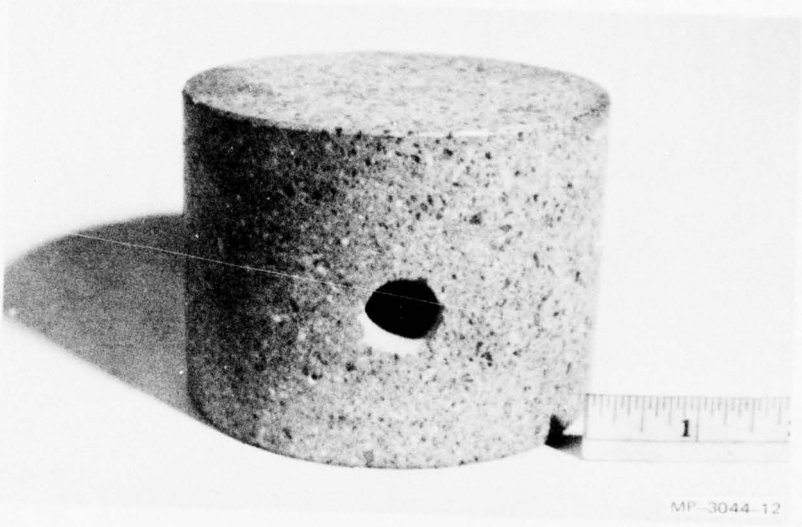

FIGURE 2-11 SIMULATED ROCK SPECIMEN

large block of grout. A 5/8-inch (1.59 cm)-diameter cavity runs through the specimen at midheight perpendicular to the specimen's cylindrical axis. The cavity simulates the unlined tunnel. In the experiments, the outer boundaries of the specimen were loaded to reproduce in our model the stresses that would exist around a buried structure undergoing the effects of a nuclear ground shock in the field. Generally, for a given vertical load, the lateral load is chosen to restrain any lateral movement of the boundaries. This is the restraint that would be provided by the surrounding rock in the field under uniaxial-strain flow. In addition, several experiments were run under isotropic loading conditions to study the effect of asymmetry in the load.

3. TESTING MACHINES

In this chapter, we describe the static and dynamic testing machines used to load our rock specimens. These machines were designed and built on a previous DNA contract [1]. During the course of the current work, several substantial modifications were made to the machines to improve their performance and extend their capabilities. A detailed description of these modifications is given in Appendix C. The current status of the machines is described below.

3.1 Dynamic Testing Machine

The basic operating technique of the dynamic testing machine is the controlled release of explosive gases from a vented chamber charged with low-density explosive. This technique was originally developed at SRI in 1971 to simulate the sudden release of energy in a nuclear reactor in a sudden-loss-of-coolant accident. In 1972, the technique was successfully applied to simulate the intense underground pressures that stem horizontal line-of-sight (HLOS) pipes in nuclear tests. The original HLOS machine was capable of applying only axisymmetric pressure around a cylindrical specimen.

In 1974, a new loading machine was designed and built during the initial buried structure program [1]. This machine has the capability of applying uniaxial strain and triaxial loadings such as occur on horizontal deep buried tunnels under nuclear attack. During the current program, modifications were made to improve its performance and give it the capability of applying isotropic loadings (symmetric around the tunnel).

3.1.1. Triaxial Loading Configuration

A photograph and an assembly drawing of the dynamic tester in the triaxial loading configuration are shown in Figure 3-1. The machine consists of a stack of thick rings with fluid passageways machined into them. The rings are held together with end plates and 12 bolts around the circumference. The rock specimen is 4 inches (10.2 cm) in diameter and can be from 3 to 6 inches (7.6 to 15.2 cm) long. It rests in the center of the machine, as shown. The tunnel is bored completely through the cylindrical rock specimen along a diameter at midheight. Viewing ports are provided in the machine at each end of the tunnel to allow high-speed photography and access for instrumentation wires (one port is shown on the left of the drawing).

Independent control of vertical and lateral pressures is provided because loading is applied by two separate explosive chambers. The upper explosive chamber applies the vertical pressure and is simply a cylindrical cavity into which an explosive charge (a mixture of PETN and microballoons) and detonator are placed. The high-pressure explosive products are vented into the expansion chamber through the series of holes shown drilled through the thick orifice plate between the explosive chamber and the expansion chamber. The expansion chamber has a baffle plate to help mix the gas and prevent sudden localized concentrations of pressure due to the jetting of the gas through the orifice plate. The load is applied directly to the specimen by the gas. The area of the holes in the orifice plate determines the rise time of the loading pulse. Fine adjustment of the rise time is provided by changing the expansion chamber volume by inserting an inert solid (Duxseal). Release venting (and therefore pulse decay time) from the explosive chamber is accomplished through holes in the vent ring between the explosive chamber ring and the end plate.

A similar arrangement at the bottom of the testing machine is used to load the sides of the specimen. However, in this case the load is transmitted by a fluid-filled lateral pressure chamber. A Bellofram is located just above the baffle plate to act as an interface between the gas and the fluid. The lower expansion chamber applies the lateral pressure through ports (on the fluid side of the Bellofram) seen connecting the lower expansion chamber to the lateral pressure chamber. The top and bottom vertical pressures are sealed from the lateral pressure chamber by thin copper cups and O-rings above and below the specimen. The cups are inverted so that the high pressure acts inside the cups and presses them against the O-rings to seal the chamber. O-rings seal the pressure chambers from the external ambient pressure, as shown. A Wilson seal separates the lateral pressure chamber and the rock and cavity (see Appendix C).

Piezoelectric gages installed in any of seven tapped ports in the machine monitor pressures in the various chambers and passageways. A pressure pulse from the vertical loading chamber above the specimen is shown in Figure 3-2(a). Figure 3-2(b) shows a pressure pulse from the lateral loading chamber, around the specimen circumference. Rise time in each is about 1 ms, and total pulse duration is about 10 ms. The machine is capable of applying pressure as high as 1.5 kbar (150 MPa). It is also capable of applying a static preload to simulate a lithostatic stress in the specimen. A more detailed description of this testing machine, its operation, and the modifications made to it during the project are given in Appendix C.

3.1.2. Isotropic Loading Configuration

Figure 3-3 shows a photograph and assembly drawing of the dynamic tester in the isotropic loading configuration. Operation of

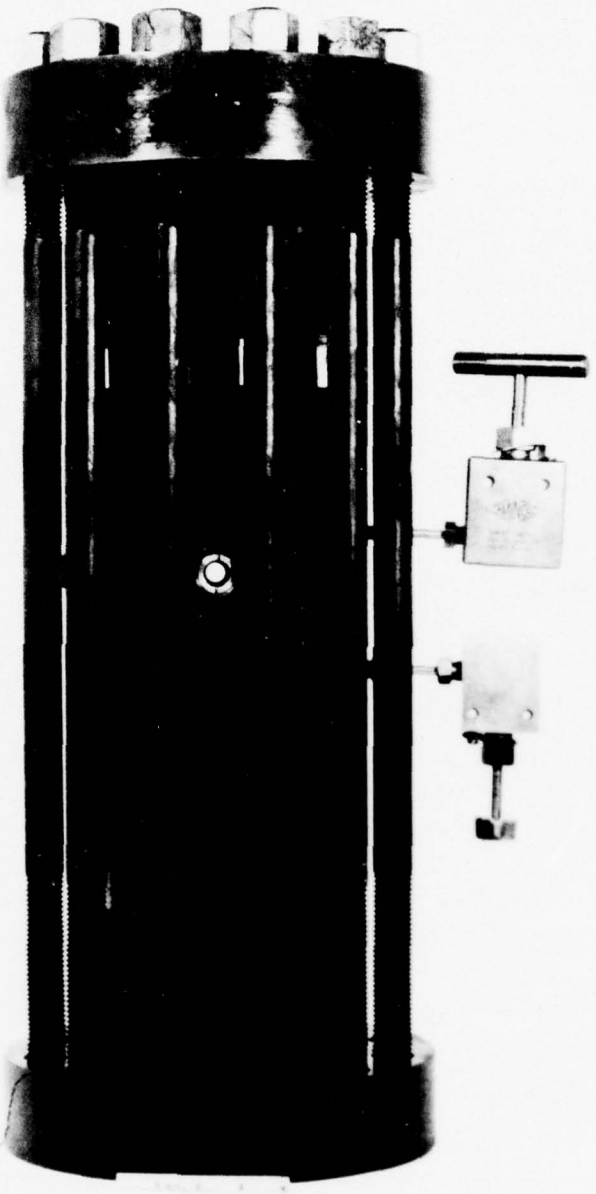

(a)

MP-3743-75A

FIGURE 3-1 DYNAMIC TESTING MACHINE — TRIAXIAL LOADING CONFIGURATION

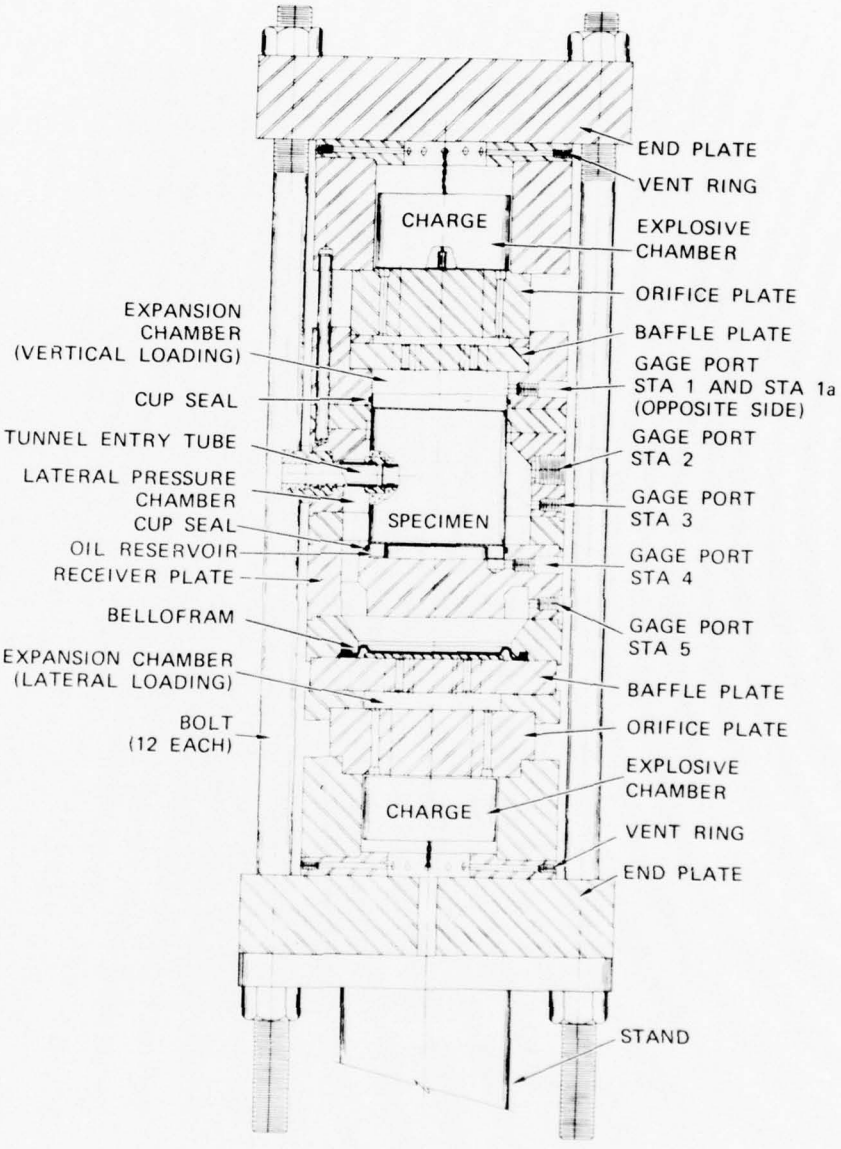

(b)

MA-3743-80

FIGURE 3-1 DYNAMIC TESTING MACHINE — TRIAXIAL LOADING CONFIGURATION

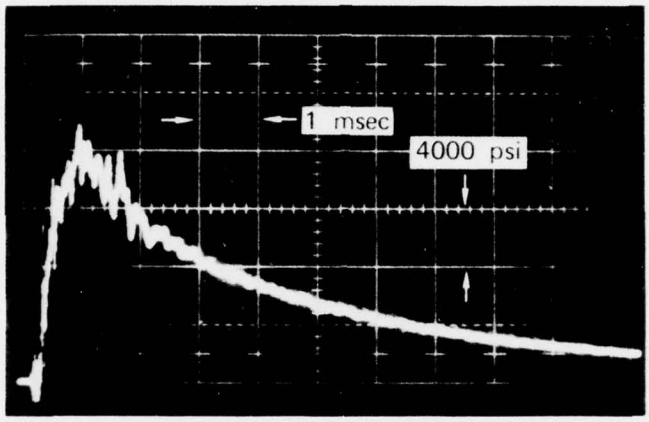

(a) VERTICAL PRESSURE PULSE—STA 4 (AT BOTTOM OF ROCK)

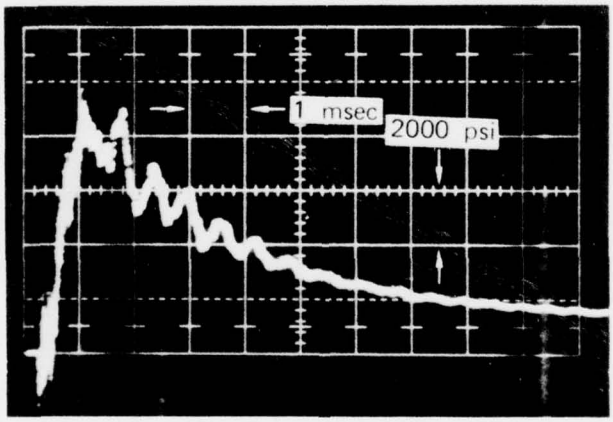

(b) HORIZONTAL PRESSURE PULSE—STA 3 (NEAR MIDHEIGHT OF ROCK)

MP-3743-76

FIGURE 3-2 TIME HISTORIES OF APPLIED LOADS—TRIAXIAL LOADING

the machine in this configuration is essentially the same as in the triaxial configuration. The main difference is that it has only one explosive chamber and one expansion chamber. The specimen is completely surrounded by fluid which transmits the load from the gas pressure in the expansion chamber to the specimen. Again, a Bellofram acts as an interface between the gas and the fluid.

Pressures are monitored at various points in the fluid by piezoelectric gages as shown. Typical pressures at Stations 1 and 3 are shown in Figure 3-4. We see that the pressure-time histories at both locations are almost identical, indicating that undesirable wave propagation effects are minimal.

3.2. Static Testing Machine

The static testing machine provides static triaxial loading of our specimens while maintaining the tunnels at atmospheric pressure and providing photographic and instrumentation access. The loads are applied hydraulically by high-pressure hand pumps. Figure 3-5 is a photograph and assembly drawing of the machine. Like the dynamic tester, this machine consists of a stack of thick rings held together with end plates and bolts around the circumference (ten in the static unit). The rock specimen, 4 inches (10.2 cm) in diameter and from 3 to 6 inches (9.6 to 15.2 cm) long, rests in the center of the machine, as shown. Viewing ports are provided in the machine (one port is shown at the top of the drawing) at the end of the tunnel to allow photographic coverage of the deformation process and access for a hole gage to measure tunnel diameter changes.

To provide independent control of vertical and lateral pressures for triaxial loading tests, the loading is applied by two hand pumps. The upper and lower chambers are pressurized by one pump, and the side

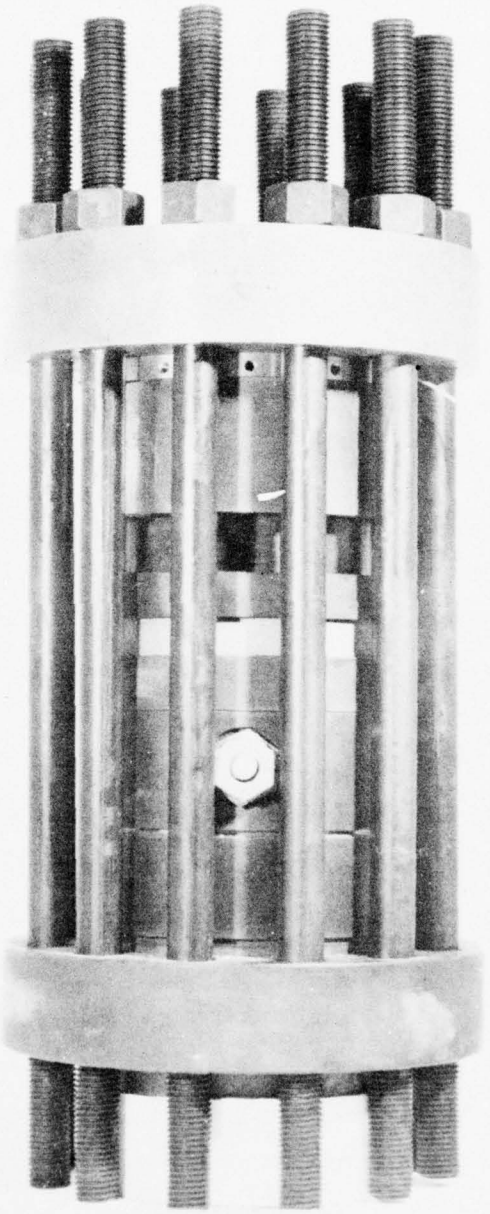

(a) PHOTOGRAPH (TUNNEL IN-LINE WITH OBSERVER)

MP-3743-77A

FIGURE 3-3 DYNAMIC TESTING MACHINE — ISOTROPIC LOADING CONFIGURATION

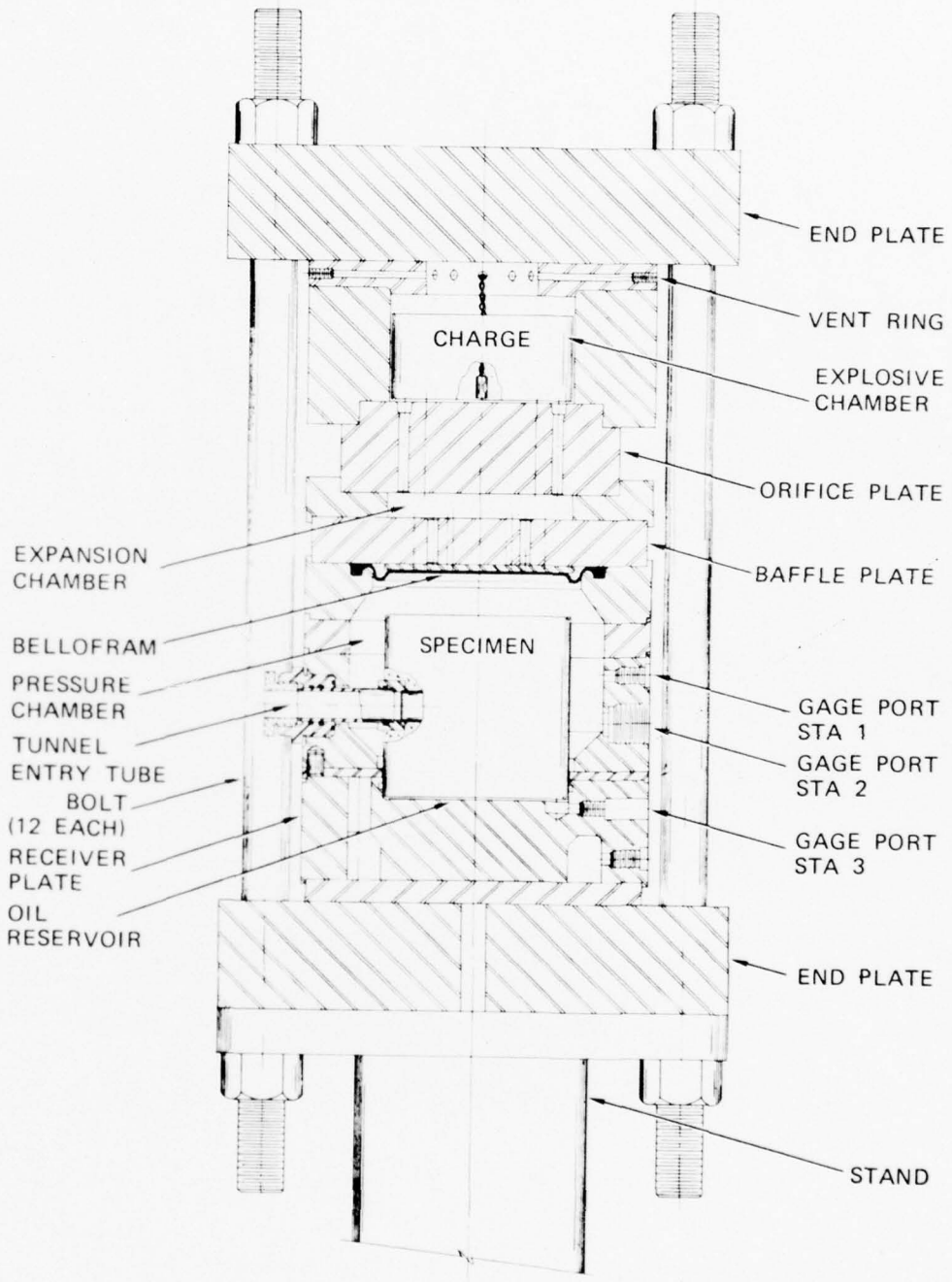

(b) SECTION DRAWING (TUNNEL PERPENDICULAR TO OBSERVER)

MA-3743-89

FIGURE 3-3 DYNAMIC TESTING MACHINE — ISOTROPIC LOADING CONFIGURATION (Concluded)

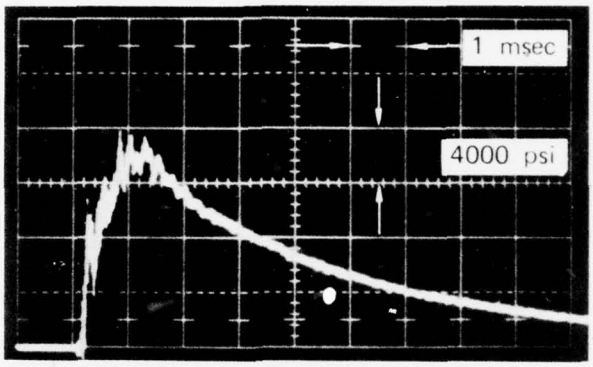

(a) STATION 1 (MIDHEIGHT OF ROCK)

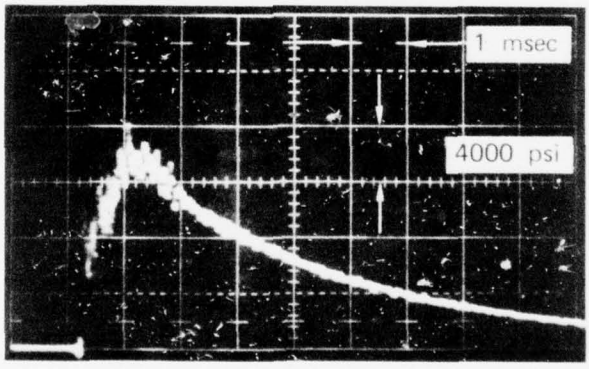

(b) STATION 3 (BOTTOM OF ROCK)

MP-3743-78

FIGURE 3-4 TIME HISTORIES OF APPLIED LOADS— ISOTROPIC LOADING

chamber is pressurized by another. Sealing between the side chamber and the upper and lower chambers is accomplished by the cup and O-ring system used in the dynamic tester. O-ring grooves are machined into the chamber walls at various heights to accommodate different length samples.

For isotropic loading, the cups and O-rings are not used, so that oil is free to flow from chamber to chamber. Only one pump is required. The machine is capable of applying pressure as high as 2 kbar. Further details are given in Appendix C.

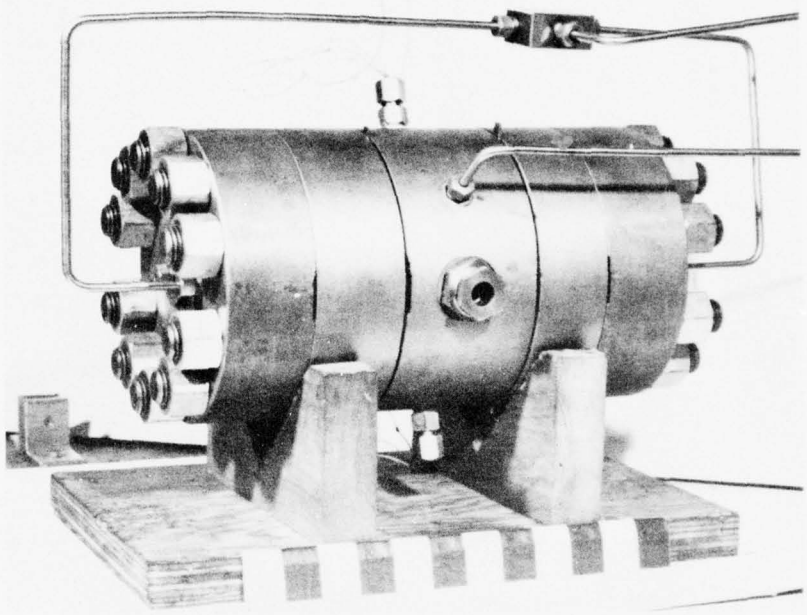

(a)

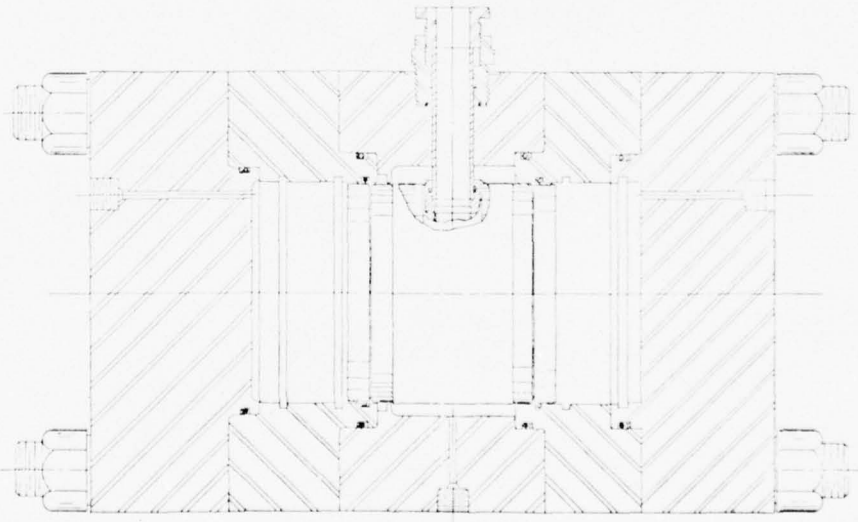

(b)

MP-3743-79

FIGURE 3-5 STATIC TESTING MACHINE — TRIAXIAL LOADING CONFIGURATION

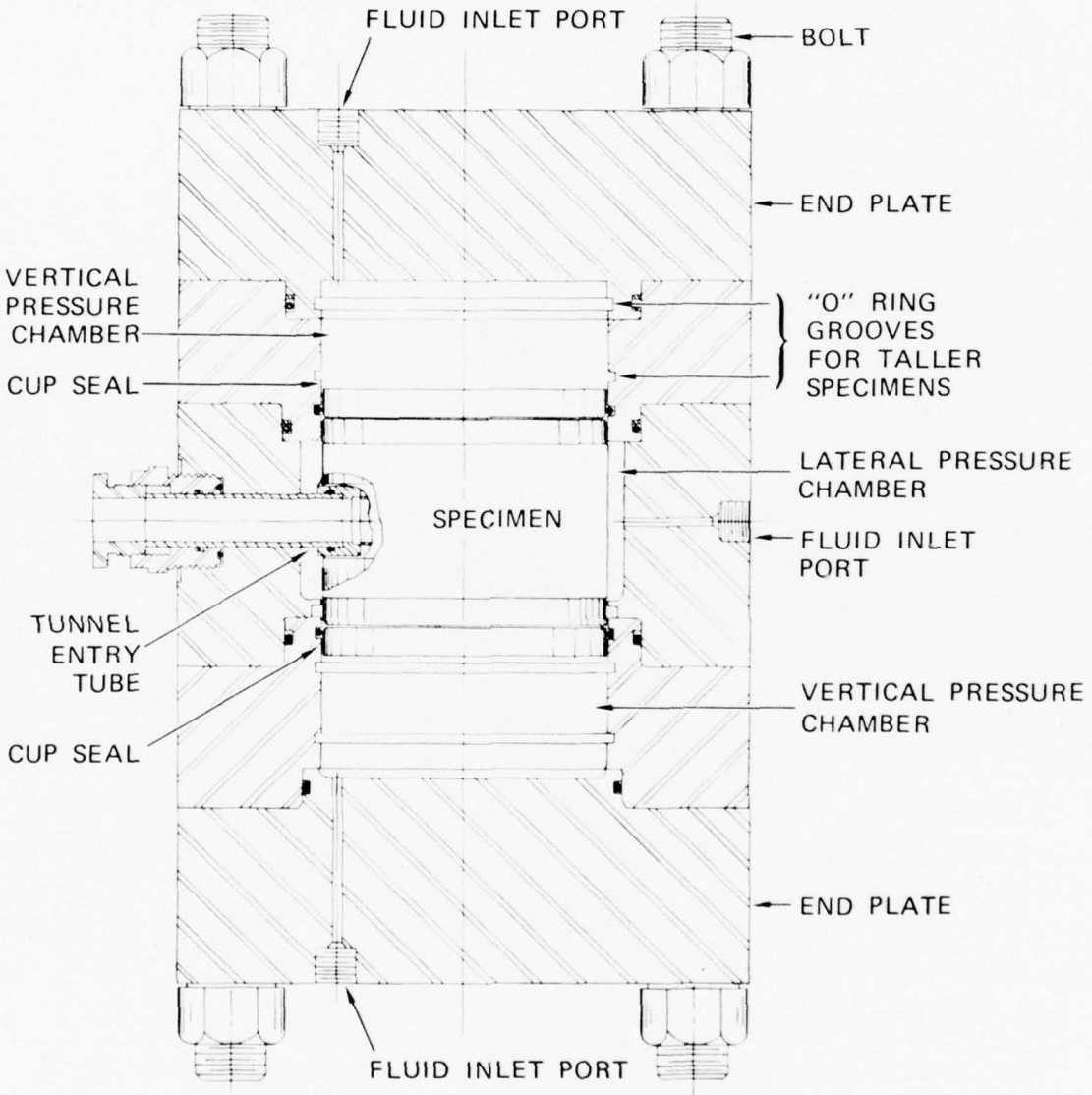

(c)

MA-3743-92

FIGURE 3-5 STATIC TESTING MACHINE — TRIAXIAL LOADING CONFIGURATION
(Concluded)

4. VALIDATION OF EXPERIMENTAL PROCEDURES

In this chapter, we present the results of tests to resolve questions concerning the validity of our experimental procedures. Subjects addressed are: the effect of the specimen boundaries on the response of the tunnel, the reproducibility of experimental results, the effect of water saturation in static and dynamic tests, and the effect of the absence of a liner on cavity response under isotropic loading.

4.1 Reproducibility and Boundary Effects

To demonstrate the validity of our experiments, we had to resolve questions of reproducibility and boundary effects. To demonstrate reproducibility, we repeated each of two experiments and compared the responses. We investigated the boundary effect (i.e., the effect of the ratio of tunnel diameter to specimen diameter) by performing experiments on tunnels with various diameters while keeping the sample size constant and then comparing the results.

For this series of tests, we used HARM grout* as our rock simulant. This material was used instead of our 6B rock simulant because of its small grain size. Small grain size was required for testing tunnels with diameters as small as 5/16 inch (0.79 cm), where large grains might have an effect on the response. HARM grout has an unconfined compressive strength of about σ_u = 1000 psi (6.89 MPa) and low internal friction. Each test was performed on a sample with a tunnel having a steel liner [yield strength σ_y = 40,000 psi (276 MPa)] with a radius-to-thickness

*HARM is an acronym for Husky Ace rock-matching grout. This is the material used to fill the DAC crosscuts in the Dining Car event.

ratio of 12.5. Tests were performed on tunnels with diameters of 5/8, 7/16, and 5/16 inch (1.59, 1.11 and 0.79 cm) in our standard 4-inch (10.2 cm)-diameter by 3-inch (7.6 cm)-long cylindrical specimens. All the experiments were static, uniaxial-strain tests. Vertical closure as a function of pressure was monitored with a small hole gage during each test.

Figure 4-1 shows sectioned views of specimens with the three different diameters.* The terminal response levels of the 5/8-inch (1.59 cm) tunnel and the 7/16-inch (1.11 cm) tunnel are almost identical. The 5/16-inch (0.79 cm) tunnel has less closure because it was subjected to a smaller final load. Each of the 5/8-inch (1.59 cm) and 7/16-inch (1.11 cm) tunnel experiments was repeated. Plots of vertical tunnel closure versus vertical pressure for all five tests are shown in Figure 4-2. We see that the amount of load required to cause a given amount of closure varies by less than 15 percent either between tests for tunnels with different diameters or between repeat tests at the same diameter. This indicates that our 5/8-inch (1.59 cm) tunnels are not significantly affected by the closeness of the boundaries for tunnel closures up to 15 percent and that our experiments are reproducible to within ± 8 percent.

4.2 Drained Versus Undrained Testing

The majority of our experiments were performed on the 6B rock in the fully saturated condition. We had to resolve whether it was more appropriate to perform these tests in the drained (without porewater pressure) or undrained (with porewater pressure) condition. Static isotropic loading tests were performed on samples with 6-mil (0.152 mm)-liners (a/h = 50) for both these conditions.

---

* In this figure and in all posttest photographs of models from uniaxial-strain tests presented throughout the report, the models are oriented with the larger loading (P_V) in the vertical direction.

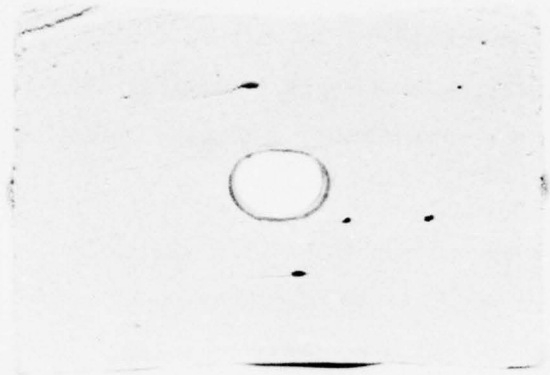

(a) D = 5/8" (SUX-45)
P_{VMAX} = 4250 psi
P_{HMAX} = 1880 psi
$\Delta D_V/D$ = 21%
$\Delta D_H/D$ = -14%

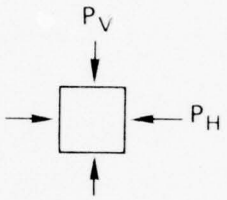

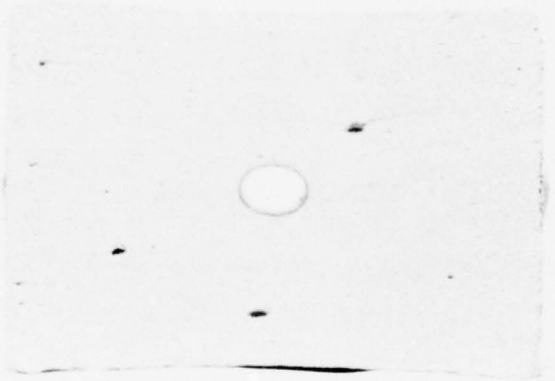

(b) D = 7/16" (SUX-46)
P_{VMAX} = 4000 psi
P_{HMAX} = 1690 psi
$\Delta D_V/D$ = 21%
$\Delta D_H/D$ = -12%

(c) D = 5/16" (SUX-42)
P_{VMAX} = 3500 psi
P_{HMAX} = 1420 psi
$\Delta D_V/D$ = 16%
$\Delta D_H/D$ = -12%

MP-3743-8A

FIGURE 4-1 THE RESPONSE OF TUNNELS WITH VARIOUS DIAMETERS TO STATIC UNIAXIAL STRAIN LOADING

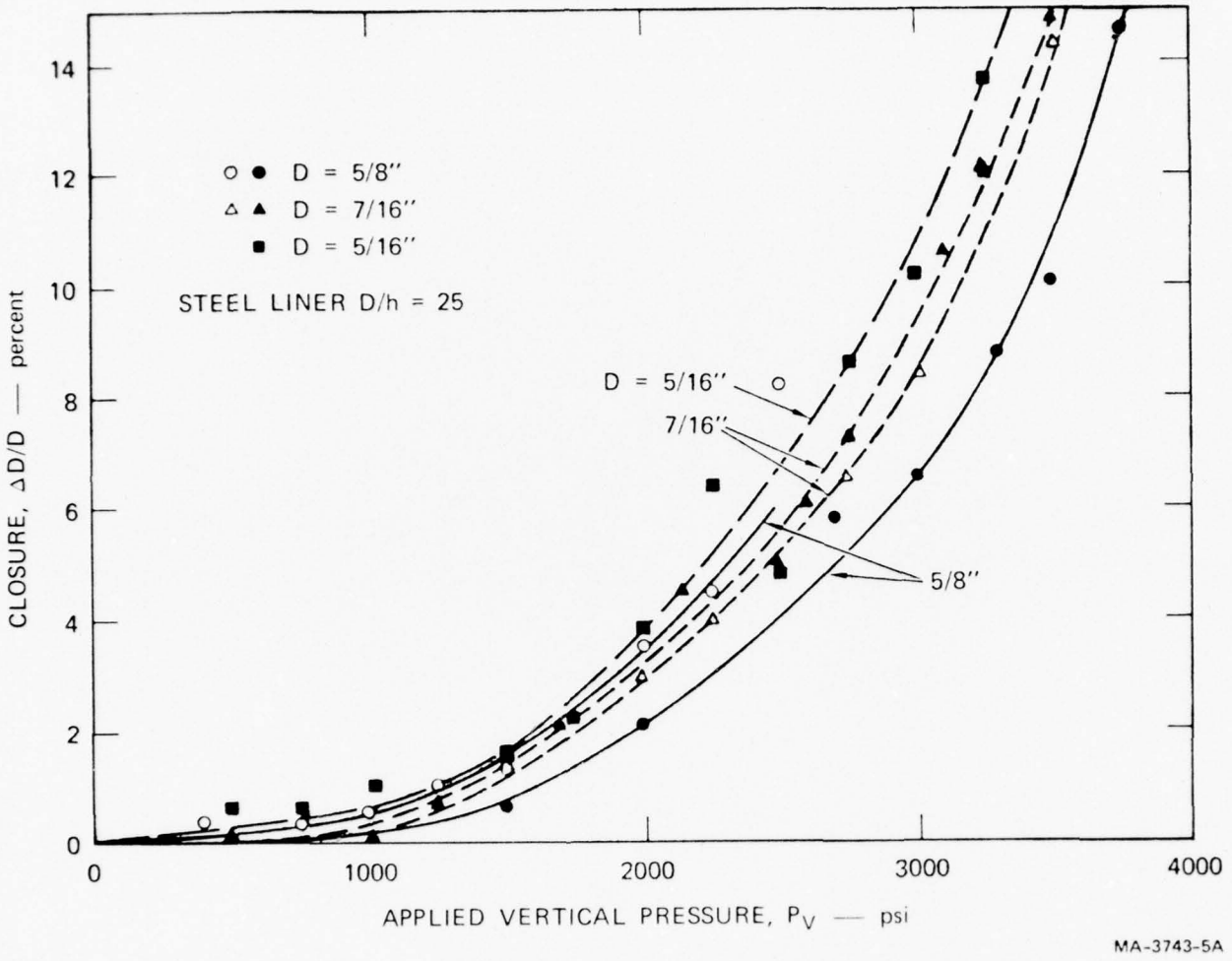

FIGURE 4-2 CLOSURE AS A FUNCTION OF VERTICAL PRESSURE FOR VARIOUS HOLE DIAMETERS UNDER UNIAXIAL STRAIN CONDITIONS

Figure 4-3 shows the results of the drained specimen test. The peak load was P_o = 22,000 psi (152 MPa), and the final closure was $\Delta D/D$ = 15 percent. During the test, buckling was observed to initiate at about 7,000 psi (48.3 MPa). At this load, the surface of the liner appeared mottled with high-order harmonic wrinkling. The buckles grew as the load and deformation increased until they reached the severe state of buckling shown in the photograph.

In the experiment just described, water was allowed to drain from the rock so that no porewater pressure developed. Generally, in the field, water does not drain, and porewater pressure could play a significant part in the stress field around a tunnel. A theoretical analysis of the effect of pore pressure was given in Section 2.4. To determine its effect experimentally, we repeated the previous experiment but with water not allowed to drain. The loading was static and isotropic as before. Results of the test are shown in Figure 4-4. Buckles first became visible in the liner when the load reached about 5000 psi (34.5 MPa), within the range observed in the drained test (this incipient buckling is difficult to observe accurately). When the load was increased to 8000 psi (155.2 MPa), the buckles became more visible but were still very small. The load was held at 8000 psi (55.2 MPa), but one of the buckles continued to grow. To maintain the 8000 psi (55.2 MPa) load in the presence of this growth, pumping of the hydraulic fluid that loaded the rock had to be continued. The reason for the continued buckle growth is that the pressure that acts on the liner results from the combination of the deformation of the rock cavity (i.e., the pressure exerted by the rock) plus the porewater pressure. As the liner buckles, it separates from the rock but the porewater follows the buckle and, hence, the porewater pressure component of the load continues to act on the liner, causing the buckles to grow. As the load was increased, this buckle continued to grow (over a time period of about 1 minute) until it reached its final state shown in the photograph at P_o = 12,000 psi (82.7 MPa).

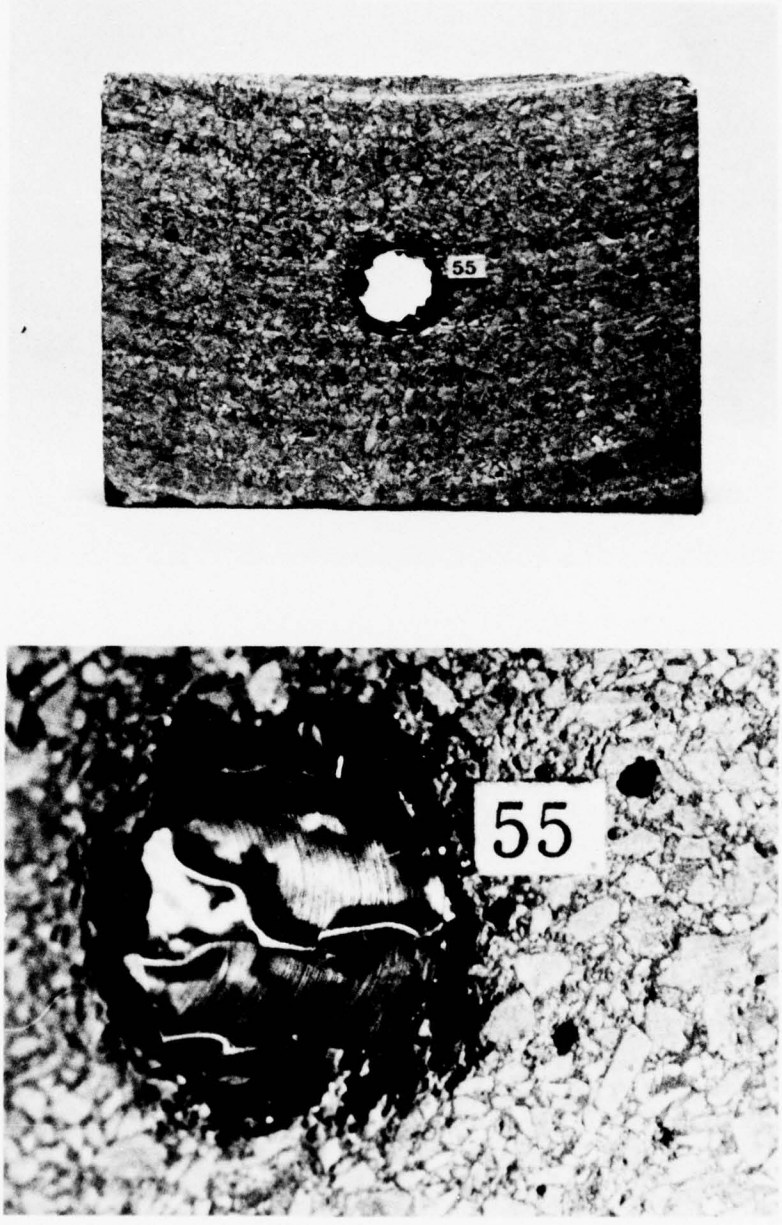

MP-3743-15

FIGURE 4-3 RESPONSE OF A STEEL-LINED TUNNEL TO A STATIC, ISOTROPIC LOAD WITHOUT PORE PRESSURE—a/h = 50, P_{omax} = 22,000 psi, $\Delta D/D$ = 0.15

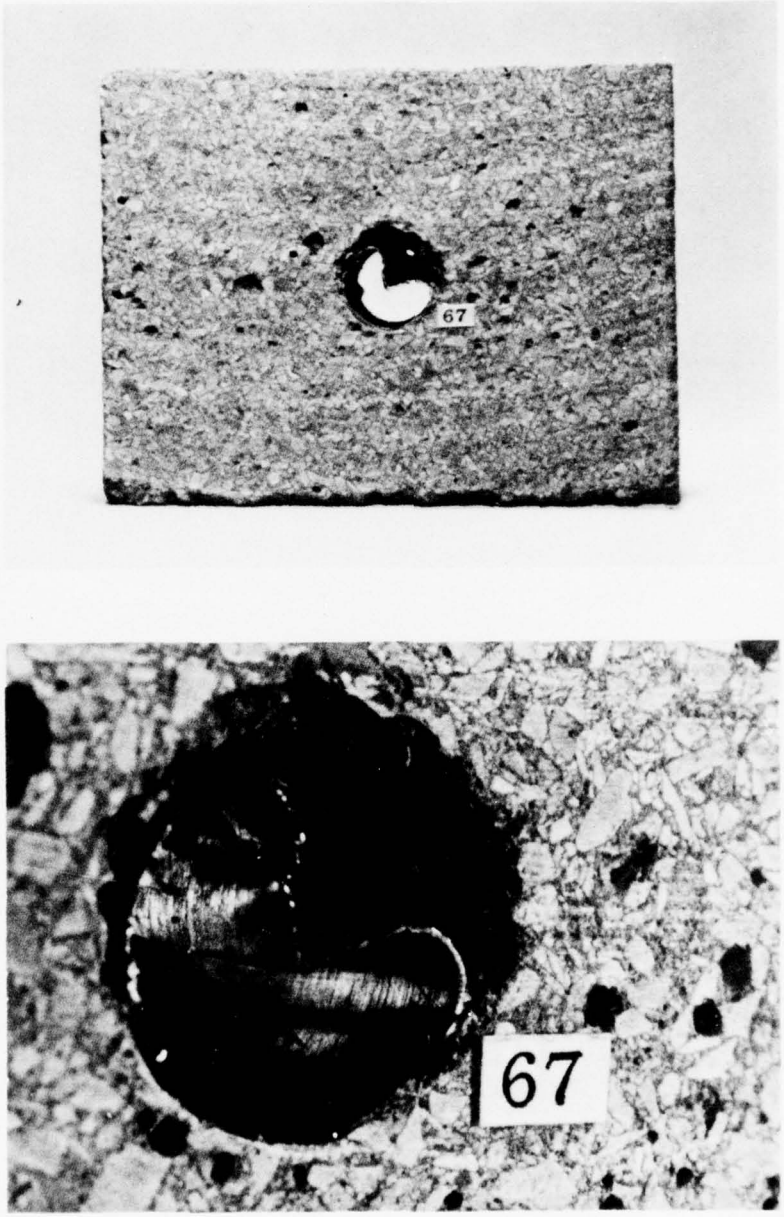

MP-3743-21

FIGURE 4-4 RESPONSE OF A STEEL-LINED TUNNEL TO A STATIC, ISOTROPIC LOAD WITH PORE PRESSURE—a/h = 50, P_{omax} = 12,000 psi

Since the growth of the buckle under constant load is a slow process governed by the rock permeability, it probably would not occur under the dynamic loading conditions that exist in the field. This indicates that tests on undrained specimens (i.e., with porewater pressure present) should be dynamic rather than static. Consequently, only drained specimens were tested in our static loader. Undrained specimens were tested in our dynamic loader.

4.3. Unlined Versus Lined Tunnel Tests

During a previous contract [1], an extensive study was made of the response of lined and unlined tunnels subjected to uniaxial-strain loading. This work was continued in the present program with the addition of isotropic loading as well as uniaxial-strain loading. Figure 4-5 shows the results of static and dynamic isotropic loading tests on unlined tunnels in saturated 6B rock. In the static test, flaking takes place in a relatively uniform way around the tunnel. Plastic flow in the rock tends to make the opening shrink under load while the flaking tends to make it increase in size. The net result is zero diameter change on the average around the hole. For the dynamically loaded specimen, the flaking is more severe at the top and bottom of the tunnel than at the sides. This asymmetric response to a symmetric load was probably caused by an instability, whereby the failure of the tunnel in one location caused the local loading to become more and more asymmetric as the failure progressed. The instability is probably caused by imperfections in the rock rather than by differences in the type of load applied (static versus dynamic). Similar behavior was observed in the previous program but the cavity ovalled in the opposite direction. In the specimen in Figure 4-5(b) the vertical diameter increased 0.8 percent while the horizontal diameter decreased 2.4 percent.

(a) STATIC LOADING (SI-31)
P_{MAX} = 15,500 psi
$\Delta D_V/D$ = 0
$\Delta D_H/D$ = 0

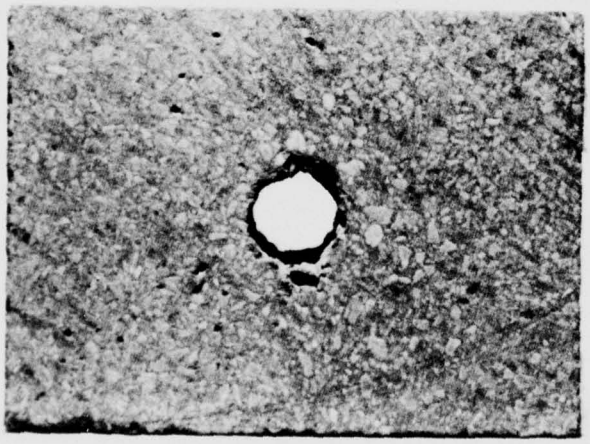

(b) DYNAMIC LOADING (DI-22)
P_{PEAK} = 13,000 psi
$\Delta D_V/D$ = -0.8%
$\Delta D_H/D$ = 2.4%

MP-3743-9

FIGURE 4-5 A COMPARISON OF UNLINED TUNNEL RESPONSE IN 6B ROCK SUBJECTED TO STATIC AND DYNAMIC ISOTROPIC LOADING

Because the flaking that takes place around the inside of the tunnel occurs in unpredictable locations and is difficult to measure, it is hard to quantify the damage that occurs in an unlined tunnel under isotropic loading. The addition of a thin liner eliminates this flaking, as demonstrated by the results of static and dynamic tests on a tunnel with a 6-mil (0.152 mm)-thick liner ($a/h = 50$, Figure 4-6). We therefore confined further investigation to the study of tunnels with either direct contact liners or backpacked liners.

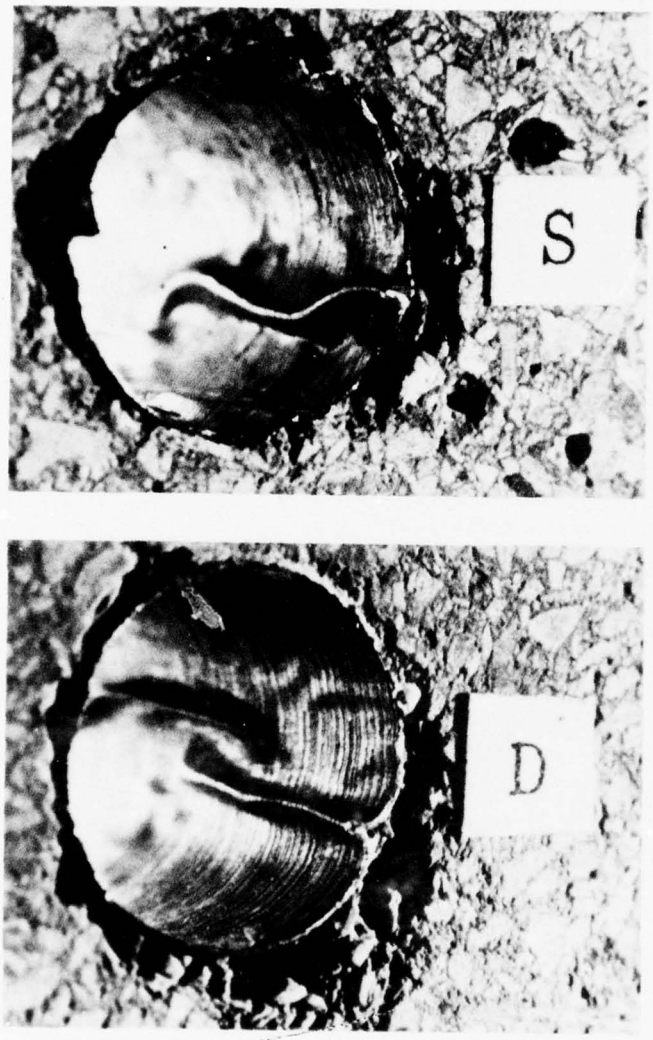

(a) STATIC LOADING (SI-35)
P_{MAX} = 20,000 psi
AVG. $\Delta D/D$ = 8%

(b) DYNAMIC LOADING (DI-28)
P_{PEAK} = 16,000 psi
AVG. $\Delta D/D$ = 5.5%

MP-3743-10A

FIGURE 4-6 A COMPARISON OF LINED (a/h = 50) TUNNEL RESPONSE IN 6B ROCK SUBJECTED TO STATIC AND DYNAMIC ISOTROPIC LOADING

5. ISOTROPIC LOADING EXPERIMENTS

In this chapter, we present the results of isotropic (axisymmetric) loading experiments in saturated 6B rock. The tests include both static and dynamic loading; the static tests are drained and the dynamic tests are undrained, as discussed in Section 4.2. The structures tested were models of the lined tunnels with and without backpacking fielded in the Dining Car experiment, all made with 4-inch-diameter rock specimens.

In addition, we present the results of a dynamic, isotropic loading test on a scale model of a structure fielded by CASES in Dining Car and the results of a static, cyclic, isotropic loading test on a lined tunnel in dry 6B rock.

5.1 Static Test Results

Six static isotropic loading experiments were performed on models of the Dining Car structures. Table 5-1 gives a list of the structures tested and the maximum loads that were applied. Figure 5-1 shows the results of a test on a tunnel with a direct contact steel liner [yield strength σ_y = 40,000 psi (276 MPa) and a/h = 50]. The final closure was $\Delta D/D$ = 15 percent. During the test, buckling was observed to initiate at about 7,000 psi (48.3 MPa). At this load, the surface of the liner appeared mottled, with high-order harmonic wrinkling. The buckles grew at the load and deformation increased until they reached the severe state of buckling shown in the photograph. The result of a repeat test with the same type liner is shown in Figure 5-2. Since the final load in this test is higher [P_o = 28,000 psi (193 MPa)], the deformation ($\Delta D/D$ = 26 percent) and buckling are more severe than in the previous case.

Table 5-1

STATIC ISOTROPIC TESTS IN SATURATED ROCK

Test Number	Structure	P_{omax} (psi)
SI-55	Steel a/h = 50	22,000
SI-63	Steel a/h = 50	28,000
SI-64	Steel a/h = 25	29,000
SI-74	Steel a/h = 12.5	25,000
SI-61	Steel a/h = 25 with backpacking	23,000
SI-58	Steel a/h = 12.5 with backpacking	24,000

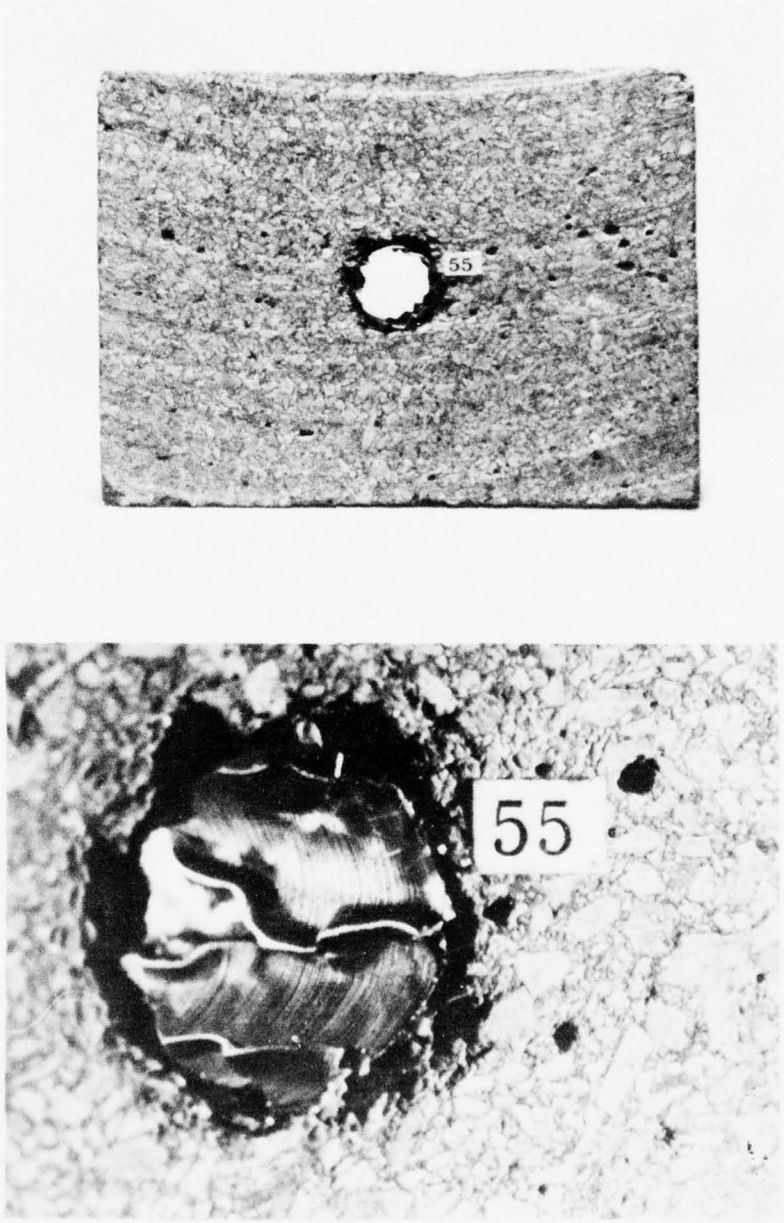

MP-3743-15

FIGURE 5-1 RESPONSE OF A STEEL-LINED TUNNEL TO STATIC, ISOTROPIC LOADING—a/h = 50, P_{omax} = 22,000 psi, $\Delta D/D$ = 0.15

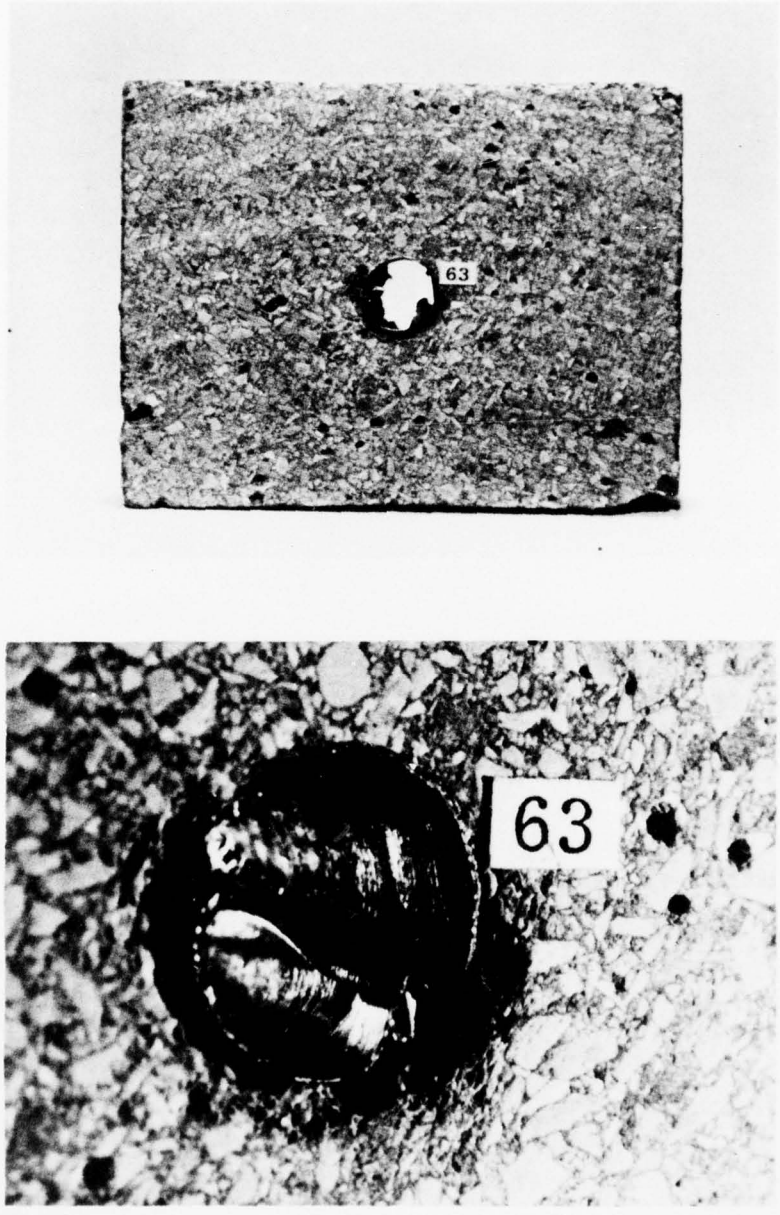

MP-3743-16

FIGURE 5-2 RESPONSE OF A STEEL-LINED TUNNEL TO STATIC, ISOTROPIC LOADING—a/h = 50, P_{omax} = 28,000 psi, $\Delta D/D$ = 0.26

Here, buckling began at about 5,000 psi (193 MPa). A plot of deformation versus load for these liners is shown in Figure 5-11, which will be discussed later.

Figure 5-3 shows the results of a test on a tunnel with a direct contact steel liner with a/h = 25. The final load was 29,000 psi (200 MPa), and closure was 12 percent. Buckling was first observed at a pressure of 8,000 psi (55.2 MPa), which is slightly higher than that for the thinner liner. Also, the final buckled state is not as severe as in the thinner liner. (Compare Figures 5-2 and 5-3).

The results of a test on a tunnel with a direct contact liner with a/h = 12.5 are shown in Figure 5-4. The liner did not buckle as did the thinner liners just discussed. The peak load was P_o = 25,000 psi (172 MPa), and the final closure was $\Delta D/D$ = 5.1 percent.

Figure 5-5 shows the results of a test on a tunnel with a steel liner (a/h = 25) surrounded by backpacking with a radius-to-thickness ratio R/H = 4.5. The backpacking is made from 12-lb (5.44 kg) polyurethane foam, which has a crush strength of about 550 psi (3.79 MPa) up to a strain of 40 percent. The backpacking is barely visible in the photograph because it has been crushed between the cavity wall and the liner during the test (crushup $\approx$ 63 percent). The final load was 23,000 psi (159 MPa), but the closure of the liner is negligible because most of the deformation of the cavity was absorbed by the backpacking. The results of a similar test with the same backpacking thickness but with a thicker liner (a/h = 12.5) are shown in Figure 5-6. Again, the closure of the liner is negligible up to a pressure of 24,000 psi (165 MPa). In this case, the backpacking crushed to a strain of almost 70 percent.

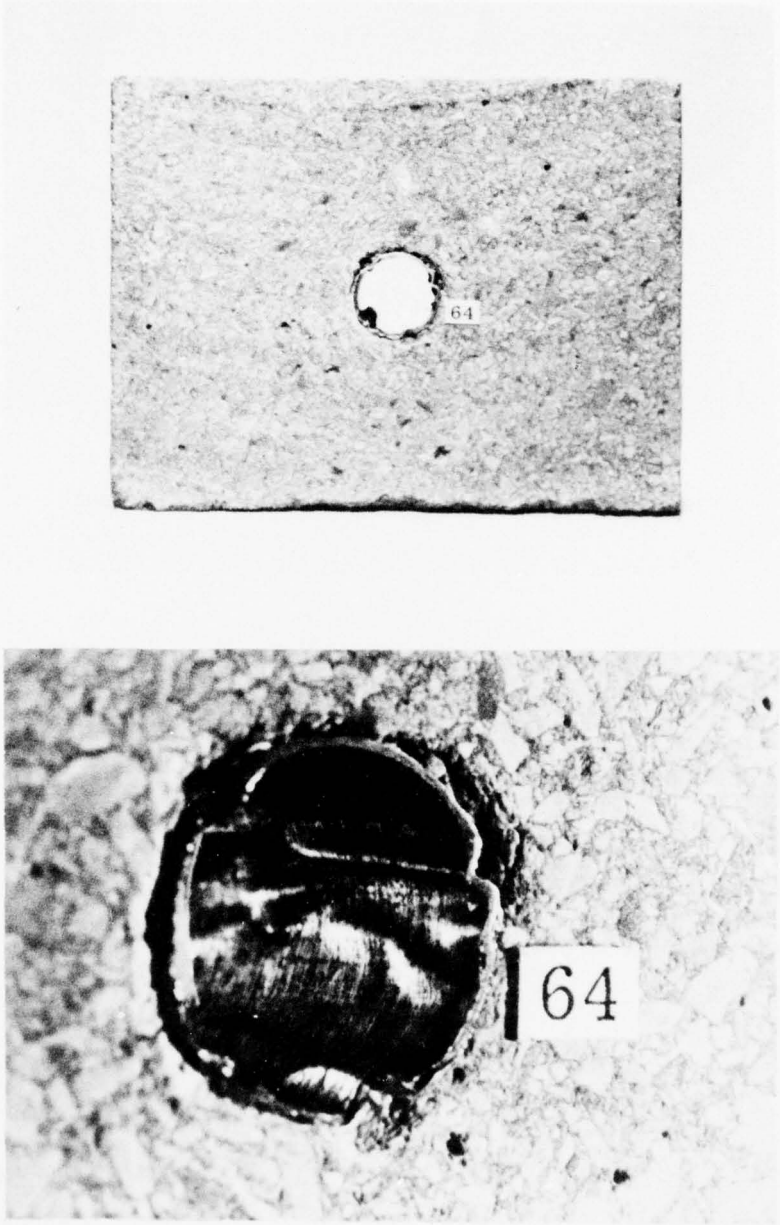

MP-3743-17

FIGURE 5-3 RESPONSE OF A STEEL-LINED TUNNEL TO STATIC, ISOTROPIC LOADING—a/h = 25, P_{omax} = 29,000 psi, $\Delta D/D$ = 0.12

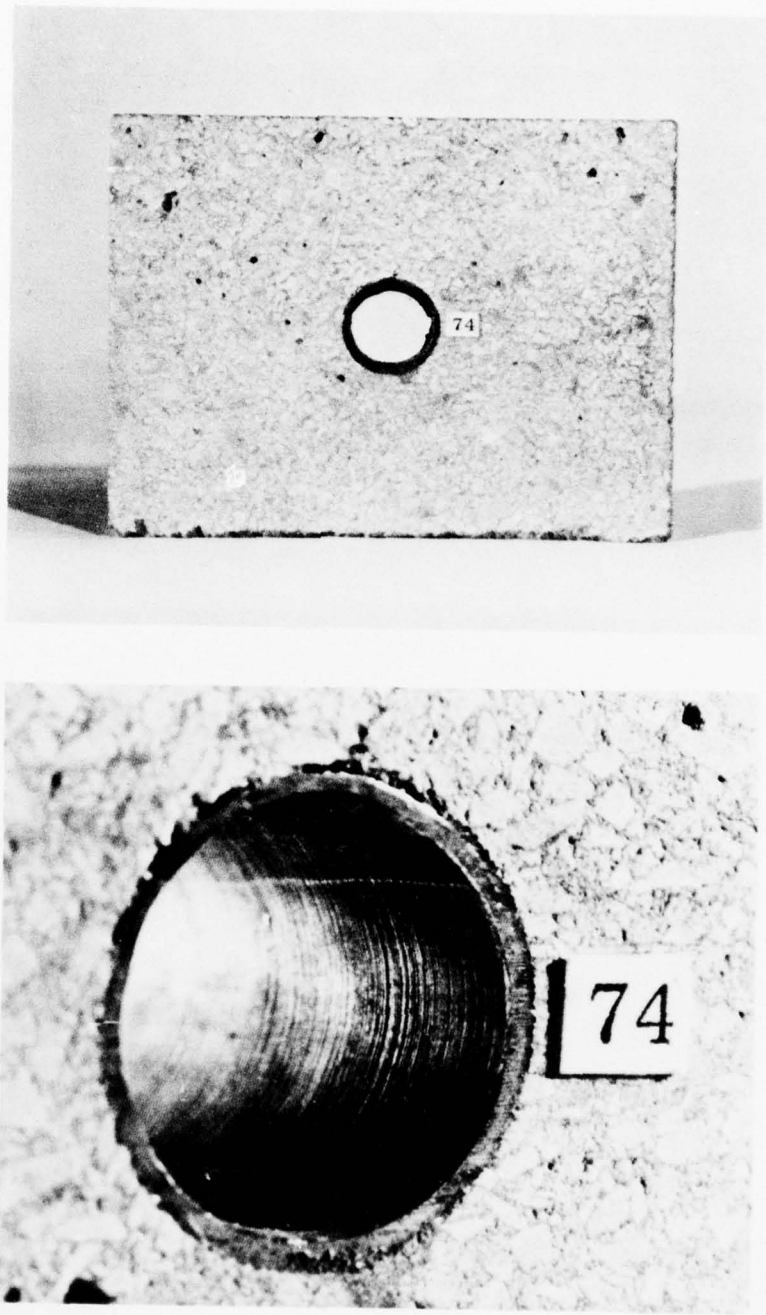

MP-3743-29

FIGURE 5-4 RESPONSE OF A STEEL-LINED TUNNEL TO STATIC, ISOTROPIC LOADING—a/h = 12.5, P_{omax} = 25,000 psi, $\Delta D/D$ = 0.051

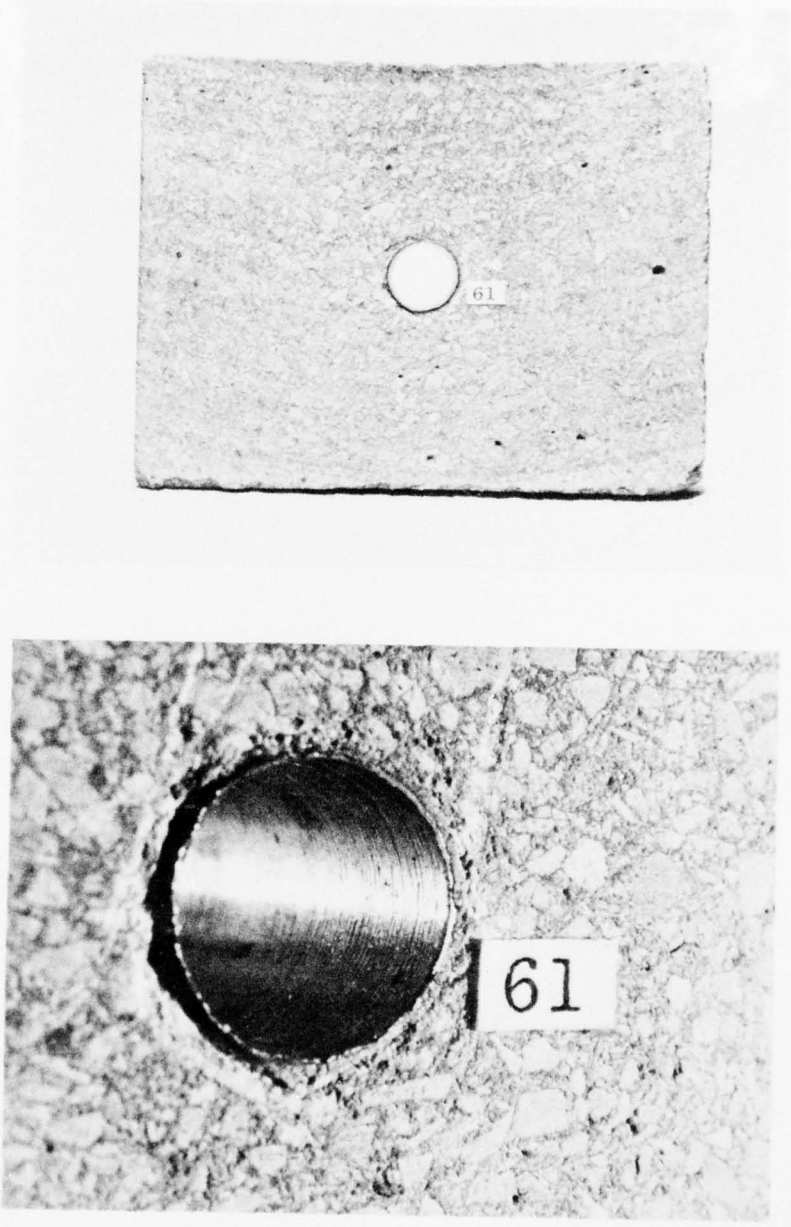

MP-3743-18

FIGURE 5-5 RESPONSE OF A STEEL LINER WITH BACKPACKING TO STATIC, ISOTROPIC LOADING—a/h = 25, P_{omax} = 23,000 psi, $\Delta D/D$ = 0.0075, R/H = 4.5

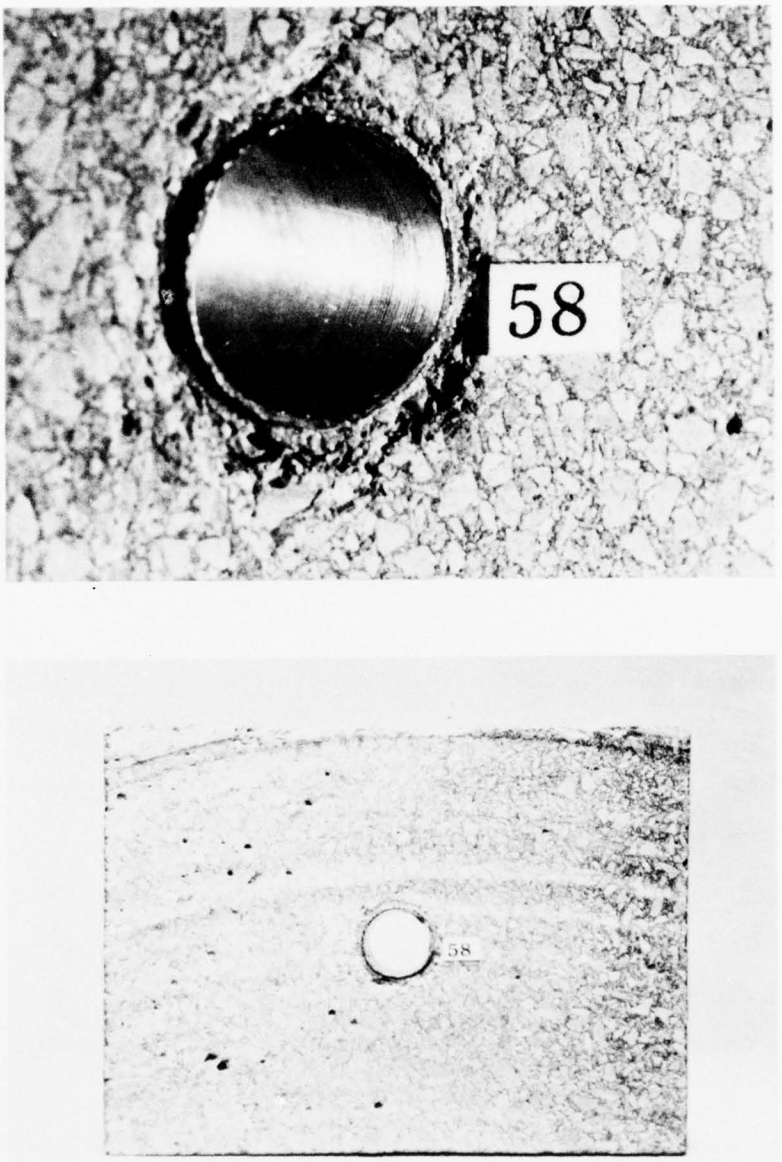

MP-3743-19

FIGURE 5-6 RESPONSE OF A STEEL LINER WITH BACKPACKING TO STATIC, ISOTROPIC LOADING—a/h = 12.5, P_{omax} = 24,000 psi, $\Delta D/D$ = 0.0025, R/H = 4.5

5.2 Dynamic Test Results

Two dynamic isotropic experiments were performed. One was on a tunnel with a direct-contact (a/h = 50) steel liner in saturated 6B rock; the other was on an aluminum model of the CASES structure, which was tested in HARM grout. Figure 5-7 shows the results of the test on the a/h = 50 liner. The peak pressure was P_o = 10,500 psi (72.2 MPa) and the final closure was $\Delta D/D$ = 2 percent. This liner is buckled, as was its static loading counterpart discussed in the previous section, where buckling started at 7,000 psi (48.3 MPa).

High-speed photographs of the response of the liner were taken during the test. A transparent plastic tube filled with a crushable plastic foam was inserted into the liner. Photographs were taken with a Hycam camera using back lighting. Figure 5-8 shows the time history of the response. The ring of light is the light transmitted through the plastic tube that follows the deformation of the liner. We observe the formation of a buckle in the lower right hand side of the liner at t = 368 μs. At t = 920 μs, the picture is completely obscured by smoke from the loading machine.

A simple model of a CASES composite integral liner (Ref. 9) was also tested. Rather than try to model the details of steel and reinforced concrete used in the composite integral liner, we decided to use a soft aluminum (Al 6061-TO with a yield stress σ_y = 15,000 psi (103 MPa)) liner that would yield at approximately the same pressure [$P_i \approx$ 2,500 psi (17.2 MPa)] as the composite integral liner. Soft aluminum was chosen as the liner material so that the radius-to-thickness ratio (a/h = 6) would be low to inhibit buckling. The liner was tested in HARM grout because this was the material that surrounded the structure in the Dining Car experiment described in Chapter 7. Figure 5-9 shows the results of a dynamic, isotropic loading test on this structure where,

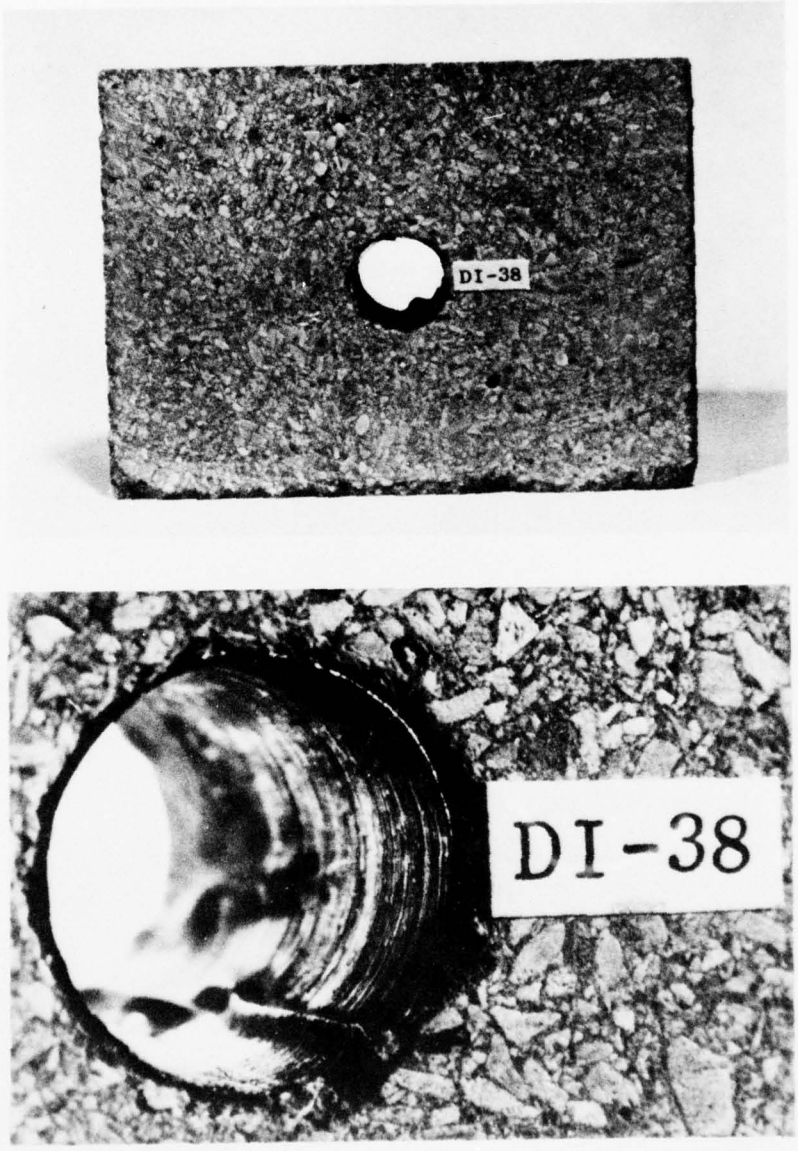

MP-3743-39

FIGURE 5-7 RESPONSE OF A STEEL-LINED TUNNEL TO DYNAMIC, ISOTROPIC LOADING—a/h = 50, P_{omax} = 10,500 psi, $\Delta D/D$ = 0.02

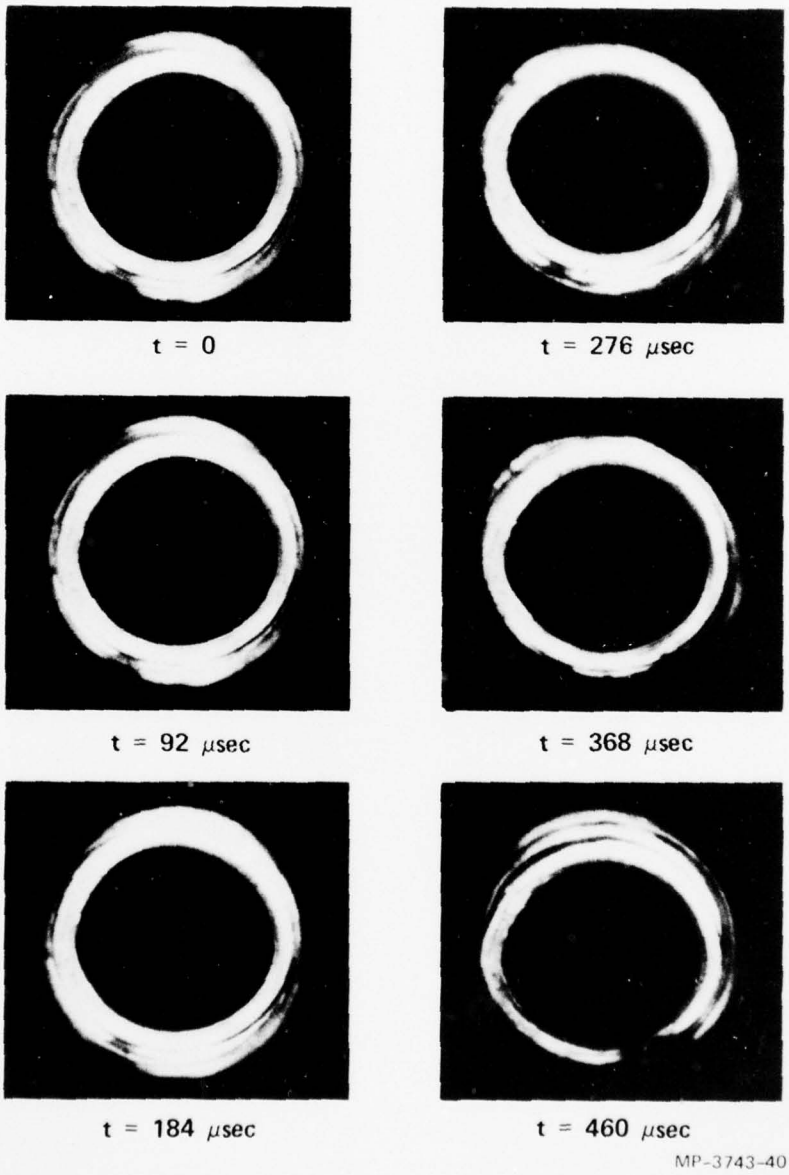

FIGURE 5-8 TIME HISTORY OF RESPONSE OF A STEEL-LINED TUNNEL TO DYNAMIC ISOTROPIC LOADING—a/h = 50, P_{omax} = 10,500 psi, $\Delta D_{max}/D$ = 0.02

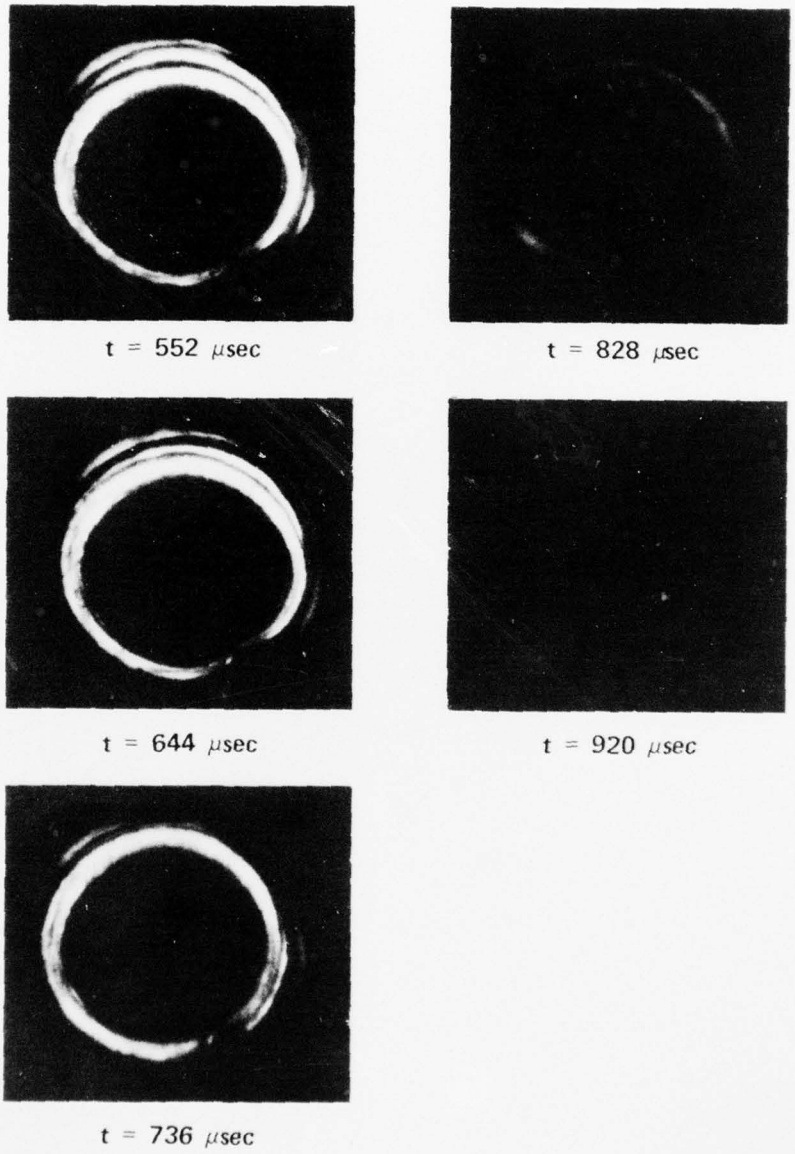

FIGURE 5-8 TIME HISTORY OF RESPONSE OF A STEEL-LINED TUNNEL TO DYNAMIC ISOTROPIC LOADING—a/h = 50, P_{omax} = 10,500 psi, $\Delta D_{max}/D$ = 0.02 (Concluded)

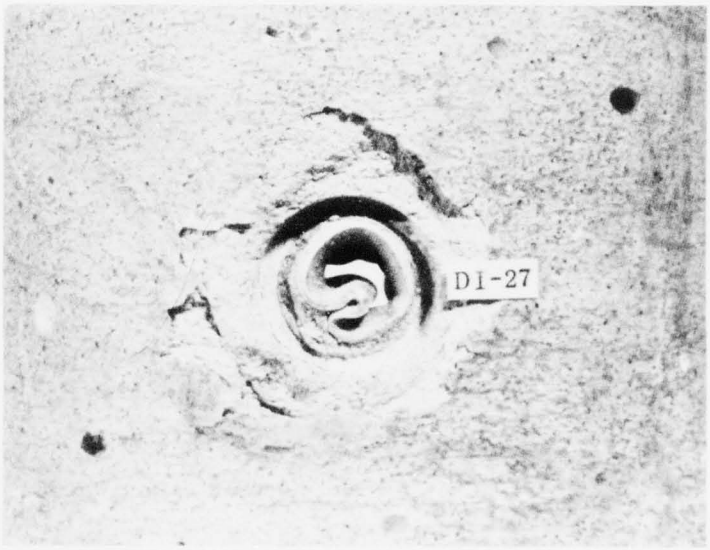

MP-3743-42

FIGURE 5-9 RESPONSE OF AN ALUMINUM-LINED TUNNEL IN HARM GROUT (CASES MODEL) TO DYNAMIC, ISOTROPIC LOADING—a/h = 6.0, P_{omax} = 11,200 psi

AD-A043 398 STANFORD RESEARCH INST MENLO PARK CALIF F/G 8/7
LABORATORY INVESTIGATION OF ROCK CAVITY REINFORCEMENT.(U)
APR 76 T C KENNEDY, H E LINDBERG DNA001-75-C-0101
UNCLASSIFIED DNA-4023F NL

2 OF 3
AD
A043 398

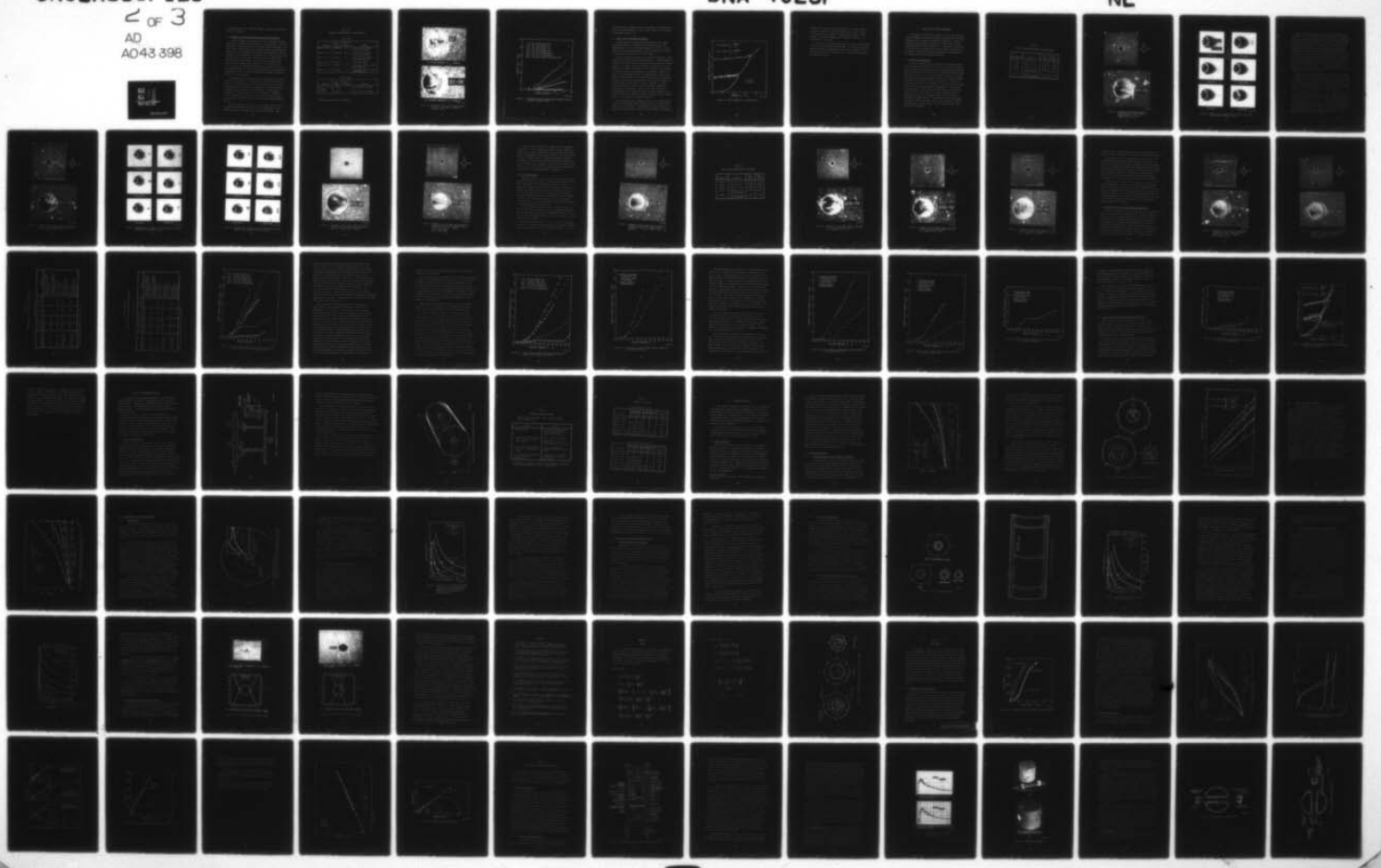

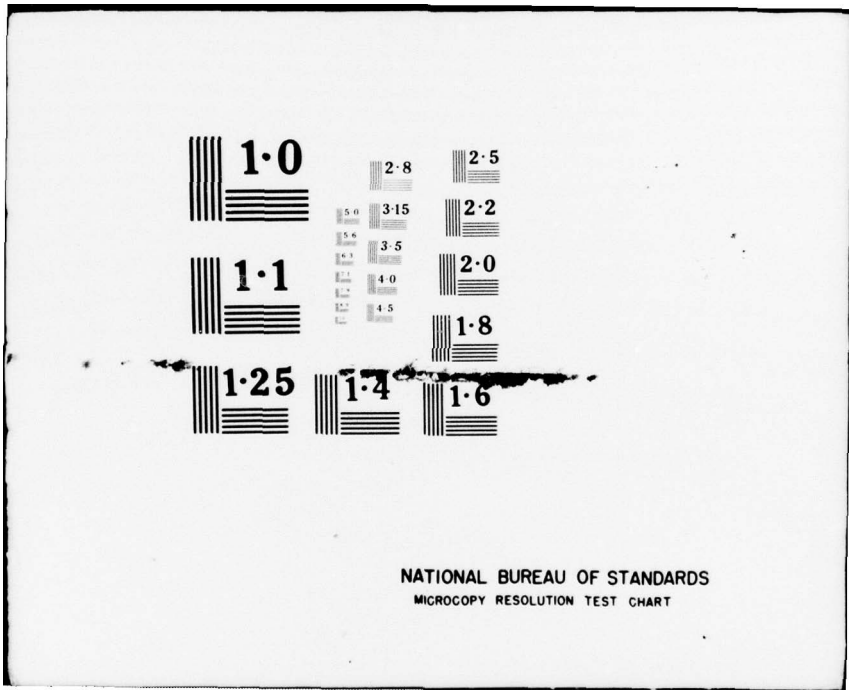
1·0
1·1
1·25
1·4
1·6
1·8
2·0
2·2
2·5
2·8
3·15
3·5
4·0
4·5
5·0
5·6
NATIONAL BUREAU OF STANDARDS
MICROCOPY RESOLUTION TEST CHART

at a peak pressure of P_o = 11,200 (77.2 MPa), we observe that this liner is severely collapsed.

5.3 Interpretation of Static and Dynamic Isotropic Loading Tests

We will now compare the results of the static and dynamic isotropic loading tests. Table 5-2 gives a summary of the test results. Figure 5-11 plots closure versus pressure for the isotropic loading experiments. The results of the two tests on the a/h = 50 direct contact liners (upper two curves) are in close agreement, demonstrating the reproducibility of the experiment. The deformation of the thicker (a/h = 25) direct contact liner is smaller than that in the a/h = 50 liner because the thicker liner applies greater confining pressure to the rock and also buckles less severely than the thinner liner. Similarly, the deformation of the a/h = 12.5 liner is smaller still since it does not buckle at all. The two backpacked liners are relatively undamaged because the backpacking has absorbed most of the rock cavity deformation without applying excessive pressure to the steel liners.

We now compare the statically loaded a/h = 50 liner with its dynamically loaded counterpart. (See Figure 5-10.) Because the final peak pressure in the static test was more than a factor of two greater than in the dynamic test, the amount of deformation for the static loading is considerably larger than for the dynamic loading. We will compare deformation at the same pressure in the next paragraph. Although the amount of deformation is different, the character of the two responses is very similar. They both show the same type of high harmonic buckling pattern.

The dynamic loading result for the a/h = 50 direct contact liner is also plotted (star symbol) in Figure 5-11. The deformation is about 40 percent lower in the dynamic case than in the static case. This

Table 5-2

SUMMARY OF ISOTROPIC TESTS IN SATURATED ROCK

Static Tests

Structure	P_{omax} (psi)	$\Delta D_{max}/D$ (percent)	Comments
Steel a/h = 50	22,000	15.0	Liner severely buckled starting at 7000 psi
Steel a/h = 50	28,000	26.0	Liner severely buckled starting at 5000 psi
Steel a/h = 25	29,000	12.0	Liner moderately buckled starting at 8000 psi
Steel a/h = 12.5	25,000	5.1	Liner not buckled
Steel a/h = 25	23,000	0.75	Backpacking severely crushed, liner undamaged
Steel a/h = 12.5	24,000	0.25	Backpacking severely crushed, liner undamaged

Dynamic Tests

Structure	P_{omax} (psi)	$\Delta D_{max}/D$ (percent)	Comments
Steel a/h = 50	10,500	2.0	Liner moderately buckled
Al 6061-T0 a/h = 6.5*	11,200	-	Liner severely collapsed

*This structure was tested in HARM grout.

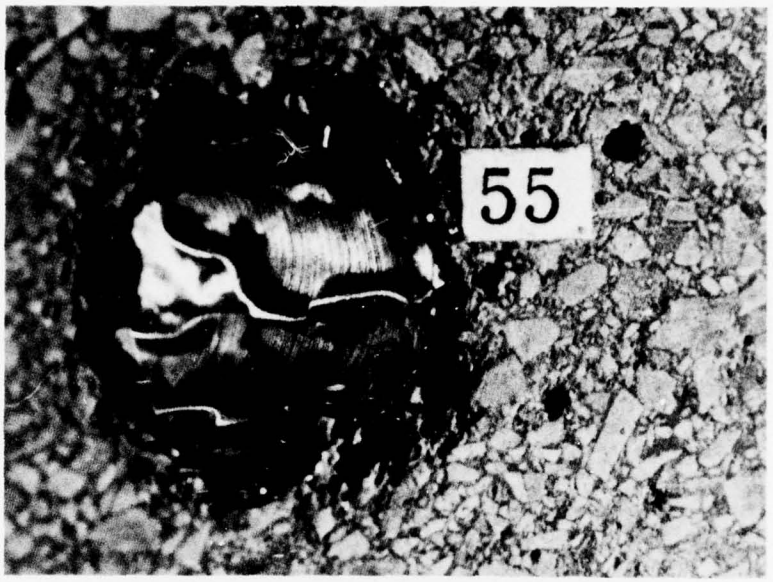

(a) STATIC RESPONSE AT P_o = 22,000 psi

(b) DYNAMIC RESPONSE AT P_o = 10,500 psi

MP-3743-43

FIGURE 5-10 COMPARISON OF STATIC AND DYNAMIC RESPONSE OF A STEEL-LINED TUNNEL TO ISOTROPIC LOADING—a/h = 50

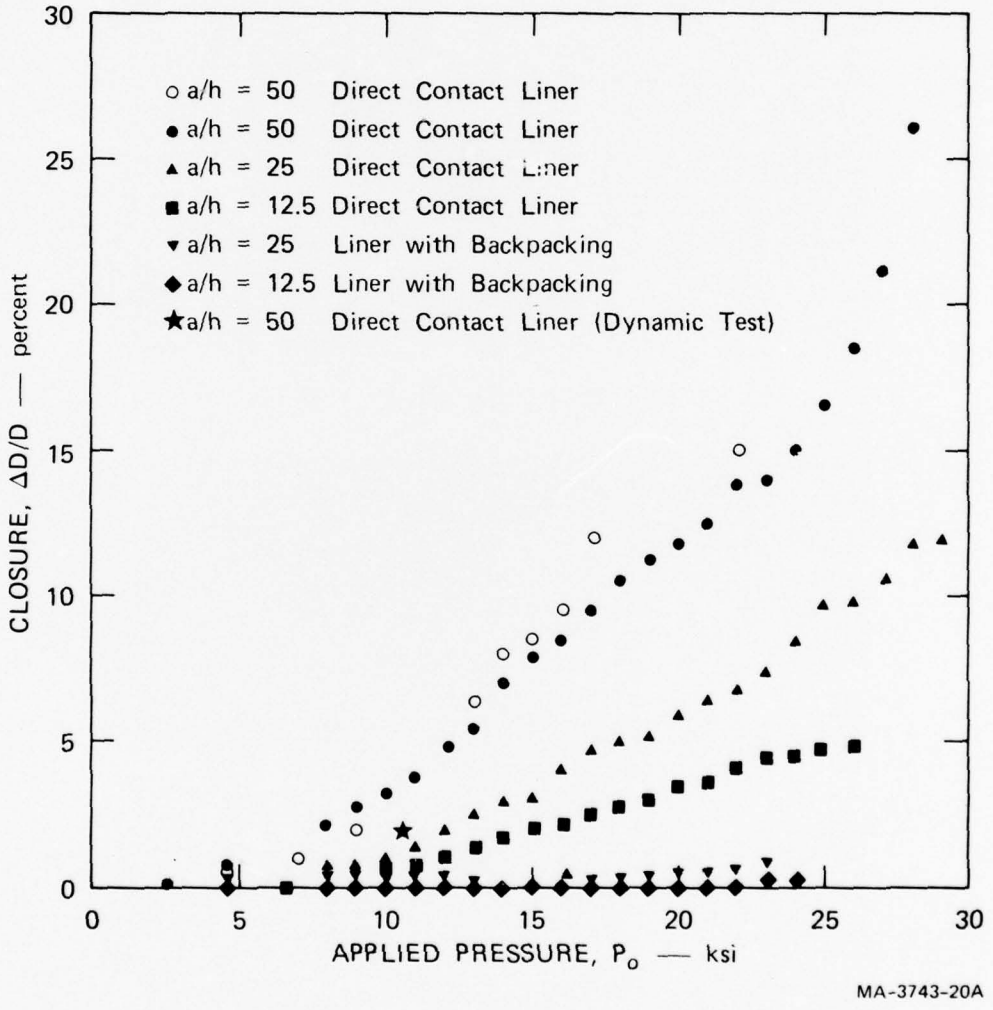

FIGURE 5-11 EXPERIMENTAL CLOSURE VERSUS APPLIED PRESSURE FOR STATIC, ISOTROPIC LOADING OF 6B ROCK

difference can be attributed in part to the presence of porewater pressure in the dynamic loading test, which tends to make the rock stronger as discussed in Section 2.4.

5.4 Static, Cyclic, Isotropic Test Results

To help answer the question of how yielding structures respond under repeated loading, we performed cyclic loading tests on rock specimens with a/h = 12.5 steel-lined tunnels in dry 6B rock. In the first test the loading was isotropic. This was followed by a uniaxial-strain loading test (described in the next chapter).

Figure 5-12 shows the results of the isotropic loading test; tunnel closure $\Delta D/D$ is plotted against applied pressure P_o. Repeated loading to the same load results in only very small additional increments in tunnel closure. For example, in the first loading to a pressure P = 11.5 ksi (79.3 MPa), the tunnel closure was $\Delta D/D$ = 1.85 percent. Upon unloading to 1.0 ksi (6.89 MPa), (a small pressure was required to maintain the seals) the liner expanded slightly to a tunnel closure of $\Delta D/D$ = 1.65 percent. Reloading back to 11.5 ksi (79.3 MPa) took place back up the unloading line to about 9 ksi (62.0 MPa) and then diverged slightly to a final closure of 2.00 percent at 11.5 ksi (79.3 MPa). A second unloading and reloading cycle to 11.5 ksi (79.3 MPa) resulted in a final closure of 2.10 percent. Thus, the fear that each cycle of reloading might give an additional closure increment comparable to the initial closure was not realized (that is, the closure did not increase from 2 to 4 to 6 percent at the end of each cycle).

Having demonstrated that repeated loading to the 2 percent initial closure load produced only small additional closure, we increased the load to 17.5 ksi (12.0 MPa). This increased the closure along an extension of the initial closure curve to a final closure of 4.03 percent.

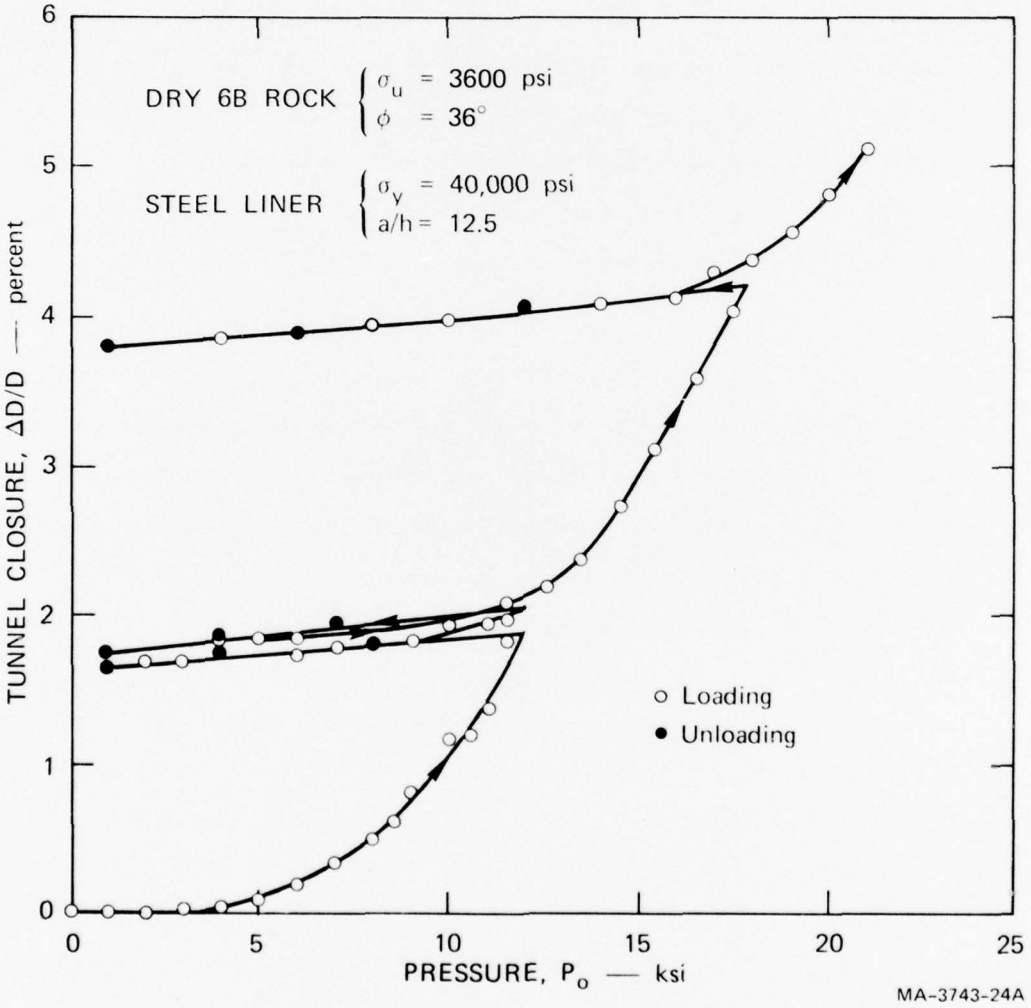

FIGURE 5-12 CYCLIC LOADING TEST—ISOTROPIC LOADING

Unloading and reloading to 17.0 ksi (117 MPa) gave a total closure of 4.3 percent, again only a very small amount greater than the closure at the initial 17.5 ksi (120 MPa). Upon continued loading to 21 ksi (145 MPa), the closure resumed its more substantial increase, to a final closure of 5.2 percent.

It appears that the final deformation of the tunnel is not seriously affected by repeated unloading and reloading. The rock and tunnel closure system apparently "shakes down" under repeated loading, so that the rock-liner structure system remains elastic to higher loads on second and subsequent loadings.

6. UNIAXIAL-STRAIN LOADING EXPERIMENTS

In this chapter, we present the results of static, uniaxial-strain loading experiments in both water-saturated and dry 6B rock. The tests in saturated rock are drained as described in Section 4.2. Again, the structures tested consisted of models of the lined tunnels with and without backpacking tested in Dining Car. We also present the results of a static, cyclic, uniaxial-strain loading test on a lined tunnel in dry 6B rock. All tests were with 4-inch-diameter rock specimens as in the isotropic tests just described in Section 5.

6.1 Saturated Rock Experiments

Five static, uniaxial-strain experiments were performed on models in saturated 6B rock. Table 6-1 gives a list of the structures tested and the maximum vertical pressure P_V and horizontal pressure P_H applied. Figure 6-1 shows the results of a test on a tunnel with a direct contact steel liner with $a/h = 50$. The peak vertical load was $P_V = 12{,}500$ psi (86.2 MPa), and the peak horizontal load was $P_H = 4{,}750$ psi (32.3 MPa). The final vertical closure was $\Delta D_V/D = 11.35$ percent. The liner is ovalled and has buckles at the springlines. Figure 6-2 shows photographs of the history of the buckling taken at increments in vertical load. The photographs were taken through a concave lens that fit inside the tunnel entry tube. The surface of the liner ranges from smooth to mottled between $P_V = 5$ ksi (34.5 MPa) and $P_V = 7.5$ ksi (51.7 MPa). The mottling is apparently due to the hard grains in the rock simulant indenting the wall of the liner. At $P_V = 8$ ksi (55.2 MPa), a buckle at the spring line is clearly visible. At $P_V = 11$ ksi (75.8 MPa), the buckle is well developed.

Table 6-1

STATIC UNIAXIAL-STRAIN TESTS IN SATURATED ROCK

Test Number	Structure	P_{Vmax} (psi)	P_{Hmax} (psi)
SUX-89	Steel a/h = 50	12,500	4,750
SUX-82	Steel a/h = 25	19,000	8,600
SUX-83	Steel a/h = 12.5	16,500	8,300
SUX-88	Steel a/h = 25 with backpacking	22,000	11,400
SUX-87	Steel a/h = 12.5 with backpacking	22,000	10,050

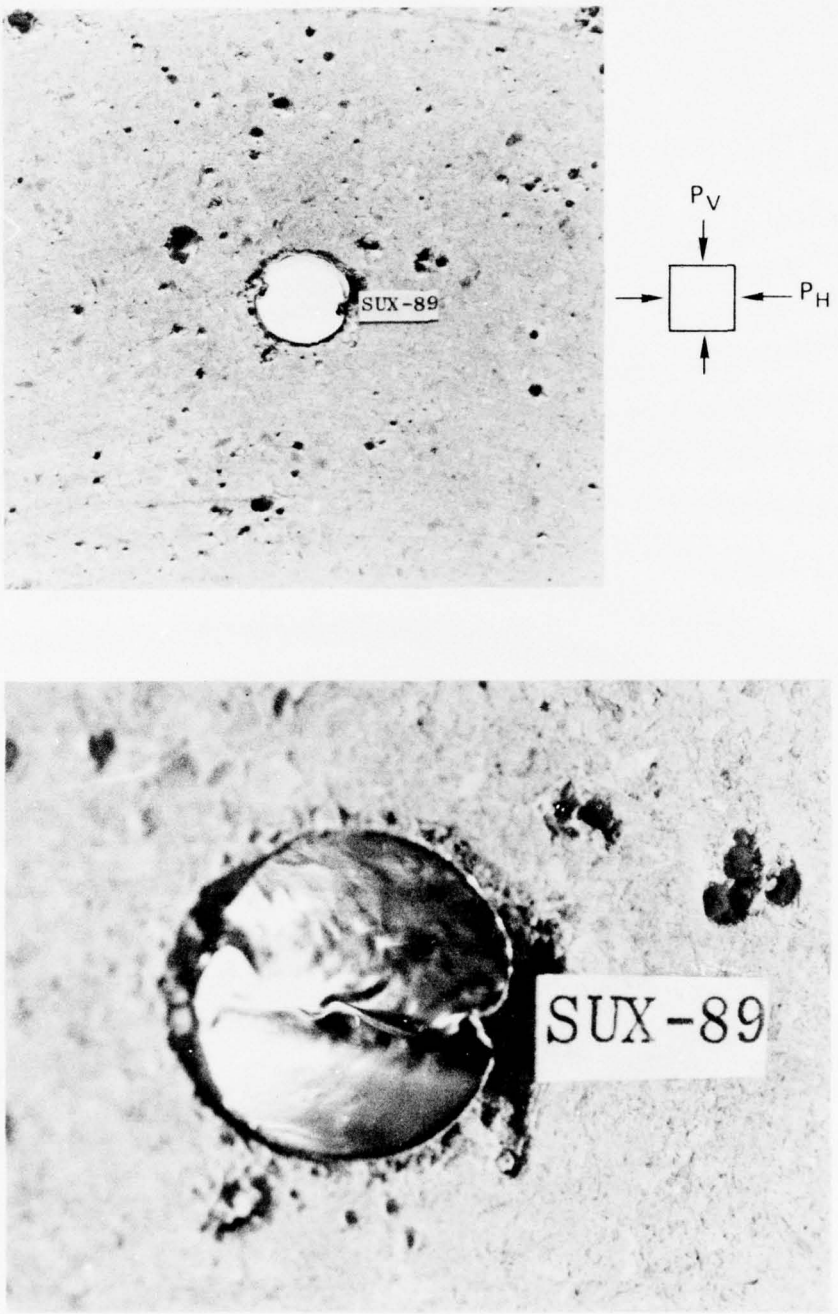

MP-3743-44

FIGURE 6-1 RESPONSE OF A STEEL-LINED TUNNEL IN SATURATED ROCK TO STATIC, UNIAXIAL STRAIN LOADING—a/h = 50, P_{Vmax} = 12,500 psi, $\Delta D_V/D$ = 0.1135

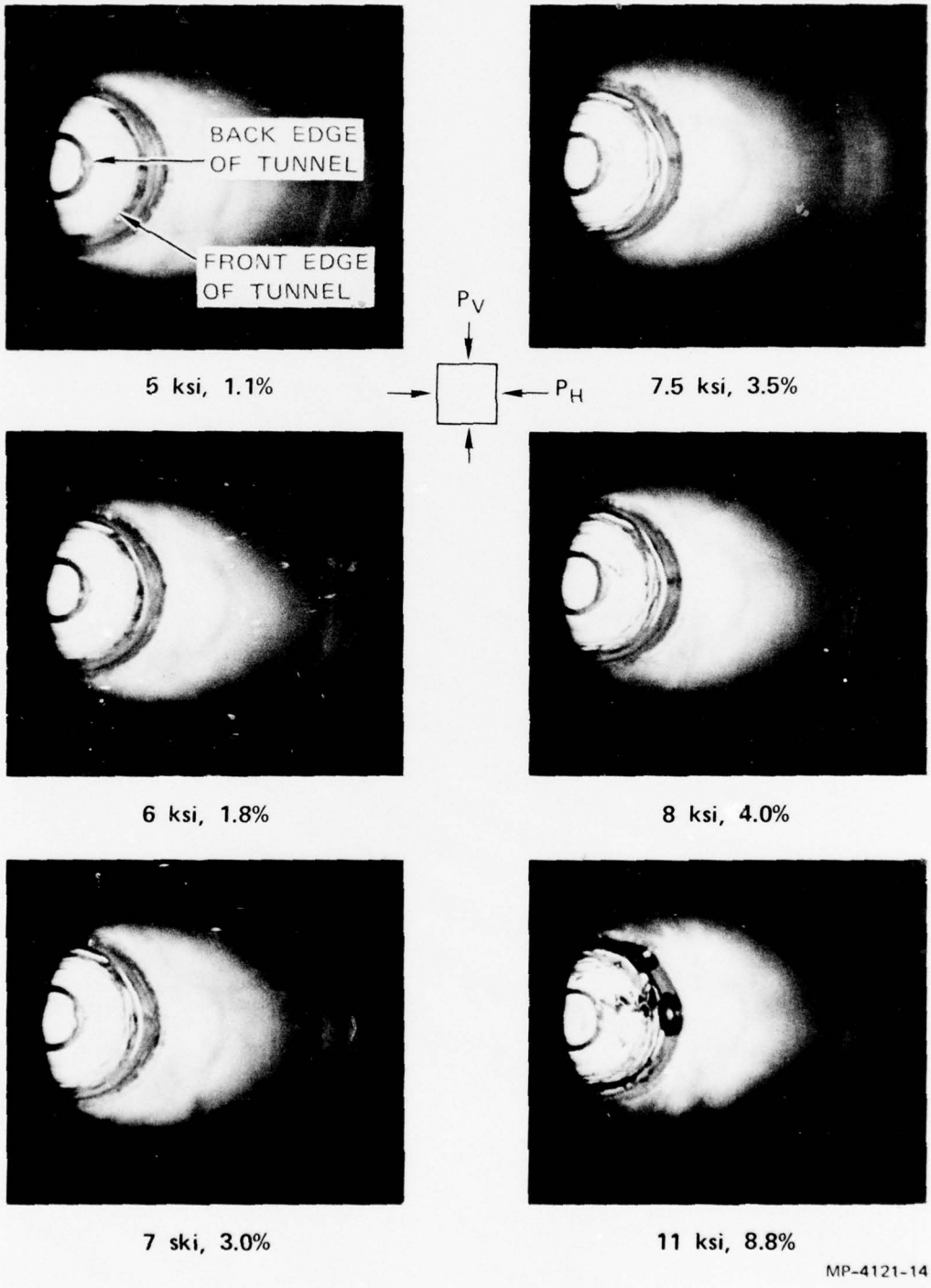

FIGURE 6-2 BUCKLING IN a/h = 50 STEEL LINER: SATURATED ROCK UNDER UNIAXIAL STRAIN LOADING (P_V, $\Delta D/D$)

Figure 6-3 shows the results of a test on a direct contact steel liner with a/h = 25. The final peak vertical load was P_V = 19,000 psi (131 MPa), and the peak horizontal load was P_H = 8,600 psi (159.3 MPa). The final vertical closure was $\Delta D_V/D$ = 14.7 percent. Again, the liner is ovalled and has buckled at the springlines. Figure 6-4 shows the buckling history. In this case, the photographs were taken with a 35-mm camera and standard 50-mm lens without the concave lens. The development of the buckles is similar to the previous case, but it takes place over a wider span of loading and tunnel closure. The surface of the liner ranges from smooth to mottled between P_V = 5 ksi (34.5 MPa) and P_V = 13 ksi (89.6 MPa) [as compared to P_V = 5 ksi (34.5 MPa) to P_V = 7.5 ksi (51.7 MPa) for the a/h = 50 liner]. A buckle at the springline is barely visible at P_V = 14,000 psi (96.5 MPa) but is well developed at P_V = 19,000 psi (130 MPa).

Figure 6-5 shows the results of a test on a tunnel with a direct contact liner with a/h = 12.5. The peak vertical load was P_V = 16,500 psi (114 MPa), and the peak horizontal load was P_H = 8,300 psi (57.2 MPa). The final vertical tunnel closure was $\Delta D_V/D$ = 9.13 percent and the final horizontal tunnel expansion was $\Delta D_H/D$ = -0.96 percent (outward movement considered negative). The liner is ovalled but not buckled.

Figure 6-6 shows the results of a test on a tunnel with a steel liner (a/h = 25) surrounded by backpacking with a radius-to-thickness ratio R/H = 4.5. The peak vertical load was P_V = 22,000 psi (152 MPa), and the peak horizontal load was P_H = 11,400 psi (78.6 MPa). We observe that the backpacking is more severely crushed at the crown and invert (66 percent crushup) than at the springlines (56 percent crushup). The final vertical tunnel closure was $\Delta D_V/D$ = 4.88 percent, and the final horizontal tunnel expansion was $\Delta D_H/D$ = -3.21 percent.

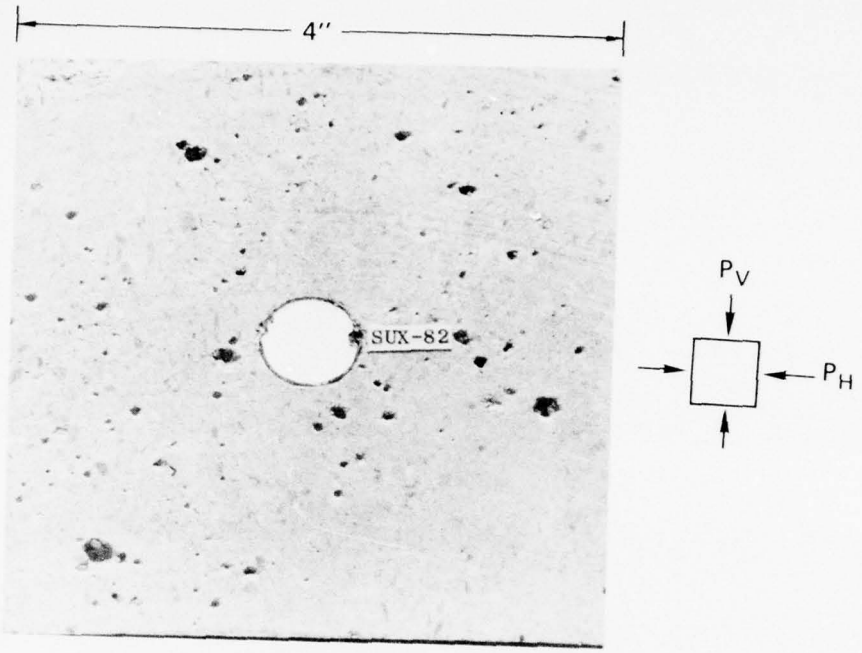

MP-3743-45A

FIGURE 6-3 RESPONSE OF A STEEL-LINED TUNNEL IN SATURATED ROCK TO STATIC, UNIAXIAL STRAIN LOADING— a/h = 25, P_{Vmax} = 19,000 psi, $\Delta D_V/D$ = 0.147

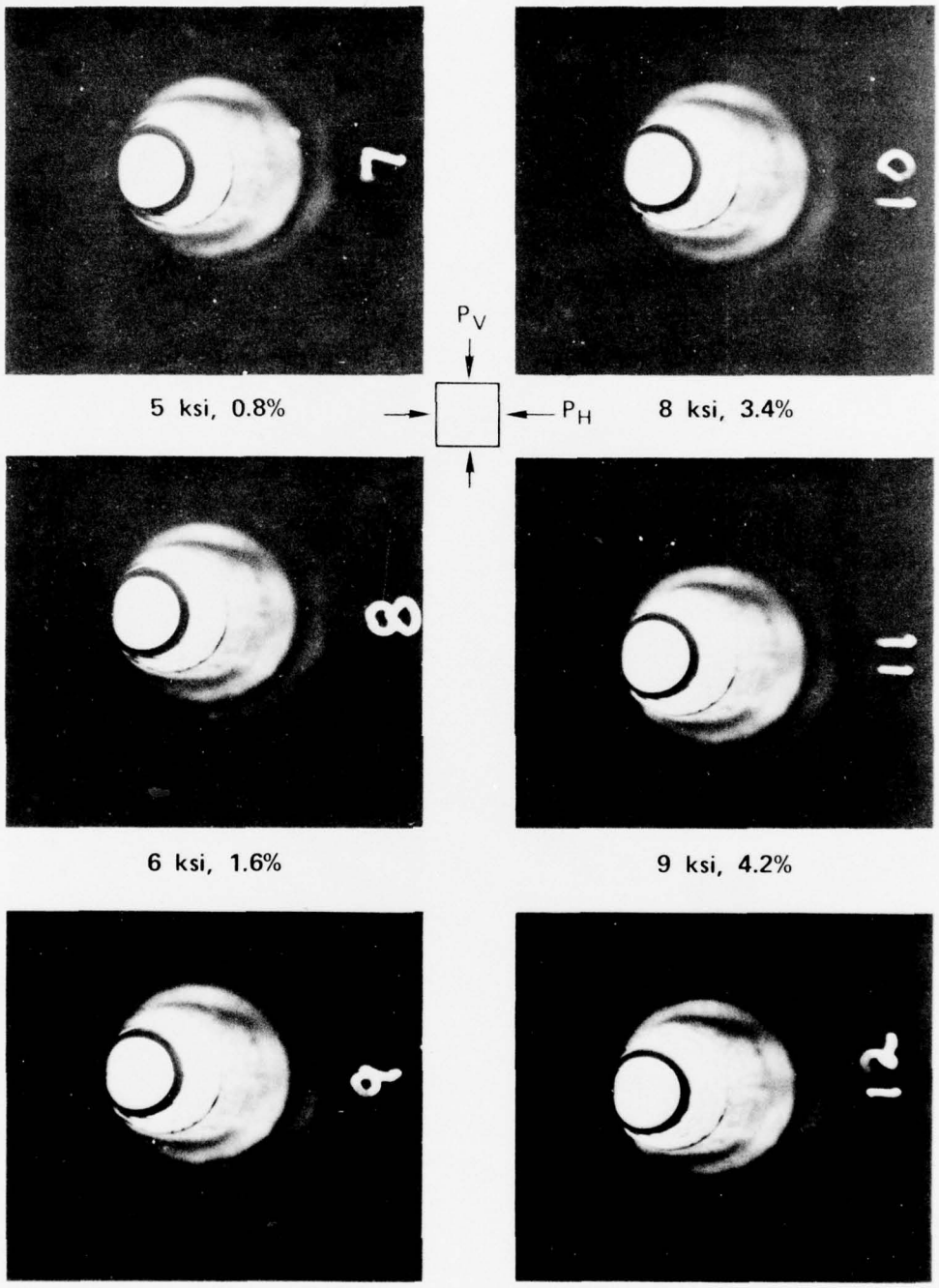

FIGURE 6-4 BUCKLING IN a/h = 25 STEEL LINER: SATURATED 6B ROCK UNDER UNIAXIAL STRAIN LOADING (P_V, $\Delta D_V/D$)

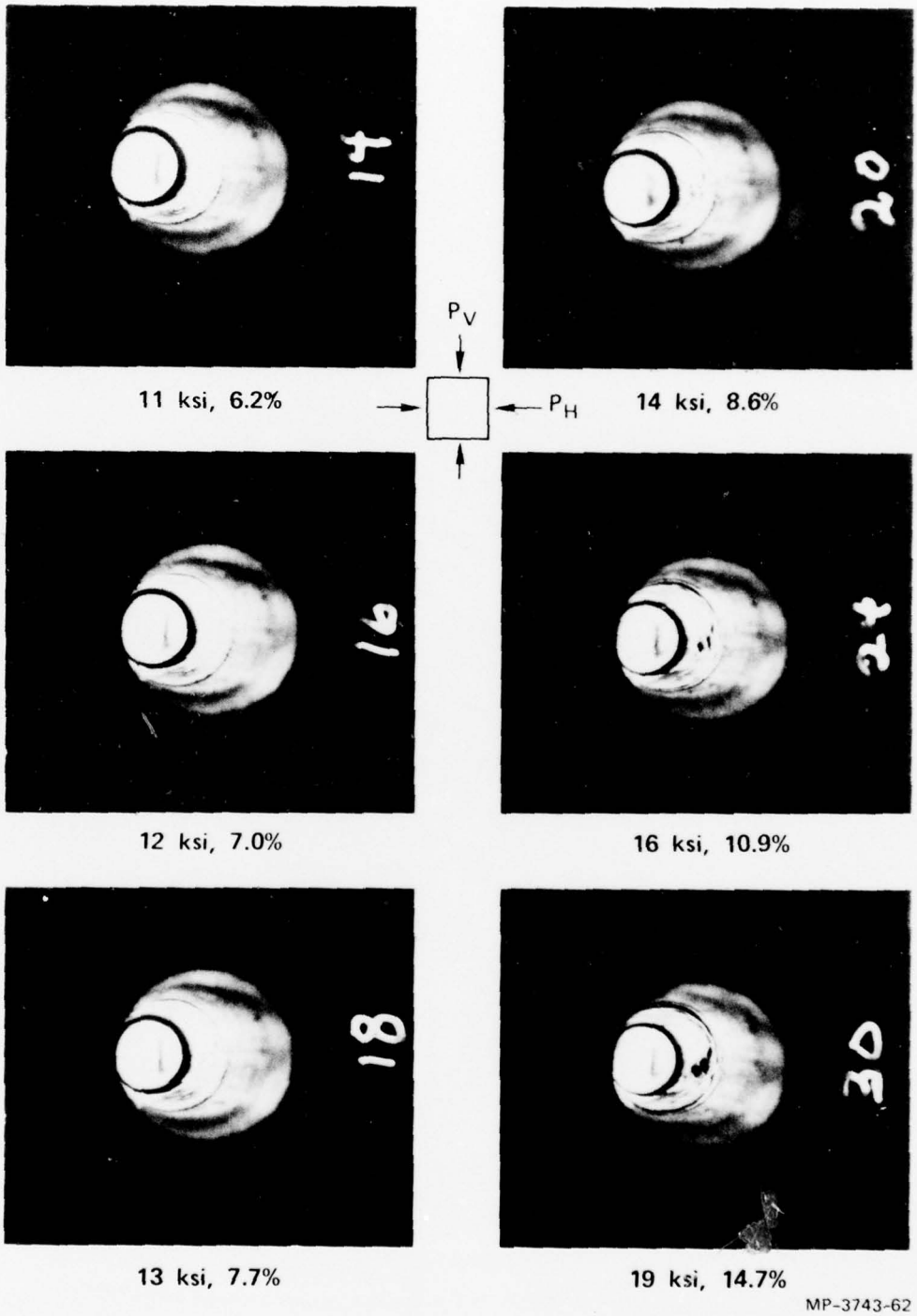

FIGURE 6-4 BUCKLING IN a/h = 25 STEEL LINER: SATURATED 6B ROCK UNDER UNIAXIAL STRAIN LOADING (P_V, $\Delta D_V/D$) (Concluded)

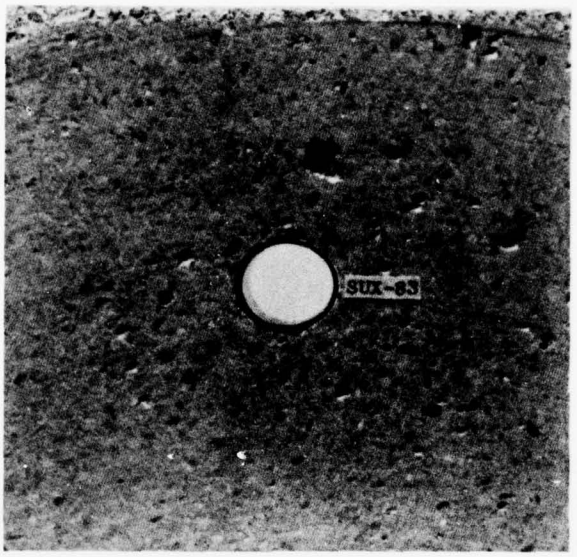

MP-3743-46

FIGURE 6-5 RESPONSE OF A STEEL LINED TUNNEL IN SATURATED ROCK TO STATIC, UNIAXIAL STRAIN LOADING—a/h = 12.5, P_{Vmax} = 16,500 psi, $\Delta D_V/D$ = 0.0913

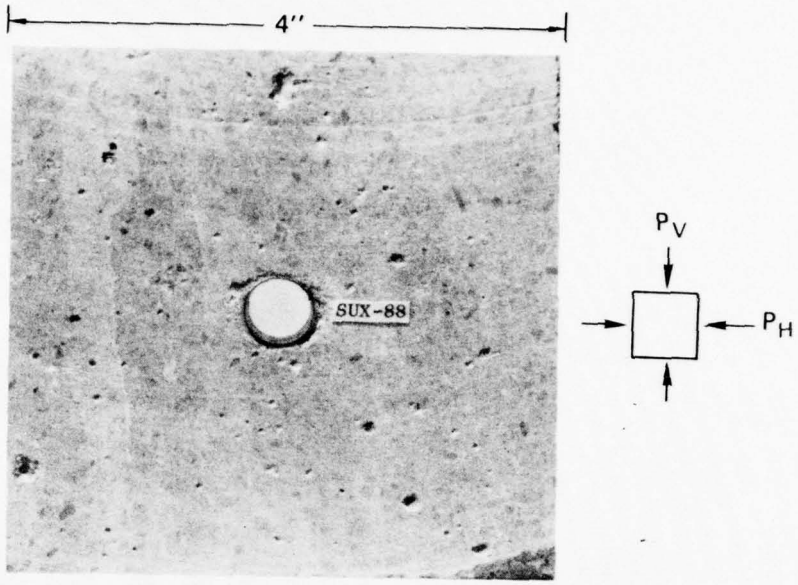

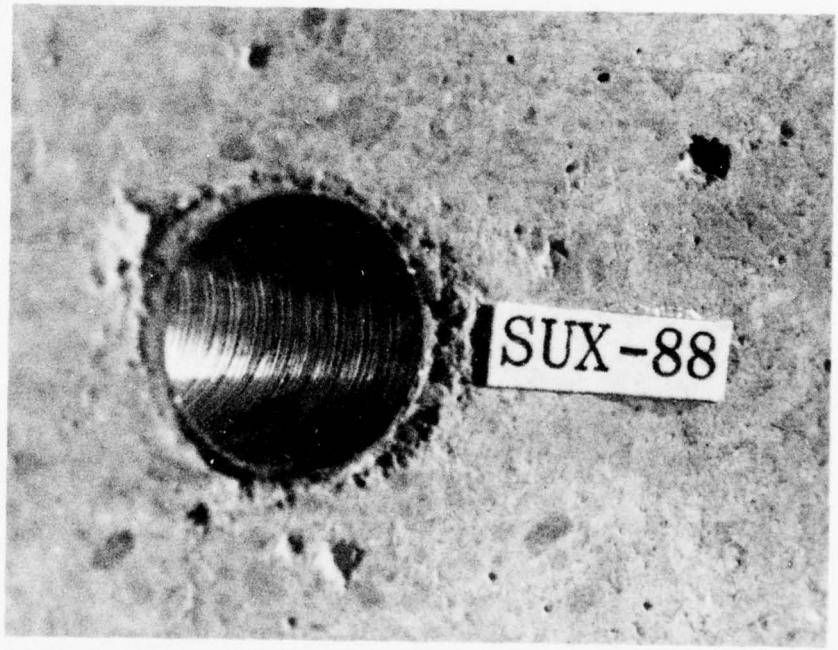

MP-3743-47A

FIGURE 6-6 RESPONSE OF A STEEL LINER WITH BACKPACKING IN SATURATED ROCK TO STATIC, UNIAXIAL STRAIN LOADING—a/h = 25, P_{Vmax} = 22,000 psi, $\Delta D_V/D$ = 0.0488 (LINER) $\Delta D_V/D$ = 0.195 (ROCK)

Figure 6-7 shows the results of a similar test on a backpacked liner with a/h = 12.5. The peak vertical load was P_V = 22,000 psi (152 MPa) and the peak horizontal load was P_H = 10,050 psi (69.3 MPa). Again the backpacking is more severely crushed at the crown and invert (76 percent crushup) than at the springlines (36 percent crushup). The reason for the difference in amount of backpacking crushup from the test reported above is unknown. In this case, the vertical tunnel closure $\Delta D_V/D$ = 4.0 percent is only slightly larger in magnitude than the horizontal tunnel expansion $\Delta D_H/D$ = -3.22 percent.

6.2 Dry Rock Experiments

Experiments similar to the ones in the previous section were also performed on models in dry 6B rock. Here we give the results of these tests; comparisons with the saturated rock results are given in Section 6.3. Table 6-2 gives a list of the structures tested and the maximum loads applied. Figure 6-8 shows the results of a test on a direct contact liner with a/h = 50. The peak vertical load was P_V = 23,500 psi (162 MPa), and the peak horizontal load was P_H = 9,800 psi (67.6 MPa). The final vertical closure was $\Delta D_V/D$ = 17.5 percent. We observe that the liner is ovalled and has buckles at the springlines as did its counterpart in saturated rock.

Figure 6-9 gives the results of a test on a direct contact liner with a/h = 25. The peak vertical load was P_V = 30,000 psi (207 MPa), and the peak horizontal load was P_H = 13,300 psi (91.7 MPa). The final vertical closure was $\Delta D_V/D$ = 20.0 percent. Again, the liner is ovalled with buckles at the springline.

Figure 6-10 shows the result of a test on a direct contact liner with a/h = 12.5. The peak vertical load was P_V = 18,000 psi (124 MPa) and the peak horizontal load is P_H = 6,960 psi (47.91 MPa). The final

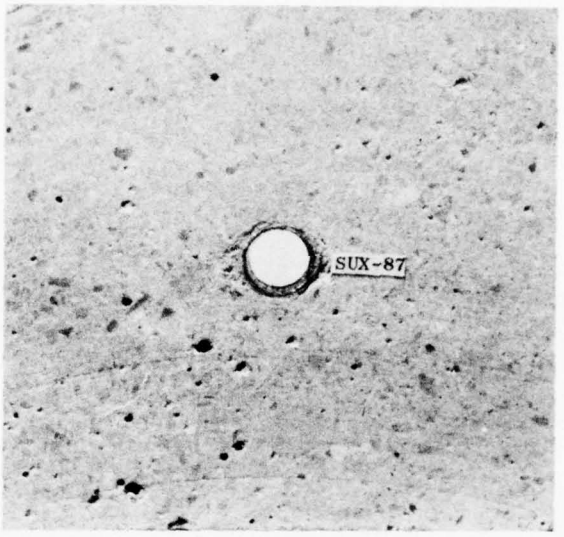

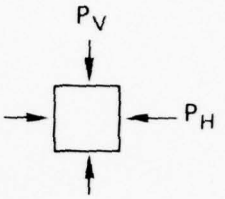

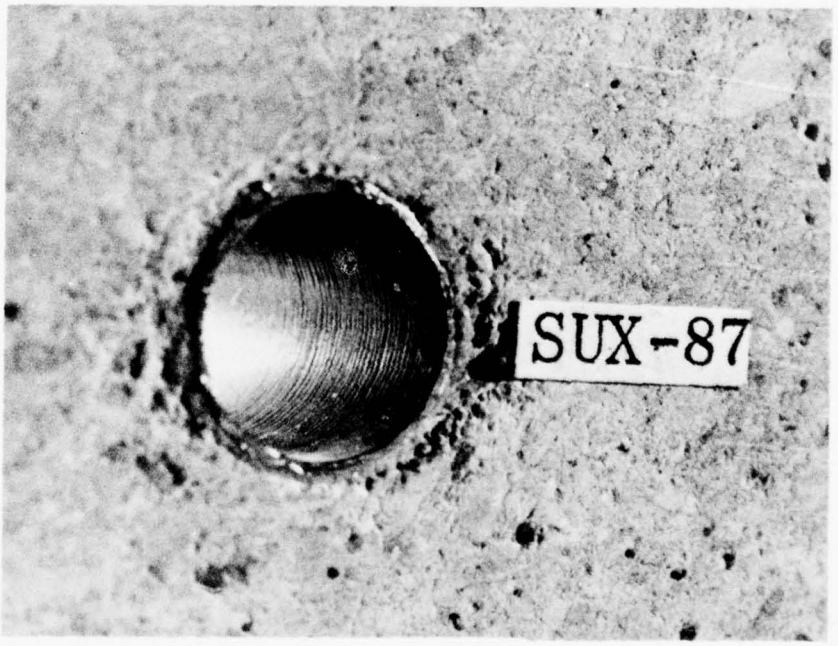

MP-3743-48

FIGURE 6-7 RESPONSE OF A STEEL LINER WITH BACKPACKING IN SATURATED ROCK TO STATIC, UNIAXIAL STRAIN LOADING—a/h = 12.5, P_{Vmax} = 22,000 psi, $\Delta D_V/D$ = 0.04, R/H = 4.5

Table 6-2

STATIC UNIAXIAL-STRAIN TESTS IN DRY ROCK

Test Number	Structure	P_{Vmax} (psi)	P_{Hmax} (psi)
SUX-75	Steel a/h = 50	23,500	9,800
SUX-76	Steel a/h = 25	30,000	13,300
SUX-84	Steel a/h = 12.5	18,000	6,950
SUX-85	Steel a/h = 25 with backpacking	24,500	10,300
SUX-86	Steel a/h = 12.5 with backpacking	26,000	10,950

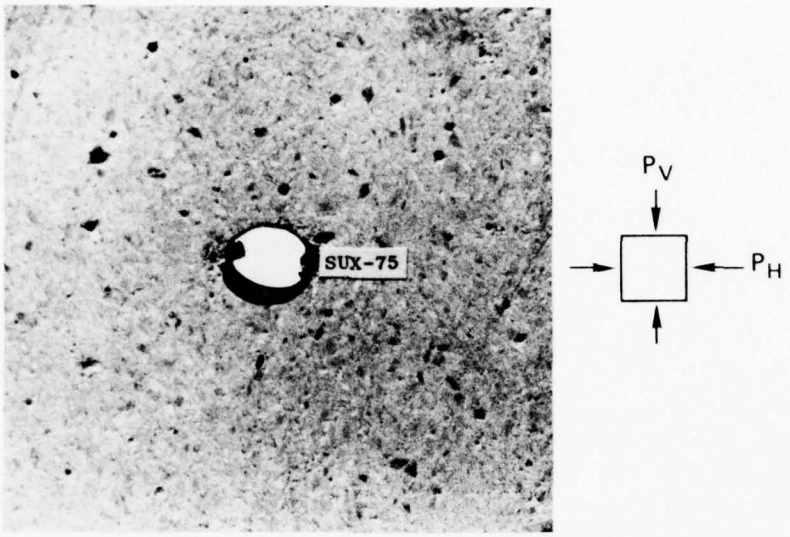

MP-3743-49

FIGURE 6-8 RESPONSE OF A STEEL-LINED TUNNEL IN DRY ROCK TO STATIC, UNIAXIAL STRAIN LOADING—a/h = 50, P_{Vmax} = 23,500 psi, $\Delta D_V/D$ = 0.175

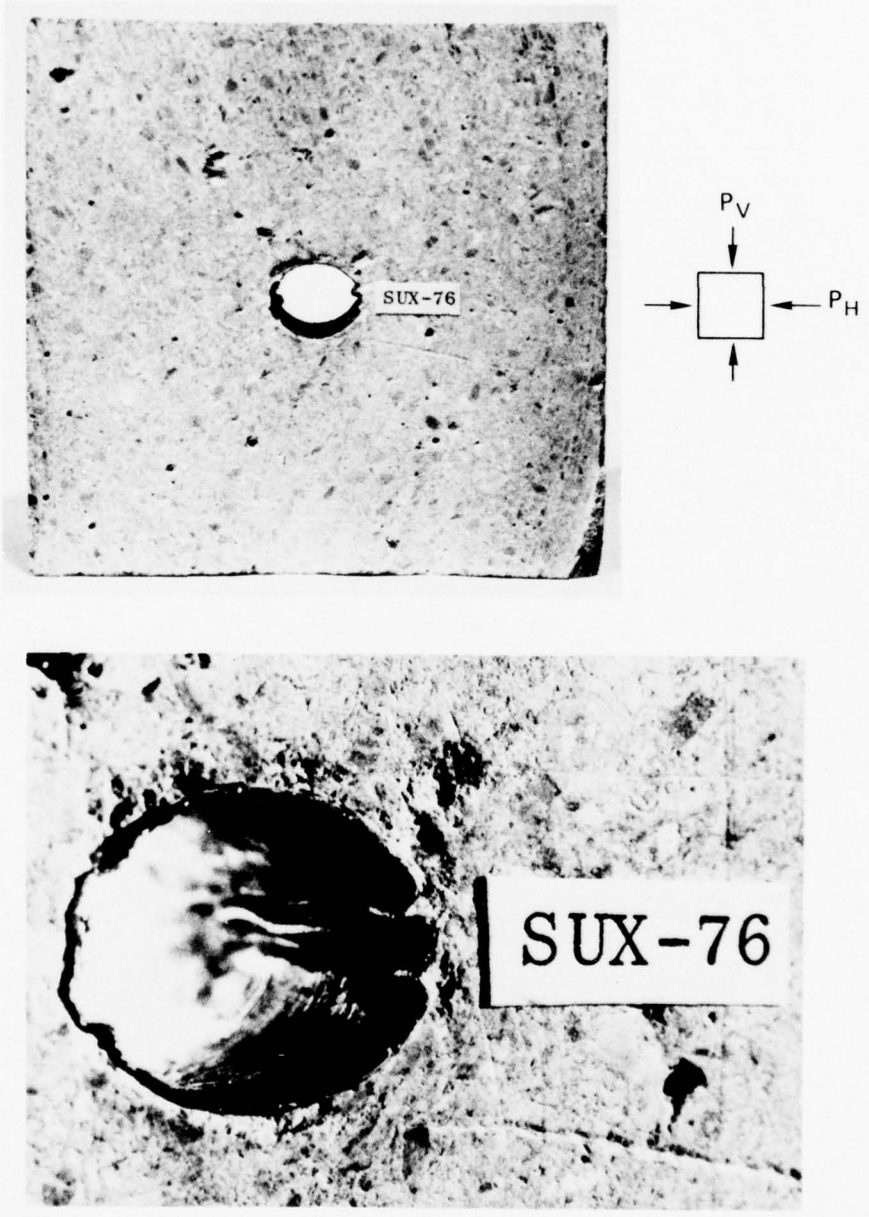

MP-3743-50

FIGURE 6-9 RESPONSE OF A STEEL-LINED TUNNEL IN DRY ROCK TO STATIC, UNIAXIAL STRAIN LOADING—a/h = 25, P_{Vmax} = 30,000 psi, $\Delta D_V/D$ = 0.20

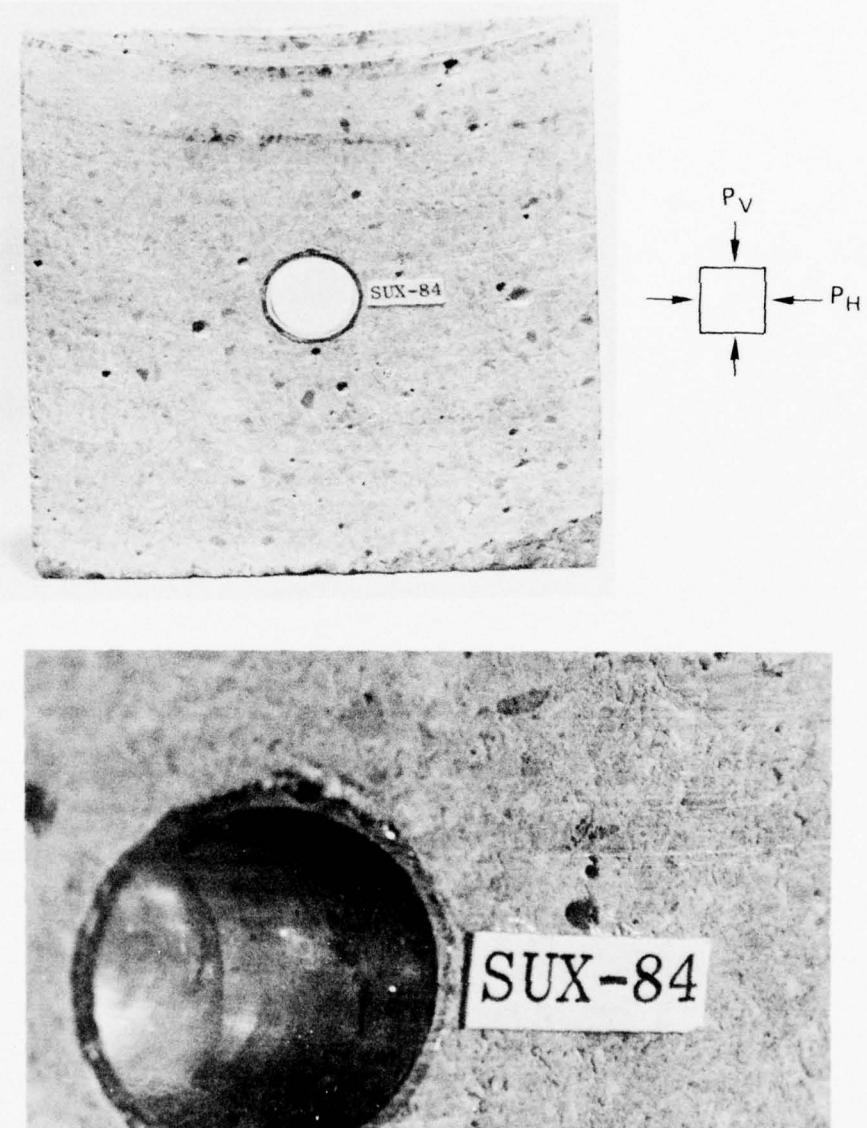

MP-3743-51

FIGURE 6-10 RESPONSE OF A STEEL-LINED TUNNEL IN DRY ROCK TO STATIC, UNIAXIAL STRAIN LOADING—a/h = 12.5, P_{Vmax} = 18,000 psi, $\Delta D_V/D$ = 0.088

vertical closure is $\Delta D_H/D$ = 8.8 percent, and the final horizontal expansion is $\Delta D_H/D$ = -2.56 percent. The liner is ovalled but not buckled.

The results of a test on a tunnel with a steel liner (a/h = 25) surrounded by backpacking (R/H = 4.5) are shown in Figure 6-11. The peak vertical load was P_V = 24,600 psi (169 MPa), and the peak horizontal load was P_H = 10,300 psi (71.0 MPa). The backpacking was more severely crushed at the crown and invert (66 percent crushup) than at the springlines (45 percent crushup). The final vertical tunnel closure was $\Delta D_V/D$ = 5.56 percent and the final horizontal expansion was $\Delta D_H/D$ = -5.14 percent, which is almost as large as the vertical tunnel closure.

Figure 6-12 shows the results of a similar test on an a/h = 12.5 liner with backpacking. The peak vertical load was P_V = 26,000 psi (179 MPa) and the peak horizontal load was P_H = 10,950 psi (75.5 MPa). Again, the backpacking is more severely crushed at the crown and invert (69 percent crushup) than at the springlines (33 percent crushup). The liner expanded laterally as much as it contracted vertically. The final vertical closure was $\Delta D_V/D$ = 2.22 percent, and the final horizontal expansion was $\Delta D_H/D$ = -2.22 percent.

6.3 Interpretation of Uniaxial-Strain Loading Experiments

Table 6-3 is a summary of the static, uniaxial-strain loading test results. The character of the response of the various structures in saturated rock is essentially the same as that of their counterparts in dry rock. For a more quantitative comparison of the response of the structures, let us examine tunnel deformation as a function of load. Figure 6-13 shows plots of vertical tunnel closure $\Delta D_V/D$ as a function of vertical pressure P_V for the structures in saturated rock. For the direct-contact liners, we observe that for a given load the tunnel closure decreases as the thickness of the liner increases.

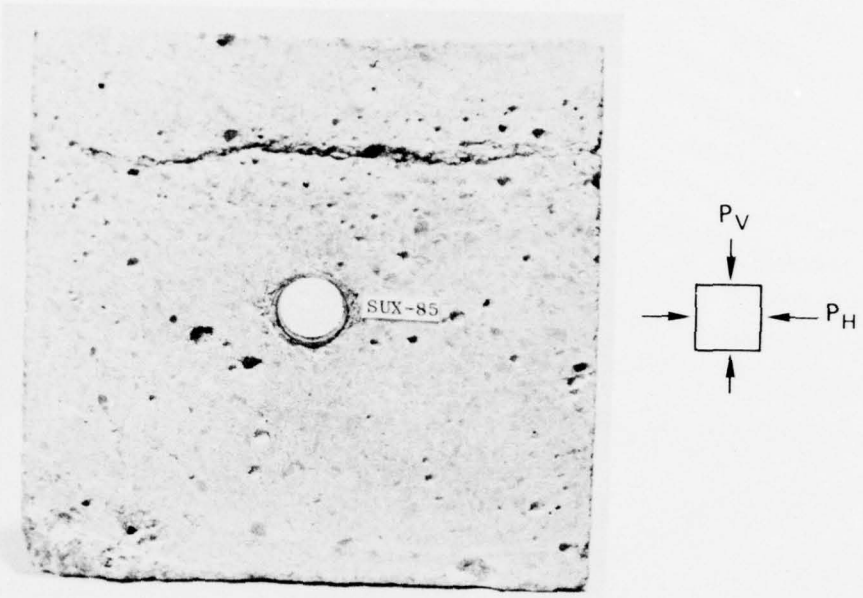

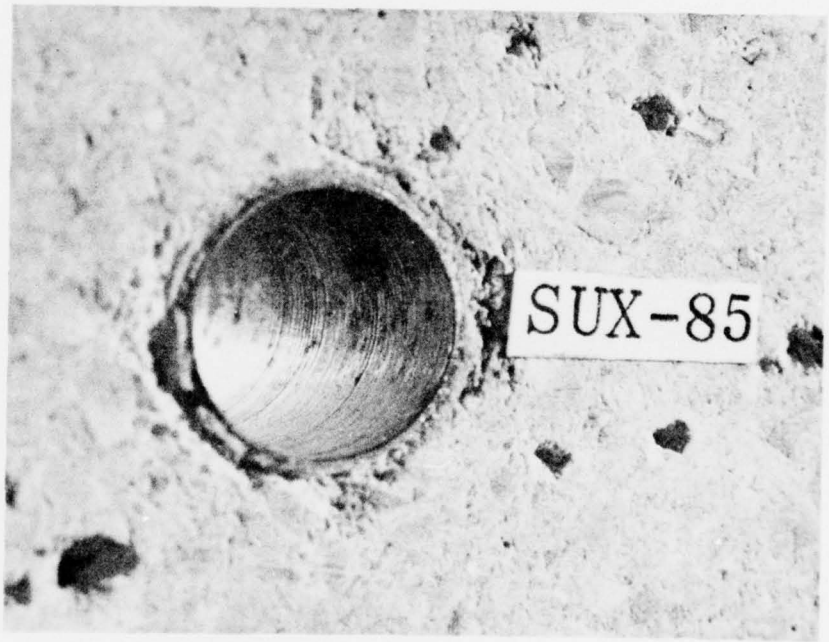

MP-3743-52

FIGURE 6-11 RESPONSE OF A STEEL LINER WITH BACKPACKING IN DRY ROCK TO STATIC, UNIAXIAL STRAIN LOADING—a/h = 25, P_{Vmax} = 24,500 psi, $\Delta D_V/D$ = 0.0556, R/H = 4.5

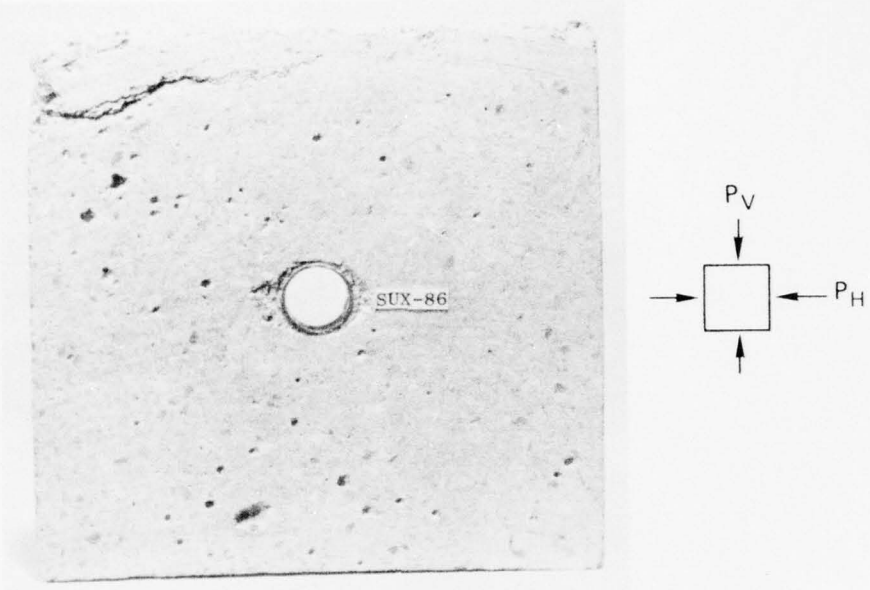

MP-3743-53

FIGURE 6-12 RESPONSE OF A STEEL LINER WITH BACKPACKING IN DRY ROCK TO STATIC, UNIAXIAL STRAIN LOADING—a/h = 12.5, P_{Vmax} = 26,000 psi, $\Delta D_V/D$ = 0.0222, R/H = 4.5

Table 6-3

SUMMARY OF STATIC, UNIAXIAL-STRAIN LOADING TESTS

Saturated Rock Tests

Structure	P_{Vmax} (psi)	P_{Hmax} (psi)	$\Delta D_V/D$ (percent)	$\Delta D_H/D$ (percent)	Comments
Steel a/h = 50	12,000	4,750	11.30	*	Liner moderately buckled at springlines (beginning at $P_V \approx 8000$ psi)
Steel a/h = 25	19,000	8,600	14.70	*	Liner moderately buckled at springlines (beginning at $P_V \approx 13,000$ psi)
Steel a/h = 12.5	16,500	8,300	9.13	-0.96	Liner ovalled but did not buckle.
Steel a/h = 25 with backpacking	22,000	11,400	4.88	-3.21	Liner ovalled. Backpacking crushed more vertically than horizontally.
Steel a/h = 12.5 with backpacking	22,000	10,050	4.00	-3.22	Liner ovalled. Backpacking crushed more vertically than horizontally.

*Springline buckles made D_H measurement impractical.

Table 6-3 (Concluded)

SUMMARY OF STATIC, UNIAXIAL-STRAIN LOADING TESTS

Dry Rock Tests

Structure	P_{Vmax} (psi)	P_{Hmax} (psi)	$\Delta D_V/D$ (percent)	$\Delta D_H/D$ (percent)	Comments
Steel a/h = 50	23,500	9,800	17.50	*	Liner moderately buckled at springlines (beginning at $P_V \approx 6,000$ psi)
Steel a/h = 25	30,000	13,300	20.00	*	Liner moderately buckled at springlines (beginning at $P_V \approx 13,000$ psi)
Steel a/h = 12.5	18,000	6,950	8.80	-2.56	Liner ovalled but did not buckle.
Steel a/h = 25 with backpacking	24,500	10,300	5.56	-5.14	Liner ovalled. Backpacking crushed more vertically than horizontally.
Steel a/h = 12.5 with backpacking	26,000	10,950	2.22	-2.22	Liner ovalled. Backpacking crushed more vertically than horizontally.

*Springline buckles made D_H measurement impractical.

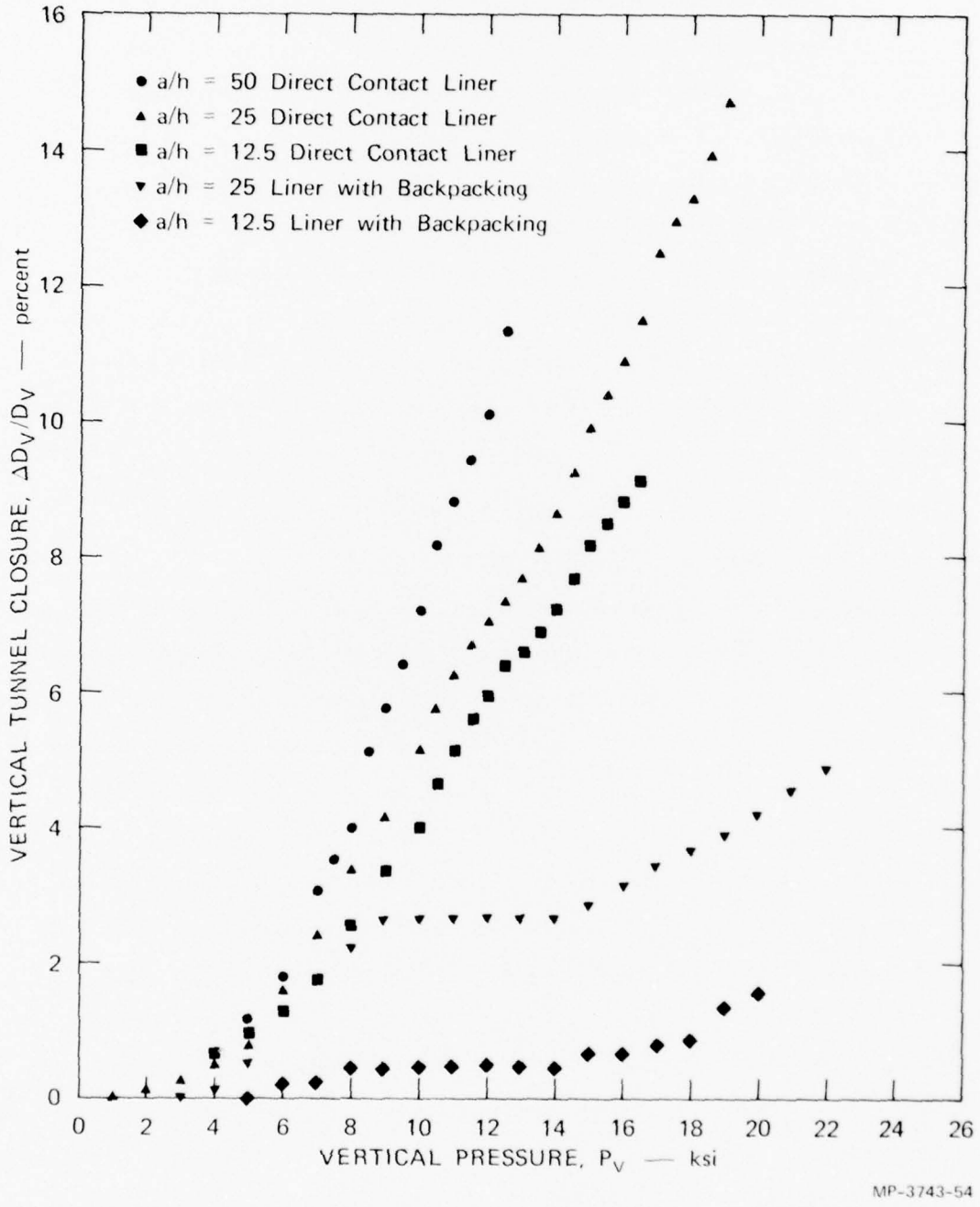

FIGURE 6-13 VERTICAL TUNNEL CLOSURE VERSUS VERTICAL PRESSURE FOR UNIAXIAL STRAIN LOADING OF SATURATED 6B ROCK

However, the difference in closure from one liner to the next is not nearly as great as it was for isotropic loading (Figure 5-11). The apparent reason is that for isotropic loading, the liner resists deformation through hoop compression, which is the most efficient means of resistance for a thin-walled shell. For isotropic loading, the liner carries a significant part of the total load, i.e., the surrounding rock does not carry all the load alone. However, for uniaxial strain loading, the liner resists deformation through a combination of hoop compression and bending, which is a less efficient means of resistance. In this case, the liner carries a smaller part of the load, with the rock carrying the major part. Since the rock carries most of the load, the type of liner used has little effect, and hence, the reduction in deformation from one liner to the next is small compared with a doubling in wall thickness from one liner type to the next.

Liner deformation is reduced substantially when backpacking is added. However, under uniaxial-strain loading, the liners now have deformations of a few percent, in contrast to less than one percent throughout the entire loading range under axisymmetric loading (compare Figures 5-11 and 6-13). The S shape of the load-deformation curves under uniaxial strain loading (Figure 6-13; the deformation rises, then remains at a plateau, and then rises again) is probably a reflection of the shape of the stress-strain curve of the foam as it crushes. During early deformation the finite initial modulus of the foam gives rise to a radial stress difference around the circumference of the steel liner as the rock cavity closes asymmetrically under uniaxial-strain loading. This causes the liner to deform into an oval shape. At larger cavity closures, this stress difference can no longer increase because the foam begins to crush at constant stress at the crown and invert, where the rock closure is largest. Thus, during this period the curve has a plateau, where the steel liner deformation remains constant as the external loading increases, even though the rock cavity continues to close. At still larger external loading and rock closure, the foam begins to

lock up so that the stress again rises and the steel liner once again deforms with increasing load.

This sequence of events is consistent with the plateaus in Figure 6-13 extending over the same loading range for both the a/h = 12.5 and a/h = 25 liners, but with the plateau at a larger deformation for the a/h = 25 liner. Being thinner, the a/h = 25 liner must oval more than the a/h = 12.5 liner to resist the stress difference around its circumference. We would expect these plateaus of deformation to be reduced for a foam with more nearly rigid-perfectly plastic stress-strain behavior (as in cellular concrete), rather than elastic-plastic behavior (as in the polyurethane foam used here).

Similar plots for the structures tested in dry rock are shown in Figure 6-14. The general behavior of the structures in dry rock is similar to that in saturated rock, and the same conclusions hold.

We will now compare the response of the individual structures tested with the three types of loading: uniaxial strain loading in saturated and dry rock and isotropic loading in saturated rock. Figure 6-15 shows plots of vertical tunnel closure versus vertical pressure for direct contact liners with a/h = 50. For uniaxial strain loading, reduction in deformation is significant in the dry rock results as compared to the saturated rock (compare the open and closed circles). This is because the dry rock maintains a larger friction angle at high load than does the saturated rock. Comparison of the uniaxial-strain and isotropic loading results for saturated rock (solid circles and triangles) shows that deformation is considerably smaller under isotropic loading. The load required to cause 5 percent tunnel closure under isotropic loading is P_V = 12,000 psi (82.7 MPa). while under uniaxial-strain loading it is P_V = 8,500 psi (58.6 MPa). Thus, for the a/h = 50 liner, the reduction in load-carrying capacity between isotropic loading and uniaxial strain loading is about 30 percent.

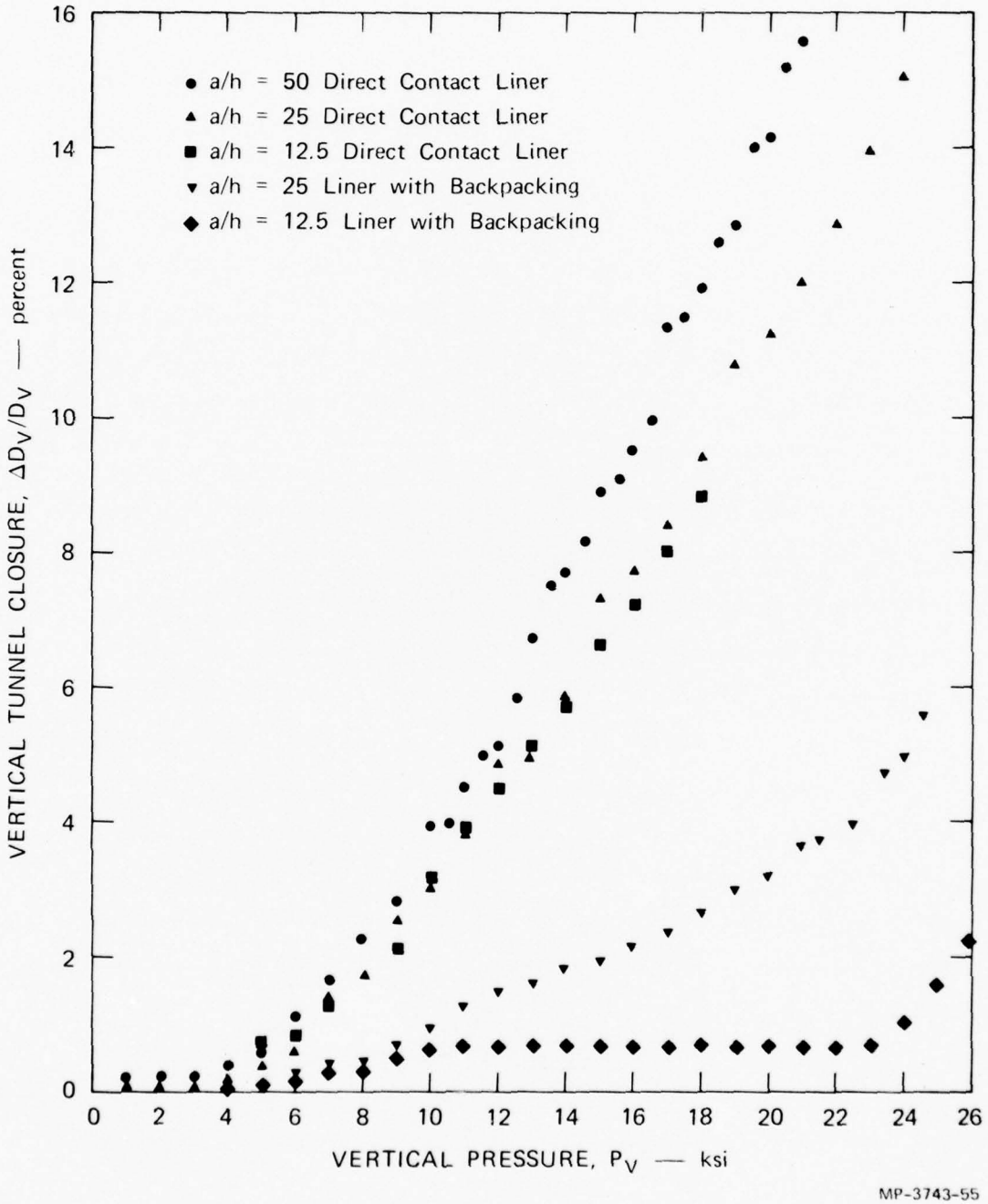

FIGURE 6-14 VERTICAL TUNNEL CLOSURE VERSUS VERTICAL PRESSURE FOR UNIAXIAL STRAIN LOADING OF DRY 6B ROCK

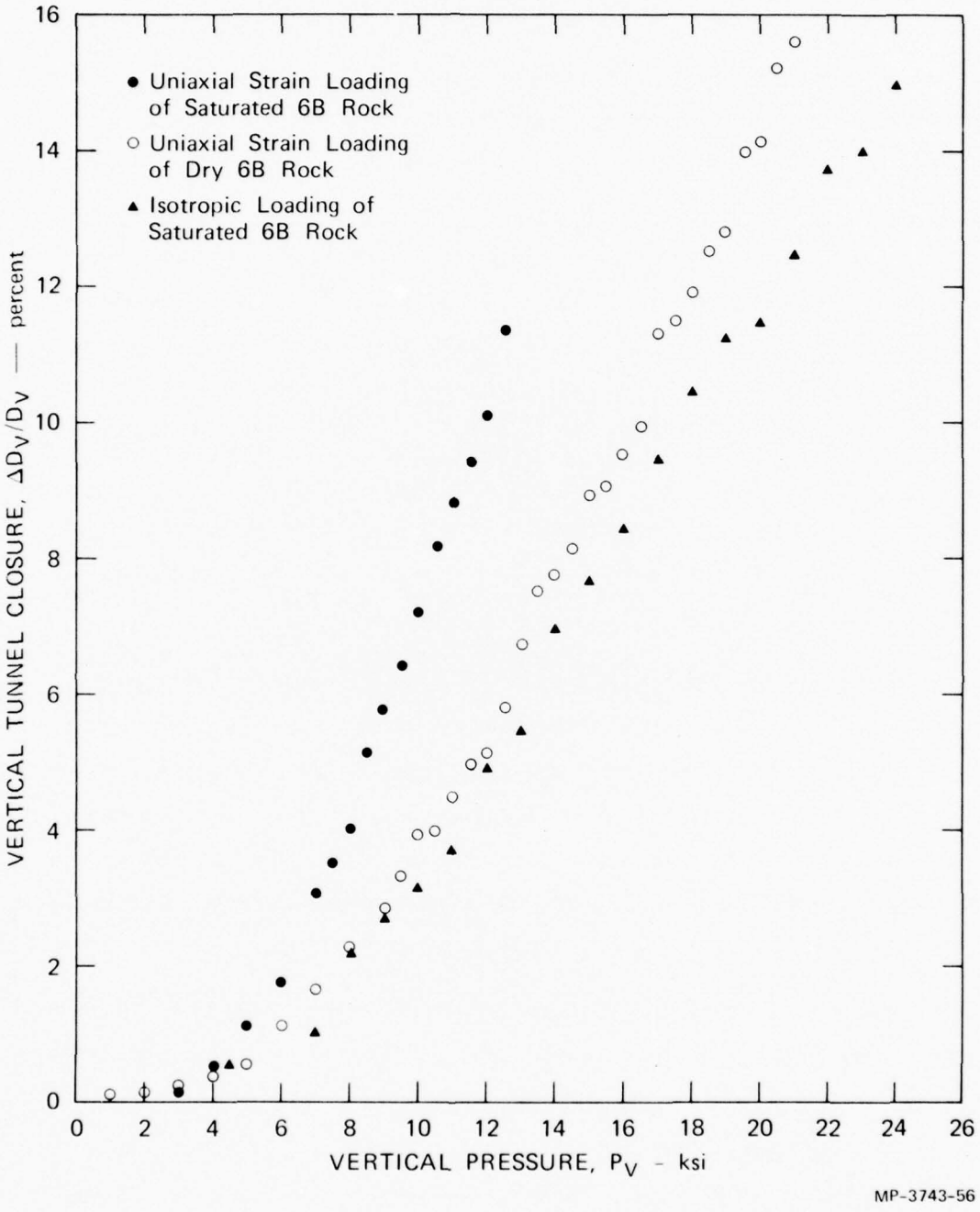

FIGURE 6-15 VERTICAL TUNNEL CLOSURE VERSUS VERTICAL PRESSURE FOR a/h = 50 DIRECT CONTACT LINER

Figure 6-16 shows similar comparisons for the direct contact liner with a/h = 25. We observe a pattern similar to the results for the a/h = 50 liner. The main difference is that with the thicker liner the separation between the isotropic and uniaxial strain loading curves is wider than before. The load required to cause 5 percent closure under isotropic loading is P_V = 18,000 psi while under uniaxial strain loading it is P_V = 10,000 psi (68.9 MPa). Thus, for the a/h = 25 liner, the reduction in load-carrying capacity is about 45 percent between isotropic loading and uniaxial-strain loading (compared with 30 percent for the a/h = 50 liner). This result is another aspect of the increased efficiency of liners under isotropic loading as compared with uniaxial-strain loading. Thus, as the hoop strength of the liner becomes more significant compared to the strength of the rock (a/h decreases), the difference in critical loads between isotropic and uniaxial-strain loading becomes larger.

Figure 6-17 shows the curves for the direct contact liner with a/h = 12.5. The same trend noted above in going from a/h = 50 to a/h = 25 continues here also. The load required for 5 percent closure under isotropic loading is P_V = 24,000 psi (116.5 MPa) while under uniaxial-strain loading it is P_V = 11,000 psi (75.8 MPa). This is a 55 percent reduction in load-carrying capacity (compared with 45 percent for a/h = 25 and 30 percent for a/h = 50).

Figure 6-18 shows the results for the backpacked liner with a/h = 25. As for direct contact liners, the tunnel closure for a given load under uniaxial strain loading in the dry rock is less than in the saturated rock since the dry rock is stronger at high loads. The peculiar "hump' in the curve between P_V = 5000 psi (34.5 MPa) and P_V = 14,000 psi (96.5 MPa) in the saturated rock is not expected. This anomalous behavior could be due to a crack running horizontally through

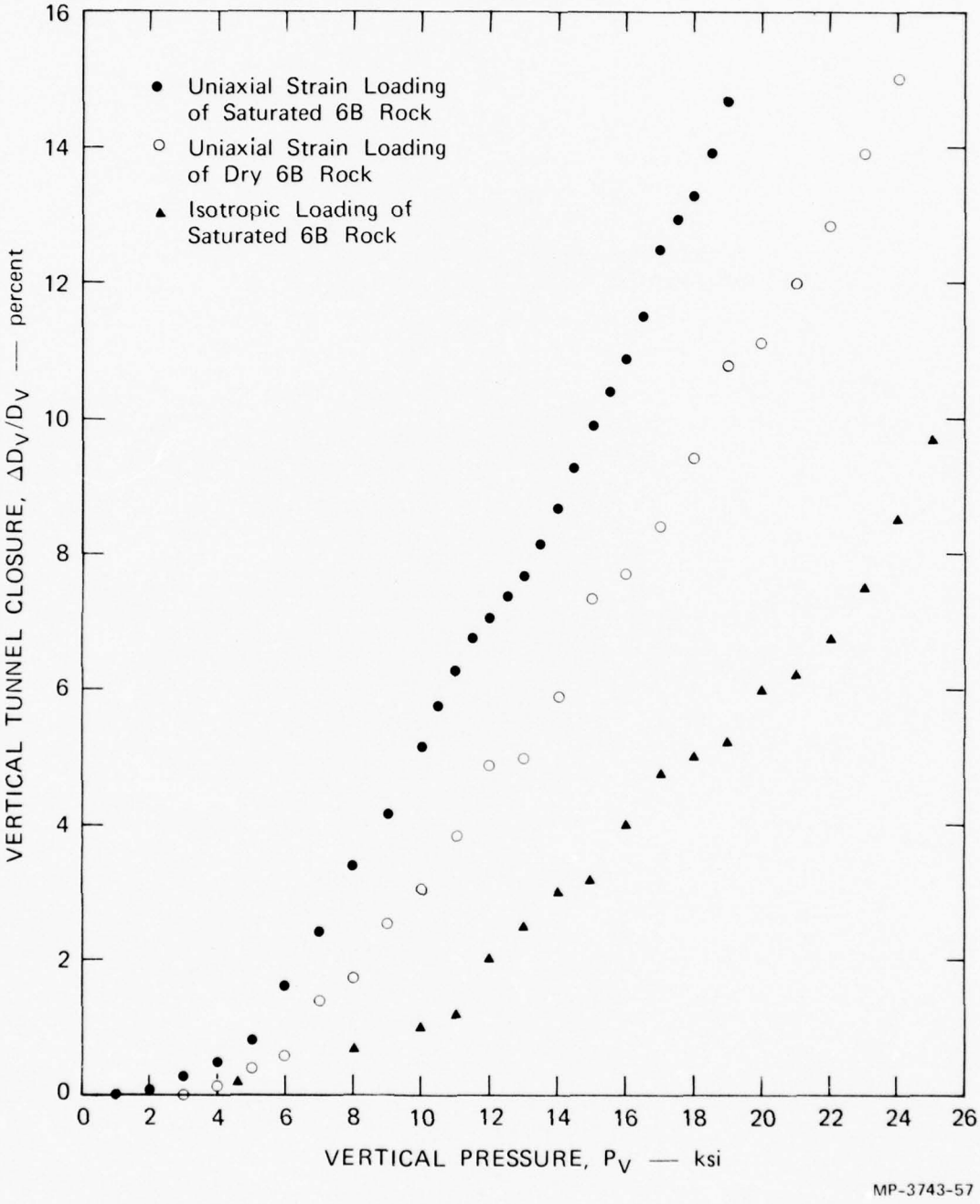

FIGURE 6-16 VERTICAL TUNNEL CLOSURE VERSUS VERTICAL PRESSURE FOR a/h = 25 DIRECT CONTACT LINER

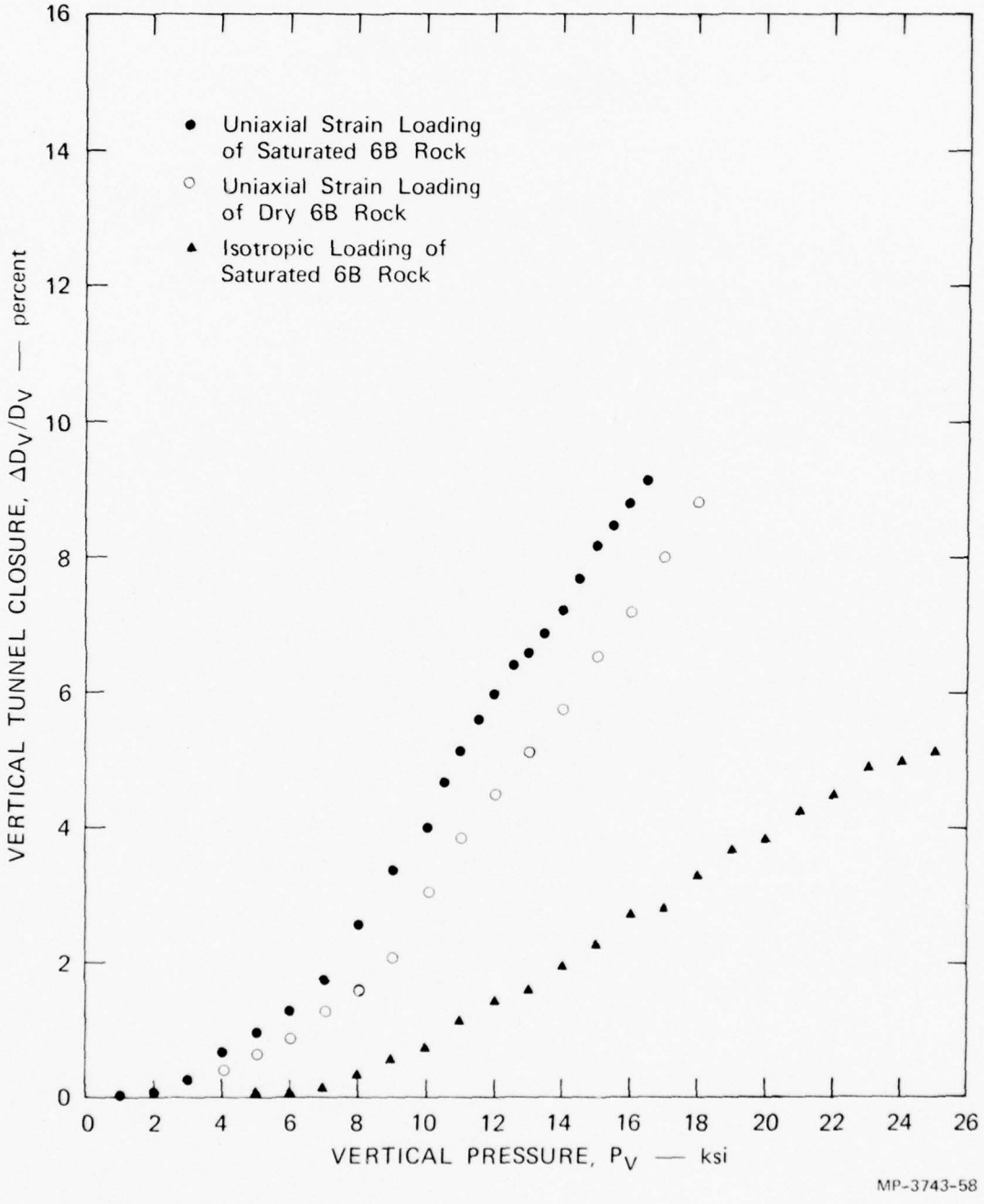

FIGURE 6-17 VERTICAL TUNNEL CLOSURE VERSUS VERTICAL PRESSURE FOR a/h = 12.5 DIRECT CONTACT LINER

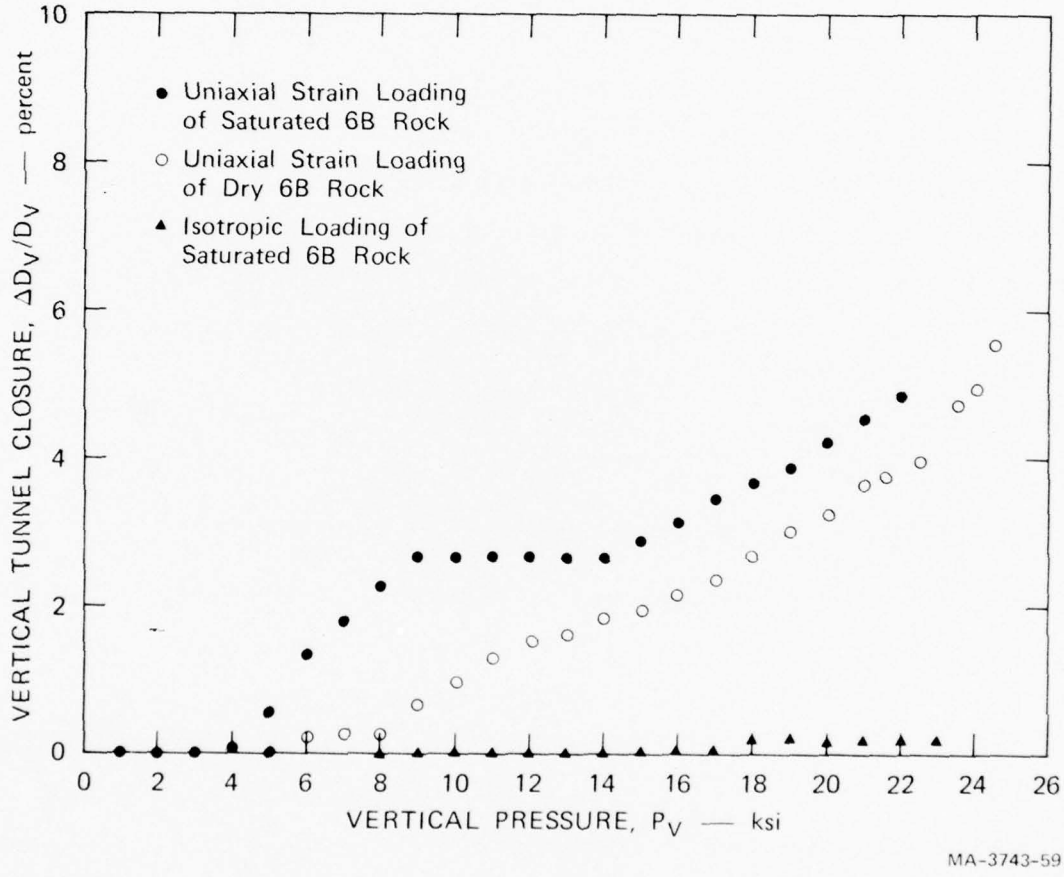

FIGURE 6-18 VERTICAL TUNNEL CLOSURE VERSUS VERTICAL PRESSURE FOR a/h = 25 LINER WITH BACKPACKING

the specimen, which was discovered after sectioning (see Figure 6-11). The uniaxial-strain loading deformations of the backpacked liners in both the saturated and dry rock are below 5 percent for vertical load up to 22,000 psi (152 MPa). Under isotropic loading the closure is less than 1 percent out to this same load.

Figure 6-19 shows the curves for the backpacked liner with a/h = 12.5. The response of the liner in this case is similar to that for the a/h = 25 liner with backpacking. Here, tunnel closure is less than 2 percent for a load up to 20,000 psi (138 MPa) under uniaxial strain loading. It appears that lockup occurs sooner in the liner in saturated rock since its slope steepens at P_V = 18,000 psi (124 MPa) while the slope of the liner in dry rock stays relatively flat out to P_V = 23,000 psi (159 MPa). The deformation of the backpacked liner under isotropic loading is negligible.

6.4 Static, Cyclic, Uniaxial Strain Loading Test Results

In Section 5.5 we described the results of a static, cyclic, isotropic loading test on an a/h = 12.5 steel-lined tunnel in dry 6B rock. We found that the final deformation of the tunnel was not seriously affected by repeated unloading and reloading. In this section, we present the results of a similar test with cyclic uniaxial-strain loading rather than cyclic isotropic loading.

The results of this test are shown in Figure 6-20, where vertical tunnel closure $\Delta D_V/D$ is plotted against vertical pressure P_V. Behavior is very similar to that for isotropic loading. The main difference is that lower pressures are required to produce a given amount of tunnel closure because the loading is asymmetric. During the initial loading to a pressure P_V = 9.5 ksi (65.5 MPa), the tunnel closure reached 2.25 percent. Upon unloading to 1.1 ksi (7.58 MPa), the tunnel expanded

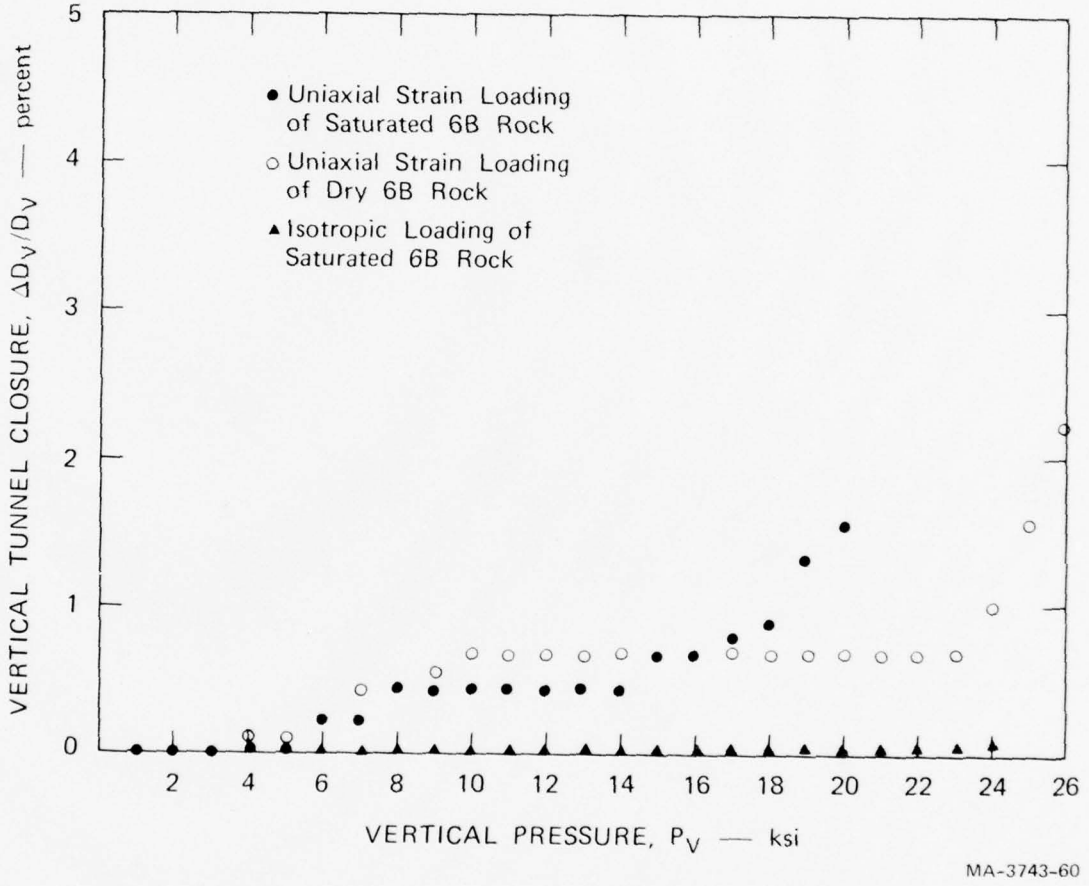

FIGURE 6-19 VERTICAL TUNNEL CLOSURE VERSUS VERTICAL PRESSURE FOR a/h ~12.5 LINER WITH BACKPACKING

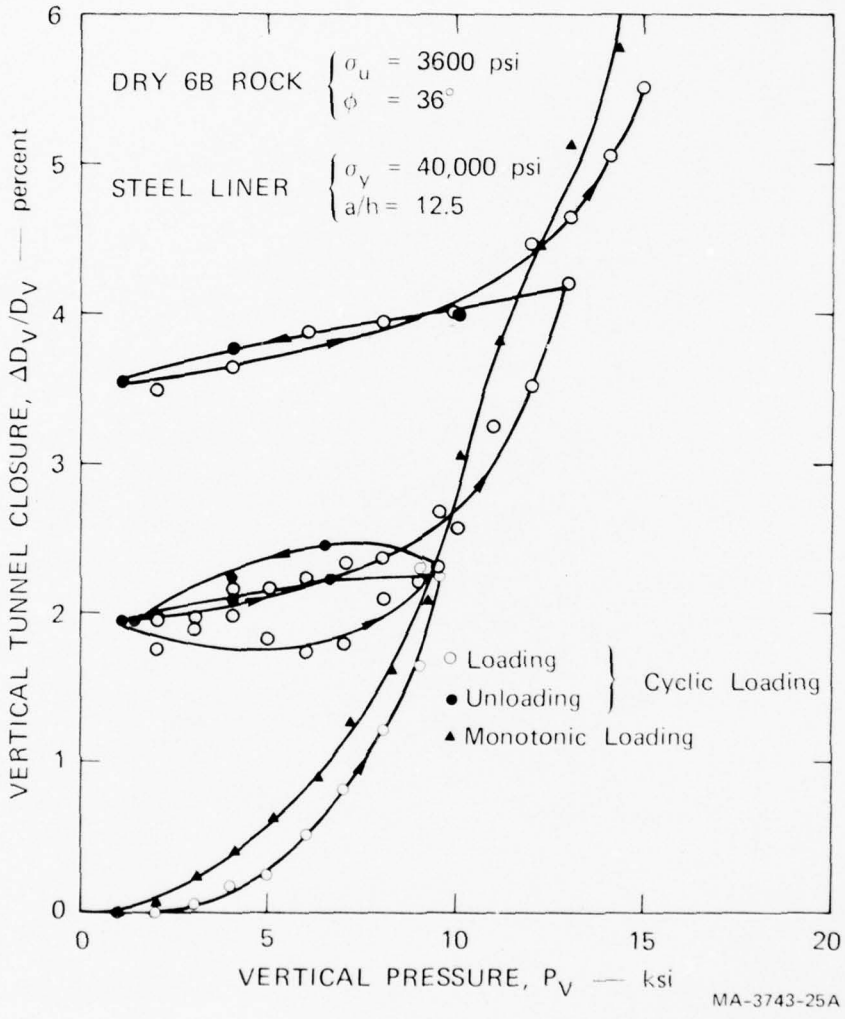

FIGURE 6-20 COMPARISON OF CYCLIC AND MONOTONIC LOADING TEST RESULTS— UNIAXIAL STRAIN LOADING

slightly to a closure of 1.95 percent. Reloading to 9.5 ksi (65.5 MPa) brought the closure to 2.35 percent, a very slight additional strain. Unloading and reloading again produced only a small additional strain. Similar behavior was observed for unloading and reloading in the vicinity of 4 percent closure. Also shown on this plot are the monotonic loading test results. The loading part of the cyclic loading results is very close to that of the monotonic loading results. We again conclude that the final deformation of the tunnel was not seriously affected by repeated unloading and reloading and that the tunnel closure system "shakes down".

7. DINING CAR STRUCTURES EXPERIMENT

In this chapter, we summarize the planning and fielding of larger scale structures as an add-on to the Dining Car event at the Nevada Test Site (NTS). Planning and fielding were done on the present contract. Posttest recovery and interpretation were performed on Contract DNA001-75-C-0245. A detailed discussion of this experiment is given in Dining Car POR 6887.

Dining Car provides a relatively low cost opportunity for a structures experiment add-on because it has two crosscut tunnels between the main line-of-sight (LOS) pipe and the access tunnel at ranges having pressures of about 0.6 and 0.9 kbar (60 and 90 MPa) (Figure 7-1). The width of the crosscut tunnels is about 5 feet (1.52 m) and the total length available for add-on models is about 100 feet (30.5 m). Thus, reasonably large models at pressure levels of interest can be fielded with virtually no additional tunneling cost.

7.1 Structures and Objectives

The native rock that surrounds these crosscut tunnels is NTS tuff, estimated to have an unconfined compressive strength of 1000-2000 psi (6.89-13.88 MPa) and a friction angle of about 5 degrees (0.087 rad). Because it is so weak, and more important, has a low friction angle, tuff has undesirable strength properties for deep basing. (However, it has the desirable property of high porosity and hence high shock attenuating ability.) To study response in higher strength rock, more representative of rock to be found at some potential deep base sites, the approach in the SRI add-on experiment was to field structure models in a rock simulant. The rock simulant 6B has been selected to be only of intermediate strength [unconfined compressive strength about 4300 psi (29.6 MPa)] so that demanding tests can be made on tunnel designs at the available 0.6 and

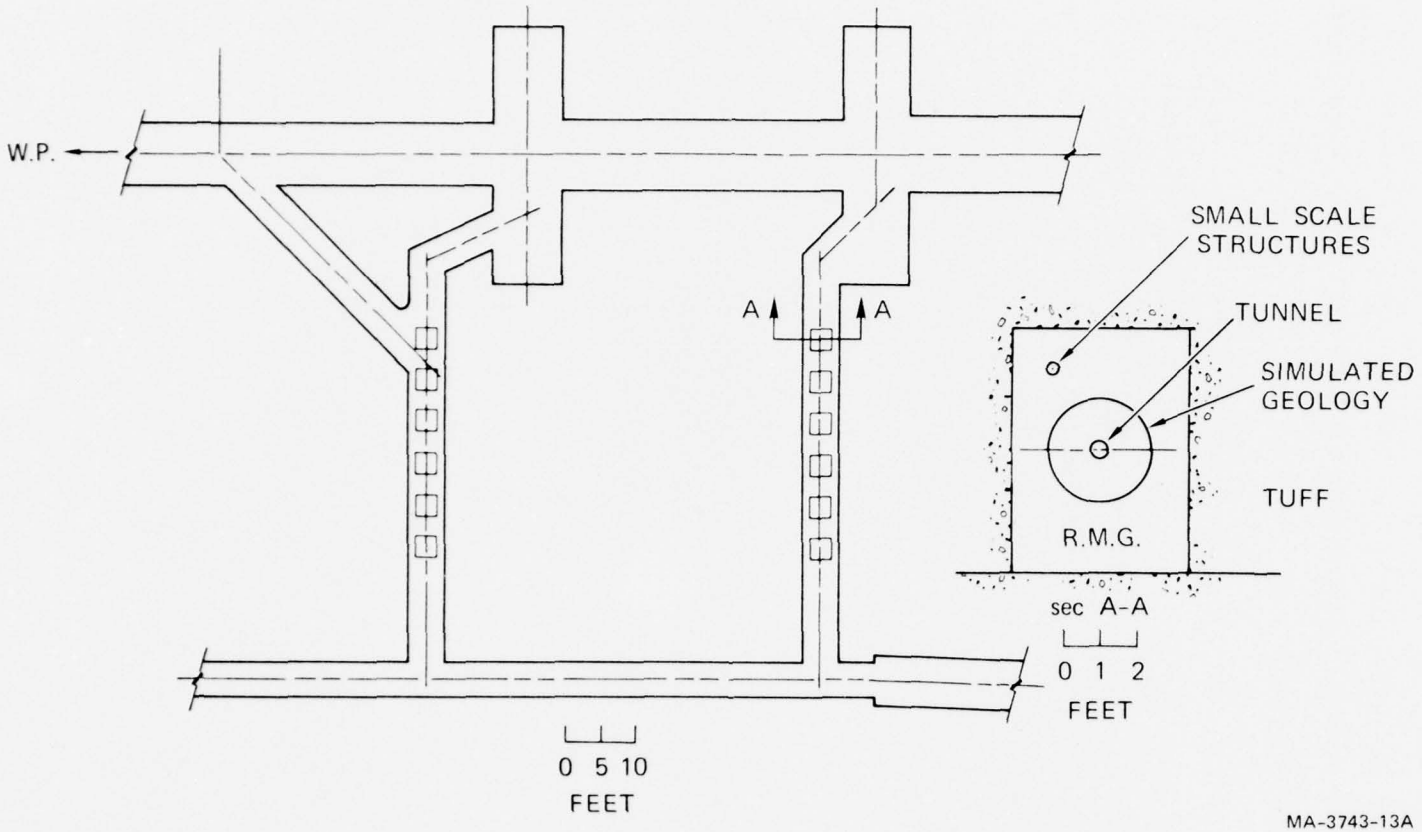

FIGURE 7-1 EXPERIMENTAL LAYOUT IN DINING CAR CROSSCUTS

0.9 kbar (60 and 90 MPa) levels predicted at the structure locations. However, unlike that of tuff, the friction angle is 33 degrees (0.576 rad) so that the crucial strengthening interaction between tunnel pressure and rock response with high friction can be investigated.

The rock simulant for each tunnel structure is 3 feet in diameter and 3 feet long (Figure 7-2). Tunnels are 6 inches (15.2 cm) in diameter, running the full 3-foot (0.914 m) length of the rock simulant so that both rock specimen-to-tunnel diameter and tunnel length-to-diameter ratio are equal to 6, large enough to make boundary effects small. As a direct tie-in to laboratory tests on smaller scale structures [5/8-inch (1.59 cm)-diameter tunnels], each 6-inch (15.2 cm)-diameter tunnel has a corresponding 5/8-inch (1.59 cm) diameter tunnel also fielded. The smaller scale specimens consist of 4-inch (10.2 cm)-diameter by 4-inch (10.2 cm)-long rock simulant cylinders.

Six different structures plus their small-scale counterparts were fielded in each of the crosscuts. The first structure is an unlined tunnel. Next are three tunnels with direct-contact steel liners of different radius-to-thickness ratios (a/h = 12.5, 25, 50). Finally, two structures with backpacking (R/H = 4.5) as well as tunnel liners (a/h = 12.5 and 25) were fielded to investigate the effect of backpacking in preventing tunnel closure. A summary of the structures fielded and their objectives is given in Table 7-1. Dimensions of the structures are given in Table 7-2.

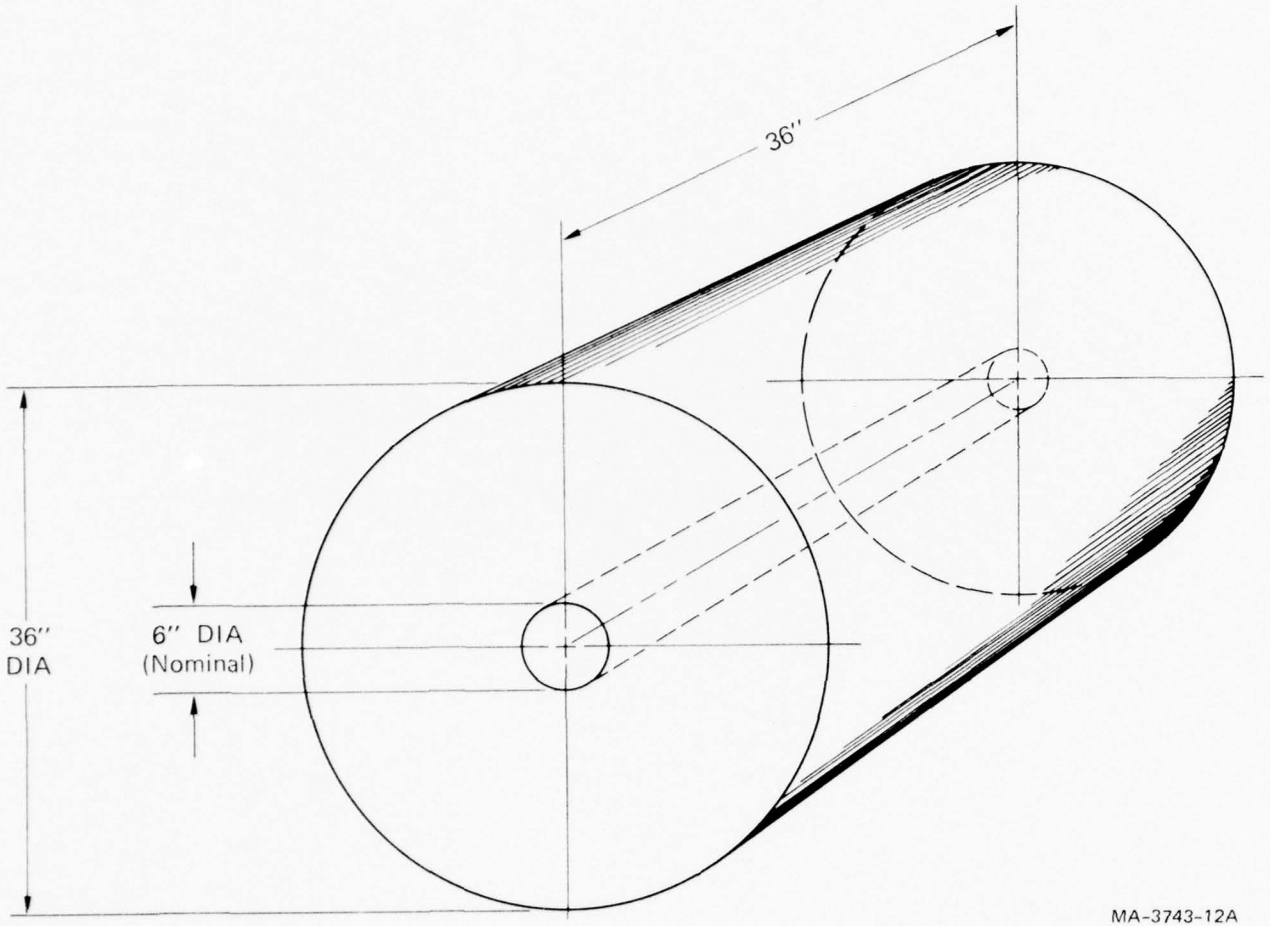

FIGURE 7-2 SCALE MODEL TUNNEL IN SIMULATED INTACT GEOLOGY

Table 7-1

DINING CAR ADD-ON STRUCTURES

Identical sets in crosscuts 1 and 2 to examine response at two loading levels.

Structures*	Objective
1 Unlined tunnel	Baseline rock specimen and tunnel response--moderate to severe closure expected
3 ea. Lined in direct contact, with a/h = 50, 25, 12.5 steel liners.	Effect of internal pressure $p_i = \sigma_y$ h/a. Bracket a/h for monocoque tunnel buckling (if it occurs)
2 ea. Liners with backpacking with a/h = 50 and 25 steel liners.	Effect of backpacking by comparison with direct contact liners
6 ea. Small-scale counterparts of above 6 tunnels at 5/8-inch size	Inexpensive tie-in to above-ground tests with smaller-scale models

*Total number of structures = 6 large (6-inch-diameter tunnels) and 6 small (5/8-inch-diameter tunnels) at each crosscut.

Table 7-2

DIMENSIONS OF LINERS

6-inch-diameter Structures

Structure	Steel Liner		Backpacking		Rock Cavity Diameter (in.)
	I. D. (in.)	Wall (in.)	I. D. (in.)	Wall (in.)	
Unlined tunnel	--	--	--	--	6.00
Contact liner	5.87	0.062	--	--	6.00
Contact liner	6.00	0.125	--	--	6.25
Contact liner	6.00	0.250	--	--	6.50
Backpacked liner	6.00	0.125	6.25	1.00	8.25
Backpacked liner	6.00	0.250	6.50	1.00	8.50

5/8-inch-diameter Structures

Structure	Steel Liner		Backpacking		Rock Cavity Diameter (in.)
	I. D. (in.)	Wall (in.)	I. D. (in.)	Wall (in.)	
Unlined tunnel	--	--	--	--	0.625
Contact liner	0.625	0.006	--	--	0.637
Contact liner	0.625	0.0125	--	--	0.650
Contact liner	0.625	0.025	--	--	0.675
Backpacked liner	0.625	0.0125	0.650	0.112	0.875
Backpacked liner	0.625	0.025	0.675	0.100	0.875

8. THEORETICAL ANALYSIS

In this chapter, we discuss the theoretical effort that supported the planning and interpretation of our experiments. This effort is based primarily on the use of an analysis described in [1] for elastic-plastic response of a cylindrical cavity in an infinite body subjected to axisymmetric loading. The solid is assumed to follow the Mohr-Coulomb yield criterion and its associated flow rule. A summary of this analysis is given in Appendix A.

This chapter includes a discussion of the effect of dilatancy, the predicted closures of the structures in the Dining Car experiment, a design approach for yielding structures, and a discussion of the effect of a liner on the fracture pattern around a cavity.

8.1 Effect of Dilatancy

The theoretical prediction of the deformations in the Dining Car experiment is based on an elastic-plastic analysis using the Mohr-Coulomb yield criterion. Employing the flow rule associated with this criterion to compute the displacements results in a volume expansion of the yielded material during plastic flow. This behavior is called dilatancy. Dilatancy is observed to occur in rock, but not necessarily to the extent predicted by the simple Mohr-Coulomb yield and flow rule. To examine the other extreme, dilatancy can be eliminated in the theory by using a nonassociated flow rule; i.e., by assuming that the plastic material is incompressible.*

* There is no theoretical basis for this assumption, but it does give an extreme.

Figure 8-1 compares the theory with and without dilatancy, and with the laboratory experiments discussed in Section 5.1. The dark triangles are data points from the a/h = 25 direct contact liner, and the hollow squares are from the a/h = 12.5 direct contact liner. Since the thinner liner buckled slightly (liner buckling is not considered in the analysis), the a/h = 12.5 liner results provide a more reliable comparison with the theory. We see that for both liners the theoretical predictions underestimate the amount of tunnel closure. However, the theory that includes dilatancy is considerably closer to the experiment than the theory without dilatancy. For example, at P_o = 24,000 psi (165 MPa), the experimental closure of the a/h = 12.5 liner is 4.9 percent; the theory with dilatancy predicts 4.2 percent; and the theory without dilatancy predicts 2.8 percent. The difference between experiment and theory without dilatancy is three times as large as the difference with dilatancy. However, before one theory can be chosen as better than the other, more extensive comparisons should be made to determine the extent to which the differences are caused by other errors (e.g., in material parameters such as E and ϕ). Nevertheless, in all the analyses that follow, the theory with dilatancy is used.

8.2 Dining Car Predictions

8.2.1 Stress Amplification in the Dining Car Experiment

The SRI structures tested in the Dining Car experiment consisted of 3-foot (0.914 m)-diameter cylinders of 6B rock simulant with 6-inch (0.152 m)-diameter tunnels running through the center along the axis of the rock cylinder. These rock models were placed in the DAC crosscuts and then the volume between the 6B rock and the crosscut wall was filled with a Husky Ace rock-matching grout (HARM grout). Because the 6B rock is stiffer and stronger than the tuff and HARM grout that

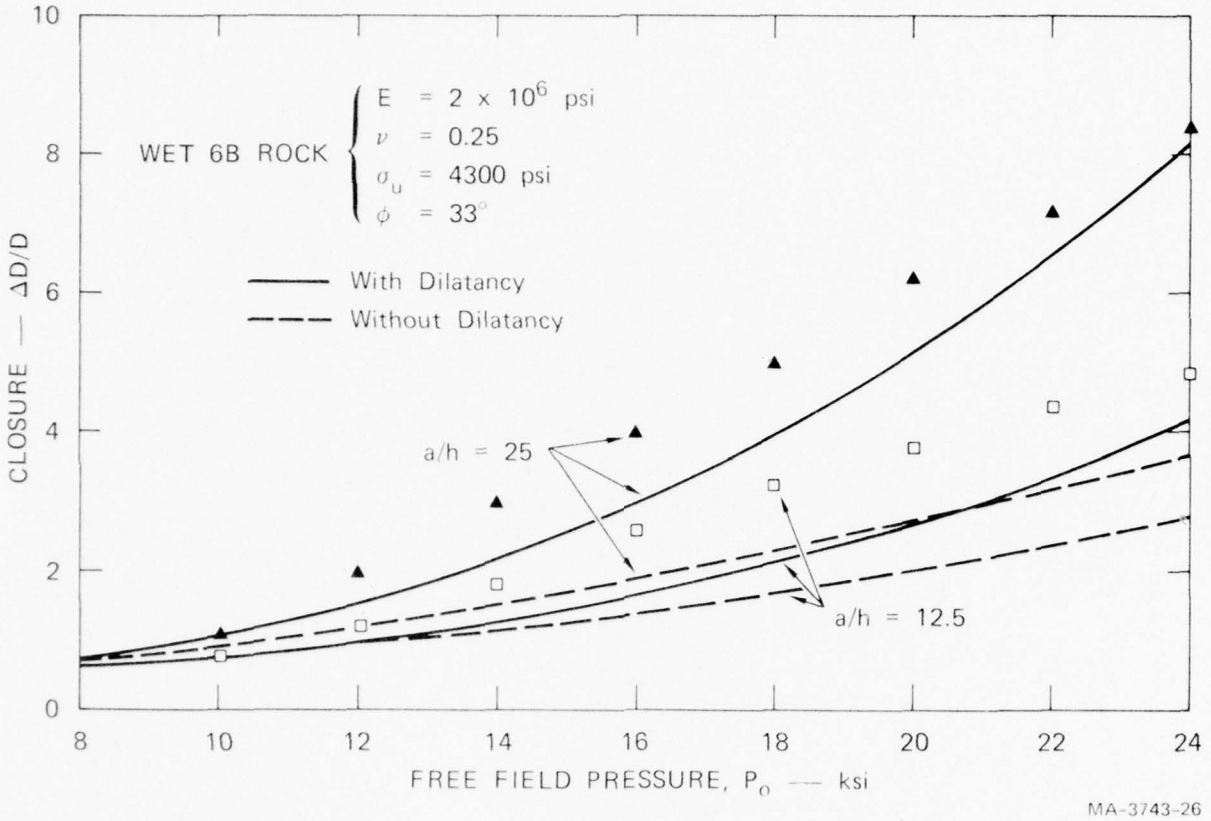

FIGURE 8-1 COMPARISON OF THEORY AND EXPERIMENT FOR PREDICTED CLOSURE OF A TUNNEL AS A FUNCTION OF FREE FIELD PRESSURE

surround it, a free field pressure P_o in the tuff will cause an amplified pressure P_I at the interface between the 6B rock and the grout. The amount of amplification will depend on the relative properties of the 6B rock, the tuff, and the HARM grout.

To estimate this amplification, an elastic-plastic analysis was performed on a model consisting of a cylinder of 6B rock surrounded by an infinite body of tuff subjected to a free field pressure P_o, as shown in Figure 8-2(a). (The HARM grout between the 6B rock and the tuff was assumed to be identical to tuff to simplify the analysis.) Both materials were assumed to follow the Mohr-Coulomb yield criterion, so that the 6B rock had a plastic region extending to R_R, and the tuff had a plastic region extending to R_T, as Figure 8-2(b) shows. Each material was treated separately, with the interface pressure P_I being unknown. P_I was found by an iterative procedure in which P_I was adjusted by regula falsi until the 6B rock and tuff displacements were equal at the interface.

Figure 8-3 shows a plot of P_I versus P_o for a weak and a strong tuff. These strength values of tuff [10] represent lower and upper bounds for tuff in the vicinity of the Dining Car tunnels at NTS. Curves are drawn for values of Poisson's ratio ν = 0.25, 0.35, and 0.45. The amount of amplification decreases appreciably with increasing tuff strength or increasing Poisson's ratio. Reasonable values of Poisson's ratio would probably be between ν = 0.25, and 0.35. Thus, at P_o equal to 1.0 kbar (14,500 psi or 100 MPa), P_I would equal 14,900 psi (102 MPa) for strong tuff with ν = 0.35 and 18,400 psi (127 MPa) for weak tuff with ν = 0.25. The amplification falls between about 2.8 percent and 27 percent, with 15 percent being an average value.

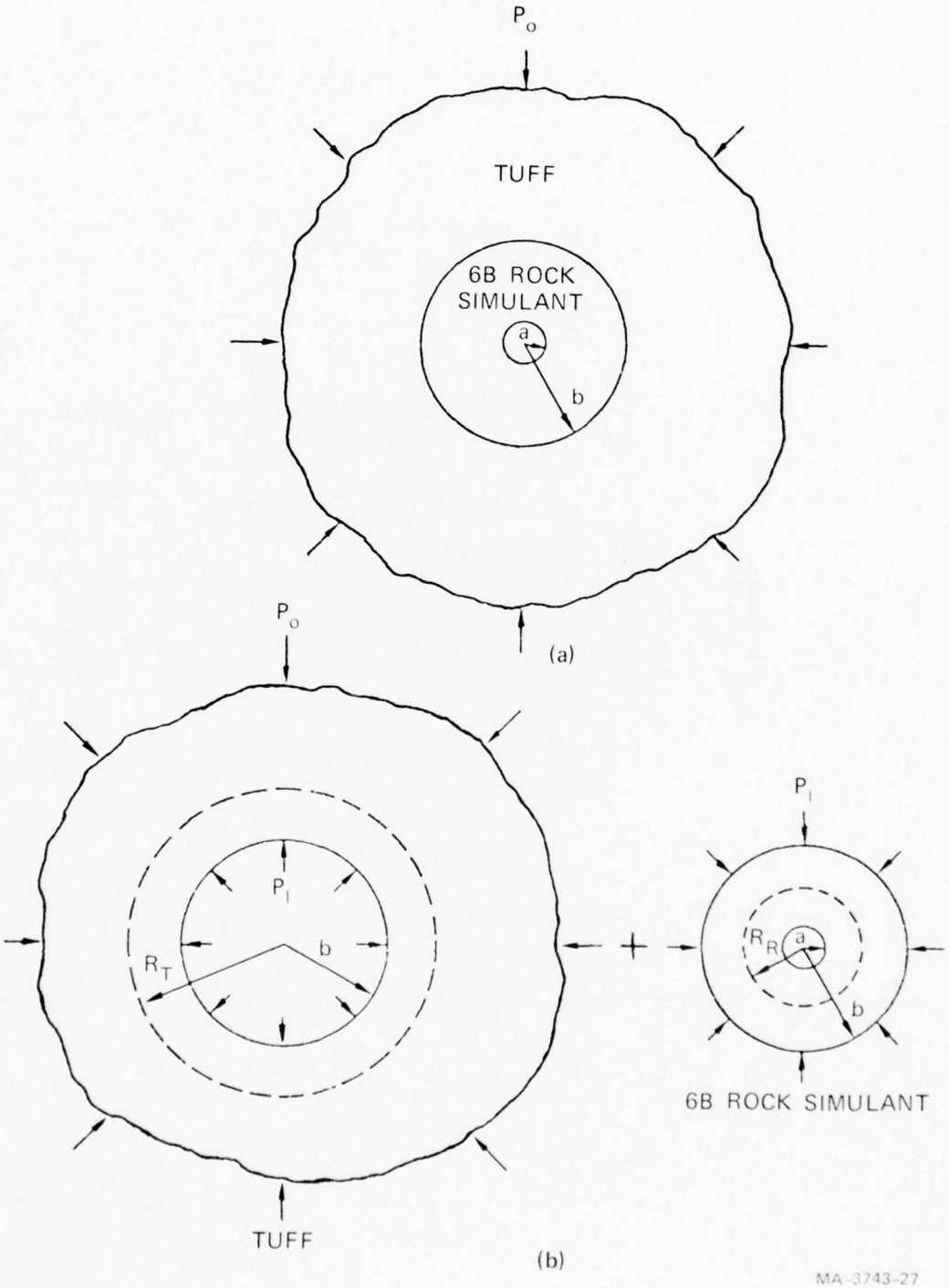

FIGURE 8-2 ELASTIC-PLASTIC ANALYSIS OF A COMPOSITE CYLINDER

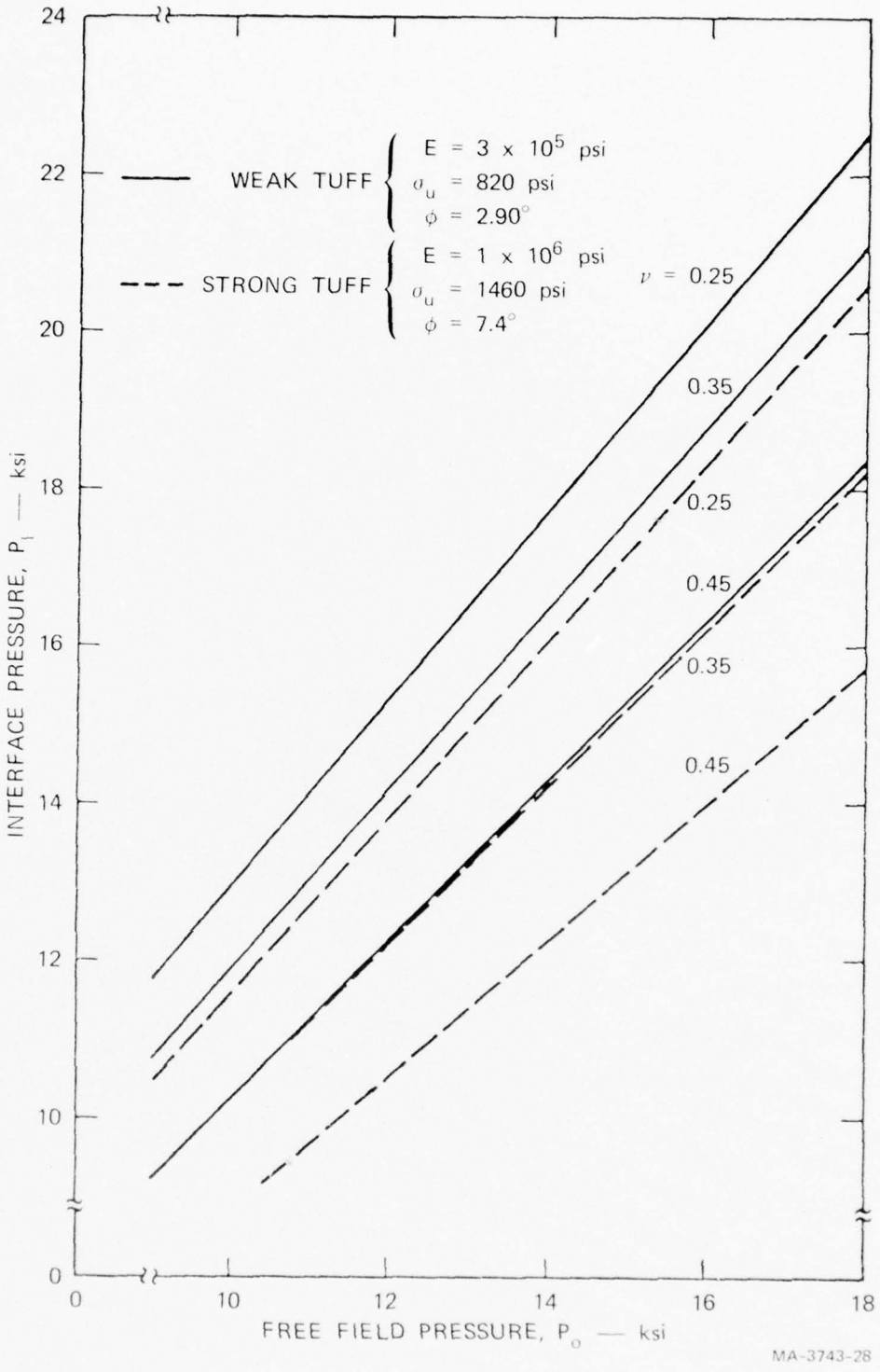

FIGURE 8-3 STRESS AMPLIFICATION AROUND DINING CAR STRUCTURES

8.2.2 Predicted Closure of Structures

The elastic-plastic analysis was used to compute the predicted closure of the Dining Car structures, and these results were compared with the experiments described in Section 5.1. The analysis was completed and reported in Progress Letter No. 2 (March, 1975) before the experiments were performed. The result is repeated here in Figure 8-4, which gives a plot of closure $\Delta D/D$ versus external pressure P_o for various internal pressures P_i. A value $P_i = 0$ corresponds to an unlined tunnel, $P_i = 833$ psi (5.74 MPa) corresponds to a liner with $a/h = 50$, $P_i = 1667$ psi (11.5 MPa) corresponds to a liner with $a/h = 25$, and $P_i = 3333$ psi (23.0 MPa) corresponds to a liner with $a/h = 12.5$. The experimental results are plotted for the $a/h = 50$ liner (the dark circles), for the $a/h = 25$ liner (the dark triangles), and for the $a/h = 12.5$ liner (the dark squares). For the $a/h = 25$ liner and the $a/h = 12.5$ liner, the agreement between theory and experiment is surprisingly good. For the $a/h = 50$ liner, the theory underestimates the amount of closure. This is attributed to liner buckling, which caused the internal pressure applied to the cavity wall to be significantly less than the simple hoop yield value used in the calculations. In fact, the $a/h = 50$ data points lie very close to the theoretical curve for $P_i = 0$.

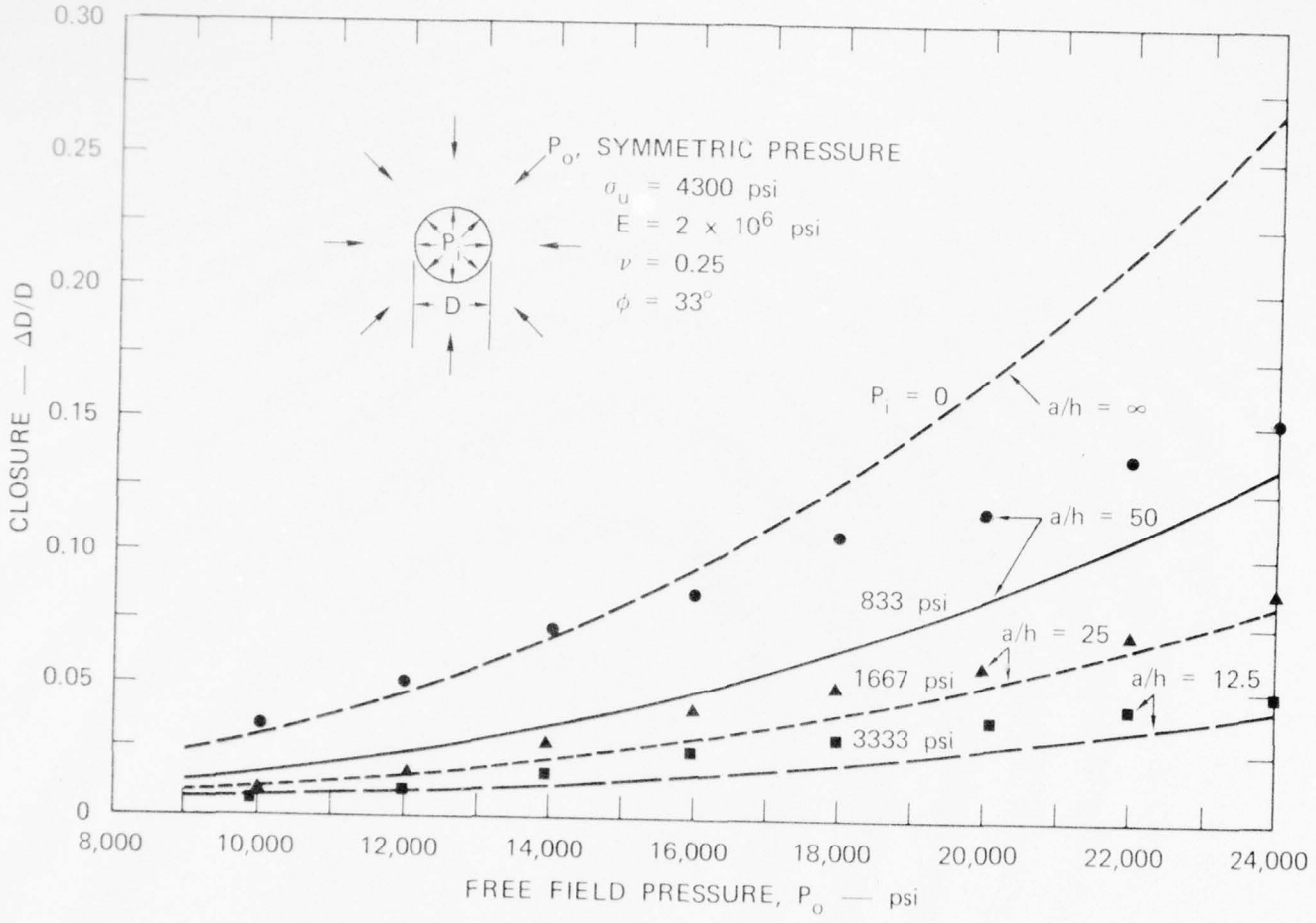

FIGURE 8-4 COMPARISON OF THEORY AND EXPERIMENT FOR PREDICTED CLOSURE OF DINING CAR STRUCTURES AS A FUNCTION OF FREE FIELD PRESSURE

8.3 Design Approach for Yielding Structures

8.3.1 Design Concept

The basic design concept of any yielding structure in rock is illustrated in Figure 8-5. All quantities are drawn to proper relative scale for the example of a structure designed and fielded at a 0.5-kbar (50 MPa) level in nominal tuff. For simplicity throughout the analysis, the load and response are idealized as symmetric around the cylindrical cavity.

The concept consists of allowing the rock cavity to close a small but finite amount, so that the rock yields throughout a plastic zone in the rock, as shown. In the theory, yielding is taken to occur according to the Mohr-Coulomb criterion, characterized by an unconfined compressive strength σ_u and friction angle φ. As more yielding is allowed, the cavity radius becomes smaller and the plastic radius (large dashed circle) becomes larger. The larger plastic radius implies a larger load P_o with no increase in cavity pressure P_i. Thus, full advantage is taken of the rock strength so that a large load P_o can be sustained by a much smaller liner restraining pressure P_i. In the example, the 0.5 kbar (7.25 ksi or 50 MPa) pressure P_o is sustained by a liner pressure of only P_i = 2 ksi by allowing the cavity to close $\Delta R/R$ = 5 percent.

The increase in P_o with increasing plastic radius is easily visualized. Throughout the plastic zone, and in particular at the plastic radius, the radial stress σ_r and tangential stress σ_θ are related by the Mohr-Coulomb yield condition $\sigma_\theta - N\sigma_r = \sigma_u$, where $N = (1 + \sin\varphi)/(1 - \sin\varphi)$. Also, we know that far from the cavity the stress field is homogeneous, $\sigma_\theta = \sigma_r = P_o$, so that $\sigma_\theta - N\sigma_r < \sigma_u$ and no yielding occurs. As the cavity is approached, in the elastic zone σ_r decreases, because at the cavity boundary $\sigma_r = P_i < P_o$, while

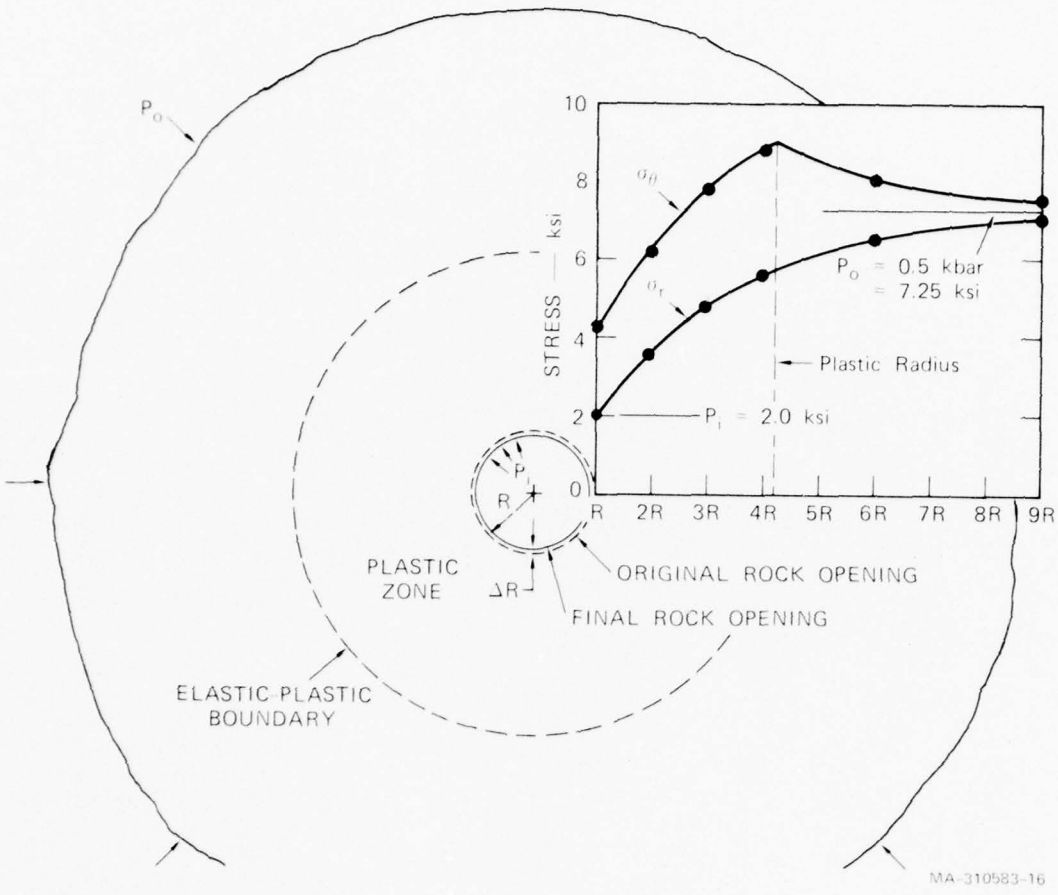

FIGURE 8-5 THE YIELDING STRUCTURE CONCEPT

A large free-field pressure P_o can be sustained by a much smaller liner resisting pressure P_i if the rock opening is allowed to close a small but finite amount ΔR (Geometry of sketch and plot of radial stress versus radius from centerline is for symmetric loading in nominal tuff: σ_u = 1480 psi, ϕ = 7.4°.)

σ_θ increases until yielding occurs at the plastic boundary (see inset graph in Figure 8-5). This is the classical situation for stress concentration around a hole.

Consider now the simple case with no friction, so that $\varphi = 0$ and the yield condition is simply the Tresca condition $\sigma_\theta - \sigma_r = \sigma_u$. Thus, throughout the plastic zone, and at the boundary, the tangential stress remains at a fixed value σ_u higher than the radial stress, regardless of the applied load P_o (so long as it is high enough to cause yielding). Because $\sigma_\theta - \sigma_r$ decreases as one moves to larger radii in the elastic zone, one can now visualize that an increase in P_o (both σ_θ, σ_r, and their difference increase) is accommodated by the plastic boundary simply moving out to a larger radius. In the more general case, with friction, the increased load is even more easily accommodated because then $N > 1$ and the allowable stress difference $\sigma_\theta - \sigma_u$ at yield also increases as P_o increases.

8.3.2 Design Chart for Yielding Structures

From the foregoing discussion we see that the three basic design parameters for a yielding structure are the loading pressure P_o, the structure resisting pressure P_i, and the cavity closure ΔR. For more general asymmetric loading, these are all functions of angle around the structure. The relationships among P_o, P_i, and ΔR are conveniently displayed on a design chart of P_i versus cavity closure with loading pressure P_o as a parameter. Figure 8-6 gives an example chart for 6B rock simulant (a moderately strong rock.) [Competent intact rocks have strengths considerably higher than the unconfined compressive strength of 4300 psi (24.7 MPa) of this rock simulant, but flaws such as joints and faults are expected to reduce their effective strengths to this lower range.]

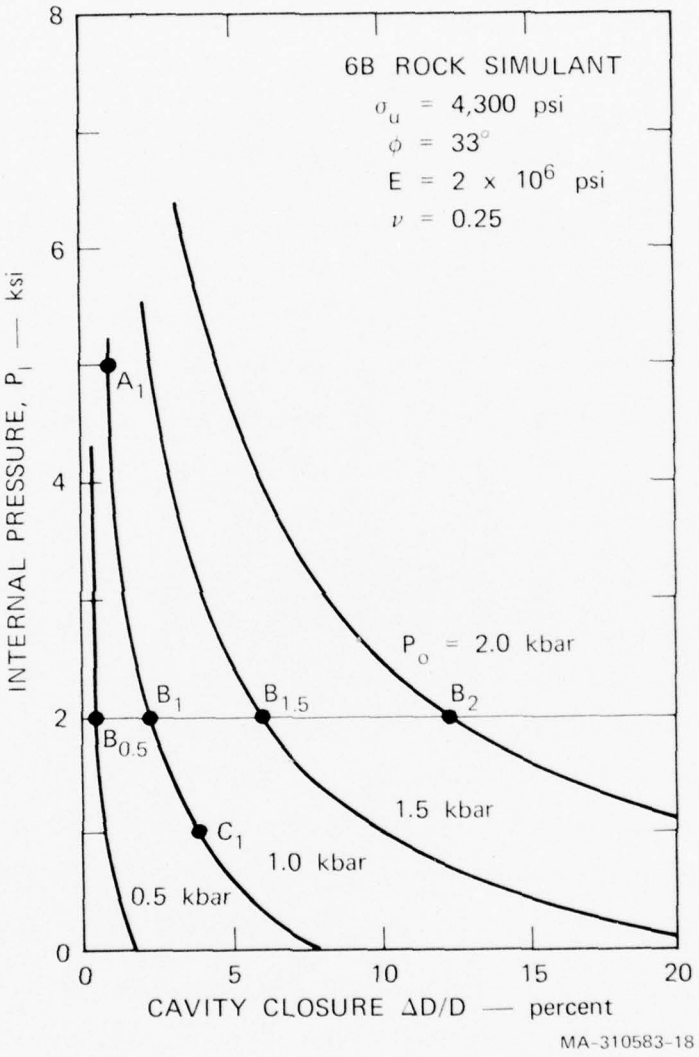

FIGURE 8-6 DESIGN CHART FOR YIELDING STRUCTURES

Shows relationships among essential parameters P_o (applied load), P_i (liner resisting pressure), and ΔD/D (rock cavity closure). Example is for moderately strong rock.

Points along each of the constant-load curves represent design options for the given load. For example, three options A_1, B_1, and C_1 are indicated on the P_o = 1.0 kbar load curve. These three points demonstrate the great reduction in required structure pressure P_i (liner strength) that can be achieved when modest amounts of cavity closure are allowed for. Point A_1 shows that the structure must have a strength of P_i = 5000 psi (34.5 MPa) to keep $\Delta D/D$ as small as 1 percent. When a closure $\Delta D/D$ = 2.1 percent is allowed, the required strength drops to P_i = 2000 psi (13.8 MPa) (point B_1). At point C_1, $\Delta D/D$ = 3.8 percent and P_i = 1000 psi (6.89 MPa). In fact, at the P_o = 1.0 kbar load, the liner structure in theory could be removed altogether and the closure would increase only to 8 percent in this relatively strong rock. However, at P_o = 1.5 kbar (150 MPa) an unlined tunnel would close more than 20 percent.

It is clear that selection of a design option consists of creating an appropriate balance between structure strength and load transfer to the native rock strength. If not enough cavity closure is allowed, then very little of the rock strength capability is used and the structure must be inordinately strong (points near A_1). On the other hand, if the structure is made too weak, then cavity closure becomes unacceptably large and there is no margin against higher loads (points near C_1). Designs near point B_1 are balanced designs for a 1.0-kbar load.

Points $B_{0.5}$, B_1, $B_{1.5}$, and B_2 show the response of the B_1 design at lower and higher loadings. The design is reasonably conservative in that at 1.5 kbar (150 MPa) the closure is 6 percent, which would be acceptable if the rest of the structure is designed accordingly. At 2.0 kbar the closure is 12 percent and would probably trigger more serious damage modes not considered here, such as buckling or failure of interior mountings.

In the following paragraphs we will follow through this design selection process for the specific example of the built-up structure. First, we will describe general yielding structure concepts and the specific approach of the built-up design and how it complements other designs in a total research program. Then we will show various options in moderately strong rock, where superhard structures are most favorable, and finally how the designs can be tested in the weaker tuff rock at NTS.

8.4 Built-Up Structure Concept and Design Options

8.4.1 General Yielding Structure Designs

Accommodation of a lined-tunnel structure to cavity closure can be accomplished by two basic methods. Either the liner itself can be designed to follow the large plastic hoop strains of several percent closure, or a crushable backpacking material can be placed between the liner and the cavity opening to isolate the liner. All the superhard yielding structure designs use either or both of these methods in various combinations.

The composite integral liner is a promising concept that accommodates closure by direct liner hoop strain. This concept has the additional feature of being made up of a composite of an interior steel liner in direct contact with an exterior reinforced concrete layer. During closure, the interior steel liner yields and provides compression against the concrete, thereby increasing the concrete strength by virtue of the high internal friction typical of concrete materials. The steel and concrete both follow the several percent closure of the cavity through large plastic flow in the hoop direction. Design problems are to prevent the relatively thin steel shell from buckling during plastic flow, and to prevent the concrete from cracking at large hoop strains. Another problem is mounting of contents within the structure also to

accommodate to the diameter change of cavity closure. This problem is faced in submarines, for example, but in submarines the hull strains are within the elastic limit so that diameter changes are only a few tenths of a percent.

Nevertheless, the composite integral liner is a promising concept because it uses inexpensive construction materials in an efficient way. The concept can be extended to cavity closures beyond the allowable hoop strain limit by using it in conjunction with a backpacking layer.

Another concept that accommodates directly to the cavity closure is the compliant liner. In this concept the continuous construction of the composite integral structure is replaced by from 4 to 8 circumferential segments with compliant piston-type connections between segments that accommodate the hoop displacements. This concept circumvents problems of plastic-flow buckling of the interior steel liner. However, the compliant mechanism may bind up, particularly at connections with adjacent sections or at end closures. Also, the amount of radial pressure that the compliant shell can transmit to the surrounding medium is limited by the crushing strength of the material in the piston. For example, in a 6-inch (15.2 cm)-thick compliant liner with 6-inch (15.2 cm) thick pistons filled with 1000 psi (16.89 MPa) cellular concrete, the hoop thrust is only F = 6000 lb/in. (1.05×10^6 N/m) of axial length compared with about 90,000 lb/in. (15.8×10^6 N/m) for a 6-inch (15.2 cm) thick composite integral liner. For a 5-ft (1.52 m) interface diameter these translate to liner-medium interface pressures of p_i = 90,000/30 = 3000 psi (20.7 MPa) for the composite integral liner and only 200 psi for the compliant liner.

The built-up structure is proposed here as an alternative concept to circumvent possible buckling of the interior steel liner, while at the same time greatly reducing the diameter change to which the mounting of the structure contents must accommodate.

8.4.2 Built-Up Structure Design

The built-up structure stands at the other extreme in the spectrum of yielding structure designs. In this design all the plastic deformation associated with cavity closure is taken up in the crushable backpacking layer so that the interior steel liner remains elastic. Because the elastic modulus of steel is at least two orders of magnitude higher than the plastic modulus, buckling then can be prevented by a modest number of ring stiffeners. The design has the added advantage that, when fabricating a full-scale structure, arc elements of the steel liner can be prefabricated and then "built up" in place. Backpacking material is then simply pumped into place around the liner.

A schematic diagram of the built-up structure and its elements is given in Figure 8-7. The resisting pressure P_i against the rock cavity is simply the crushing stress of the backpacking material. If the small hoop thrust also created in the backpacking layer is neglected, this pressure P_i must be sustained by the interior steel liner. To ensure that the liner remains elastic, we keep the corresponding hoop stress in the liner within the working stress of the steel. Figure 8-8 is a longitudinal section through a typical built-up structure design.

8.4.3 Built-Up Design Options for Moderately Strong Rock

Typical backpacking and steel liner thickness-to-radius ratios for designs in the range discussed earlier are given in Figure 8-9. This figure is simply Figure 8-6 with these quantities added as variables at the top and right-hand sides. Backpacking thickness-to-radius ratios were calculated under the reasonable assumption that inexpensive materials can be developed that will crush 20 percent of their original thickness ($\varepsilon_{bp} = 0.2$). The backpacking thickness-to-radius ratio is related to cavity closure by $H/R = (1/\varepsilon_{bp})\Delta R/R$. With $\varepsilon_{bp} = 0.2$, the H/R values are

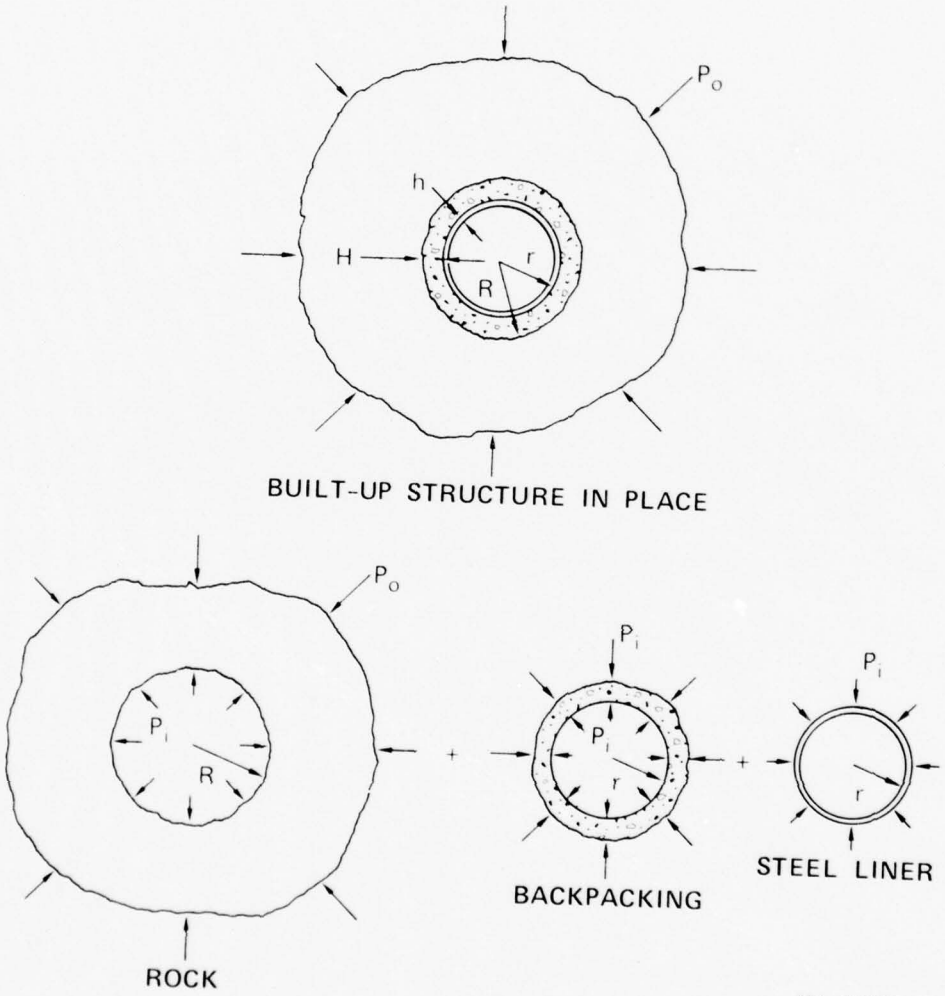

FIGURE 8-7 BUILT-UP STRUCTURE CONCEPT

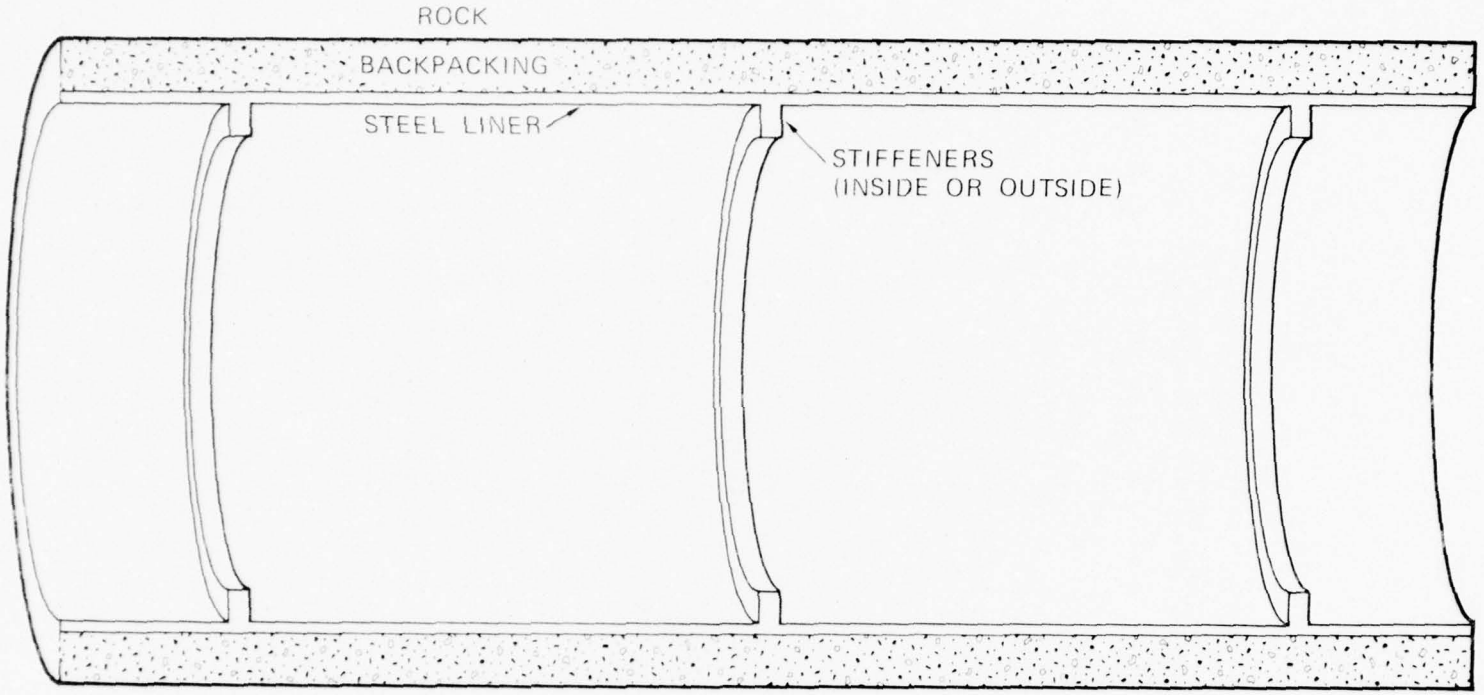

FIGURE 8-8 BUILT-UP STRUCTURE LONGITUDINAL SECTION

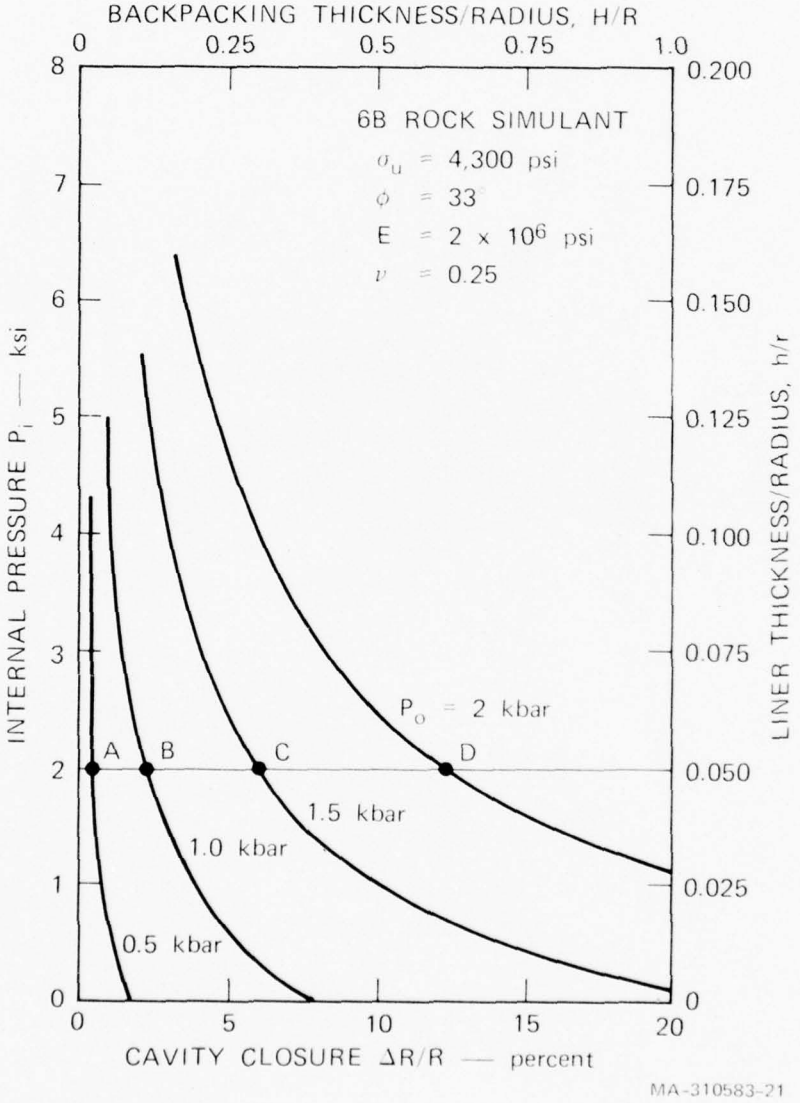

FIGURE 8-9 BUILT-UP STRUCTURE DESIGN CHART FOR MODERATELY HARD ROCK

then 5 times the cavity closures given on the bottom coordinate. Liner thickness-to-radius ratios are related to P_i by $H/R = P_i/\sigma_w$, with the working stress σ_w of the steel taken as 40,000 psi (276 MPa). All these numbers will change slightly when actual material properties are used, but these round numbers are realistic values.

We see from points A, B, C, D in the figure that, with a backpacking crushing stress of 2000 psi (13.8 MPa), load pressures P_o up to about 1.5 kbar (150 MPa) can be sustained. These are in the range of interest for superhard structures. Near P_o = 1.5 kbar (150 MPa), $\Delta V/V = 1 - (1 - 0.1)^2 = 0.19$. These are reasonable values and can be reduced if desired by using crushable materials with a larger crushing strain. Aluminum honeycomb, for example, will crush 70 percent of its original thickness. With this material, the above volume fractions would be reduced to 0.14 at 1.5 kbar (150 MPa) and 0.06 at 1.0 kbar (100 MPa). This material is very expensive, of course, but, when considered together with excavation and transportation costs, exotic materials of this type are worth exploring for truly superhard, reliable structures.

The steel liner at P_i = 2000 psi (13.8 MPa) has a thickness-to-radius ratio of 0.05. At a 4-ft (1.22 m) diameter its thickness is therefore 1.2 inches (3.05 cm), about twice that of a comparable liner in a composite integral design for the same load P_o. The increased cost of the thicker liner would be compensated by the elimination of the network of concrete reinforcing bars, closely spaced liner anchoring bolts, and the compliant internal mounting of contents required for the composite integral liner. Either design looks promising. The justification for following both through the research phase is that each represents a reasonable design at the two extremes of accommodating cavity closure entirely with liner hoop strain or entirely with backpacking crush. Also, the composite integral liner pushes to the limit

conventional reinforced concrete design, typical of massive structures, while the built-up design uses conventional stiffened shell design but on a massive scale.

8.4.4 Design Options for Structures Experiment in Tuff

Underground tests at NTS offer a unique opportunity to test superhard structures, but in the porous, relatively weak, tuff rock found at the site. Testing of superhard structures in porous rock is of interest in itself because in such rock the load P_o that must be sustained is reduced because of the highly shock-attenuating property of porous materials. The ideal superhard site, however, would combine this desirable shock-attenuating feature in upper layers of rock with the higher strength of harder rock in a lower layer in which the structure is situated. Also, if such ideal sites are unavailable, the higher strength of more competent rock may make it possible to design a structure hard enough to compensate for the higher shock transmission in hard rock. Thus, there is interest in structure response in both hard and soft rock. A logical question for testing at NTS is therefore whether tests in the soft tuff material can be used to investigate response that would take place in hard rock.

To answer this question, we compare the design chart of Figure 8-9, for moderately hard rock, with a similar design chart (again based on an axisymmetric analysis) in Figure 8-10, for tuff. The comparison shows that the design curves are reasonably similar if we associate the 1.0 to 2.0 kbar (100 to 200 MPa) curves in the harder rock with the 0.32 to 0.5 kbar (32 to 50 MPa) curves for the softer tuff material. For similar cavity closures in the harder and softer rocks, the P_i = 2000 psi (13.8 MPa) structures in Figure 8-9 compare closely with P_i = 1500 psi (10.3 MPa) structures in Figure 8-10. The

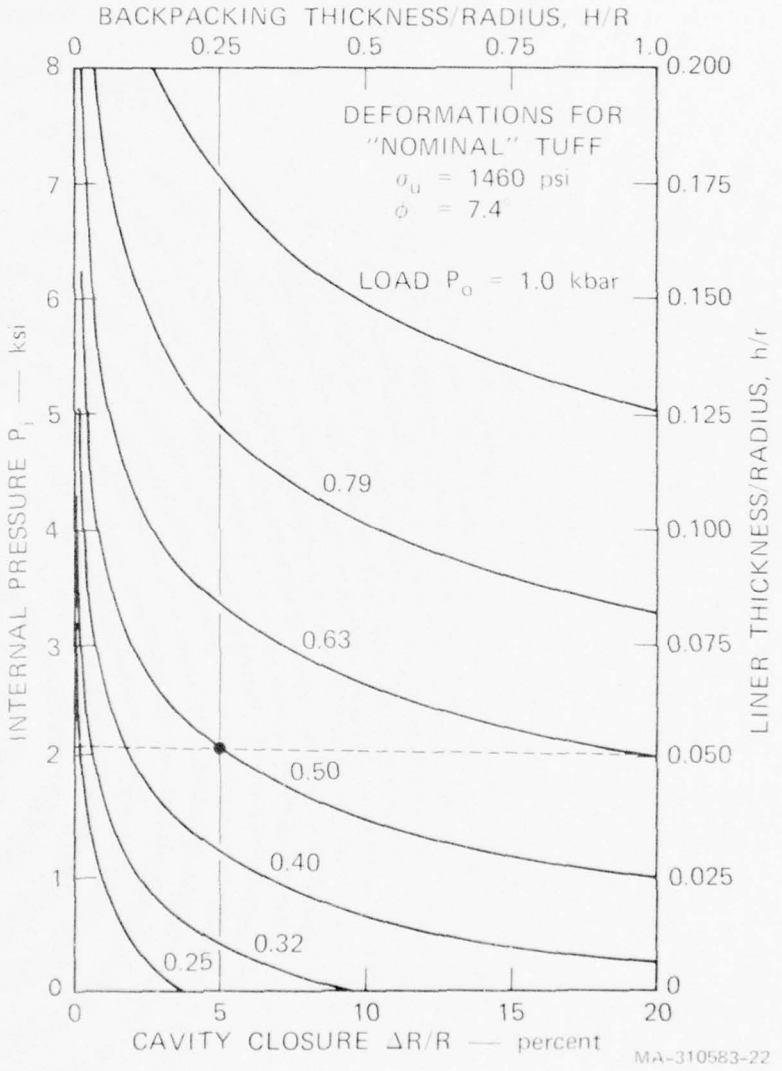

FIGURE 8-10 BUILT-UP STRUCTURE DESIGN CHART FOR NOMINAL TUFF

main difference is that the sensitivity of cavity closure to load is greater in the softer rock than in the harder rock. Furthermore, observe that the range of design structural strengths P_i to be considered for, say, a 5 percent cavity closure design, is from $P_i \approx 500$ psi (3.45 MPa) to $P_i \approx 4000$ psi (27.6 MPa) for loads from $P_o = 1.0$ to 2.0 kbars (100 to 200 MPa) in the harder rock. In the softer rock this same range in structure strengths P_i corresponds to loads from 0.35 to 0.7 kbar (35 to 50 MPa).

Thus, experiments in tuff will give response data on the same structures (same P_i) and to the same deformations that are of interest for harder rock, if the loading pressures are reduced from the 1.0 to 2.0 kbar (100 to 200 MPa) range down to the 0.35 to 0.7 kbar (35 to 70 MPa) range. With this range of loads and associated structure strengths, the test will therefore provide response data that can be used for both hard rock and soft rock siting.

The most important feature of hard rock siting not included in the test is joints. However, omission of this complicating feature has the advantage that the test results will be much less clouded by rock response idiosyncrasies. Then, in future tests with joints, response features caused by joints can be separated out from response features observed in this test caused by load asymmetry and basic rock strength properties.

8.5 Slip Lines Around Lined and Unlined Tunnels

During the course of our experiments on unlined and lined tunnels for the previous project [1], we observed the formation of shear fractures that start at the tunnel and move nearly vertically into the rock medium [see Figures 8-11(a) and 8-12(a).] With a simple elastic analysis [7] and the Mohr-Coulomb failure criterion, we have computed

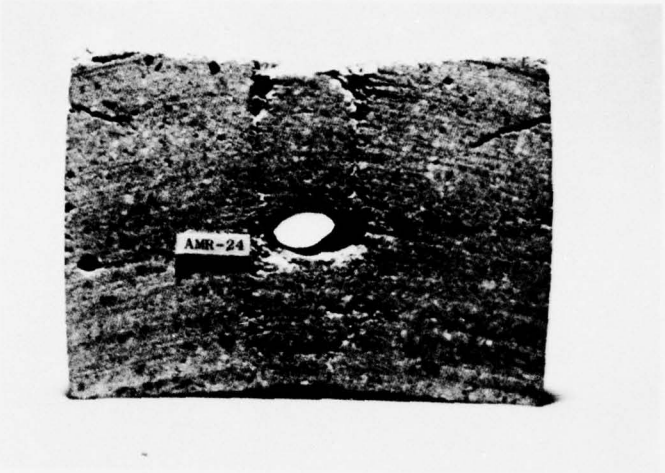

(a) UNLINED TUNNEL EXPERIMENT - P_V = 20,000 psi, P_H = 5,000 psi

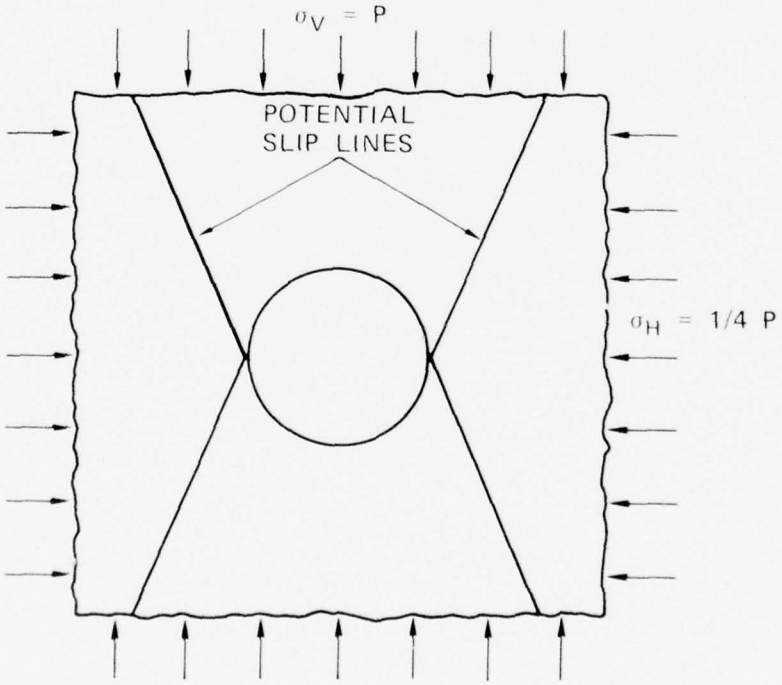

(b) THEORETICAL SLIP LINES FOR UNLINED TUNNEL

MP-3743-2

FIGURE 8-11 SLIP LINE PREDICTION FOR UNLINED TUNNEL

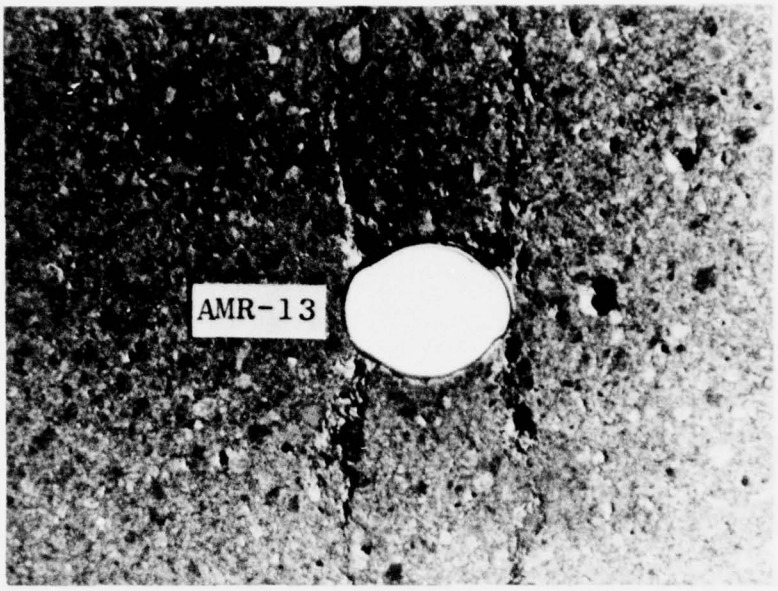

(a) LINED TUNNEL EXPERIMENT - P_V = 20,000 psi, P_H = 5,000 psi

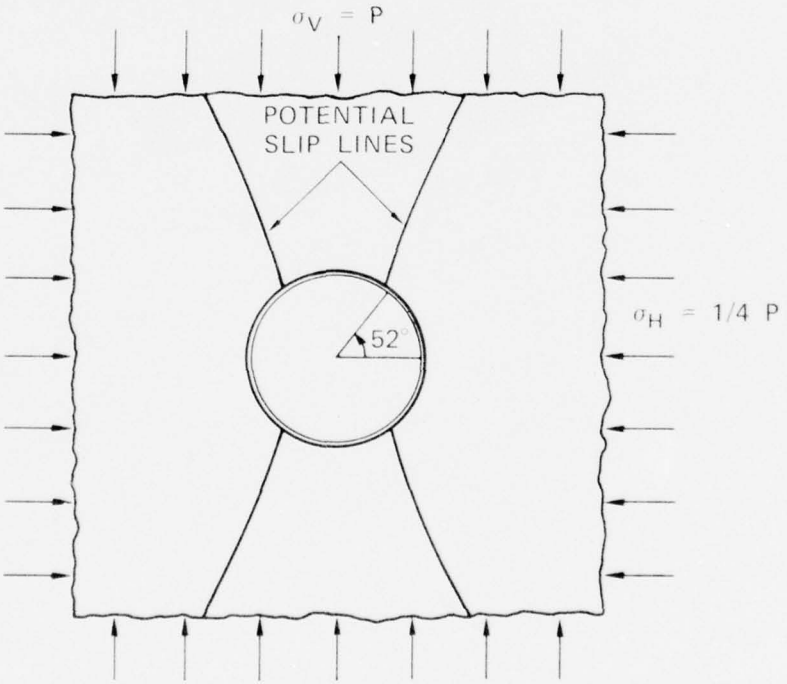

(b) THEORETICAL SLIP LINES FOR LINED TUNNEL

MP-3743-1

FIGURE 8-12 SLIP LINE PREDICTION FOR LINED TUNNEL

a first approximation of the location of slip lines in an infinite body with a cylindrical cavity subjected to asymmetric loading by assuming that the principal stress trajectories in the inelastic case are similar to those under elastic loading [4].

The locations of these slip lines depend on the internal friction angle φ of the material and on the ratio of the applied vertical and horizontal loads, but not on their magnitudes. For a nonfriction material, these lines would coincide with lines of maximum shear stress, which lie midway[45 degrees (0.785 rad)] between the principal stress directions. In our calculations, we have assumed a material with φ = 30 degrees (0.524 rad). This causes the slip lines to be inclined at an angle of 45 degrees - $\varphi/2$ = 30 degrees (0.524 rad) to the direction of maximum principal stress. For an infinite body with an unlined tunnel subjected to a vertical free field pressure $P_V = P$ and a horizontal free field pressure $P_H = P/4$, the Mohr-Coulomb criterion predicts that failure will occur first at the springlines of the tunnel and then move at a steep slope through the body as shown in Figure 8-11(b), since the principal stress trajectories are tangent and normal to the tunnel at the springlines. By comparing this with the specimen in Figure 8-11(a) which has an unconfined compressive strength σ_u = 8500 psi (58.6 MPa) and φ = 30 degrees (0.524 rad), we see that the theoretical prediction is in surprisingly good agreement with experiment, considering that the elasticity solution is no longer valid once fracture has begun.

A similar analysis was done for a tunnel with a steel liner having a radius-to-thickness ratio of 15. With this liner, the slip lines do not initiate at the springlines as for the unlined tunnel, but start at points 52 degrees above and below the springlines [11], as shown in Figure 8-12(b). By comparing this with its experimental counterpart in Figure 8-12(a), we see that fractures in the specimen also begin at appreciable angles away from the springline, in reasonable agreement with the predicted location.

REFERENCES

1. T. C. Kennedy, J. V. Zaccor, and H. E. Lindberg, "Laboratory Investigation of Response of Deep Based Structures," SRI Final Report, DNA 3610F, Menlo Park, California (October 1975).

2. H. F. Cooper and H. L. Brode, "Ground Shock and the Survivability of Deep Underground Superhard Facilities," R and D Associates, Draft Report RDA-TR-RS-DNA (November 1972).

3. I. M. Daniel, R. E. Rowlands, and M. M. Singh, "Experimental Investigation of Small Scaled Lined and Unlined Cylindrical Cavities in Rock," IIT Research Institute, AFWL-TR-70-55 (November 1970).

4. R. E. Heuer and A. J. Hendron, "Tests on Unlined Openings in Intact Rock," U.S. Army Engineer Waterways Experiment Station, DACA 39-67-6-009 (February 1971).

5. A. J. Hendron, P. Engeling, and A. K. Aiyer, "Tests on Lined Openings in Jointed and Intact Rock," U.S. Army Engineer Waterways Experiment Station, DACA 39-67-C-0009 (June 1972).

6. A. J. Hendron and P. Engeling, "Model Tests of Lined Tunnels in a Jointed Rock Mass," M-41, Construction Engineering Research Laboratory (May 1973).

7. S. Timoshenko and J. N. Goodier, Theory of Elasticity (McGraw-Hill Book Company, New York, 1951).

8. K. G. Stagg and O. C. Zienkiewicz, ed., Rock Mechanics in Engineering Practice, (John Wiley and Sons, London, 1968).

9. J. L. Merritt, Consulting and Special Engineering Services, Inc., private communication (August 1974).

10. S. W. Butters, et al., Mechanical Properties of Nevada Test Site Tuffs from Selected Exploratory Drill Holes, DNA 3181F, Terra Tek, Inc., September 1973.

11. G. N. Savin, Stress Concentration Around Holes (Pergamon Press, New York, 1961).

Appendix A

THEORY

In [1] an analysis was presented for the static, elastic-perfectly plastic behavior of a thick-walled cylinder subjected to internal and external pressurization, illustrated in Figure A-1. Here, we give expressions for the stresses and strains when the external radius of the cylinder is infinite. These are the relations used in the calculations in Sections 8.1, 8.2, and 8.3.

Plastic region: $a < r < R$

$$\sigma_r = \frac{\sigma_u}{1 - N_\varphi} + \left(\frac{\sigma_u}{N_\varphi - 1} + P_i\right)\left(\frac{r}{a}\right)^{N_\varphi - 1}$$

$$\sigma_\theta = \frac{\sigma_u}{1 - N_\varphi} + N_\varphi\left(\frac{\sigma_u}{N_\varphi - 1} + P_i\right)\left(\frac{r}{a}\right)^{N_\varphi - 1}$$

$$\varepsilon_r = \frac{1}{E'}\left\{\frac{(1 - \nu')}{1 - N_\varphi}\sigma_u + \left[1 - \nu' N_\varphi + \frac{1}{2}(N_\varphi^2 - 1)\right]\left(\frac{\sigma_u}{N_\varphi - 1} + P_i\right)\left(\frac{r}{a}\right)^{N_\varphi - 1}\right\}$$

$$- \frac{(N_\varphi^2 - 1)}{2E'}\left(\frac{\sigma_u}{N_\varphi - 1} + P_i\right)\left(\frac{R}{a}\right)^{N_\varphi - 1}\left(\frac{R}{r}\right)^{N_\varphi + 1}$$

$$\varepsilon_\theta = \frac{1}{E'}\left\{\frac{(1 - \nu')}{1 - N_\varphi}\sigma_u - \left[\frac{(N_\varphi^2 - 1)}{2N_\varphi} - N_\varphi + \nu'\right]\left(\frac{\sigma_u}{N_\varphi - 1} + P_i\right)\left(\frac{r}{a}\right)^{N_\varphi - 1}\right\}$$

$$+ \frac{(N_\varphi^2 - 1)}{2N_\varphi E'}\left(\frac{\sigma_u}{N_\varphi - 1} + P_i\right)\left(\frac{R}{a}\right)^{N_\varphi - 1}\left(\frac{R}{r}\right)^{N_\varphi + 1}$$

Elastic region: $R < r < \infty$

$$\sigma_r = P_o - \frac{\left[\sigma_u + P_o(N_\varphi - 1)\right]}{N_\varphi + 1}\left(\frac{R}{r}\right)^2$$

$$\sigma_\theta = P_o + \frac{\left[\sigma_u + P_o(N_\varphi - 1)\right]}{N_\varphi + 1}\left(\frac{R}{r}\right)^2$$

$$\varepsilon_r = \frac{P_o(1 - \nu')}{E'} - (1 + \nu')\frac{\left[\sigma_u + P_o(N_\varphi - 1)\right]}{E'(N_\varphi + 1)}\left(\frac{R}{r}\right)^2$$

$$\varepsilon_\theta = \frac{P_o(1 - \nu')}{E'} + (1 + \nu')\frac{\left[\sigma_u + P_o(N_\varphi - 1)\right]}{E'(N_\varphi + 1)}\left(\frac{R}{r}\right)^2$$

where

$$R = \left\{\frac{2}{1 + N_\varphi}\left[\frac{\sigma_u + P_o(N_\varphi - 1)}{\sigma_u + P_i(N_\varphi - 1)}\right]\right\}^{1/(N_\varphi - 1)} a$$

$$N_\varphi = \frac{1 + \sin\varphi}{1 - \sin\varphi}$$

$$E' = \frac{E}{(1 - \nu^2)} \qquad \nu' = \frac{\nu}{1 - \nu}$$

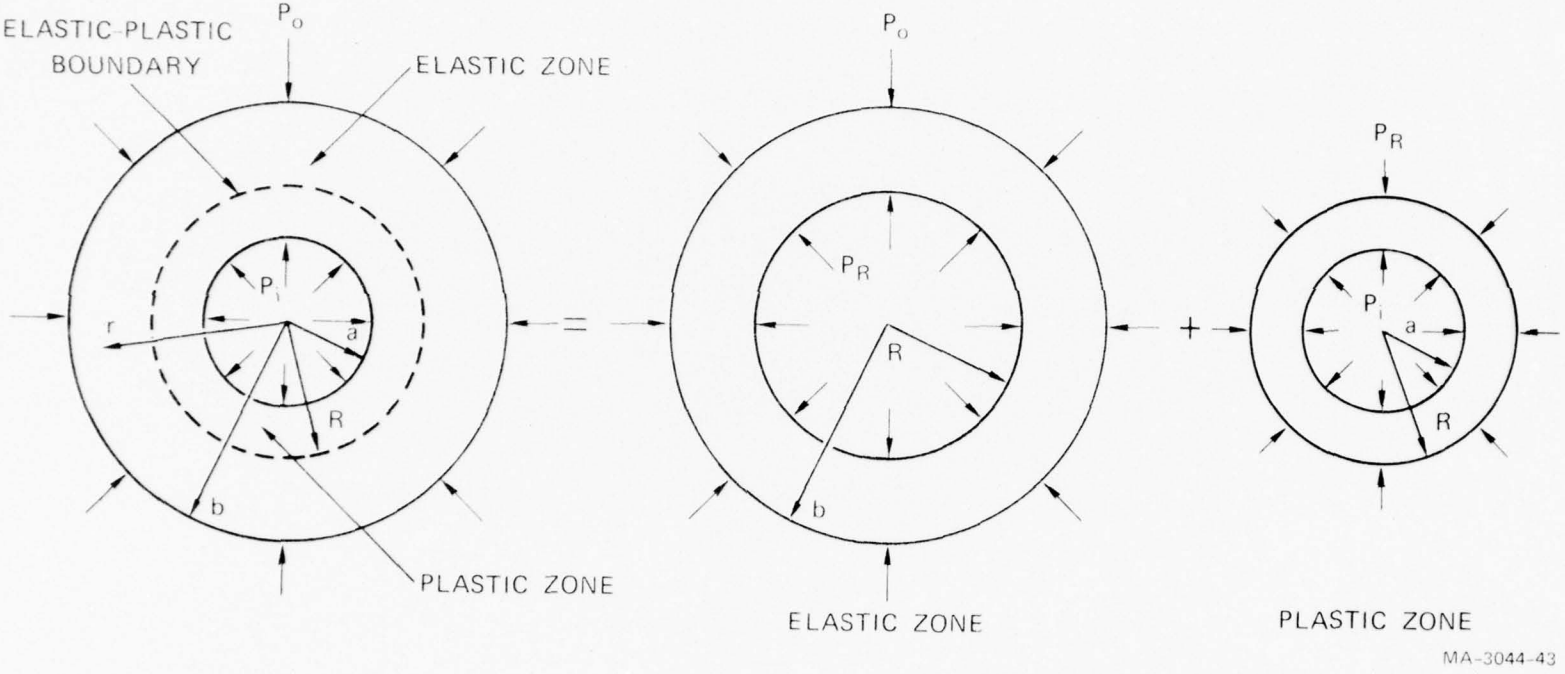

FIGURE A-1 ELASTIC-PLASTIC ANALYSIS OF A THICK-WALLED CYLINDER

Appendix B

ROCK MODELING

In this appendix, we present the material properties of the rocks used in our experiments. Rather than attempt to model details of rock structure and texture, we used a grout especially designed to simulate the general characteristics of a rock of interest. Waterways Experiment Station (WES) provided us with grout specimens (called 6B rock simulant) that simulate medium strength rock or jointed higher strength rock. The 6 designates that the rock was made from commercial grade sand but with large grains removed by a number 6 sieve. The B designates that it is the second formulation studied by WES. The A formulation is stronger and was used in our first program [1]. Tunnel experiments were performed on the rock in both the dry and fully water-saturated conditions. The properties of the rock under each of these conditions are described next.

B.1 Properties of Saturated 6B Rock

Material property tests were performed by WES and by SRI on samples of the rock in the fully water-saturated condition. Stress-strain curves for unconfined rock are shown in Figure B-1. The curve on the left is taken from data provided by WES, the dashed line representing a secant or average elastic modulus. The curve on the right is from tests done at SRI. The curve is offset from the WES data because of the large amount of fictitious strain required to seat the specimen. The unconfined strength and average modulus from the curves are in good agreement. Both curves indicate an unconfined strength of 4000-4500 psi (27.6 - 31.0 MPa) and an average elastic modulus slightly over 2×10^6 psi (13.8 GPa).

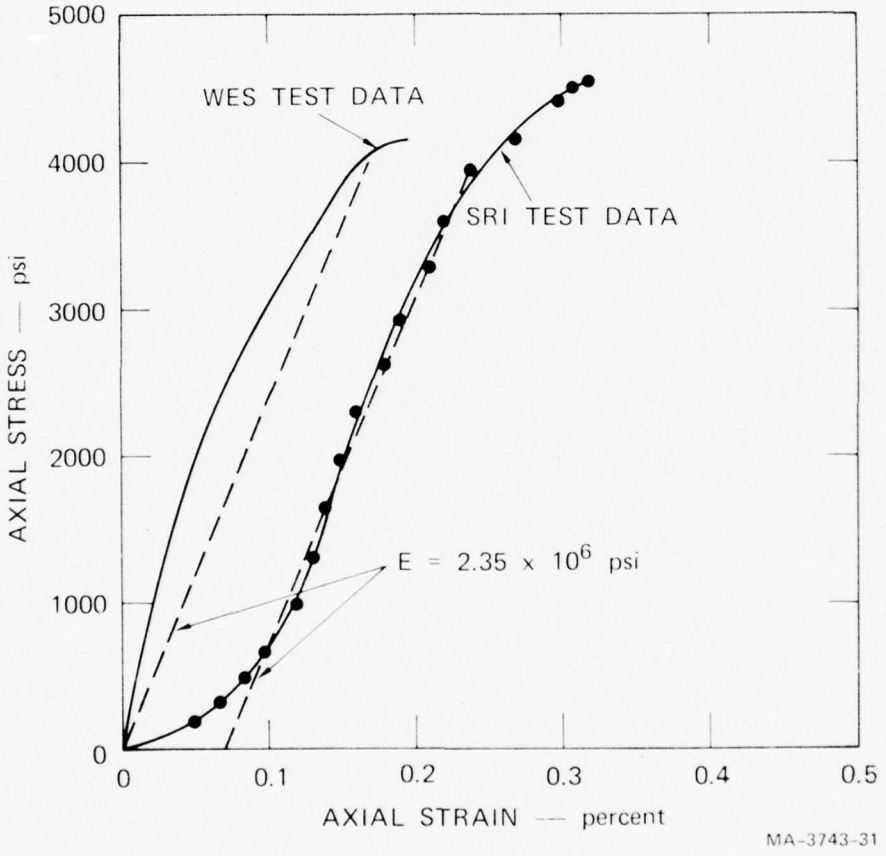

FIGURE B-1 STRESS-STRAIN CURVES FOR MOISTURIZED 6B ROCK SIMULANT

The behavior of the rock under uniaxial-strain conditions is of interest since many of our tunnel experiments were performed under this type of loading. Figure B-2 shows a plot of horizontal pressure versus vertical pressure for uniaxial strain. The curves (A and B) are data provided by WES. The square and triangular symbols are data obtained from our tunnel experiments. The data are in reasonable agreement except for an inflection at about 15 ksi (103 MPa) in the WES curves that does not occur in the SRI data. The more nearly hydrostatic behavior above 15 ksi (103 MPa) in the WES curves is attributed to the presence of porewater pressure in the WES tests. The WES tests were performed on undrained samples while the SRI tests were performed on drained samples. Figure B-3 is a plot of axial stress versus axial strain from WES uniaxial-strain tests on two specimens of the 6B rock.

Mohr failure envelopes for the saturated rock at various test ages are shown in Figure B-4. The rock was kept moist during aging. As the test age increases, the moisture content and degree of saturation increase. This causes the amount of porewater pressure that develops during the test to increase since the specimens are undrained during the test. In the bottom diagram, the specimen is fully saturated and the Mohr circles are shifted a considerable distance to the right owing to the porewater pressure. It appears that the angle of internal friction for the effective Mohr failure envelope would be between 30 and 40 degrees (0.524 and 0.698 rad) for low stress levels. For high stress levels [normal stress above 10 ksi (168.9 MPa)], the effective friction angle is considerably reduced.

B.2 Properties of Dry 6B Rock

Material property tests were also performed on samples of the rock in the dry (~20% saturation) condition. Figure B-5 shows the stress-strain curve provided by WES for unconfined rock. The elastic modulus

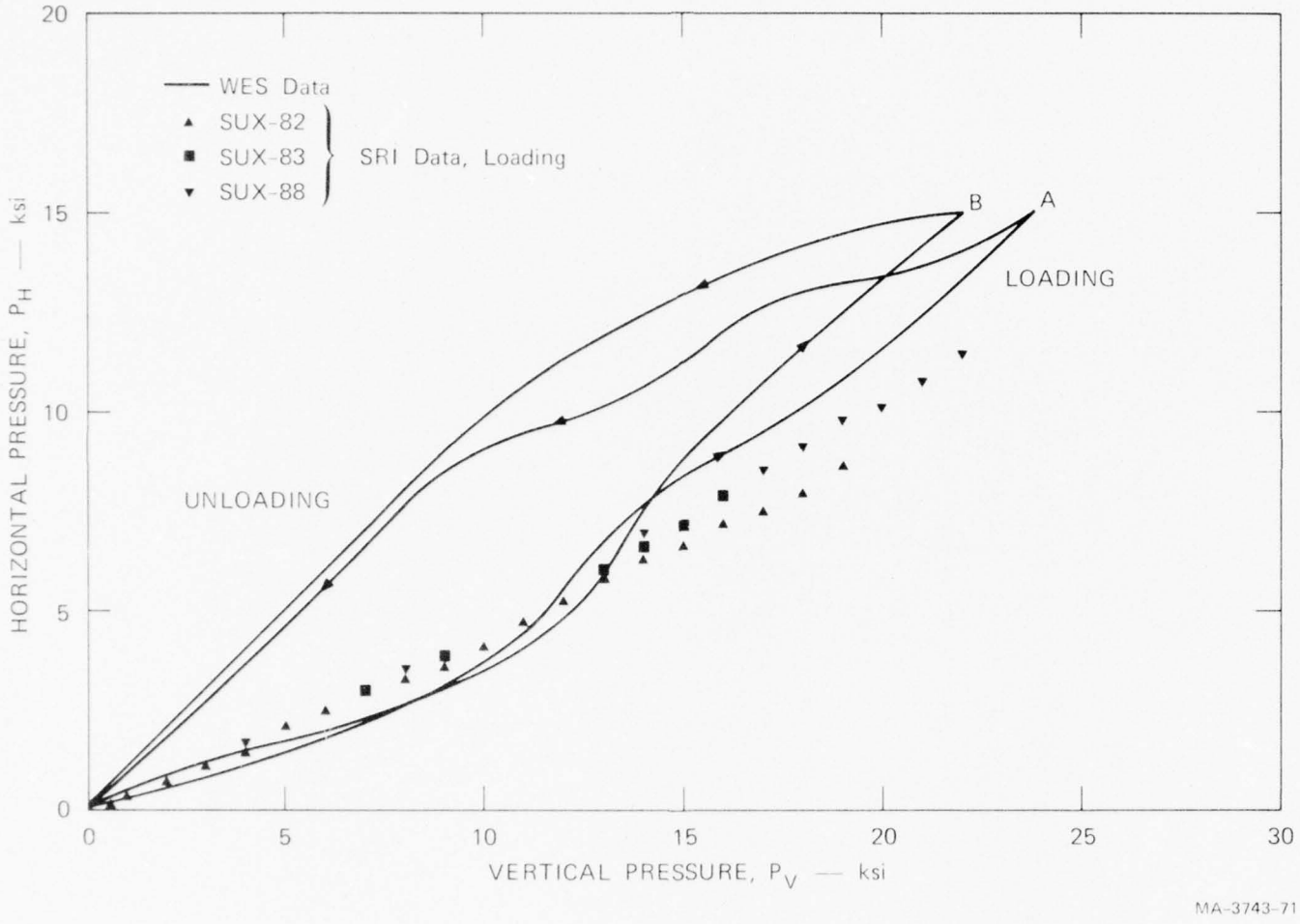

FIGURE B-2 HORIZONTAL PRESSURE VERSUS VERTICAL PRESSURE FOR UNIAXIAL STRAIN FOR SATURATED 6B ROCK SIMULANT

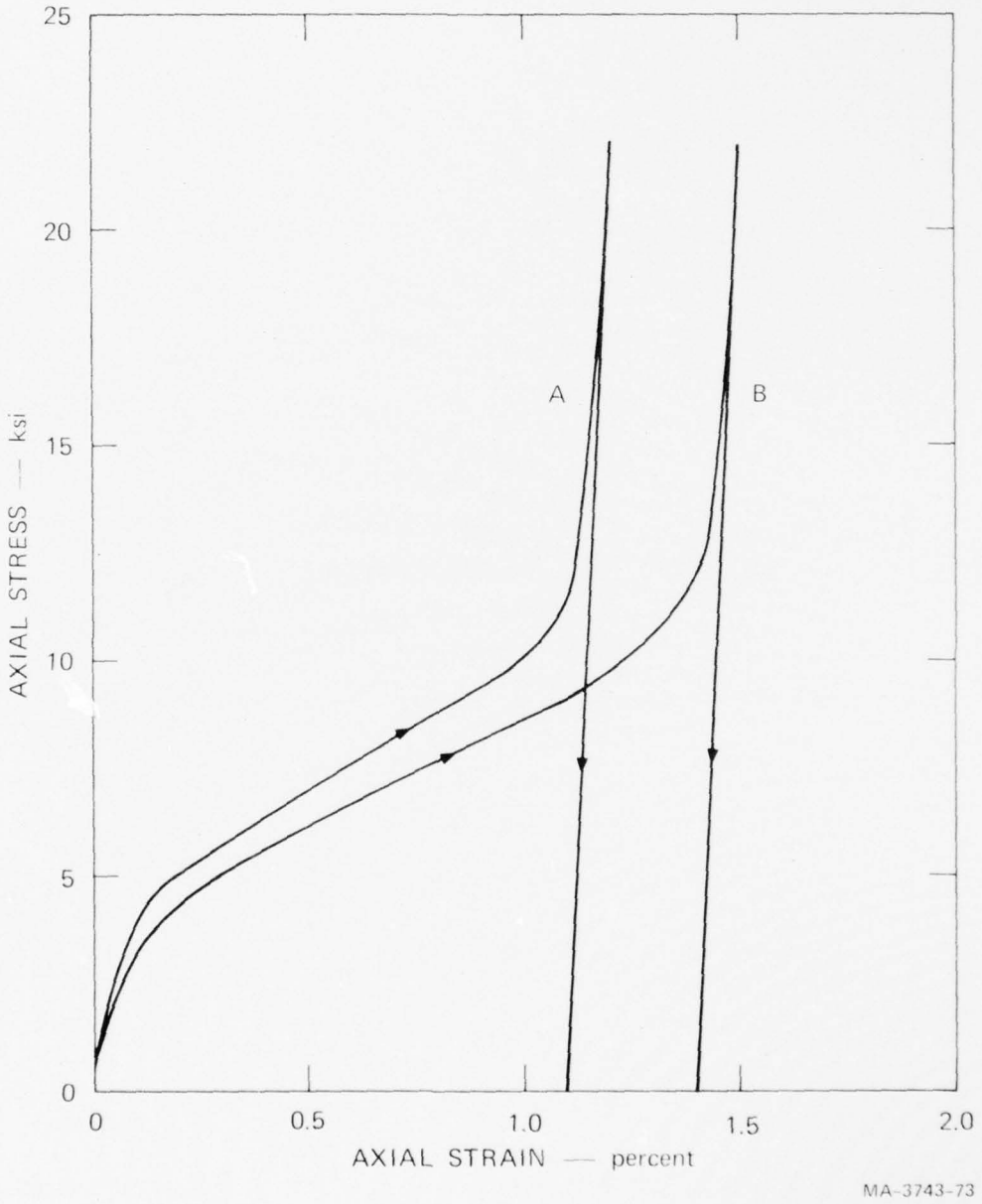

FIGURE B-3 STRESS-STRAIN CURVE UNDER UNIAXIAL STRAIN LOADING FOR SATURATED 6B ROCK SIMULANT

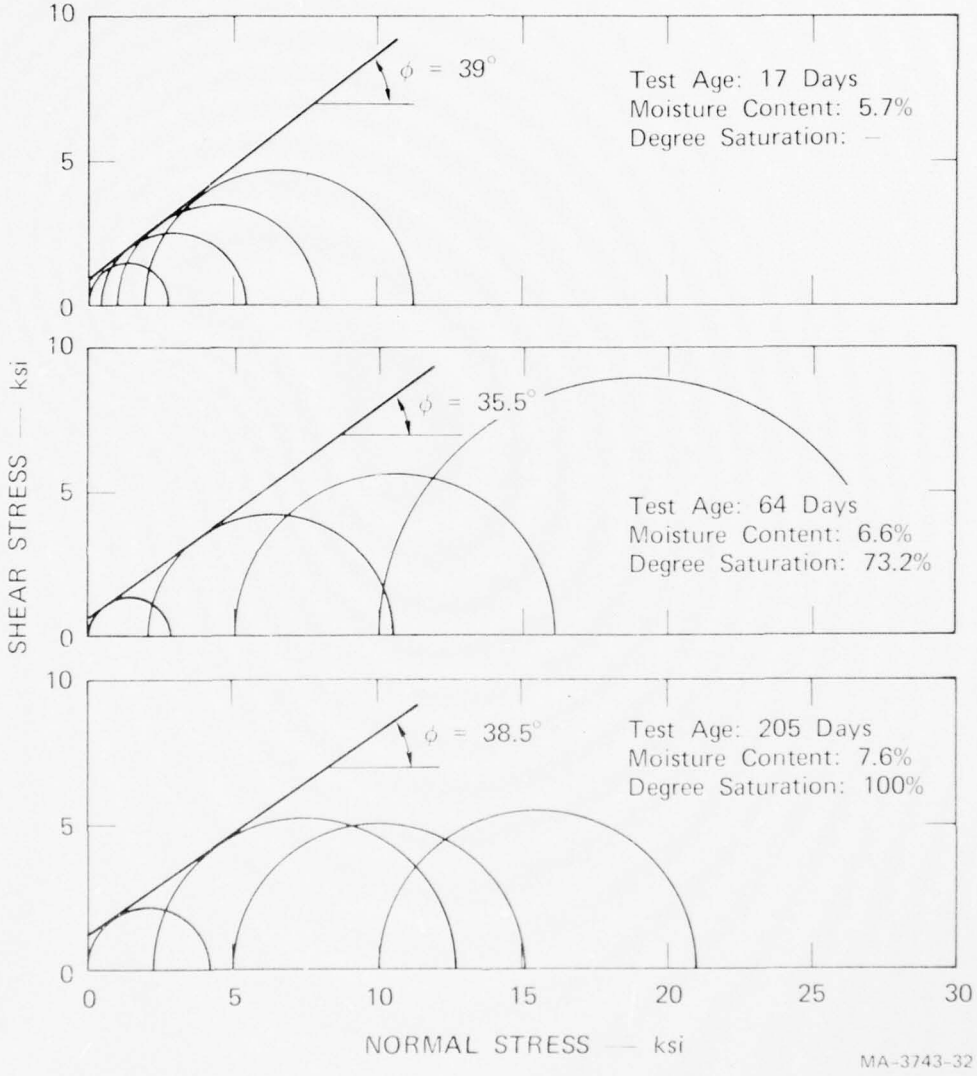

FIGURE B-4 MOHR DIAGRAMS FOR MOISTURIZED 6B ROCK AT DIFFERENT TEST AGES (R. L. STOWE, WES)

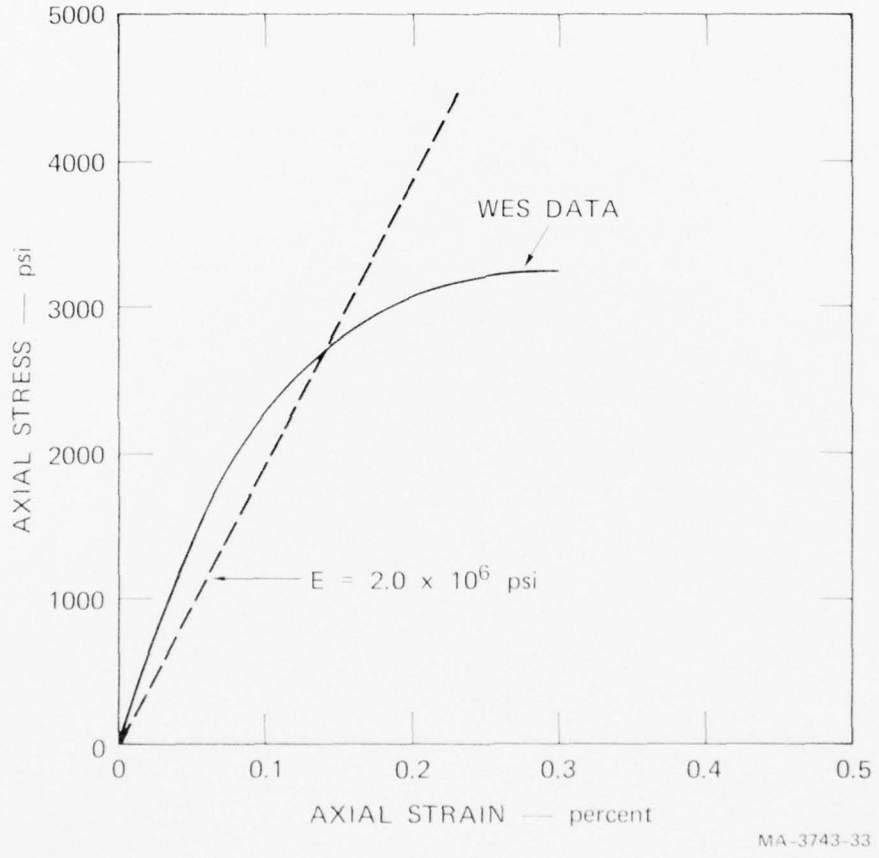

FIGURE B-5 STRESS-STRAIN CURVES FOR DRY 6B ROCK SIMULANT

and unconfined compressive strength are slightly lower than the values for the saturated rock. The curve indicates an unconfined strength of 3000-4000 psi (20.7-27.6 MPa) and an average elastic modulus of about 2×10^6 psi (13.8 x GPa).

Figure B-6 shows a plot of horizontal pressure versus vertical pressure for uniaxial strain. The data were taken from the SRI tunnel experiments on dry rock. These data are very close to those for the saturated rock.

Figure B-7 shows a Mohr failure envelope obtained by WES for dry 6B rock. Since no porewater pressure is present, the friction angle $\phi = 36^o$ remains high for normal stresses up to 2 kbar (200 MPa).

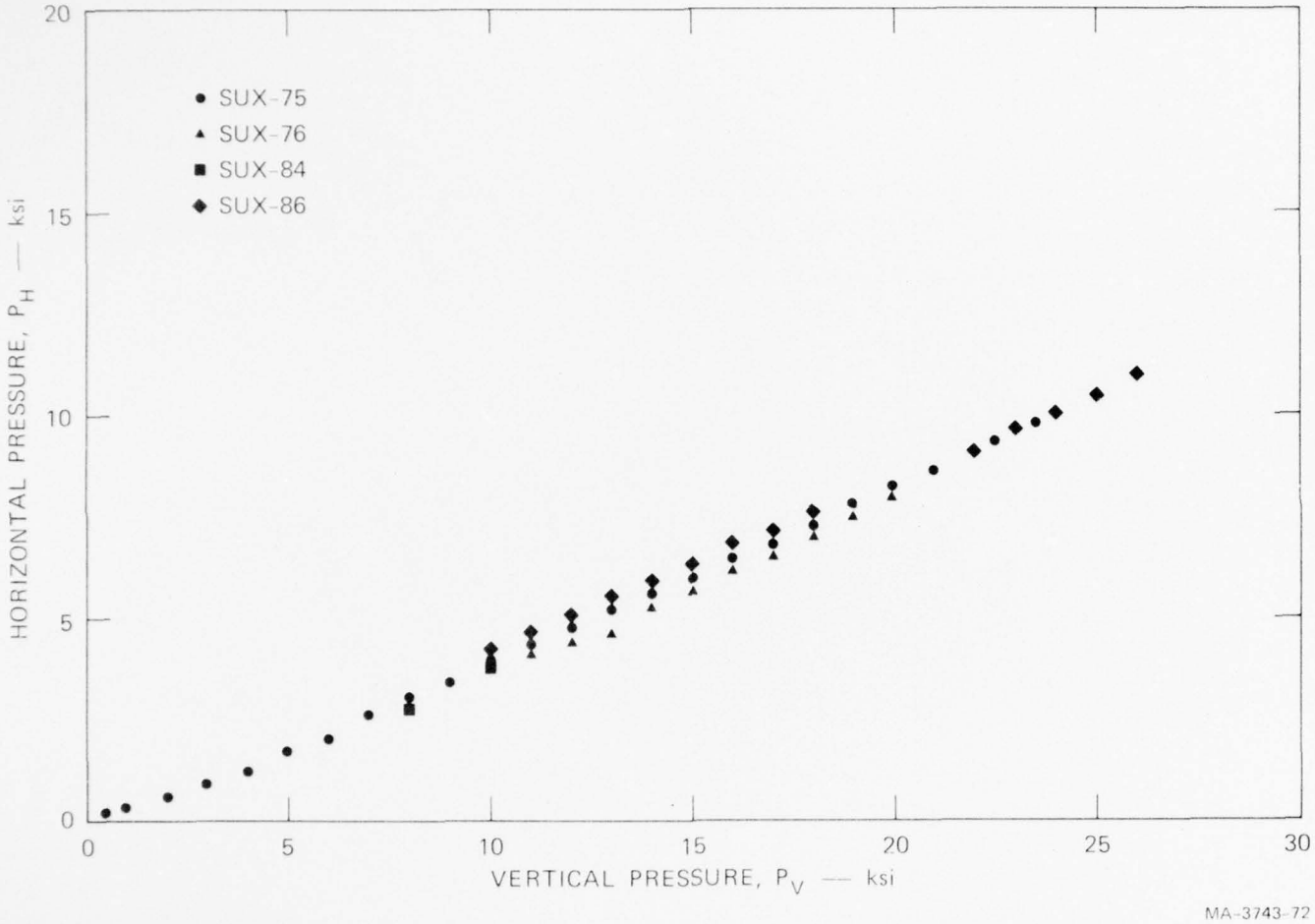

FIGURE B-6 HORIZONTAL PRESSURE VERSUS VERTICAL PRESSURE FOR UNIAXIAL STRAIN FOR DRY 6B ROCK SIMULANT

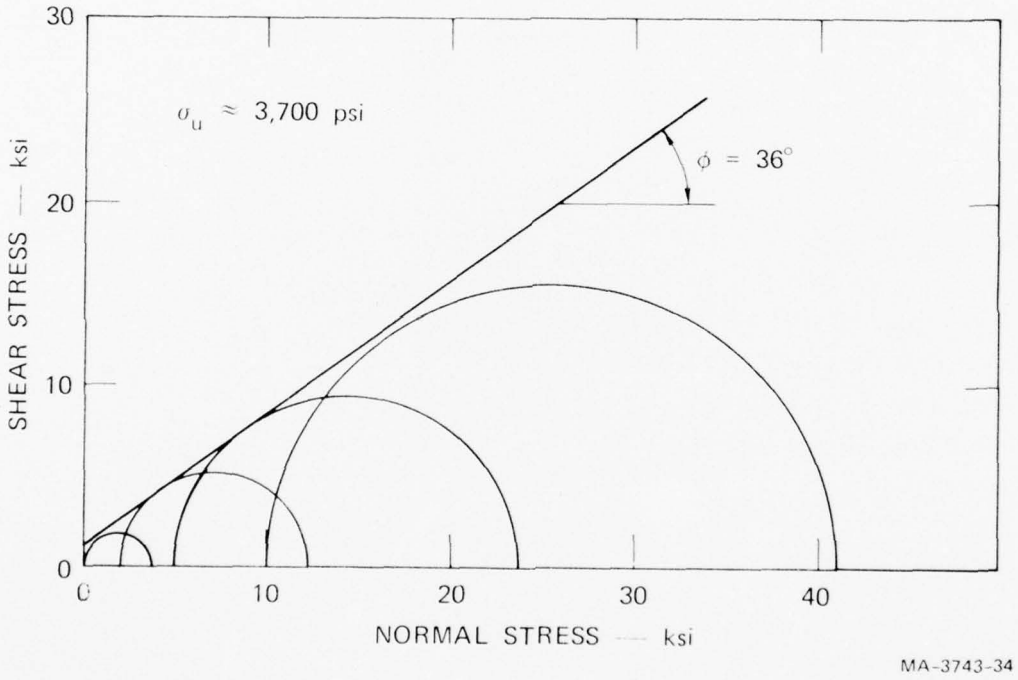

FIGURE B-7 MOHR DIAGRAM FOR DRY 6B ROCK

Appendix C

TESTING MACHINES AND EXPERIMENTAL PROCEDURES

In this appendix, we describe the static and dynamic testing machines and the procedures used for our experiments. The machines were designed and built on a previous DNA project [1], but several crucial modifications were made to the machines during the course of the current project to improve their performance and extend their capabilities.

C.1 Dynamic Testing Machine

The basic operating technique of the dynamic testing machine is the controlled release of explosive gases from a vented chamber charged with low-density explosive. This technique was originally developed at SRI in 1971 to simulate the sudden release of energy in a nuclear reactor in a sudden-loss-of-coolant accident. In 1972, the technique was successfully applied to simulate the intense underground pressures that stem horizontal line-of-sight (HLOS) pipes in nuclear tests. The original HLOS machine was capable of applying only axisymmetric pressure around a cylindrical specimen. In 1974, a new loading machine was designed and built which has the capability of applying uniaxial-strain and triaxial loadings as occur on horizontal deep-buried tunnels under nuclear attack [1]. During the current program, modifications were made to this machine to improve its performance and to give it the capability of applying isotropic loadings. In the following paragraphs we describe the current status of this machine and our test procedure.

C.1.1 Triaxial Loading Configuration

An assembly drawing of the dynamic tester in the triaxial loading configuration is shown in Figure C-1. The machine consists of

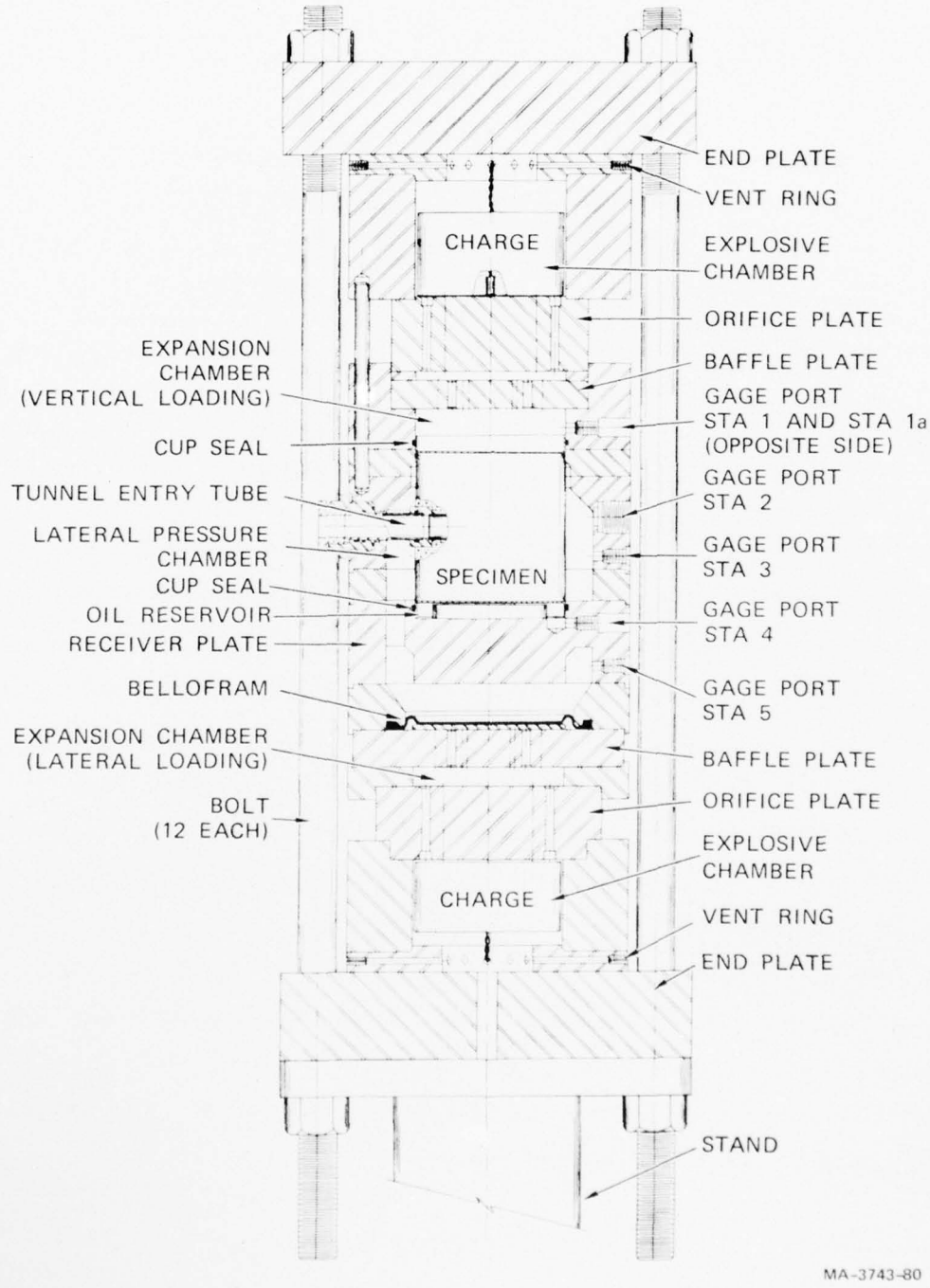

FIGURE C-1 DYNAMIC TESTING MACHINE—TRIAXIAL LOADING CONFIGURATION

a stack of thick rings with fluid passageways machined into them. The rings are held together with end plates and 12 bolts around the circumference. The rock specimen is 4 inches (10.2 cm) in diameter and 3 to 6 inches (7.6 to 15.2 cm) long and rests in the center of the machine, as shown. The tunnel is bored completely through the cylindrical rock specimen along a diameter at midheight. Viewing ports are provided in the machine at each end of the tunnel to allow high-speed photography and access for instrumentation wires (one port is shown on the left of the drawing).

To provide independent control of vertical and lateral pressures, loading is applied by two separate explosive chambers. The upper explosive chamber applies the vertical pressure and is simply a cylindrical cavity into which an explosive charge (a mixture of PETN and microballoons) and a detonator are placed. The high-pressure explosive products are vented into the expansion chamber through the series of holes shown drilled through the thick orifice plate between the explosive chamber and expansion chamber. In the expansion chamber is a baffle plate to help mix the gas and carry the sudden localized concentrations of pressure of the gas as it jets through the orifice plate. The load is applied directly to the specimen by the mixed gas downstream of the baffle plate. The area of the holes in the orifice plate determines the rise time of the loading pulse. Fine adjustment of the rise time is provided by changing the expansion chamber volume by inserting an inert solid material, such as Duxseal. Release venting (and therefore pulse decay time) from the explosive chamber is accomplished through holes in the vent ring between the explosive chamber ring and the end plate.

A similar arrangement at the bottom of the testing machine is used to load the sides of the specimen. However, in this case, the load is transmitted by a fluid-filled lateral pressure chamber. A Bellofram is

located just above the baffle plate to act as an interface between the gas and the fluid. The lower expansion chamber applies the lateral pressure through ports (on the fluid-filled side of the Bellofram) seen connecting the lower expansion chamber to the lateral pressure chamber. The top and bottom vertical pressures and the lateral pressure chamber are sealed off by thin copper cups and O-rings above and below the rock specimen. The cups are inverted so that the high pressure acts inside the cups and presses them against the O-rings to seal the chamber. (A closer view of these seals is given in Figure C-12, for the static machine discussed later.) Sealing between the pressure chambers and external ambient pressure is provided by O-rings as shown. A Wilson seal described in the next section seals the lateral pressure chamber from the rock and cavity.

Pressures are monitored in the various chambers and passageways by piezoelectric gages installed in any of seven tapped ports in the machine. Figure C-2(a) shows a pressure pulse from the vertical loading chamber above the specimen and Figure C-2(b) shows a pressure pulse from the lateral loading chamber, around the specimen circumference. Rise time in each is about 1 ms, and total pulse duration is about 10 ms. The machine is capable of applying pressure as high as 1.5 kbar (150 MPa). It is also capable of applying a static preload to simulate a lithostatic stress in the specimen.

Specimen Preparation--The rock specimens are cored into 4-inch (10.2 cm)-diameter by 14-inch (35.5 cm)-long sections from one large block of grout. The specimens are then cut to the desired length [3, 4, or 6 inches (7.6, 10.2, or 15.2 cm), as desired]. The tunnel opening is drilled through the specimen at midheight as shown in Figure C-3(a) (a recess for the liner end fitting is also cut into the rock at the tunnel opening). Also shown in Figure C-3(a) is a liner

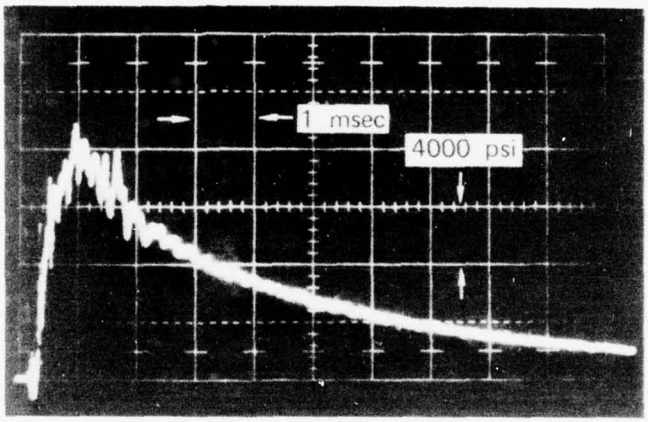

(a) VERTICAL PRESSURE PULSE—STA 4 (AT BOTTOM OF ROCK)

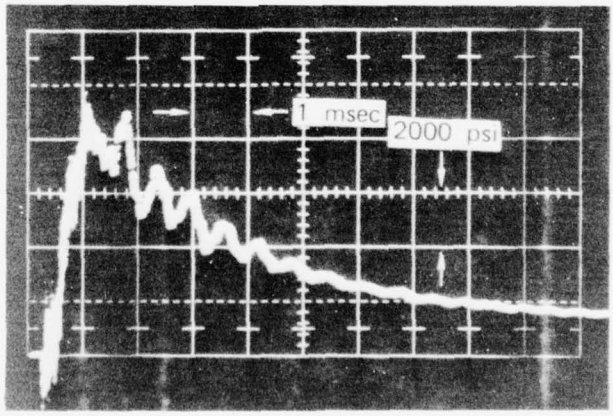

(b) HORIZONTAL PRESSURE PULSE—STA 3 (NEAR MIDHEIGHT OF ROCK)

MP-3743-76

FIGURE C-2 TIME HISTORIES OF APPLIED LOADS—TRIAXIAL LOADING

(a)

(b)

MP-3743-81

FIGURE C-3 SPECIMEN LINER ASSEMBLY

(with backpacking in this case) with end fittings and O-rings for sealing the tunnel entry tube system. Direct contact liners are grouted into the tunnel, and backpacked liners are pressed in without grout, as shown in Figure C-3(b).

Figure C-4 shows an exploded view of the tunnel liner assembly for an undrained test (water is not permitted to drain from the saturated rock during the test). One end of the liner is sealed by being soldered to the end fitting. The other end is sealed by an O-ring in the end fitting as shown. The liner assembly for drained tests (water drains from the saturated rock during the test) is shown in Figure C-5. As in the undrained case, one end of the liner is soldered to the liner end fitting. This end of the tunnel is sealed so that photographs may be taken without being obscured by leaking water. At the other end of the liner, a gap is left between the liner and the end fitting so that water may drain from the rock during the test.

After the liner and end fittings are in place, copper end caps [Figure C-6(a)] are placed on the specimen to seal the top and bottom [Figure C-6(b)]. Strain gages are mounted circumferentially to the caps, as shown, to measure the lateral expansion of the specimen during the test. Next, a Wilson seal [Figure C-7(a)] is placed around the midsection of the sample [Figure C-7(b)] to seal it from the surrounding fluid in the testing machine. The Wilson seal consists of a section of a motorcycle inner tube with two small holes cut in the center. The Wilson seal is stretched over the specimen as shown.

Machine Assembly--After the specimen has been prepared, it is placed in the testing machine during the assembly process. The machine (Figure C-8) is assembled by stacking one part onto another in the following sequence:

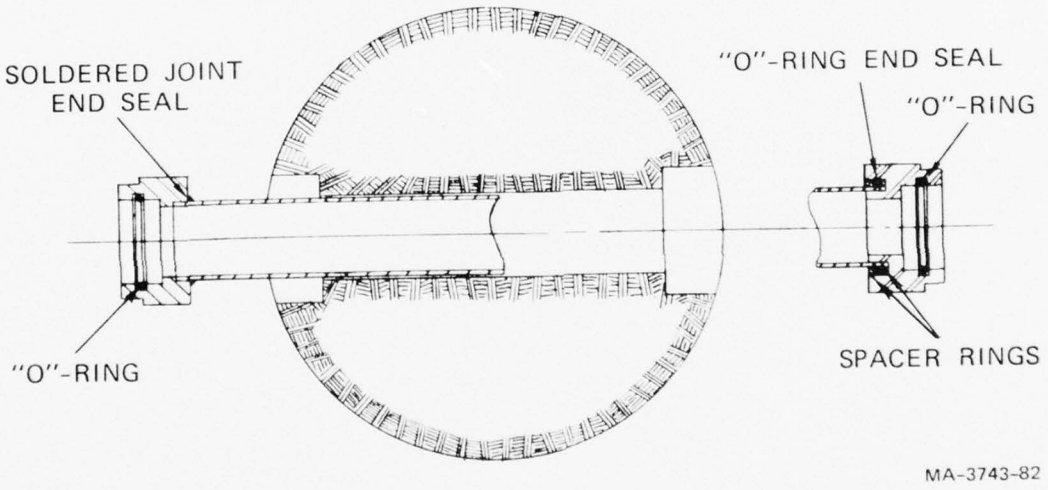

FIGURE C-4 LINER ASSEMBLY FOR UNDRAINED TEST

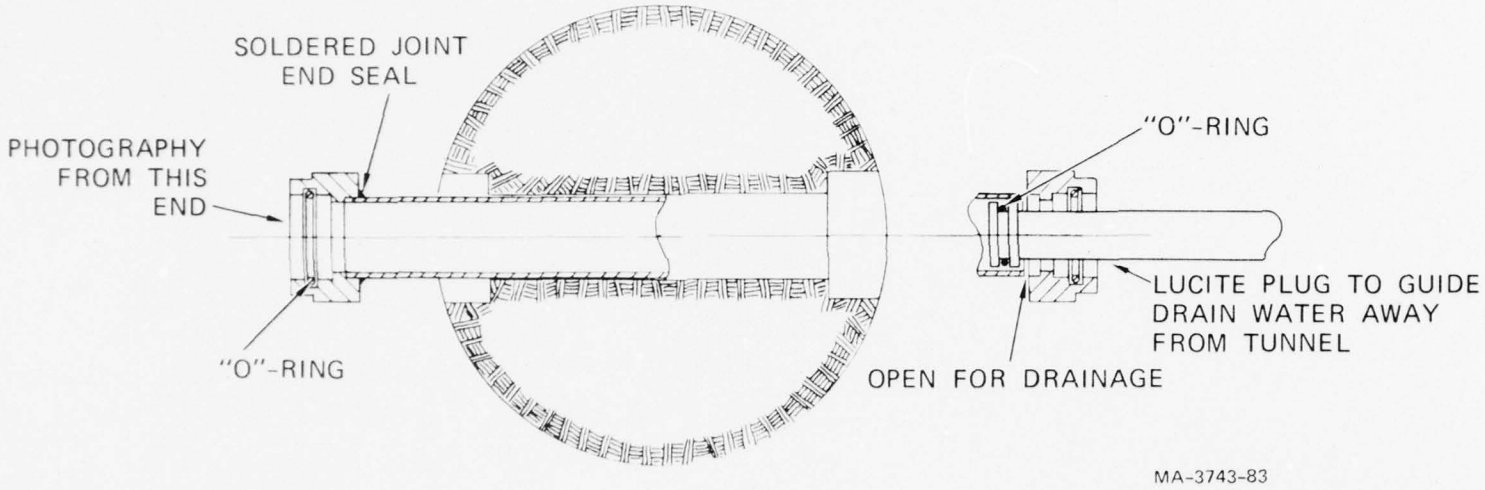

FIGURE C-5 LINER ASSEMBLY FOR DRAINED TEST

AD-A043 398 STANFORD RESEARCH INST MENLO PARK CALIF F/G 8/7
LABORATORY INVESTIGATION OF ROCK CAVITY REINFORCEMENT.(U)
APR 76 T C KENNEDY, H E LINDBERG DNA001-75-C-0101
UNCLASSIFIED DNA-4023F NL

3 OF 3
AD
A043 398

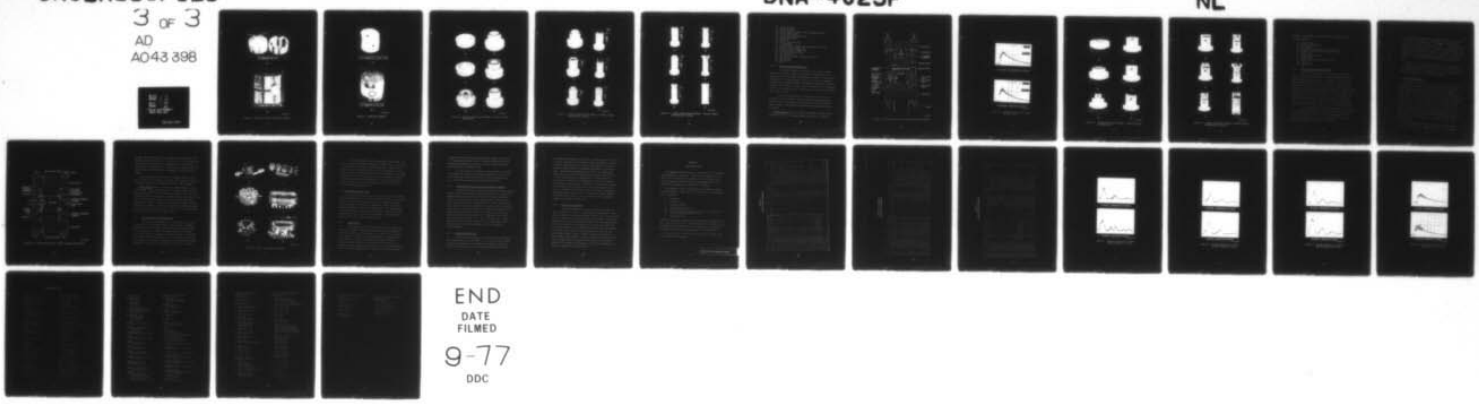

END
DATE
FILMED
9-77
DDC

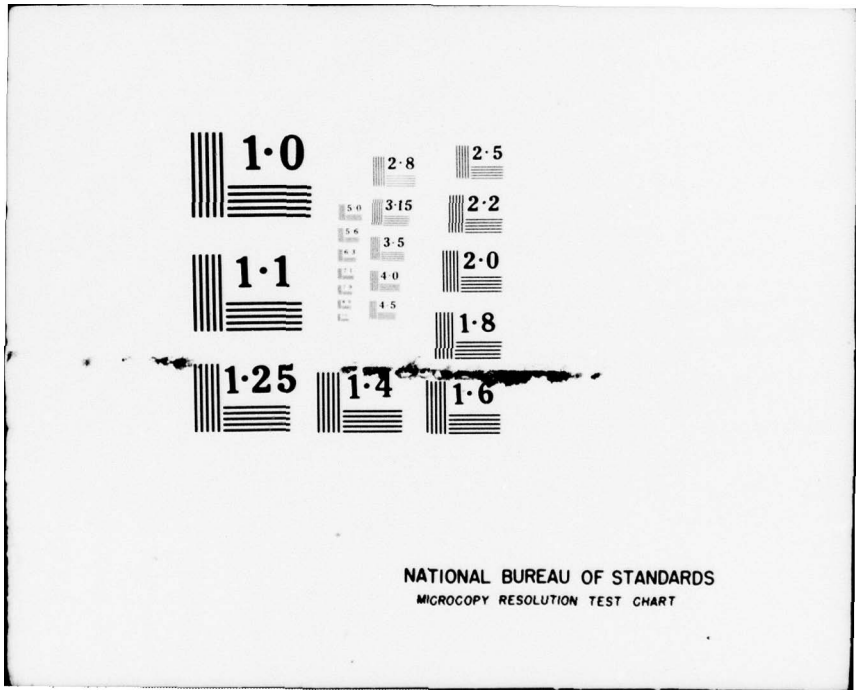
1·0
1·1
1·25
1·4
1·6
1·8
2·0
2·2
2·5
2·8
3·15
3·5
4·0
4·5
5·0
5·6
6·3
NATIONAL BUREAU OF STANDARDS
MICROCOPY RESOLUTION TEST CHART

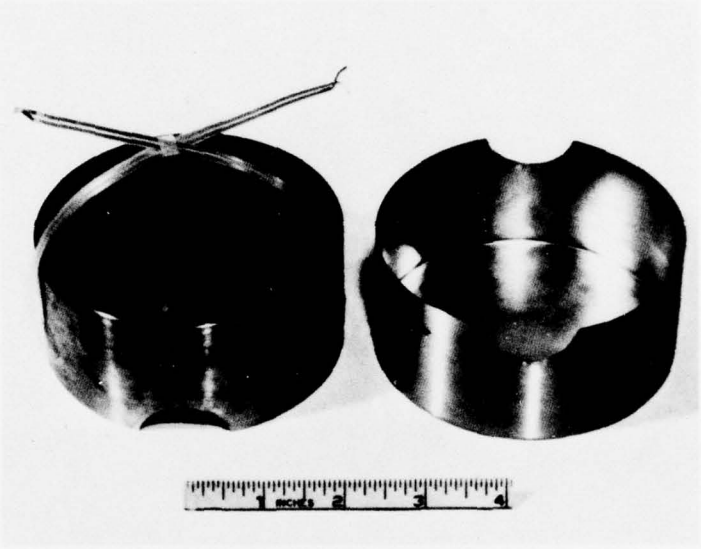

(a)

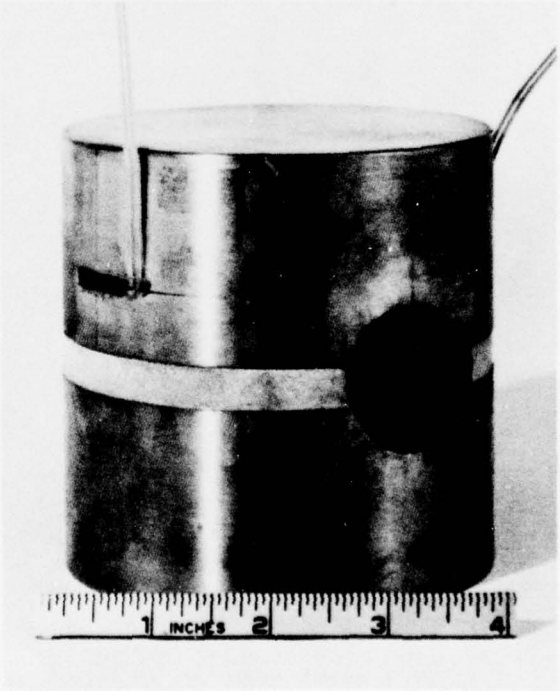

(b)

MP-3743-84

FIGURE C-6 COPPER END CAP AND STRAIN GAGE ASSEMBLY

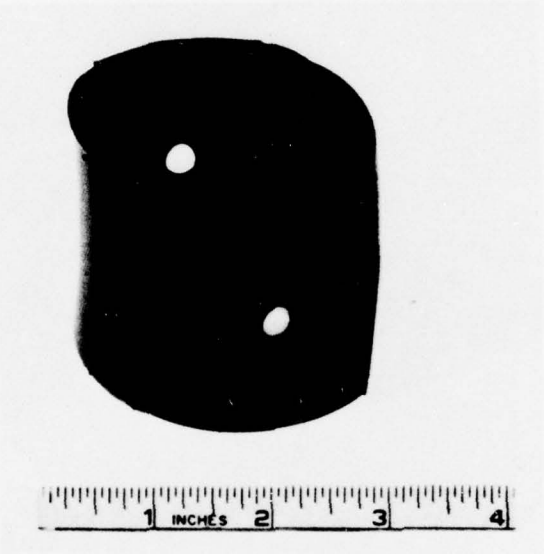

(a)

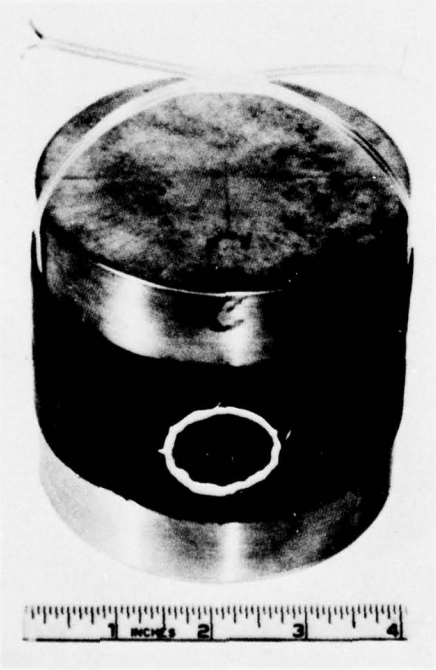

(b)

MP-3743-85

FIGURE C-7 WILSON SEAL ASSEMBLY

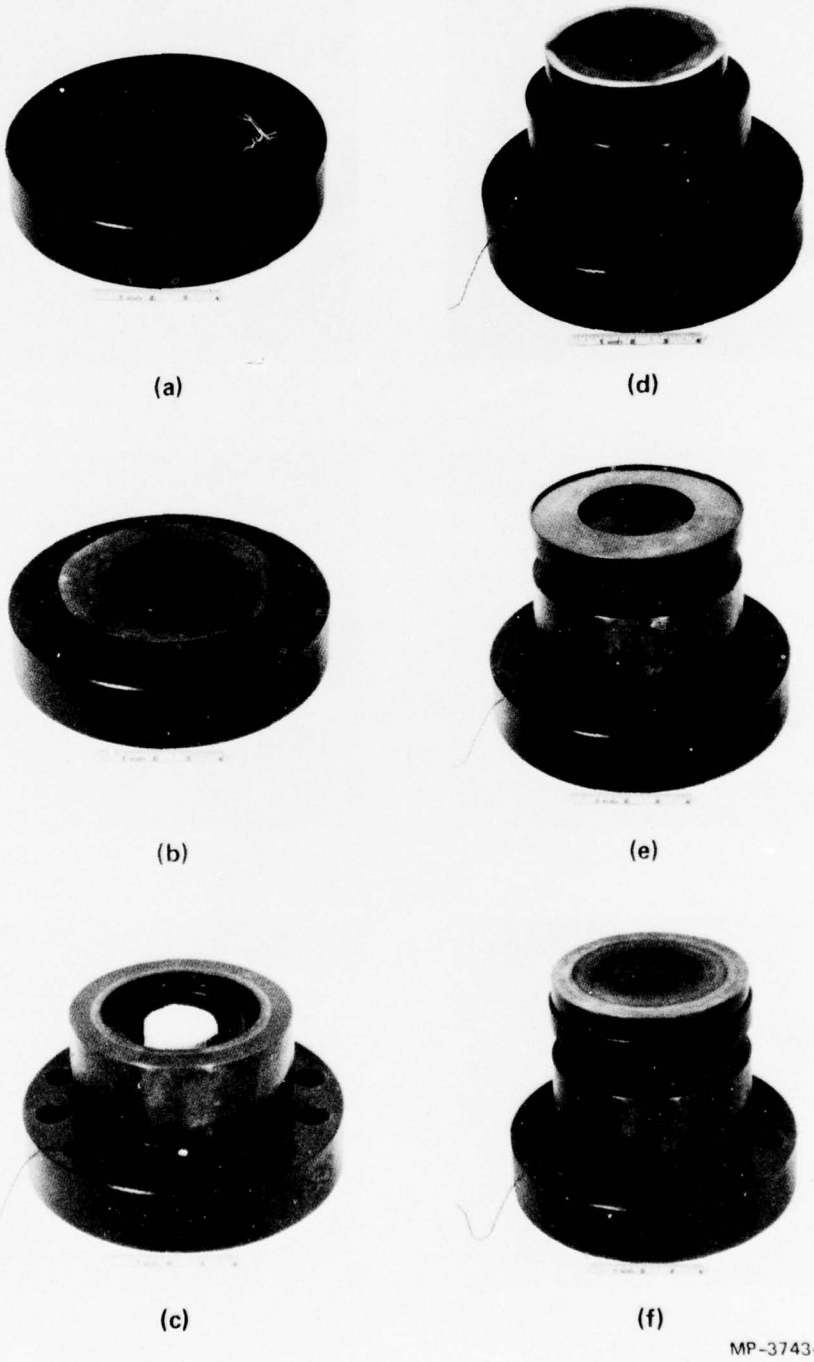

FIGURE C-8 DYNAMIC TESTING MACHINE ASSEMBLY—TRIAXIAL LOADING CONFIGURATION

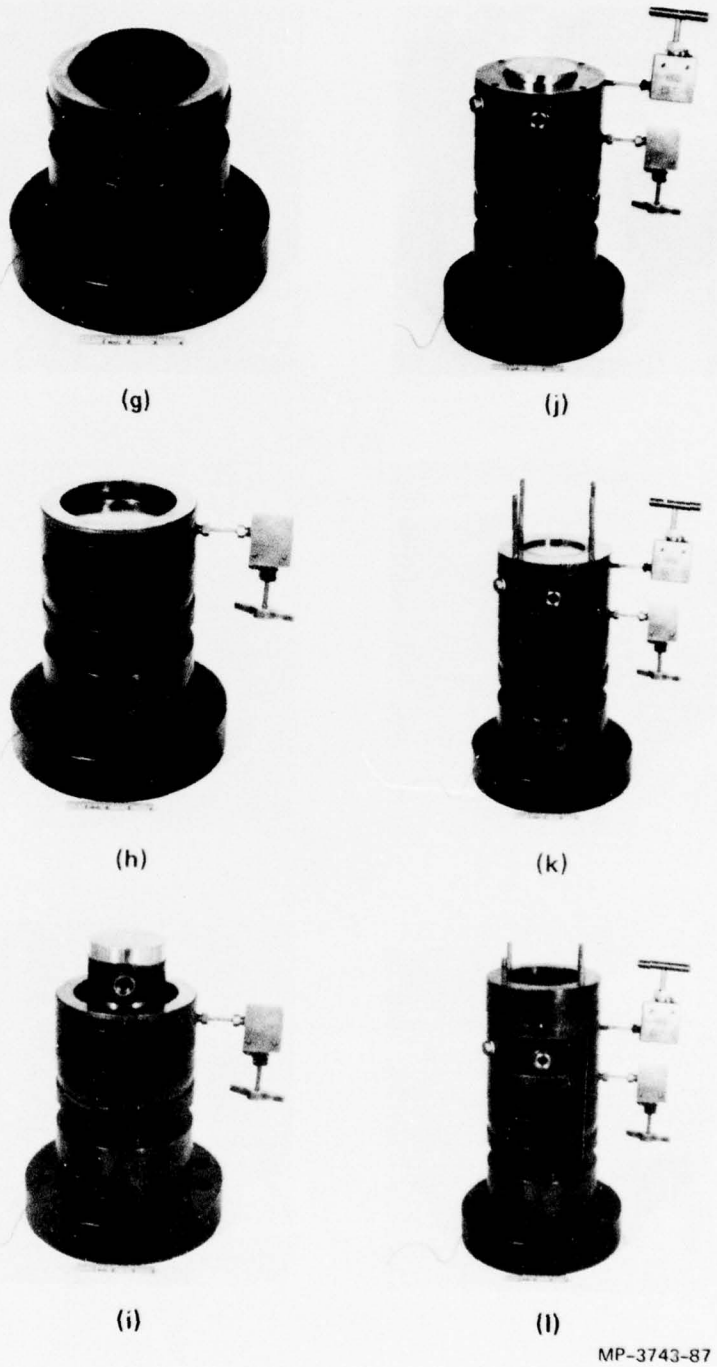

FIGURE C-8 DYNAMIC TESTING MACHINE ASSEMBLY—TRIAXIAL LOADING CONFIGURATION (Continued)

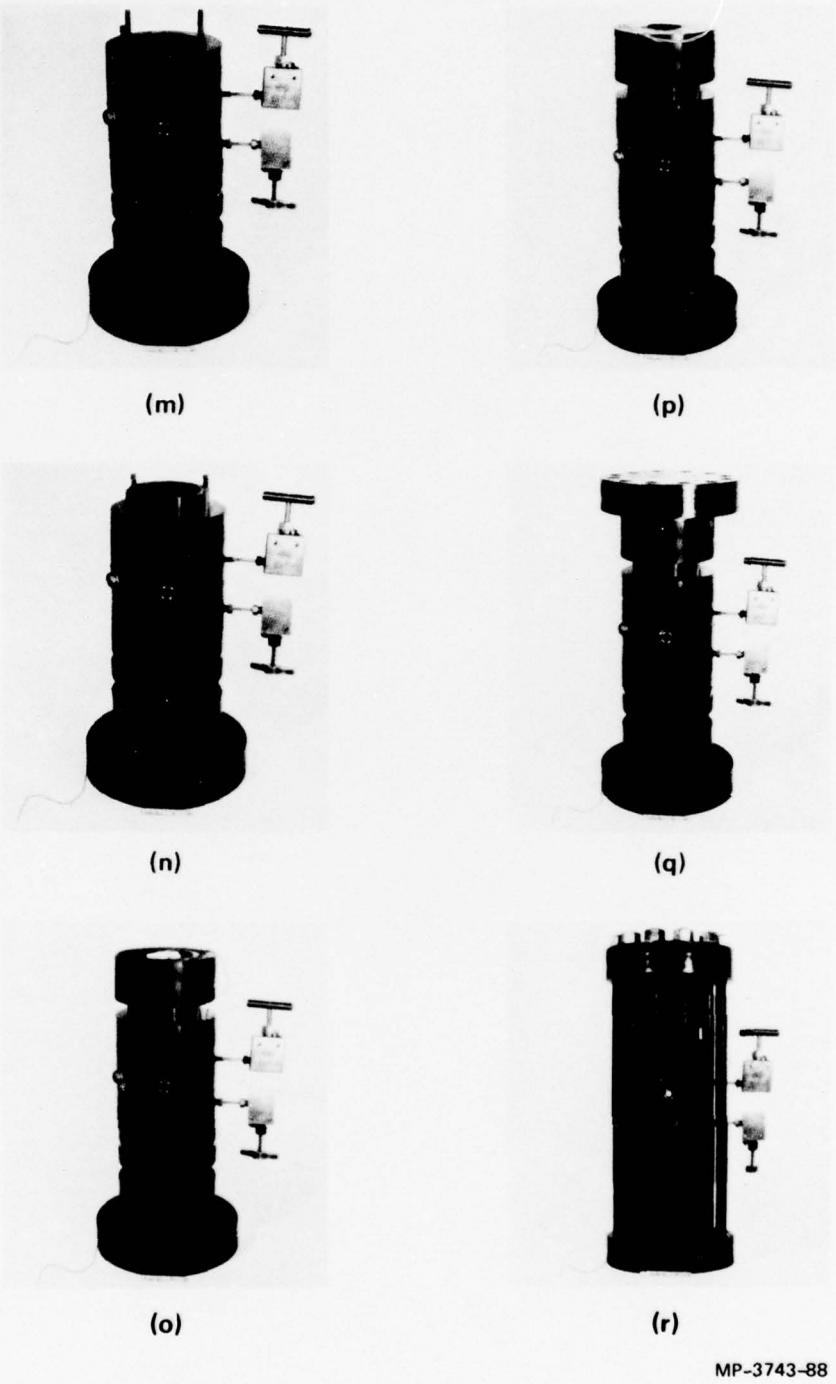

FIGURE C-8 DYNAMIC TESTING MACHINE ASSEMBLY—TRIAXIAL LOADING CONFIGURATION (Concluded)

(a) bottom end plate
(b) bottom vent ring
(c) bottom explosive chamber ring and explosive charge
(d) bottom orifice plate
(e) bottom expansion chamber ring
(f) bottom baffle plate
(g) Bellofram
(h) receiver plate and ring
(i) rock specimen
(j) lateral pressure chamber ring and tunnel entry tubes
(k) extender ring and dowel pins
(l) vertical pressure chamber ring
(m) top baffle plate and spacer
(n) top orifice plate
(o) top explosive chamber and explosive charge
(p) top vent ring
(q) top end plate
(r) bolts.

C.1.2 Isotropic Loading Configuration

An assembly drawing of the dynamic tester in the isotropic loading configuration is shown in Figure C-9. The operation of the machine in this configuration is essentially the same as in the triaxial configuration. The main difference is that it has only one explosive chamber and one expansion chamber. The specimen is completely surrounded by fluid, which transmits the load from the gas pressure in the expansion chamber to the specimen. Again, a Bellofram acts as an interface between the gas and the fluid.

Pressures are monitored at various points in the fluid by piezoelectric gages, as shown. Figure C-10 shows typical pressures at Stations 1 and 3. The pressure-time histories at both locations are almost identical, indicating that undesirable wave propagation effects are minimal.

Machine Assembly--Figure C-11 shows the assembly procedure for the dynamic machine in the isotropic loading configuration. As before,

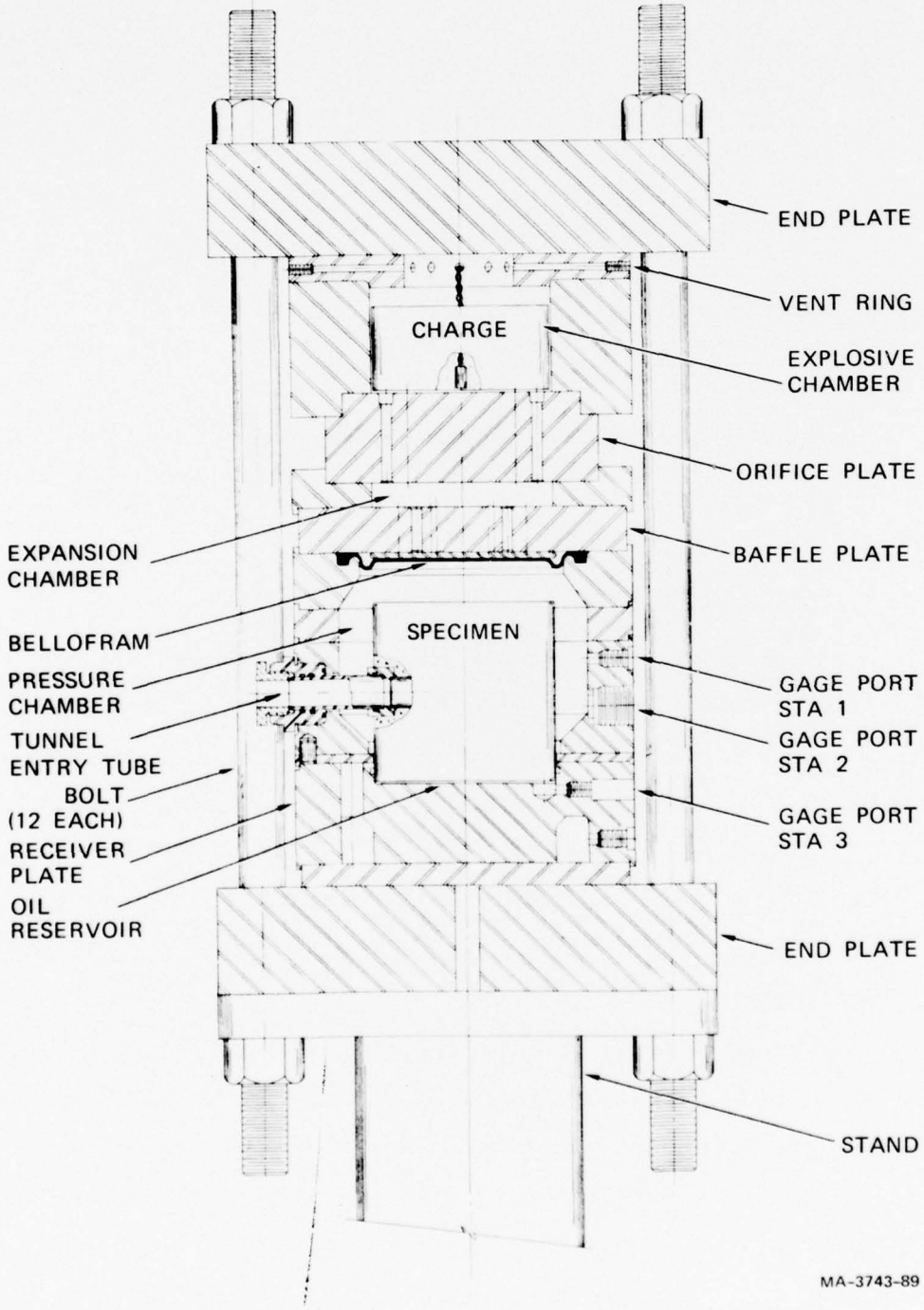

FIGURE C-9 DYNAMIC TESTING MACHINE—ISOTROPIC LOADING CONFIGURATION

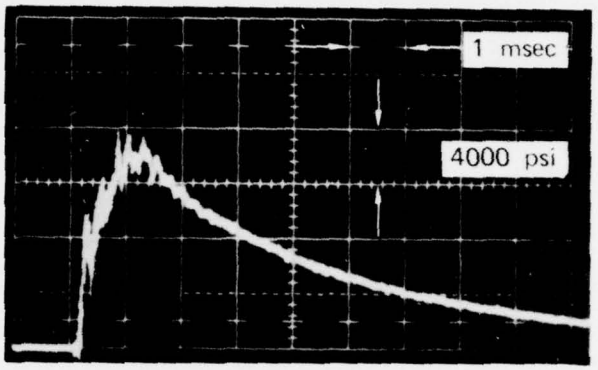

(a) STATION 1 (MIDHEIGHT OF ROCK)

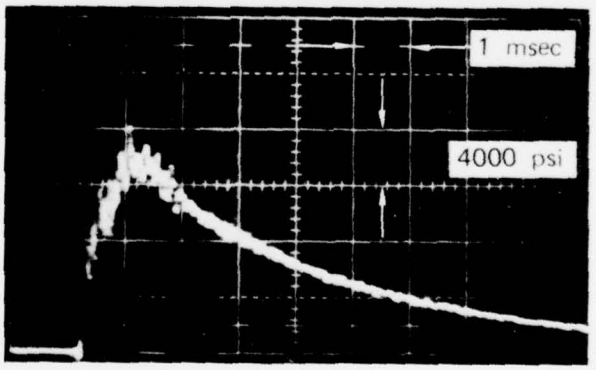

(b) STATION 3 (BOTTOM OF ROCK)

MP-3743-78

FIGURE C-10 TIME HISTORIES OF APPLIED LOADS— ISOTROPIC LOADING

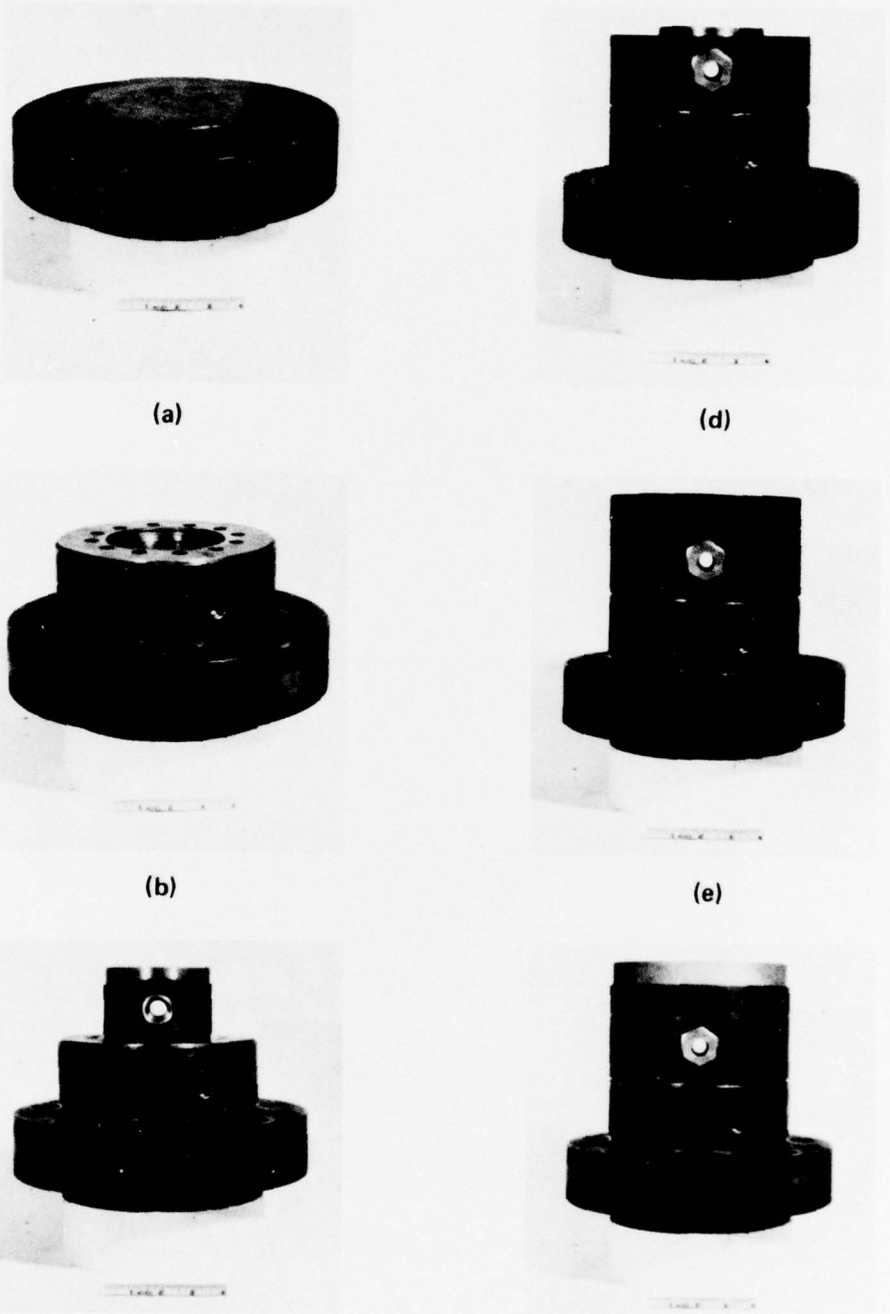

FIGURE C-11 DYNAMIC TEST MACHINE ASSEMBLY—ISOTROPIC LOADING CONFIGURATION

(g)

(j)

(h)

(k)

(i)

(l)

MP-3743-91

FIGURE C-11 DYNAMIC TEST MACHINE ASSEMBLY—ISOTROPIC LOADING CONFIGURATION (Concluded)

assembly is accomplished by stacking one part onto another in the following sequence:

(a) bottom end plate
(b) specimen receiver plate
(c) rock specimen
(d) main pressure chamber ring with entry tubes
(e) pressure chamber extender ring and Bellofram
(f) baffle plate
(g) expansion chamber ring
(h) orifice plate
(i) charge chamber ring and explosive charge
(j) vent ring
(k) top end plate
(l) bolts

C.1.3 Test Procedure and Instrumentation

After the test preparations are completed, the specimen is loaded by detonating the explosive. Pressure transducers located at various points in the test machine record pressure. For the triaxial loading configuration (Figure C-1), pressures are recorded at five locations. Station 1 is in the vertical pressure chamber. Stations 2 and 3 are located in the lateral pressure chamber, with Station 2 being slightly above the center of the specimen and Station 3 slightly below. Station 4 is located in the oil reservoir in the receiver plate and measures the pressure on the bottom of the specimen. Station 5 is located in one of the holes in the receiver plate, which transmit the load from the lower expansion chamber to the lateral pressure chamber.

For the isotropic loading configuration (Figure C-9), pressures are recorded at three locations. Station 1 is located slightly above the center of the specimen, and Station 2 is located slightly below. Station 3 is located in the oil reservoir in the receiver plate to measure the pressure on the bottom of the specimen.

High-speed photographs of the deforming tunnel are taken with a Hycam camera. The framing rate is determined from fiducial marks recorded on the film by a timing light, pulsed by a standard oscillator. Zero time is recorded by pulsing a flashbulb simultaneously with the electronic detonating unit that initiates the explosive. Elapsed time between events is determined simply by the number of frames and the framing rate. Percent collapse may be computed from relative image sizes.

After the test, the specimen is removed from the testing machine and tunnel diameter changes are measured with a small hole gage. Also, the outside dimensions of the specimen are measured with a micrometer. Finally, the specimen is sectioned and photographed.

C.2 Static Testing Machine

The static testing machine provides static triaxial loading of our specimens while maintaining the tunnels at atmospheric pressure and providing photographic and instrumentation access. The loads are applied hydraulically by high-pressure hand pumps. An assembly drawing of the machine is shown in Figure C-12. Like the dynamic tester, this machine consists of a stack of thick rings held together with end plates and ten bolts around the circumference. The rock specimen, which is 4 inches (10.2 cm) in diameter and 3, 4, or 6 inches (7.6, 10.2, or 15.2 cm) long, rests in the center of the machine, as shown. Viewing ports are provided in the machine (one port is shown on the left of the drawing) at the end of the tunnel to allow photographic coverage of the deformation process and access for a hole gage to measure tunnel diameter changes.

To provide independent control of vertical and lateral pressures for triaxial loading tests, the loading is applied by two hand pumps.

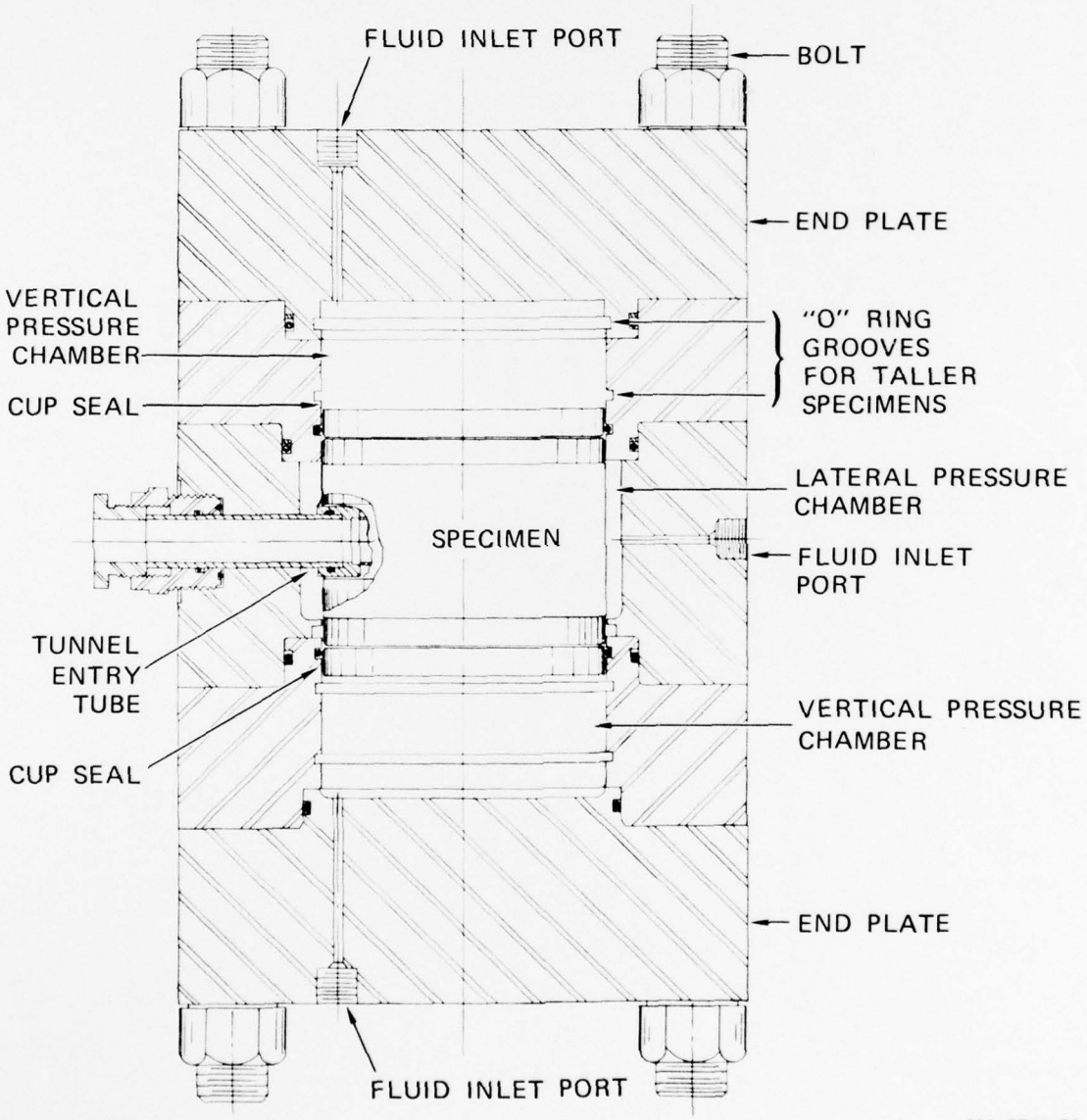

FIGURE C-12 STATIC TESTING MACHINE—TRIAXIAL LOADING CONFIGURATION

The upper and lower chambers are pressurized by one pump, and the side chamber is pressurized by another. Sealing between the side chamber and the upper and lower chambers is accomplished by the cup and O-ring system used in the dynamic tester. O-ring grooves are machined into the chamber walls at various heights to accommodate the different length samples.

The cups and O-rings are not used for isotropic loading, so that oil is free to flow from chamber to chamber. Only one pump is required. The machine has been used to pressures as high as 2 kbar (200 MPa).

Machine Assembly--Figure C-13 shows the assembly procedure for the static machine. Figure C-13(a) shows the entry tube system. After the copper caps and Wilson seal have been placed around the rock, the rock is inserted into the lateral pressure chamber rings shown in Figure C-13(b). The entry tubes are then inserted and strain gage wires connected as shown in Figure C-13(c). The top and bottom pressure chamber rings and end plates are assembled as shown in the exploded view in Figure C-13(d). The bolts are then torqued down [Figure C-13(e)] and the fluid lines and strain gage leads are connected [Figure C-13(f)].

C.2.1 Test Procedure and Instrumentation

During an isotropic loading test, the pressure in the tester is increased in small increments [500 or 1000 psi (3.45 or 6.89 MPa) depending on the rate of tunnel deformation] by a hand-operated pump. After each increment of loading, the tunnel diameter at the center section of the tunnel is measured with a small hole gage. We generally take readings at three orientations [$\theta = 0^{o}$, 45^{o}, 90^{o} (0, 0.785, 1.57 rad)] unless we are prevented from doing so by the presence of a buckle. Photographs of the inside of the tunnel are also taken at this time.

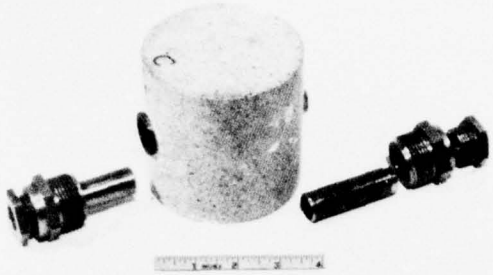

(a)

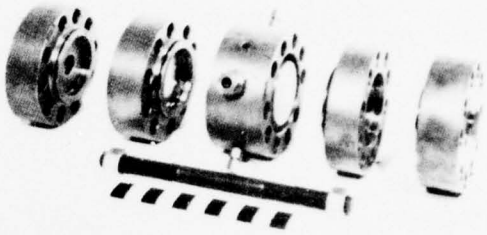

(d)

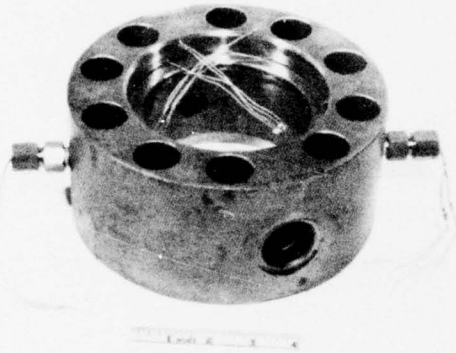

(b)

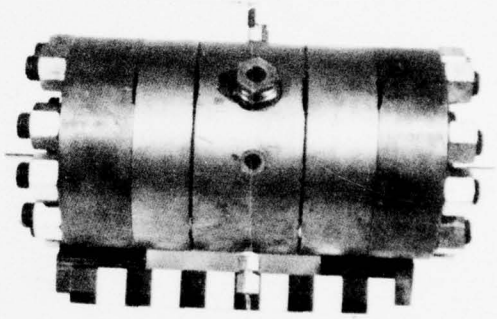

(e)

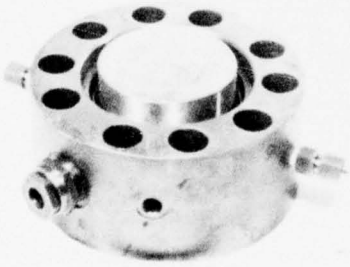

(c)

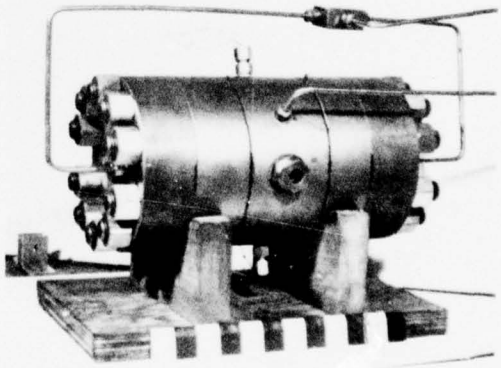

(f)

MP-3743-93

FIGURE C-13 STATIC TESTING MACHINE ASSEMBLY

A similar procedure is used for uniaxial-strain loading. In this case, the vertical pressure increment is applied first. This causes the rock specimen to expand a small amount laterally, which in turn causes the strain gages mounted on the side of the specimen to record a positive strain. The lateral pressure is then increased until the strain gages indicate zero average strain. Since the strain gages are mounted at different locations on the specimen, they do not record identical strains. However, it has been our experience that they do not differ by more than $\pm$ 0.03 percent strain.

C.3 Testing Machine Improvements

The testing machines used in this project were originally developed on a previous DNA project [1]. However, during the course of the current project, several modifications were made to the machines to improve their performance and extend their capabilities. These modifications produced improvements in the four following areas: (1) tunnel access, (2) sealing between vertical and lateral pressure chambers, (3) dynamic pressure pulses, and (4) general test procedures. The modifications made in each of these areas are described next.

C.3.1 Tunnel Access

The tunnel access system was modified in both the static and dynamic test machines to provide a passage through the test apparatus wall with an opening the full diameter of the tunnel. The new system, which consists of a relatively thin hollow tube of very high strength steel (Vascomax), replaces the old thick tube system in which the opening was smaller than the tunnel diameter. The objective is to provide unobstructed physical and optical access. Unobstructed physical access has enabled deformation as a function of load to be monitored by

a small hole gage that measures tunnel diameter changes at the center of the specimen during static tests. Unobstructed optical access has permitted photographs to be taken of the tunnel deformation process during both static and dynamic tests.

An entry tube with an opening the full diameter of the tunnel was provided, and a liner sealing system was devised to prevent water in the saturated rock from jetting into the liner and obscuring the view. This system was described in detail in Section C.1.1.

C.3.2 Sealing Between Vertical and Lateral Pressure Chambers

Because the difference in pressure between the vertical pressure chamber and the lateral pressure chamber can become quite large during a uniaxial strain test, sealing between these two chambers can become difficult, especially in the static testing machine. This seal in the static fixture was originally accomplished by an O-ring. Unfortunately, this system was found to be inadequate at high load levels, particularly with soft rock. It was then replaced by a complicated diaphragm sealing system that performed well for fairly stiff rocks (e.g., 6B) but was still not effective for softer rocks (e.g., HARM grout) that undergo large volume changes during a test. To test such materials, a copper cup seal, which is described in Section C.1.1, was developed. This system is easy to use and has performed well for pressures up to 2 kbars (200 MPa).

C.3.3 Dynamic Pressure Pulses

The pressure-time histories of our initial dynamic experiments were scaled pulses of a nuclear burst) i.e., rise time of about 100 μs and duration of about 1 ms. Unfortunately, the pressure transducers located at various points in the testing machine indicated that some

undesirable wave propagation effects were occurring because of the fast rise time, especially in the isotropic loading configuration. Instead of having a smooth pulse with a rapid rise and exponential decay, we obtained a pulse having many sharp peaks superimposed on the desired pulse. These peaks were apparently the result of the loading wave reverberating in the fluid. Fortunately, as discussed in Section 2.3, it is not necessary that our loading pulse be closely scaled to a nuclear burst. Therefore, we increased the rise time of the pulse to 1 ms and the duration to 10 ms. The effect of stretching out the pulse in this manner is to reduce the effect of the reverberations of the wave to a tolerable level so that the pulse that loads our specimen is reasonably smooth (see Figure C-10). To reduce undesirable "spikes" in the pulse still further, we use a baffle plate in the expansion chamber as discussed in Section C.1.1.

C.3.4 General Test Procedures

Several improvements of a general nature were also made and will be listed here. First, the testing machines were modified to give them the capability of accepting specimens 4 inches (10.2 cm) and 6 inches (15.2 cm) in length as well as the 3-inch (7.6 cm) length. The longer specimens are used in the nonsymmetric loading tests where perturbations in the stress field due to the presence of the tunnel may extend well into the rock medium. Also, a Bellofram is used as an interface between the explosive gases and the fluid that surrounds the specimen. The Bellofram was found to be more reliable and easier to use than the Mylar membrane used previously. Finally, we found that mounting strain gages to copper caps on the specimen rather than to the rock itself produces more reliable strain readings of the lateral expansion of the specimen, especially for saturated rock.

Appendix D

EXPERIMENTAL DATA

This appendix presents a summary of the results of all the experiments performed on this project. Table D-1 is a summary of all the static tests, and Table D-2 is a summary of all the dynamic tests. This is followed by pressure transducer oscilloscope traces for the dynamic tests discussed in the main body of the report.

Each experiment is given a designation that consists of several letters followed by a hyphen and then a test number. The letters signify the following:

- S - static test
- D - dynamic test
- I - isotropic loading
- UX - uniaxial-strain loading
- TX_ - triaxial loading (the number following TX indicates the lateral confining pressure in ksi)
- C - calibration test

The number following the hyphen indicates the sequential number of the test. Static tests run from 1 to 89 and dynamic tests run from 1 to 40. For example, STX1.0-2 indicates static test number 2; the loading is triaxial with a lateral confining pressure of 1 ksi (6.89 MPa).

Figures D-1 to D-4 give the pressure histories for dynamic tests DI-22, DI-27, DI-28, and DI-38.

Table D-1

STATIC TEST SUMMARY

Test No.	Date	Rock				Liner			Filler		Drainage	No. of E-Gages	No. of P-Gages	Hole Gage	Camera	$P_{V_{max}}$ (psi)	$P_{H_{max}}$ (psi)	$\Delta D_V/D_V$ (%)	$\Delta D_H/D_H$ (%)	Observations
		No.	Size	% Sat.	Cavity Dia. (in.)	Mat'l	I.D. (in.)	Wall (in.)	Mat'l	Wall (in.)										
STX 0.0-1	10/25/74	6A7-1	4x3	20	0.625	none	-	-	-	-	-	0	1	0	0	7,500	0	-	-	Specimen fractured vertically and horizontally.
STX 1.0-2	10/30/74	6A7-2	4x3	20	0.625	none	-	-	-	-	-	0	2	0	0	10,200	1,000	-	-	Specimen fractured vertically and horizontally.
STX 3.0-3	10/31/74	6A7-3	4x3	20	0.625	none	-	-	-	-	-	0	2	0	0	8,500	3,000	-	-	Oil leaked into rock.
SUX-4	11/1/74	6A7-4	4x3	20	0.673	steel	0.625	0.020	HS	0.004	-	2	2	0	0	16,000	5,900	-	-	Diaphram end seals lost due to rock fracture.
STX 4.0-5	11/12/74	6A7-5	4x3	20	0.625	none	-	-	-	-	-	0	2	0	0	15,000	4,000	-	-	Specimen fractured vertically and horizontally.
SUX-6	11/12/74	6A7-6	4x3	20	0.625	none	-	-	-	-	-	2	2	0	0	20,000	7,400	6	-25	Springline flaking began at P_V = 11,000 psi.
SUX-7	11/13/74	6A7-7	4x3	20	0.673	steel	0.625	0.020	HS	0.004	-	2	2	0	0	25,000	10,000	7	-2	No fractures in rock.
STX 0.0-8	11/13/74	6A7-8	4x3	20	0	-	-	-	-	-	-	0	1	-	0	9,600	0	-	-	Reached limit of Baldwin. No visible damage.
STX 0.0-9	11/13/74	6A7-9	4x3	20	0	-	-	-	-	-	-	0	1	-	0	9,600	0	-	-	Reached limit of Baldwin. No visible damage.
STX 0.0-10	11/14/74	6B2-1	4x3	20	0	-	-	-	-	-	-	0	1	-	0	5,670	0	-	-	Several vertical fractures were visible.
STX 0.0-11	11/14/74	6B2-2	4x3	20	0	-	-	-	-	-	-	0	1	-	0	5,850	0	-	-	Several vertical fractures were visible.
SUX-12	11/14/74	6B2-3	4x3	20	0.625	none	-	-	-	-	-	2	2	0	0	13,000	7,000	-	-	Test invalid due to improper loading path.
SUX-13	11/18/74	6B2-4	4x3	20	0.625	none	-	-	-	-	-	2	2	0	0	13,600	5,300	40	-5	Springline flaking but no fractures in rock.
STX 0.0-14	11/19/74	6A7-10	4x3	20	0	-	-	-	-	-	-	0	1	0	0	12,800	0	-	-	Pieces fractured off boundaries.
STX 0.0-15	11/19/74	6B2-5	4x3	20	0.625	none	-	-	-	-	-	0	1	0	0	4,500	0	-	-	Vertical and horizontal fractures at springline
SUX-16	11/21/74	6B2-6	4x3	20	0.673	steel	0.625	0.020	HS	0.004	-	2	2	0	0	23,000	8,900	24	-6	No fractures in rock.
SUX-17	11/26/74	6B2-7	4x3	20	0.625	none	-	-	-	-	-	2	2	0	0	18,000	7,400	13	-15	Springline flaking began at P_V = 8,500 psi.
STX 0.0-18	12/2/74	6A7-11	4x3	90	0	-	-	-	-	-	yes	0	1	-	0	9,100	0	-	-	Severe fracturing of rock.
STX 0.0-19	12/2/74	6A7-12	4x3	90	0	-	-	-	-	-	yes	0	1	-	0	8,700	0	-	-	Several vertical fractures were visible.
STX 0.0-20	12/2/74	6B2-8	4x2.5	90	0	-	-	-	-	-	yes	0	1	-	0	5,840	0	-	-	Several vertical fractures were visible.
STX 0.0-21	12/2/74	6B2-9	4x2.5	90	0	-	-	-	-	-	yes	0	1	-	-	5,440	0	-	-	Several vertical fractures were visible.
SI-22	12/11/74	6B2-10	4x3	90	0.625	none	-	-	-	-	yes	0	1	0	Nikon	20,000	20,000	-	-	Oil leak developed during test.
STX 0.0-23	12/13/74	6B2-11	4x3	97	0	-	-	-	-	-	yes	0	1	-	0	4,560	0	-	-	Several vertical fractures were visible.
SI-24	12/16/74	6B2-12	4x3	97	0.625	none	-	-	-	-	yes	0	1	0	Nikon	9,000	9,000	-	-	Wilson seal failed.
SI-25	12/18/74	6B2-13	4x3	97	0.625	none	-	-	-	-	yes	0	1	0	Nikon	9,500	9,500	-	-	Wilson seal failed.
STX 0.0-26	12/18/74	6B2-14	4x3	100	0	-	-	-	-	-	yes	0	1	-	0	3,670	0	-	-	Several vertical fractures were visible.
STX 0.0-27	12/19/74	6B2-15	4x3	100	0	-	-	-	-	-	yes	0	1	-	0	3,280	0	-	-	Several vertical fractures were visible.
STX 0.0-28	12/19/74	6B2-16	4x3	100	0	-	-	-	-	-	yes	0	1	-	0	3,310	0	-	-	Several vertical fractures were visible.
SI-29	12/23/74	6B2	4x3	90	0.625	none	-	-	-	-	yes	0	1	0	0	2,500	2,500	-	-	Wilson seal failed.
SI-30	12/27/74	6B2	4x3	20	0.625	none	-	-	-	-	-	0	1	0	0	19,000	19,000	-	-	Specimen fractured horizontally thru tunnel.
SI-31	12/30/74	6B2-17	4x3	97	0.625	none	-	-	-	-	yes	0	1	0	Nikon	15,500	15,500	-	-	Entry tube O-ring failed.
SI-32	1/7/75	6B2-18	4x3	97	0.625	none	-	-	-	-	yes	0	1	0	Nikon	19,000	19,000	-	-	Pressure lost at 19,000 psi.
SCI-33	1/8/75	Steel	4x3	-	-	-	-	-	-	-	-	0	1	-	-	27,500	27,500	-	-	Entry tube O-ring failed.
SI-34	1/9/75	6B2-19	4x3	97	0.625	none	-	-	-	-	yes	0	1	0	Nikon	18,000	18,000	-	-	Rock fractured and oil leaked into tunnel.
SI-35	1/10/75	6B2-20	4x3	97	0.641	steel	0.625	0.006	HS	0.002	yes	0	1	0	Nikon	20,500	20,500	8	7.5	Liner buckled.
SI-36	1/13/75	6B2-21	4x3	97	0.250	none	-	-	-	-	yes	0	1	0	Nikon	24,500	24,500	-	-	Slight tunnel damage.
SI-37	1/20/75	6B2-22	4x3	97	0.657	steel	0.625	0.012	HS	0.004	yes	0	1	1	0	-	-	-	-	Aborted test due to seal damage during assembly
STX 0.0-38	1/20/75	6B2-23	4x3	97	0	-	-	-	-	-	yes	0	1	0	0	4,800	0	-	-	Several vertical fractures were visible.
STX 0.0-39	1/20/75	6B2-24	4x3	100	0	-	-	-	-	-	yes	0	1	0	0	3,900	0	-	-	Several vertical fractures were visible.
SUX-40	1/21/75	HARM-1	4x3	dry	0.655	steel	0.625	0.012	HS	0.003	-	2	2	1	0	3,500	1,650	22	12	Liner ovaled. No fractures in rock.
SUX-41	1/22/75	HARM-2	4x3	dry	0.687	steel	0.625	0.025	HS	0.006	-	2	2	1	0	1,900	680	5.5	-	Oil leaked into tunnel.
SUX-42	1/23/75	HARM-3	4x3	dry	0.3455	steel	0.3125	0.025	HS	0.004	-	2	2	1	0	3,500	1,420	25	-	Liner ovaled. No fractures in rock.
SUX-43	1/24/75	HARM-4	4x3	dry	0.483	steel	0.437	0.017	HS	0.006	-	2	2	1	0	4,000	1,690	17.7	-	Liner ovaled. No fractures in rock.
SUX-44	1/27/75	HARM-5	4x3	dry	0.786	steel	0.625	0.025	HS	0.006	-	2	2	1	0	2,750	1,110	17.2	-	Liner ovaled. No fractures in rock.
SUX-45	1/30/75	HARM-6	4x3	dry	0.687	steel	0.625	0.025	HS	0.006	-	2	2	1	0	4,250	1,870	21.5	-	Liner ovaled. No fractures in rock.
SUX-46	1/31/75	HARM-7	4x3	dry	0.483	steel	0.437	0.017	HS	0.006	-	2	2	1	0	4,000	1,690	23	-	Liner ovaled. No fractures in rock.
SCTX0.0-47	2/5/75	Steel	4x3	-	-	-	-	-	-	-	-	0	1	-	-	27,500	0	-	-	Cap seal functioned properly.
SUX-48	2/6/75	HARM-8	4x3	dry	0	-	-	-	-	-	-	2	2	-	-	4,000	3,900	-	-	Oil soaked into specimen.
STX 0.0-49	2/13/75	6A6-1	4x3	20	0	-	-	-	-	-	-	0	1	-	0	9,100	0	-	-	Reached limit of Baldwin. No visible damage.
STX 0.0-50	2/13/75	6A6-2	4x3	20	0	-	-	-	-	-	-	0	1	-	0	9,100	0	-	-	Reached limit of Baldwin. No visible damage.
STX 0.0-51	2/13/75	6A6-3	4x3	20	0	-	-	-	-	-	-	0	1	-	0	9,100	0	-	-	Reached limit of Baldwin. No visible damage.
STX 0.0-52	2/13/75	6A6-4	4x3	20	0	-	-	-	-	-	-	0	1	-	0	9,100	0	-	-	6A6 rock is comparable in strength to 6A7 rock.

Table D-1 (Concluded)
STATIC TEST SUMMARY

Test No.	Date	Rock				Liner			Filler		Drainage	No. of E-Gages	No. of P-Gages	Hole Gage	Camera	P_{Vmax} (psi)	P_{Hmax} (psi)	$\Delta D_V/D_V$ (%)	$\Delta D_H/D_H$ (%)	Observations
		No.	Size	% Sat	Cavity Dia. (in.)	Mat'l	I.D. (in.)	Wall (in.)	Mat'l	Wall (in.)										
SI-53	2/19/75	6B2-25	4x3	100	0.683	steel	0.625	0.025	HS	0.004	yes	0	1	0	0	6,000	6,000	-	-	Test was invalid due to fluid leakage.
SI-54	2/21/75	6B2-25	4x3	100	0.683	steel	0.625	0.025	HS	0.004	yes	0	1	1	0	15,000	15,000	-	-	Specimen chamber seal failed.
SI-55	2/21/75	6B2-26	4x3	100	0.645	steel	0.625	0.006	HS	0.004	yes	0	1	1	0	22,000	22,000	22.4	22.4	Liner buckling started at 7,500 psi.
SI-56	2/24/75	6B2-27	4x3	100	0.658	steel	0.625	0.012	HS	0.004	yes	0	1	1	0	15,000	15,000	5.8	5.8	Liner bulged at 8,000 psi.
SCI-57	2/26/75	Al	4x3	-	0	-	-	-	-	-	-	0	1	0	0	25,000	25,000	-	-	Leather backup rings tested successfully.
SI-58	2/26/75	6B2-28	4x3	100	0.625	steel	0.448	0.018	BP	0.070	yes	0	1	1	0	25,000	25,000	-0.4	0.7	Backpacked liner showed little deflection.
SCI-59	2/26/75	Steel	4x3	-	0	-	-	-	-	-	-	0	1	0	0	30,000	30,000	-	-	O-ring and backup ring locations reversed.
SCI-60	2/27/75	Steel	4x3	-	0	-	-	-	-	-	-	0	1	0	0	27,000	27,000	-	-	O-ring failure at 27,000 psi.
SI-61	3/3/75	6B2-29	4x3	100	0.625	steel	0.466	0.009	BP	0.070	yes	0	1	1	0	23,000	23,000	1.5	-1.5	Backpacked liner showed little deflection.
SI-62	3/20/75	6B2-30	4x3	100	0.683	steel	0.625	0.025	HS	0.004	no	0	1	1	Nikon	8,000	8,000	-	-	Large bulge in liner occurred.
SI-63	3/26/75	6B2-31	4x3	100	0.645	steel	0.625	0.006	HS	0.004	yes	0	1	1	0	29,000	29,000	26	-	Severe buckling in liner.
SI-64	3/27/75	6B2-32	4x3	100	0.658	steel	0.625	0.012	HS	0.004	yes	0	1	1	0	30,000	30,000	11.8	-	Severe buckling in liner.
SI-65	3/28/75	6B2-33	4x3	100	0.687	steel	0.625	0.025	HS	0.006	no	0	1	1	Nikon	7,400	7,400	-	-	Large bulge in liner occurred as in SI-62.
SCI-66	4/1/75	6B2-33	4x3	100	0.625	none	-	-	-	-	yes	0	1	0	0	22,000	22,000	-	-	Modified seal found to work adequately.
SI-67	4/7/75	6B2-34	4x3	100	0.641	steel	0.625	0.006	HS	0.002	no	0	1	1	Nikon	10,500	10,500	-	-	Large bulge in liner occurred at 8,000 psi.
SI-68	5/13/75	6B2-35	4x3	20	0.687	steel	0.625	0.025	HS	0.006	-	0	1	1	Nikon	500	500	-	-	Wilson seal failed at 500 psi.
SI-69	5/14/75	6B2-35	4x3	20	0.687	steel	0.625	0.025	HS	0.006	-	0	1	1	Nikon	21,000	21,000	5.16	5.38	Successful isotropic cyclic loading test.
SUX-70	5/29/75	6B2-36	4x3	20	0.687	steel	0.625	0.025	HS	0.006	-	2	2	1	Nikon	8,000	2,900	-	-	Wilson seal failed when P_H dropped to zero.
SUX-71	6/6/75	6B2-37	4x3	20	0.687	steel	0.625	0.025	HS	0.006	-	2	2	1	Nikon	8,500	3,150	-	-	Wilson seal failed due to soaking in oil. fluid.
SCUX-72	6/10/75	Dummy	4x3	-	0	-	-	-	-	-	-	0	2	0	0	16,000	12,000	-	-	Wilson seal survived with glycerin as working/
SUX-73	6/18/75	6B2-38	4x3	20	0.687	steel	0.625	0.025	HS	0.006	-	2	2	1	Nikon	15,000	5,950	5.6	-	Successful uniaxial cyclic loading test.
SI-71	6/20/75	6B2-39	4x3	100	0.687	steel	0.625	0.025	HS	0.006	yes	0	1	1	Nikon	25,000	25,000	4.9	5.3	Liner did not buckle.
SUX-75	6/27/75	6B2-40	4x4	20	0.641	steel	0.625	0.006	HS	0.002	-	2	2	1	Nikon	23,500	9,800	17.5	-	Liner buckled at springlines.
SUX-76	6/30/75	6B2-41	4x4	20	0.656	steel	0.625	0.012	HS	0.003	-	2	2	1	Nikon	30,000	13,300	20.0	-	Liner buckled at springlines. tunnel.
SUX-81	10/27/75	6B2-42	4x4	100	0.643	steel	0.625	0.006	HS	0.003	yes	2	2	1	0	20,000	7,700	14.7	-	Rock fractured horizontally at springline of /
SUX-82	10/29/75	6B2-43	4x4	100	0.655	steel	0.625	0.012	HS	0.003	yes	2	2	1	Nikon	19,000	8,600	14.7	-	Liner moderately buckled at springlines.
SUX-83	10/31/75	6B2-44	4x4	100	0.681	steel	0.625	0.025	HS	0.003	yes	2	2	1	0	16,500	8,300	9.13	-0.96	Liner ovaled but did not buckle.
SUX-84	11/5/75	6B2-45	4x4	20	0.681	steel	0.625	0.025	HS	0.003	-	2	2	1	0	18,000	6,950	8.8	-2.56	Liner ovaled but did not buckle.
SUX-85	11/15/75	6B2-46	4x4	20	0.624	steel	0.466	0.009	BP	0.070	-	2	2	1	0	24,500	10,300	5.56	-5.14	Liner ovaled but did not buckle.
SUX-86	11/18/75	6B2-47	4x4	20	0.625	steel	0.450	0.018	BP	0.070	-	2	2	1	0	26,000	10,950	2.22	-2.22	Liner ovaled but did not buckle.
SUX-87	11/19/75	6B2-48	4x4	100	0.625	steel	0.450	0.018	BP	0.070	yes	2	2	1	0	22,000	10,050	4.00	-3.22	Liner ovaled but did not buckle.
SUX-88	11/25/75	6B2-49	4x4	100	0.625	steel	0.467	0.009	BP	0.070	yes	2	2	1	0	22,000	11,400	4.88	-3.21	Liner ovaled but did not buckle.
SUX-89	12/2/75	6B2-50	4x4	100	0.643	steel	0.625	0.006	HS	0.003	yes	2	2	1	Nikon	12,500	4,750	11.35	-	Liner buckled at springlines.

Table D-2
DYNAMIC TEST SUMMARY

Test No.	Date	Rock			Liner			Filler		Drainage	No. of E-Gages	No. of P-Gages	Camera	$P_{V_{max}}$ (psi)	$P_{H_{max}}$ (psi)	Pulse Quality	$\Delta D_V/D_V$ (%)	$\Delta D_H/D_H$ (%)	Observations
		No.	Size	Cavity Dia. (in.)	Mat'l	I.D. (in.)	Wall (in.)	Mat'l	Wall (in.)										
DCUX-1	11/6/74	Steel	4x3	0	-	-	-	-	-	-	0	4	0	20,000	2,000	Poor	-	-	Excessive noise in pulse.
DCUX-2	11/6/74	Steel	4x3	0	-	-	-	-	-	-	0	4	0	4,800	6,000	Poor	-	-	Excessive noise in pulse.
DCUX-3	11/8/74	Steel	4x3	0	-	-	-	-	-	-	0	4	0	9,000	1,200	Poor	-	-	Excessive noise in pulse.
DC-4	11/8/74	Steel	4x3	0	-	-	-	-	-	-	0	2	0	-	5,500	Poor	-	-	Excessive noise in pulse.
DC-5	11/13/74	Steel	4x3	0	-	-	-	-	-	-	0	2	0	-	3,500	Poor	-	-	Excessive noise in pulse.
DCUX-6	11/13/74	Steel	4x3	0	-	-	-	-	-	-	0	3	0	12,000	2,500	Fair	-	-	Pulse improved.
DUX-7	11/15/74	6A7	4x3	20	0.625	none	-	-	-	-	2	3	0	23,000	9,000	Fair	-	-	Specimen fractured horizontally.
DC-8	11/25/74	Steel	4x3	0	-	-	-	-	-	-	0	1	0	-	2,000	Static	-	-	Steel plug ejected due to O-ring leak.
DC-9	11/27/74	Steel	4x3	0	-	-	-	-	-	-	0	1	0	-	2,500	Static	-	-	Gasket leaked oil from chamber.
DC-10	12/9/74	Steel	4x3	0	-	-	-	-	-	-	0	1	0	-	9,000	Static	-	-	Seals function properly.
DC-11	12/10/74	6A7-1	4x3	20	0	-	-	-	-	-	0	1	0	-	2,000	Static	-	-	Specimen fractured horizontally.
DC-12	12/11/74	6A7-2	4x3	20	0	-	-	-	-	-	0	1	0	-	2,000	Static	-	-	Specimen fractured horizontally.
DCI-13	12/17/74	Steel	4x3	0	-	-	-	-	-	-	0	2	0	15,000	15,000	Poor	-	-	Undesirable pulse shape.
DCI-14	12/17/74	Steel	4x3	0	-	-	-	-	-	-	0	2	0	15,000	15,000	Poor	-	-	Undesirable pulse shape.
DCI-15	12/19/74	Steel	4x3	0	-	-	-	-	-	-	0	2	0	14,000	14,000	Poor	-	-	Undesirable pulse shape.
DCI-16	12/30/74	Steel	4x3	0	-	-	-	-	-	-	0	2	0	7,000	7,000	Poor	-	-	Undesirable pulse shape.
DCI-17	12/31/74	Steel	4x3	0	-	-	-	-	-	-	0	2	0	6,600	6,600	Fair	-	-	Pressure too low.
DCI-18	1/2/75	Steel	4x3	0	-	-	-	-	-	-	0	2	0	9,000	9,000	Fair	-	-	Pulse decay not correct.
DCI-19	1/2/75	Steel	4x3	0	-	-	-	-	-	-	0	2	0	12,000	12,000	Poor	-	-	Rise and decay not correct.
DCI-20	1/3/75	Steel	4x3	0	-	-	-	-	-	-	0	2	0	11,000	11,000	Poor	-	-	Pulse decay not correct.
DCI-21	1/3/75	Steel	4x3	0	-	-	-	-	-	-	0	2	0	14,000	14,000	Fair	-	-	Pulse improved.
DI-22	1/6/75	6B2-1	4x3	97	0.625	none	-	-	-	yes	0	2	Hycam	13,600	13,600	Fair	0.5	0.4	Uniform flaking inside tunnel.
DI-23	1/8/75	6B2-2	4x3	97	0.625	none	-	-	-	yes	0	2	Hycam	12,000	12,000	Fair	-	-	Flaking primarily at crown and invert of tunnel.
DI-24	1/14/75	6B2-3	4x3	97	0.625	none	-	-	-	yes	0	2	Hycam	13,200	13,200	Fair	-	-	Uniform flaking inside tunnel.
DI-25	1/17/75	6B2-4	4x3	97	0.250	none	-	-	-	yes	0	2	Hycam	12,000	12,000	Fair	-	-	0.25-inch diameter hole is too small.
DI-26	1/17/75	6B2-5	4x3	97	0.645	steel	0.625	0.012	HS	0.004	yes	0	2	Hycam	12,000	12,000	Fair	-	-	No apparent tunnel damage.
DI-27	1/20/75	HARM-1	4x3	97	0.734	Al	0.625	0.050	HS	0.004	yes	0	2	Hycam	11,200	11,200	Fair	-	-	Liner severely damaged.
DI-28	1/29/75	6B2-6	4x3	97	0.650	steel	0.625	0.006	HS	0.006	yes	0	2	Hycam	16,000	16,000	Fair	5.4	5.6	Liner buckled.
DCI-29	2/3/75	6B2-7	4x3	97	0.750	steel	0.625	0.025	HP	0.100	yes	0	2	Hycam	15,000	15,000	Fair	-	-	Test invalid due to seal loss.
DI-30	2/10/75	HARM-2	4x3	97	0.743	Al	0.625	0.050	HS	0.004	yes	0	2	Hycam	17,000	17,000	Fair	-	-	Specimen crushed due to high pressure.
DCI-31	4/23/75	Dummy	4x3	-	0	-	-	-	-	-	-	0	2	0	5,000	5,000	Poor	-	-	Pressure too low.
DCI-32	4/24/75	Dummy	4x3	-	0	-	-	-	-	-	-	0	2	0	6,000	6,000	Poor	-	-	Wilson seal failed.
DCI-33	5/8/75	Dummy	4x3	-	0	-	-	-	-	-	-	0	2	0	8,000	8,000	Poor	-	-	Bellofram ruptured.
DCI-34	5/9/75	Dummy	4x3	-	0	-	-	-	-	-	-	0	2	0	5,200	5,200	Fair	-	-	Pressure too low.
DCI-35	5/12/75	Dummy	4x3	-	0	-	-	-	-	-	-	0	2	0	10,000	10,000	Fair	-	-	Pressure too low.
DCI-36	5/30/75	Dummy	4x3	-	0	-	-	-	-	-	-	0	2	0	8,000	8,000	Poor	-	-	Testing machine bolts failed.
DCI-37	7/10/75	Dummy	4x3	-	0	-	-	-	-	-	-	0	2	0	10,200	10,200	Poor	-	-	Explosive chamber had unexpected leak.
DI-38	7/11/75	6B2	4x3	100	0.650	steel	0.625	0.006	HS	0.006	no	0	2	Hycam	10,500	10,500	Poor	2.1	1.6	Liner slightly buckled.
DCI-39	8/12/75	Dummy	4x3	-	0	-	-	-	-	-	-	0	2	Hycam	14,800	14,800	Poor	-	-	Undesirable spike in pulse.
DCI-40	8/14/75	Dummy	4x3	-	0	-	-	-	-	-	-	0	2	Hycam	14,800	14,800	Fair	-	-	Undesirable spike in pulse.

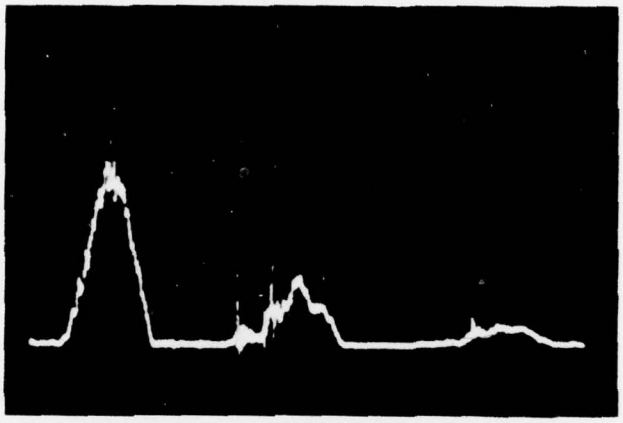

STATION 1 (MIDHEIGHT OF ROCK)

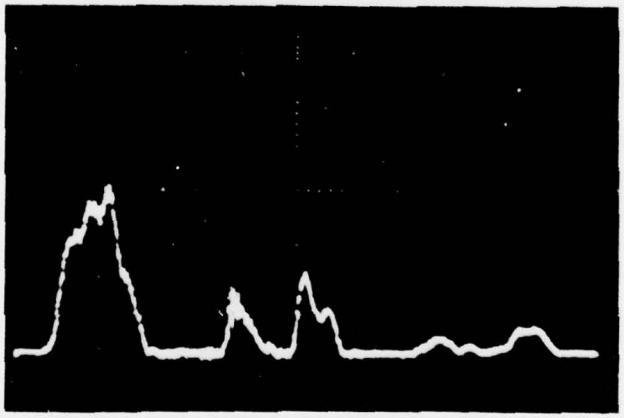

STATION 3 (BOTTOM OF ROCK)

MP-3163-63

FIGURE D-1 PRESSURE HISTORIES FOR DYNAMIC TEST DI-22 (200 μsec/div, 4 ksi/div)

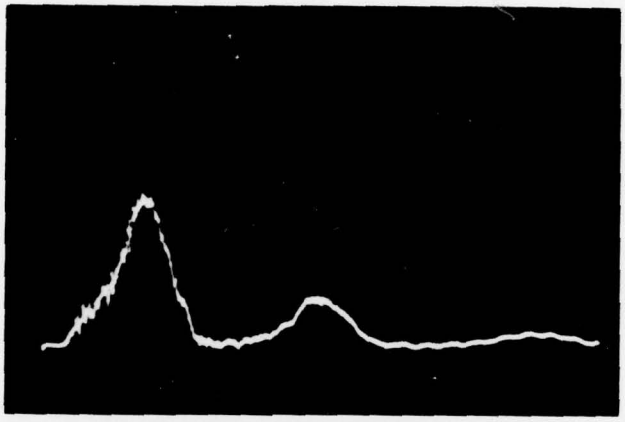

STATION 1 (MIDHEIGHT OF ROCK)

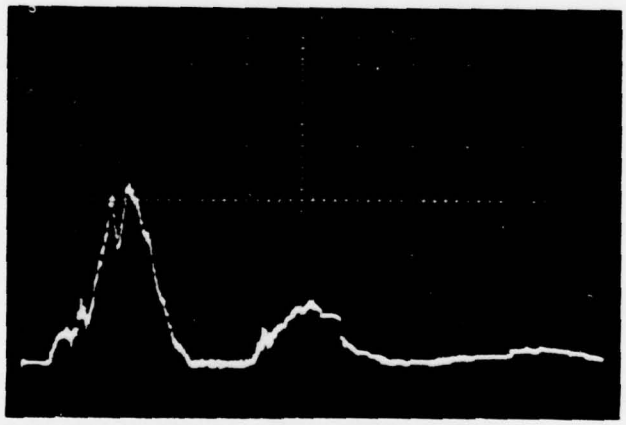

STATION 3 (BOTTOM OF ROCK)

MP-3163-64

FIGURE D-2 PRESSURE HISTORIES FOR DYNAMIC TEST DI-27 (200 μsec/div, 4 ksi/div)

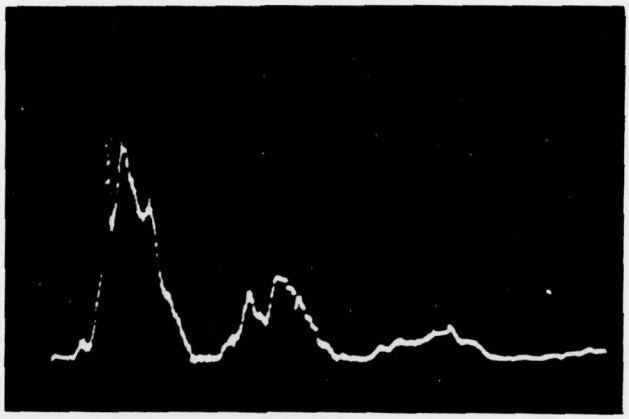

STATION 1 (MIDHEIGHT OF ROCK)

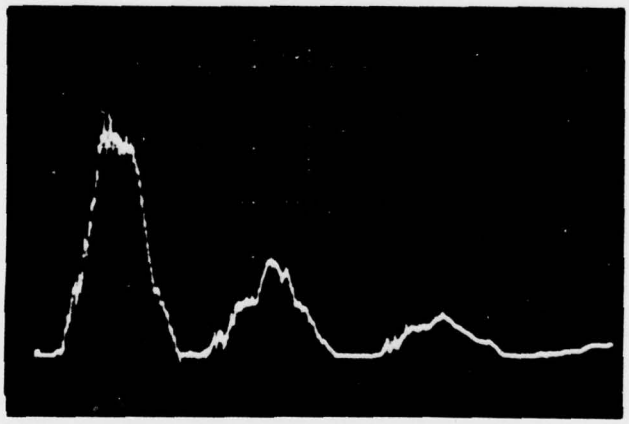

STATION 3 (BOTTOM OF ROCK)

MP-3163-65

FIGURE D-3 PRESSURE HISTORIES FOR DYNAMIC TEST DI-28 (200 μsec/div, 4 ksi/div)

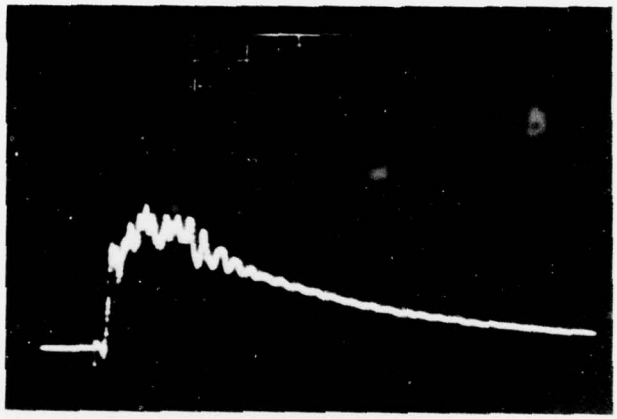

STATION 1 (MIDHEIGHT OF ROCK)

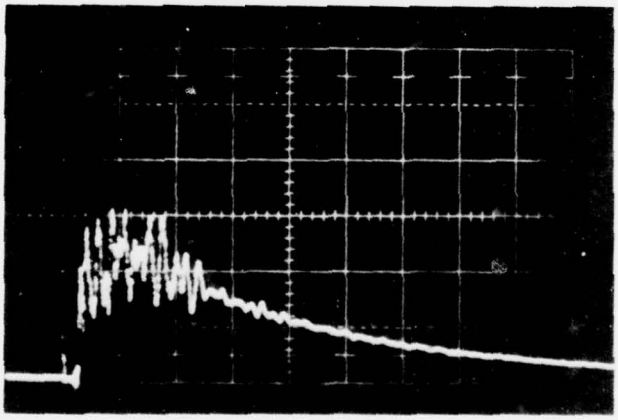

STATION 3 (BOTTOM OF ROCK)

MP-3163-66

FIGURE D-4 PRESSURE HISTORIES FOR DYNAMIC TEST DI-38 (1 msec/div, 4 ksi/div)

DISTRIBUTION LIST

DEPARTMENT OF DEFENSE

Assistant to the Secretary of Defense
Atomic Energy
ATTN: Honorable Donald R. Cotter

Director
Defense Advanced Rsch Proj Agency
ATTN: NMRO
ATTN: PMO
ATTN: STO
ATTN: Technical Library

Director
Defense Civil Preparedness Agency
ATTN: Admin Officer
ATTN: Staff Dir Resr, George N. Sisson

Defense Documentation Center
12 Cy ATTN: TC

Director
Defense Intelligence Agency
ATTN: DB-4C, Edward O'Farrell
ATTN: Technical Library
ATTN: DT-2 Wpns & Sys Div

Director
Defense Nuclear Agency
ATTN: DDST
ATTN: STSI, Archives
3 Cy ATTN: STTL, Technical Library
4 Cy ATTN: SPSS

Director
Defense Rsch & Engineering
ATTN: S&SS(OS)

Commander
Field Command, DNA
ATTN: FCPR
ATTN: FCTMOF

Director
Interservice Nuclear Weapons School
ATTN: Document Control

Director
Joint Strat Tgt Planning Staff, JCS
ATTN: STINFO Library

Chief
Livermore Division, FC, DNA
ATTN: FCPRL

DEPARTMENT OF THE ARMY

Director
BMD Advanced Tech Ctr
Huntsville Off
ATTN: ICRDABH-X
ATTN: CRDABH-S

Director
Construction Engineering Rsch Lab
ATTN: CERL-SL

DEPARTMENT OF THE ARMY (Continued)

Dep Chief of Staff for Rsch Dev & Acq
ATTN: Technical Library

Chief of Engineers
ATTN: DAEN-MCE-D
ATTN: DAEN-RDM

Dep Chief of Staff for Ops & Plans
ATTN: Technical Library

Commander
Harry Diamond Laboratories
ATTN: DRXDO-TI, Technical Library
ATTN: DRXDO-NP

Commander
Redstone Scientific Information Ctr
ATTN: Chief, Documents

Director
US Army Ballistic Research Labs
ATTN: W. Taylor
ATTN: DRXBR-X, Julius J. Meszaros
ATTN: Technical Library, Edward Baicy

Commander
US Army Communications Cmd
ATTN: Technical Library

Commander
US Army Engineer Center
ATTN: ATSEN-SY-L

Division Engineer
US Army Engineer Div Huntsville
ATTN: HNDED-SR

Division Engineer
US Army Engineer Div Ohio River
ATTN: Technical Library

Director
US Army Engr Waterways Exper Sta
ATTN: Technical Library
ATTN: John N. Strange
ATTN: James Ballard
ATTN: William Flathau
ATTN: Richard Stowe
ATTN: Paul Mlakar

Commander
US Army Mat & Mechanics Rsch Ctr
ATTN: Technical Library

Commander
US Army Materiel Dev & Readiness Cmd
ATTN: Technical Library

Commander
US Army Mobility Equip R&D Ctr
ATTN: Technical Library

Commander
US Army Nuclear Agency
ATTN: Technical Library

DEPARTMENT OF THE NAVY

Chief of Naval Material
ATTN: MAT 0323

Chief of Naval Operations
ATTN: OP 03EG
ATTN: OP 981

Chief of Naval Research
ATTN: Technical Library
ATTN: Code 464, Jacob L. Warner
ATTN: Code 464, Thomas P. Quinn
2 Cy ATTN: Nicholas Perrone

Officer-In-Charge
Civil Engineering Laboratory
ATTN: Stan Takahashi
ATTN: Technical Library
ATTN: Warren Shaw

Commander
David W. Taylor Naval Ship R&D Ctr
ATTN: Code L42-3 Library

Commander
Naval Facilities Engineering Command
ATTN: Technical Library

Superintendent (Code 1424)
Naval Postgraduate School
ATTN: Code 2124, Tech Rpts Librarian

Director
Naval Research Laboratory
ATTN: Code 2600, Technical Library

Commander
Naval Sea Systems Command
ATTN: ORD-91313, Library

Commander
Naval Ship Engineering Center
ATTN: Technical Library

Commander
Naval Ship Rsch and Development Ctr
ATTN: Technical Library

Commander
Naval Surface Weapons Center
ATTN: Code WX21, Technical Library

Commander
Naval Surface Weapons Center
Dahlgren Laboratory
ATTN: Technical Library

Director
Strategic Systems Project Office
ATTN: NSP-43, Technical Library

DEPARTMENT OF THE AIR FORCE

AF Geophysics Laboratory, AFSC
ATTN: LWW, Ker C. Thompson
ATTN: SUOL AFCRL Rsch Library

AF Institute of Technology, AU
ATTN: Library, AFIT Bldg 640, Area B

DEPARTMENT OF THE AIR FORCE (Continued)

AF Weapons Laboratory, AFSC
ATTN: SUL
ATTN: DEP, Jimmie L. Bratton
ATTN: DES-S, M. A. Plamondon

Headquarters
Air Force Systems Command
ATTN: DLCAW
ATTN: Technical Library

Commander
Foreign Technology Division, AFSC
ATTN: TD-BTA, Library

Hq USAF/PR
ATTN: PRE

Hq USAF/RD
ATTN: RDQSM

Commander
Rome Air Development Center, AFSC
ATTN: EMTLD, Doc Library

SAMSO/MN
ATTN: MNN

Commander in Chief
Strategic Air Command
ATTN: NRI-STINFO Library

ENERGY RESEARCH & DEVELOPMENT ADMINISTRATION

University of California
ATTN: Larry W. Woodruff, L-96
ATTN: Technical Info Dept L-3

Los Alamos Scientific Laboratory
ATTN: Doc Control for Reports Library

Sandia Laboratories
Livermore Laboratory
ATTN: Doc Control for Technical Library

Sandia Laboratories
ATTN: Doc Control for 3141 Sandia Rpt Coll

US Energy Rsch & Dev Admin
Albuquerque Operations Office
ATTN: Doc Control for Technical Library

US Energy Rsch & Dev Admin
Division of Headquarters Services
ATTN: Doc Control for Class Technical Library

US Energy Rsch & Dev Admin
Nevada Operations Office
ATTN: Doc Control for Technical Library

Union Carbide Corporation
Holifield National Laboratory
ATTN: Doc Control for Technical Library
ATTN: Civil Def Res Proj

OTHER GOVERNMENT AGENCIES

Department of Interior
Bureau of Mines
ATTN: Technical Library

DEPARTMENT OF DEFENSE CONTRACTORS

Aerospace Corporation
ATTN: Tech Info Services

Agbabian Associates
2 Cy ATTN: M. Agbabian

Applied Theory, Inc.
2 Cy ATTN: John G. Trulio

Avco Research & Systems Group
ATTN: Research Library A830, Rm 7201

Battelle Memorial Institute
ATTN: Technical Library

The BDM Corporation
ATTN: Technical Library

The Boeing Company
ATTN: Aerospace Library
ATTN: Robert Pyrdahl

California Research & Technology, Inc.
ATTN: Sheldon Shuster
ATTN: Ken Kreyenhagen
ATTN: Technical Library

Calspan Corporation
ATTN: Technical Library

Civil/Nuclear Systems Corporation
ATTN: Robert Crawford

University of Dayton
Industrial Security Super KL-505
ATTN: Hallock F. Swift

Unversity of Denver
ATTN: Sec Officer for Fred P. Venditti
ATTN: Sec Officer for J. Wisotski

EG&G, Inc.
Albuquerque Division
ATTN: Technical Library

The Franklin Institute
ATTN: Zenons Zudans

Gard, Inc.
ATTN: G. L. Neidhardt

General Electric Company
TEMPO-Center for Advanced Studies
ATTN: DASIAC

IIT Research Institute
ATTN: R. E. Welch
ATTN: Milton R. Johnson
ATTN: Technical Library

Institute for Defense Analyses
ATTN: IDA Librarian, Ruth S. Smith

Kaman Avidyne
ATTN: Technical Library
ATTN: E. S. Criscione
ATTN: Norman P. Hobbs

DEPARTMENT OF DEFENSE CONTRACTORS (Continued)

Kaman Sciences Corporation
ATTN: Library

Lockheed Missiles & Space Company
ATTN: Technical Info Ctr D/Coll
ATTN: Tom Geers, D/52-33, Bldg 205

Lovelace Foundation for Medical Education & Research
ATTN: Assist Dir of Res, Robert K. Jones
ATTN: Technical Library

McDonnell Douglas Corporation
ATTN: Robert W. Halprin

Merritt Cases, Inc.
ATTN: Technical Library

The Mitre Corporation
ATTN: Library

Newmark, Nathan M.
ATTN: Nathan M. Newmark
ATTN: William Hall

Physics International Company
ATTN: Doc Control for Robert Swift
ATTN: Doc Control for Charles Godfrey
ATTN: Doc Control for E. T. Moore
ATTN: Doc Control for Dennis Orphal
ATTN: Doc Control for Larry A. Behrmann
ATTN: Doc Control for Technical Library

R&D Associates
ATTN: William B. Wright, Jr.
ATTN: Albert L. Latter
ATTN: Harold L. Brode
ATTN: Jerry Carpenter
ATTN: Henry Cooper
ATTN: J. G. Lewis
ATTN: Robert Port
ATTN: Technical Library

Science Applications, Inc.
ATTN: D. E. Maxwell
ATTN: David Bernstein

Science Applications, Inc.
ATTN: Technical Library

Southwest Research Institute
ATTN: Wilfred E. Baker
ATTN: A. B. Wenzel

Stanford Research Institute
ATTN: George R. Abrahamson
ATTN: H. Lindberg
ATTN: T. C. Kennedy

Systems, Science and Software, Inc.
ATTN: Donald R. Grine
ATTN: Technical Library

Terra Tek, Inc.
ATTN: Sidney Green
ATTN: Technical Library

Tetra Tech, Inc.
ATTN: Li-San Hwang
ATTN: Technical Library

DEPARTMENT OF DEFENSE CONTRACTORS (Continued)

TRW Systems Group
ATTN: Tech Info Center/S-1930
2 Cy ATTN: Peter K. Dai, R1/2170

TRW Systems Group
ATTN: E. Y. Wong, 527/712

Universal Analytics, Inc.
ATTN: E. I. Field

URS Research Company
ATTN: Technical Library

Wang, The Eric H.
Civil Engineering Rsch Fac
ATTN: Larry Bickle
ATTN: Neal Baum

DEPARTMENT OF DEFENSE CONTRACTORS (Continued)

Washington State University
Administrative Office
ATTN: Arthur Miles Hohorf for
George Duval

Weidlinger Assoc Consulting Engineers
ATTN: Melvin L. Baron

Weidlinger Assoc Consulting Engineers
ATTN: J. Isenberg

Westinghouse Electric Company
Marine Division
ATTN: W. A. Volz